Examining the developmental roles of STRIPAK components, FARL-11 and CASH-1, in *C. elegans*

By

Sterling C.T. Martin

A dissertation submitted in partial fulfillment of the requirements for the degree of

Doctor of Philosophy

(Biophysics)

at the

UNIVERSITY OF WISCONSIN-MADISON

2022

Date of final oral examination: May 6th, 2022

The dissertation is approved by the following members of the Final Oral Committee:

Jeff Hardin, Professor, Integrative Biology
Melissa Harrison, Associate Professor, Biomolecular Chemistry
Yongna Xing, Professor, Oncology
Claire Richardson, Assistant Professor, Genetics
Silvia Cavagnero, Professor, Chemistry

ACKNOWLEDGEMENTS

Shí éí Sterling Martin *yinishyé. Kinłichii'nii nishłį. Tódichi'ii'nii bashishchiin. Bit'ahnii shicheii. Táchii'nii shinalí. Ákót'éego Diné nishłį. T'iis Názbąs déé' naashá. Shimá ei* Delphine McThomas, *dóó shizhé'é ei* Leo Martin. *Shimásani eí* Doris McThomas.

Firstly, I would like to thank the *C. elegans* that gave their lives and progeny so I may contribute to the scientific body of knowledge; your loss is not in vain. I would like to thank my advisor Jeff Hardin for allowing me to follow my intellectual curiosity and to develop my own project. Thank you for keeping the lab funded throughout my tenure here. To a previous lab member Elise Walck-Shannon, I would like to give many thanks. As my unofficial Genetics professor, you taught me all the advanced genetics I know, and always answered any crazy genetic question I had, including heterozygous disadvantage. To our (former) Postdoc Joanna Bundus, I would like to say thanks for coming into the lab at the perfect time. You helped quell my fears about the next step and reassured me it's going to be okay. To Bryan Lakey and Katie Wozniak: I'm so glad to call you my friends, and I am excited to see what unique path you forge for yourselves. Thank you so much for all the laughs, memories, and visits to "The Library"; they helped me get through those tough lab days and also gave me something to look forward to. Devi Santhosh, thank you for checking in on me and always making room in your busy schedule for my impromptu calls and texts. To my DnD group, thanks for providing me a weekly afternoon of fun that made sure I didn't forget to get out of lab. Mary Susan Lopez, my partner in crime "nuff" said.

Finally, to Joel Serre, my fellow comrade *in-pipette* I would be no where without you. You've been with me through this bumpy ride and helped me get through this. You were always there for whatever outrageous question I had. You helped me celebrate the successes and weather the failures. In the words of your favorite Captain, "You have been my trusted right arm for [8] years. You have kept my course true and steady… I wish you clear horizons. My good friend, make it so". I can't wait to see where your future takes you.

To *shí k'é: shimá, shizhé'é, shimásani, dóó shitsilí*, the word *ahé'éé* can't even begin to explain everything you've done for me. You helped me grow and become the person and n*a'alkaahí* I am today. I am so proud to be called your *níyaazh, niye, ninaaí dóó hatsóī ashkiígíí. Ákót'éego Diné nishlį*.

To everyone else there isn't enough room in the world to express my gratitude. Thank you so much for, the laughs, the joy, the memories, everything. This would not at all be possible without you. This thesis is not mine alone; a part of it is yours as well.

TABLE OF CONTENTS

ABSTRACT

The STRIPAK (STRiatin Interacting Phosphatase And Kinase) Complex is an evolutionarily conserved Protein Phosphatase 2A (PP2A) holoenzyme complex found in all metazoans. How the STRIPAK complex functions in a living organism is therefore of great interest. While substantial effort has been expended to elucidate the *in vitro* interactions an assembly of STRIPAK components, the roles of STRIPAK *in vivo* remain poorly illuminated. Chapter 1 of this thesis briefly reviews what is known about STRIPAK function in various standard model organisms, and identifies several key unanswered questions addressed within the remainder of this thesis. In Chapter 2 I use *C. elegans* as a model organism to uncover functions of STRIPAK during animal development. As early as the first cytokinetic event, I show that the STRIPAK components FARL-11/Strip and CASH-1/Striatin function to prevent ectopic contractile events at the cell cortex. Given that Striatin is the structural backbone of the STRIPAK complex, I go on to demonstrate that individual domains of CASH-1 are essential for its function, not only by affecting the localization pattern of FARL-11, but also by regulating clustering and activity of the Centralspindlin component ZEN-4/MKLP1. The most parsimonious model based on my results is that STRIPAK, via its enzymatic activity as a phosphatase holoenzyme, may regulate the phosphostatus, and hence activity, of ZEN-4. In Chapter 3, I show that CASH-1/Striatin and FARL-11/Strip are both necessary for organizing sarcomeres; in particular, STRIPAK is necessary for spatial localization and organization of the sarcoplasmic reticulum in body wall muscle. In Chapter 4 I suggest areas for future study, including further exploration of the intriguing DLG-1/AJM-1-dependent localization of STRIPAK components at epidermal junctions during embryonic elongation, when the epidermis is subject to mechanical tension. The Appendices of this thesis document additional work I have done to generate reagents for single-

molecule mechanobiological analysis of HMP-1/α-catenin, and to explore the role of salt-bridge-dependent stabilization of the HMP-1 M domain in recruitment of SRGP-1/srGAP at junctions during morphogenesis. Taken together, these experiments make novel contributions to our understanding of key conserved molecular complexes that regulate the cell cortex and cell-cell junctions in all metazoans.

CHAPTER 1

Unpacking STRIPAK: A Multipurpose Complex for Building Better Tissues

My contributions to this work were writing the rough draft and creating the figures

Summary

The Stratin Interacting Phosphatase and Kinase (STRIPAK) complex is an evolutionarily conserved multiprotein complex found in all metazoans. Since its discovery in 2009, significant effort has been directed toward determining its biochemical properties in vitro. However, the *in vivo* functional roles of the STRIPAK complex have only recently begun to be elucidated. Here we discuss work done in major model organisms (the mouse, *Mus musculus*, the nematode, *C. elegans*, the zebrafish, *Danio rerio*, and the fruit fly, *Drosophila melanogaster*). We discuss findings from work in these model organisms that implicate STRIPAK in JNK and Hippo signaling, intracellular trafficking, cell migration, and cell division. While these studies have identified several roles for the STRIPAK complex *in vivo*, they raise additional questions. These include how STRIPAK-dependent regulation might serve as a hub for integrating cell signaling, how the complex leads to spatially specific regulation of the endomembrane system, and how it is dynamically assembled at precise locations to regulate PP2A phosphotargets. This thesis addresses novel aspects of STRIPAK function, particularly the core components FARL-11/Strip ad CASH-1/Striatin by harnessing the power of *C. elegans* as a model organism in multiple cellular contexts.

Introduction: STRIPAK Is "Complex"

Cells face a continual and fundamental regulatory challenge. Many of the thousands of different proteins any particular differentiated cell produces must be post-translationally modified in precise ways. There is often spatial specificity to these modifications, so that subpopulations of precisely post-translationally modified proteins reside in specific cellular subcompartments. One common set of post-translational modifications involves tight maintenance of phosphorylation of cellular proteins on serines, threonines and tyrosines by the opposing effects of kinases and phosphatases. Protein Phosphatase 2A (PP2A) is a major serine/threonine phosphatase that modulates the activity of myriad protein targets (Sandal et al., 2021; Reynhout and Janssens, 2019). The standard nomenclature might lead to the erroneous conclusion that PP2A is a single enzyme. In fact, however, there are a variety of PP2A macromolecular complexes (Fig. 1). Each possesses a core enzyme, which contains an A-structural subunit and a C-catalytic subunit.

The essential PP2A A-C heterodimer interacts with various B-regulatory subunits, which are thought to bring specificity to the core enzyme by facilitating the arrival of various assembled PP2A complexes to their correct subcellular locations, and by allowing such complexes to interact with the correct target (Shi, 2009; Virshup and Shenolikar, 2009). These B regulatory subunits are thought to fine-tune the activity of PP2A; this inference arises from the effects of loss of single B regulatory subunits, which tends to result in less severe phenotypes than loss of the entire PP2A holoenzyme (Neal et al., 2020; Reynhout and Janssens, 2019; Neisch et al., 2017)(e.g., *C. elegans*; this thesis).

PP2A B subunits fall into several classes. These include the B (B55), B' (B56), and B'' (PR72/130) subunits, which associate with the A and C subunits to form heterotrimeric holoenzyme complexes. The fourth B regulatory subunit (B’’’), depends on the protein B''''/Striatin/STRN3/STRN4 to assemble a much larger complex of proteins that function as the B regulatory component known as the *STRIPAK (STRiatin Interacting Phosphatase And Kinase) complex,* which is the focus of this review. Striatin contains a coiled-coil region and a WD40 repeat (Fig. 2). The coiled-coil and WD40 domains are thought to feature prominently in the functions of Striatin in assembly of the STRIPAK complex and in facilitating interaction of the assembled complex with its targets, respectively.

The STRIPAK complex is evolutionarily conserved from yeast to humans (Hwang and Pallas, 2014). Striatin forms the backbone of the complex (Figure 2A), (Moreno et al., 2000; Ribeiro et al., 2010; Goudreault et al., 2009; Jeong et al., 2021), and is thought to target the STRIPAK complex to subcellular compartments via the WD40 scaffold domain (Shi, 2009). A crystal structure revealed that Striatin undergoes homodimerization mediated by a non-canonical coiled-coil domain containing three conserved leucines; when this domain is disrupted Striatin no longer associates with the PP2A core enzyme (Chen et al., 2014).

In the original tandem affinity purification (TAP) and FLAG affinity purification screen for PP2A catalytic subunit interactors various members of the STRIPAK complex were discovered, including Striatin, Striatin Interacting proteins 1 and 2 (STRIP1 and 2), the GCK-III family of Ste20 protein kinases (STK24, STK25, and MST4), and cerebral cavernous malformation protein 3 (CCM3) (Goudreault et al., 2009). Additional proteins identified in this screen included

cortactin-binding protein 2, N-terminal-like (CTTNBP2NL), sarcolemmal membrane-associated protein (SLMAP) and SIKE/FGFR10P2. CTTNBP2NL and SLMAP were identified as potentially mutually exclusive binding partners (Goudreault et al., 2009).

While the proteomics work implicated numerous proteins in STRIPAK assembly and function, the stoichiometric details of the entire assembled complex remained unclear. A recent cryoEM structure of the human STRIPAK complex sheds additional light on the structure of the fully assembled STRIPAK complex (Jeong et al., 2021). The structure revealed that, unlike canonical PP2A holoenzymes, STRIPAK comprises four STRN3 protomers that homotetramerize to form a backbone to which the rest of the complex is attached (Fig. 2A). The N-terminal coiled-coil (CC) domains of STRN3 proteins mediate the homotetramerization, which is consistent with data from a previous crystal structure. Significantly, the cryoEM structure revealed that, unlike other PP2A holoenzymes, the PP2A catalytic subunit does not make contact with Striatin, but instead only makes direct contact with the structural subunit, PP2A-A. Based on the cryoEM structure, STRIP1 mediates the PP2A structural subunit association with Stratin.

A single WD40 domain from one of the STRN3 protomers is resolved in the structure of Jeong et al. The remaining three WD40 domains are not resolved, suggesting a high degree of mobility or flexibility. Jeong et al speculate that the additional WD40 domains are part of a tentacular "search and capture" mechanism by which the complex binds its targets, "reeling" them in so that they can be dephosphorylated by the PP2A complex (Fig. 2B). The cryoEM structure also revealed that STRIP1 acts as a potential hub within the STRIPAK complex, interacting with the structural PP2A subunit, PP2A-C as well as STRN3; STRIP1 interacts with one side of the

immobile WD40 domain, while the other side binds MOB4. Perturbations of any of the binding interfaces disrupted STRIPAK assembly, with the STRN3-MOB4 interaction being the exception (Jeong et al., 2021).

STRIP1 may interact with PP2A substrates to contribute to the specificity of STRIPAK substrates (discussed in (Huang et al., 2021)). In addition, Jeong et al found an inositol hexaphosphate (IP_6) molecule bound at the center of STRIP1. Whether inositide signaling regulates STRIPAK complex function is an interesting question for future investigation.

While substantial progress has recently been made in understanding how the basic STRIPAK complex assembles, identifying functionally relevant targets of the STRIPAK complex has been difficult. A powerful complement to biochemical and structural biological analysis of STRIPAK is the functional characterization of subcellular pathways regulated by the STRIPAK complexes. Model organisms that permit genetic dissection of functionally relevant pathways regulated by the STRIPAK complex have been key to this complementary analysis. The remainder of this review focuses on several pathways affected by STRIPAK that have been identified using major model organisms: mouse (*Mus musculus*), nematodes (*Caenorhabditis elegans*), zebrafish (*Danio rerio*), and fruit flies (*Drosophila melanogaster*).

STRIPAK and cell signaling pathways

Signal transduction is well known to be regulated by modulation of the phosphostatus of various signal transduction components. Thus it might not be surprising that the STRIPAK complex would be implicated in cellular signaling cascades. Recent work has identified roles for

STRIPAK in two evolutionarily conserved pathways: Jun N-terminal kinase (JNK) and Hippo signaling.

JNK Signaling and the STRIPAK complex

The morphogenetic movement known as dorsal closure in *Drosophila* is well known to depend on Jun-N-terminal kinase signaling, which is important for specifying cell identity and function around the edges of the closing epidermis (Ríos-Barrera and Riesgo-Escovar, 2013; Mishra et al., 2021; Noselli and Agnès, 1999; Harden, 2002). The STRIPAK complex has been implicated in JNK signaling in *Drosophila*; Striatin/Cka (Connector of kinase to AP-1) has been shown to bind DJun and DFos in embryonic lysates (Chen et al., 2002). *Cka* genetically interacts with the JNK *basket* (*bsk*) and FOS/*kayak*. Loss of *Cka* function (via a p-element induced mutation) results in dorsal closure defects with mislocalized Decapentaplegic/BMP. Loss of *cka* function in weak hypomorphic alleles for kay^{2} and bsk^{1} caused enhancement of the dorsal open phenotype, whereas constitutively activated *Djun* or *hemipterous* (*hep*/JNKK) rescues the dorsal open phenotype in *cka* mutants. These results together suggest that Cka positively regulates the JNK pathway during dorsal closure.

Interestingly, in a separate *Drosophila* tissue, the testis, a core member of the STRIPAK complex, *strip*, was found to negatively regulate JNK signaling during spermatogenesis (La Marca et al., 2019). The mutant *jam packed* (*jam*) is an allele of *Strip*, and Cka RNAi knockdown was shown to be important for spermatogenesis in the *Drosophila* L3 male gonad. The resulting phenotypes caused disruptions in the morphology and differentiation of the gonads, which could be attributed to increased JNK signaling, as shown by elevated phosphorylated JNK

and Matrix metalloproteinase 1 (a target of JNK signaling) (Uhlirova and Bohmann, 2006). STRIPAK was genetically linked with JNK signaling, as lowering the genetic dosage of *bsk* (via RNAi) or Bsk activity (via bsk^{DN}) can partially rescue the *jam* gonadal defects.

A similar connection between JNK signaling and STRIPAK was identified in the zebrafish *Danio rerio* (Ahmed et al., 2022). Embryos homozygous for a *strip1* allele (*rw147)* or a CRISPR generated $strip^{\Delta 10}$ allele exhibit apoptotic death of the retinal ganglion cells (RGCs). The authors noted by day 6 post fertilization $strip1^{rw147}$ embryos died due to cardiac edema which has also been reported for morpholino knockdown of *Strip2* in zebrafish (Wagh et al., 2014). As might be expected, Strn3 was identified as a Strip interactor by mass spectrometry; *strn3* knockdown also causes RGC death. RNAseq using eye cups from $strip1^{rw147}$ mutants, as well as optic nerve injury experiments, showed genes involved in MAPK signaling were upregulated, particularly *jun* which was further confirmed by increased p-Jun staining. To further confirm the role of *strip* in JNK signaling, knockdown of *jun* was able to rescue the RGC apoptosis. Interestingly, overexpression of the apoptotic gene Bcl2 in neurons was able to rescue excess apoptosis of $strip1^{rw147}$ but did not rescue a second defect in dendrite projection. This result suggest that the apoptosis defect is due to JNK signaling, while the innervation defect could be due to a trafficking defect, since Strip1 has been shown to be involved in neuronal elongation in *Drosophila (Sakuma et al., 2014)* (see below).

Hippo Signaling and STRIPAK

Hpo and STRIPAK in developing tissues

STRIPAK has been implicated in a second major signaling pathway. In *Drosophila* the STRIPAK complex has been shown to genetically interact with the Hippo (Hpo) (Ribeiro et al., 2010). The STRIPAK component SLMAP appears to mediate the interaction with Hpo (Zheng et al., 2017). coIP revealed that the forkhead-associated (FHA) domain of SLMAP interacts with Hpo through 4 different threonine residues in the linker region, with T356 being the most important (Zheng et al., 2017). To further confirm the Slmap interaction, Slmap was depleted in the wing imaginal disc of *Drosophila*, resulting in the reduction of the posterior compartment of adult wings. This reduction in wing size closely phenocopies the results seen with Cka or Fgop2 depletion (Ribeiro et al., 2010) or the use of a *hpo* mutant unable to bind Slmap (Ribeiro et al., 2010). Furthermore, a CRISPR generated 19-bp deletion of *slmap* (*slmap*^{4}) showed elevated levels of Hpo phosphorylation in the eye and antennal imaginal discs. Interestingly, the basis of this Hpo-STRIPAK interaction was argued to be dependent on the interaction of Hpo with Slmap but not with the core B''' regulatory subunit (Cka), as FLAG-Cka was able to coIP with Hpo in a WT background but not in a *slmap*^{4} background. Intriguingly, this is different from the situation with JNK signaling, where the B''' regulatory subunit was shown to bind to JNK (see Chapter 3 of this thesis).

In an affinity purification coupled with mass spectrometry, and a genome wide RNAi screen Microtubule Star (Mts; a catalytic subunit of PP2A) and Cka were identified to interact with Hpo from *Drosophila* S2 cells (Ribeiro et al., 2010). *In vivo,* overexpression of Hpo using the Glass Multimer Reporter (GMR) causes apoptosis to occur, resulting in a decrease in adult eye size; this phenotype was enhanced by reducing the genetic dosage of *cka* or a *FGOP2/ FGFR1 oncogene partner 2*. FGOP2 was shown to bind to SLMAP in a yeast two hybrid(Giot et al.,

2003) and functions as linker between the Hpo and STRIPAK complex (Zheng et al., 2017). Interestingly, following *hpo* and *cka* depletion, the wings were undersized. The undersized wings could be due to the role of *cka* in other pathways, a prime candidate being JNK-mediated apoptosis. Moreover, the downstream target *expanded* (*ex*) (which encodes a Band 4.1 family member) showed increased expression when *warts* (*wts,* the Lats kinase homologue*)* was depleted via RNAi, while *FGOP2* or *Cka* RNAi depletion caused an increase in *ex* expression. That the genetic interaction of the Hippo pathway with STRIPAK is specific is suggested by the fact that knockdown of other phosphatases and other PP2A-B regulatory subunits did not phenocopy these effects.

In addition to effects on tissue growth in imaginal discs, a STRIPAK/Hippo interaction has been demonstrated in a cell fate choice in the *Drosophila* retina (Neal et al., 2020). In an RNAi screen, Cka knockdown was revealed to cause the eye disc to lose the peripodial epithelium and switch its fate to a retinal identity, thereby causing a "double retina" phenotype, a phenotype replicated in Cka^{05836}/Cka^{S1883} mutants. That the double retina phenotype is PP2A specific was confirmed using a CKA-RNAi sensitized background along with recessive loss of function for *mts,* which led to a 100% penetrant double retina phenotype. Similarly, *Strip* and *Slmap* RNAi also caused a double retina phenotype. To further tie STRIPAK to the Hpo pathway, reducing *hpo* (either via knockdown or loss of function) rescued the *Cka, Strip, and Slmap*-RNAi double retina phenotype. The rescue of the double retina phenotype was also seen in wts^{X1} heterozygotes, further confirming STRIPAK genetically interacts with *hpo*. Lastly, overexpression of Yorkie (Yki), the YAP homologue, was able to rescue the Cka-RNAi phenotypes.

STRIPAK and Hippo signaling in non-developmental contexts

Postmitotically, STRIPAK has been shown to interact with Hippo to regulate synaptic terminal structures at the neuromuscular synapse in *Drosophila (Sakuma et al., 2016b)*. A CRISPR generated Strip-myc localizes to presynapses; knockdown of *strip* via RNAi caused an increase in the number of satellite boutons at the end of the neurons (which could be rescued with a *strip* transgene). Similar to other contexts, a *wts* heterozygous background or *wts* knockdown was able to suppress the effects of *strip* knockdown. Intriguingly, a significant difference from other studies emerged when epistasis experiments with *strip* and *yki* failed to demonstrate an interaction: overexpressing Yki was not able to rescue the *strip* knockdown phenotypes, nor did *yki* mutants alone show an increase in satellite bouton number. It was ultimately determined that Wts phosphorylates Ena/VASP at residue 187, which in turn regulates F-actin organization at the synapse. Functional confirmation of this result was provided by a EnaS187A phosphomutant, which suppressed the satellite bouton phenotype of *strip* knockdown; conversely, the phosphomimetic EnaS187D mutant did not. Taken together, these results indicate a postmitotic role for the Hippo pathway, modulated by the STRIPAK complex, which regulates the phosphostatus of Ena. This result further highlights the challenge of elucidating indirect regulation of subcellular pathways by STRIPAK, including the F-actin cytoskeleton.

The STRIPAK complex has also been implicated in Hippo-dependent regulation of the innate immune response to Gram-positive bacteria in *Drosophila (Liu et al., 2016)*. Hippo was implicated in the innate immune response as *mats* (mob as a tumor suppressor, a coactivator of Wts kinase) mutants were shown to be susceptible to Gram-positive infections. STRIPAK was further tied to this pathway, as it had been shown to be important for regulating Thr 195 of Hpo

(Ribeiro et al., 2010) via Cka. Examining larval fat bodies revealed that *cka* mutants display cytoplasmic localization of Yki, suggesting Hpo activation. Coexpression of the protein kinase Pelle (PII) and Cka caused reduced mobility of Cka on an SDS-gel, suggesting that PII phosphorylates Cka; moreover, Pll overexpression in fat bodies revealed a decrease in Cka levels (via staining), suggesting that that phosphorylated Cka undergoes preferential degradation. Fat body-specific knockdown of Cka caused decreased *cactus* mRNA levels (Cactus, an inhibitory Dorsal-binding protein, normally inhibits antimicrobial peptide expression) and increased *drs* mRNA levels (Drosomycin is an antimicrobial peptide) in infected adult flies. Overall, these results suggest a model in which Pelle kinase regulates Cka/STRIPAK, which in turn regulates Hpo signaling upon Gram-positive bacterial infection.

The foregoing studies suggest that STRIPAK can regulate Hippo pathway function developmentally during cell proliferation and in the developing eye, as well as post-mitotically at neuromuscular junctions and in innate immunity. These studies raise several questions. First, does the STRIPAK/Hippo interaction extend to other tissues? Second, given that JNK signaling can also regulate cell proliferation and differentiation, is there crosstalk between JNK and Hippo signaling? Addressing these questions in the *Drosophila* system, and determining whether these interactions can be generalized to other organisms, are interesting areas for future study.

STRIPAK and trafficking

A consistent finding across higher eukaryotes is that STRIPAK localizes to the endomembrane system, including the endoplasmic reticulum and Golgi (for *C. elegans*, see Chapters 2 and 3 of this thesis). Studies in various model organisms implicate the STRIPAK complex in a variety of

cellular events known to be regulated by vesicular trafficking. In this section I review what has been learned about the STRIPAK complex in vesicular trafficking in the *Drosophila* neuron and how those principles can be applied to tubulogenesis in *C. elegans* and mesodermal migration in *Mus musculus*.

Neurogenesis in Drosophila

In *Drosophila*, the STRIPAK complex was identified to regulate vesicular trafficking in neurons in multiple studies (Sakuma et al., 2014, 2016b; a; Neisch et al., 2017). In $Strip^{dogi}$ mutants there were defects in axon elongation and dendrite branching of olfactory neurons. The Strip interactome was further refined via a yeast-two-hybrid screen, which identified p150glued and Sprint, a GEF for Rab5, as Strip binding partners (Sakuma et al., 2014). Functional roles for members of this interactome were also revealed, as the branching phenotype of $strip^{dogi}$ was enhanced by either expression of a dominant negative form of *Glued* or *spri* knockdown via RNAi, which resulted in shorter axons, this was only seen with this combination and never observed in the $strip^{dogi}$ mutant . Furthermore, HA-synaptotagmin (a dynein dependent cargo) and early endosomes accumulated in the axon stalk in a $strip^{dogi}$ background. Decreased axon elongation was shown to be a result of STRIPAK regulation of Rab5: *rab5* null mutants phenocopied the $strip^{dogi}$ neuronal branching defect while also phenocopying the axon shortening seen in the double mutants. A constitutively active form of Rab5 was able to rescue the early endosome defect in $strip^{dogi}$ mutants, and was able to partially rescue the short axon phenotype; this phenotype was enhanced in a dominant-negative Rab5 background. Strip could be co-immunoprecipitated with Rab5 from S2 lysates, suggesting both a physical and genetic interaction of Rab5 and STRIPAK.

Subsequent to the initial study by Sakuma et al implicating STRIPAK in regulation of neuronal morphology, STRIP1 was also shown to influence the stability of microtubules by regulating TBCD, a tubulin-folding cofactor (Sakuma et al., 2016a). *TBCD*^{1} mutants (or overexpression) phenocopied the excessive dendrite branching and short axon phenotype of olfactory projection neurons in *strip*^{dogi} mutants (Sakuma et al., 2014) which was enhanced in in *shRNA-TBCD* or *TBCD*^{1} lines when combined with a *strip*^{dogi} mutant. Since TBCD interacts with Dscam in mushroom body neurons, Sakuma investigated whether *Dscam* and *strip* also genetically regulate mushroom body morphology. In a Dscam overexpression line the alpha and beta lobes of the mushroom body are missing; *strip*^{dogi} and *TBCD*^{1} heterozygotes could rescue this defect. It is possible that as in the olfactory projection neurons, where Strip forms a complex with Glued and Spri, that Strip forms a complex with Glued and Dscam to regulate mushroom body morphogenesis.

In addition to the studies of Sakuma and colleagues, STRIPAK has also been shown to regulate neuronal autophagosome transport via Hpo signaling (Neisch et al., 2017). Depletion of CKA via RNAi leads to accumulation of autophagosomes in terminal boutons, as does dynein RNAi, suggesting a trafficking defect. In a sensitized *syntaxin17* background there were fewer autophagosomes in axons after CKA or dynein RNAi, as well as alterations in retrograde transport, leading to an increase in anterograde and stationary autophagosomes. GFP-CKA can bind to dynein and dynactin in cell extracts, showing that Cka can complex with the entire Dynein/Dynactin complex; Strip is a candidate linker based on previous work (Sakuma et al., 2014). Cka was also shown to bind Atg18 via the Lir2 domain. Atg8 is a cytoplasmic protein that

is linked to autophagosomal membranes. A connection to autophagosomal membranes was confirmed by depletion of Strip or Mob4, which also caused robust accumulation of autophagosomes in terminal boutons. However, CCM-3 or GCKIII knockdown did not phenocopy the autophagosome accumulation, suggesting that these proteins are non-obligate members of the STRIPAK, at least as it relates to autophagosomes.

Given that STRIPAK has been implicate din Hippo signaling (see above), Neisch et al then went on to test if autophagosome transport is regulated via Hpo. Hpo depletion causes fewer terminal boutons with accumulated autophagic vesicles. Depleting both CKA and Hpo via RNAi caused a reduced accumulation of autophagic vesicles compared to CKA RNAi alone, while expression of *hpo* or phosphomimetic hpo^{T195E} caused an accumulation of autophagosomes in terminal boutons. These results suggest that STRIPAK negatively regulates Hpo activity, thereby regulating autophagosome transport. Dense core vesicle (DCV) transport and number were also affected by depletion of STRIPAK or dynein components, which also resulted in nerve swellings reminiscent of those in dynein, kinesin, and JNK mutants. To test if STRIPAK components were acting via PP2A, depletion of the PP2A structural subunit and Mts via RNAi caused an increase in accumulation of autophagosomes in terminal boutons. Dominant negative Mts also caused a significant increase in autophagosome accumulation. Taken together, this work helps expand the role of STRIPAK-mediated transport to include not merely endosome fusion (Sakuma et al., 2014), but also dense core vesicles and autophagosomes. A key question moving forward is what role Strip might be playing in helping dynein/dynactin to associate with its target vesicles.

STRIPAK and Tubulogenesis

In the *C. elegans* excretory canal, STRIPAK has been shown to be important for tube extension via endocytic recycling (Lant et al., 2015). In excretory cells, a CCM-3 transgene was shown to localize to the apical membrane, while also displaying localization along the luminal membranes of the gonad and pharynx. *ccm-3* deletion mutants are sterile (suggesting a gonadal issue) and also exhibit canal truncations. These mutants also display discontinuous lumens, cysts, swollen cytoplasmic vesicles and ectopic lumens separated from the primary lumen. These phenotypes are reminiscent of the neuronal branching phenotypes seen in *strip*^{dogi} mutants (Sakuma et al., 2014). A canal driven CCM-3 transgene was able to rescue the canal defects. GCK-1 was shown to colocalize with CCM-3 along the apical membrane and the two were able to IP from HEK293T cells (Lant et al., 2015). GCK-1 was shown to be downstream of CCM-3. Ablation of *gck-1* phenocopied the *gck-1* canal defects and a *gck-1* kinase dead transgene was not able to rescue the canal defects. In excretory cells, ablation of EXC-5 (a CDC-42 GEF) caused canal cell defects similar to loss of Spr-GEF in *Drosophila* neurons (Sakuma et al., 2014). Loss of RAB-11 (a recycling endosome component) also phenocopies the CCM-3 mutant canal defects. In a CCM-3 mutant, there were decreased levels of CDC-42 and decreased puncta containing activated CDC-42. CDC-42 is needed for endocytic trafficking, so its disruption could cause the canal cell defects, since CCM-3 mutants also had decreased recycling endosomes.

Lant et al also exploited Transmission Electron Microscopy (TEM) to assess effects on basolateral and apical membranes of canal cells in *ccm-3* mutants. They observed no rough ER or Golgi bodies in the canals as well as excess vesicles in canal cells, suggesting that a defect in recycling did not allow their incorporation into the lumen. Loss of all STRIPAK members (except MOB3 and CTTNBP2/NL) caused canal truncations. *gck-1* and *cash-1*/Striatin ablation

also caused Golgi and recycling endosomal defects. Ablation of *cdc-42* also caused canal truncation and cysts as in *ccm-3* mutants, as well as reduced Golgi and recycling endosomes. CDC-42 is predicted to be the only GTPase involved in canal cell elongation, as *rho-1* and *chw-1* (RhoU/RhoV) depletion via RNAi did not lead to canal defects. Interestingly, overexpressing *act-5*/actin was able to rescue the canal truncations in *ccm-3* mutants as well as RAB-11 puncta, possibly suggesting a role for the cytoskeleton in elongation of the canal cells. This connection to F-actin is reminiscent of the *Drosophila* neuromuscular junction, in which Ena/VASP phosphorylation is regulated via STRIPAK (Sakuma et al., 2016b).

Lant et al also investigated possible downstream components associated with CDC-42 that regulate canal cell morphogenesis. Ablation of *mrck-1* caused a reduction in Golgi and recycling endosomes and CDC-42 activity (measured using a *GBDwsp-1* reporter), suggesting CCM-3 works through MRCK-1. Elucidating what roles the rest of the STRIPAK complex plays in canal cells would be of interest, given that the rest of the complex is genetically implicated in canal cell formation. It is possible, for example, that STRIPAK regulates the phosphostatus of CDC-42 or possibly MRCK-1.

In addition to single-celled tubes such as the canal cells, the STRIPAK complex has been implicated in regulating receptor recycling in the multicellular, tubular gonad of *C. elegans (Pal et al., 2017)*. *ccm-3* and *farl-11*/Strip mutants display gonadal defects. In *ccm-3* mutants, there is defect Notch signaling, possibly due to the effect of CCM-3 on GLP-1/Notch receptor trafficking. The possibility that GLP-1 trafficking is defective in *farl-11* mutants is consistent with defects observed in *farl-11* mutants (Maheshwari et al., 2016). Furthermore, in *ccm-3*

mutants RME-2 (a recycling endosomal component) was reduced on the surface of oocytes. RAB-11, a component of the recycling endosome, was also seen to localize with RME-2 in *ccm-3* mutants. Defective recycling may explain gonadal defects; prevention of the expansion of the gonad may result from lower levels of activated CDC-42 similar to that observed in truncated canals in *ccm-3* mutants (Lant et al., 2015). Maheshwari et al also examined upstream regulators of FARL-11. They found that FARL-11 expression in gonads was regulated by PUF-8, an RNA-binding protein (Maheshwari et al., 2016). It would be interesting to see if PUF-8 also regulates other members of the STRIPAK complex and promotes tubulogenesis in the gonad.

STRIPAK and cell migration

Work in *Drosophila* implicated STRIPAK in regulation of the F-actin cytoskeleton via indirect effects on Ena/VASP (see above). Work in cultured endothelial cells has further suggested that STRIPAK may regulate stress fibers (Suryavanshi et al., 2018), raising the question whether STRIPAK regulates F-actin-dependent structures in migrating cells *in vivo*. A possible linkage between STRIPAK and the cytoskeleton comes from the examination of STRIPAK in *Mus musculus* mesoderm migration (Bazzi et al. 2017) and moesin regulation of tissue integrity in the *Drosophila* wing pouch (Jamblinne et al. 2020). *Mus musculus* embryos homozygous for *strip* display in a "cinchy" phenotype, in which axial mesoderm fails to migrate to the anterior of the mutant embryos. Explants of mutant mesodermal cells are more compact, have enriched cortical F-actin, and fewer focal adhesions (Bazzi et al. 2017). Mouse embryonic fibroblasts (MEFs) from *strip* mutant embryos also showed delayed migration in a scratch wound assay similar to that seen in tissue culture following knockdown of *strip1* (Bai et al., 2011).

A possible connection between the STRIPAK complex and regulation of F-actin networks comes from the *Drosophila* wing pouch. The single ERM (ezrin/radixin/moesin family) family protein in *Drosophila*, Moesin, is well known to link actin to the plasma membrane, thereby promoting epithelial integrity (Fehon et al., 2010; Speck et al., 2003). The Ste 20-like kinase Slik regulates phosphorylation of Moesin (Hipfner et al., 2004). Slik can coIP with Cka and Strip in S2 cells (De Jamblinne et al., 2020). *In vivo*, the functional consequences of depleting Cka are tissue undergrowth (predicted to be due to effects on Hpo signaling). DeJamblinne et al used a tissue-specific promoter to drive RNAi of Strip and Cka , leading to apoptosis of the cells below the wing pouch region. RNAi depletion of Cka and Strip caused decreased levels of p-Moesin in the wing pouch as well as loss of Slik localization. Taken together these results suggest that STRIPAK could regulate the phosphostatus of Slik to control its localization, which then regulates moesin activity.

STRIPAK and Cell Division

Finally, the STRIPAK complex has been shown to play a role in cell division. Much of this work has been done in *C. elegans*, where CCM-3, the germinal center kinase GCK-1, and FARL-11/Strip have been implicated cell division events in the gonad and early embryo. Interestingly, during cytokinesis in the *C. elegans* embryo CCM-3 and GCK-1 are found at the contractile ring and are recruited to the midbody at the end of division, where they and localize with NMY-2 (Bai et al., 2011). In the *C. elegans* embryo, stable localization of CCM-3 is dependent on GCK-1, suggesting that CCM-3 and GCK-1 may work together in the embryo as they do in canal cells. FARL-11, in addition to being present at the cleavage furrow, is an ER resident protein (Maheshwari et al., 2016). While both FARL-11 and CASH-1 appears to be important for ER

integrity as a *farl-11* mutant and *cash-1* knockdown causes disruption of the ER in the *C. elegans* embryo (Maheshwari et al., 2016).

Functional roles for CCM-3 and GCK-1 in cell division have been identified in two contexts. The first is in the multicellular portion of the *C. elegans* gonad (Pal et al., 2017; Rehain-Bell et al., 2017). Intercellular bridges reflect incomplete closure of cytokinetic furrows during cell divisions in the germline, and stability of bridges depends on ANI-1/anillin, a scaffold for non-muscle myosin and other contractile ring components, as well as AN-2, a truncated anillin; both anillins localize to bridges (Pal et al., 2017; Rehain-Bell et al., 2017). Rehain-Bell et al went on to identify a physical association of GCK-1 and ANI-1 in a co-IP/mass spectrometry analysis, implicating STRIPAK components in bridge maintenance as both CCM-3 and GCK-1 localize to intercellular bridges. Loss of function for *gck-1* or *ccm-3* results in reduced length of distal gonad arms, reduced rachis diameter, brood size, and loss of ANI-2 (Pal et al., 2017; Rehain-Bell et al., 2017). Co-depletion of ANI-1 partially rescued these defects (Rehain-Bell et al., 2017), suggesting an intricate interplay of anillin isoforms in stabilizing intercellular bridges in which ANI-2 is a regulator of ANI-1 (Pal et al., 2017; Rehain-Bell et al., 2017).

The second context in which CCM-3 and GCK-1 are implicated in cell division in *C. elegans* is during cytokinesis in the one-celled zygote. STRIPAK components may play multiple roles in the zygote; CCM-3 appears to be required for anterior-posterior polarization of the zygote prior to cleavage (Pal et al., 2017). Later, CCM-3 and GCK-1 are also required for normal completion of cytokinesis. *ccm-3* mutant embryos initiate a cleavage furrow which then regresses, creating multinucleate cells (Pal et al., 2017). Examination of GCK-1 and CCM-3 vis-à-vis RHO-1/RhoA

indicates a complex, reciprocal interplay between the STRIPAK components and Rho. Depletion of RhoA causes decreased levels of cortical GCK-1 and CCM-3 at the incipient furrow (Bell et al., 2020), suggesting that initial recruitment of GCK-1 and CCM-3 requires RhoA activity. Once recruited, however, GCK-1 and CCM-3 are then thought to negatively regulate RhoA contractility, as knockdown of either CCM-3 or GCK-1 caused an increase in recruitment of a RhoA biosensor, thereby contributing to a cytokinetic "braking" mechanism (Bell et al., 2020).

These studies on CCM-3 and GCK-1 strongly implicate STRIPAK in regulation of cytokinesis. Several issues remain, however. First, the role of the core structural components of STRIPAK have been unexplored. In particular, the roles of Striatin and Strip have not been examined *in vivo*. Second, the core function of STRIPAK is to recruit PP2A to post-translationally modify targets. Thus far, however, potential PP2A targets relevant to cytokinesis (or pathways regulated by PP2A) have not been identified. Future work to determine the role of FARL-11 or CASH-1 is needed to examine whether this effect is dependent on the STRIPAK complex or is working independently through CCM-3 and GCK-1. This thesis makes an initial contribution to both of these issues. In Chapter 2 I identify clear roles for Striatin/CASH-1 and Strip/FARL-11 in cytokinesis for the first time. I also show that loss of *cash-1* and/or *farl-11* function phenocopies defects that result from defects in Centralspindlin aggregation triggered by mutant forms of ZEN-4/MKLP1, identifying a potential regulatory target of PP2A during cytokinesis.

Conclusions

Perhaps not surprisingly, this brief review indicates that STRIPAK plays multiple regulatory roles in a variety of cellular events in model organisms. These include STRIPAK's role in Hpo

and JNK signaling, ubiquitous and crucial cellular signaling pathways that regulate myriad cellular events, including tissue growth and morphogenesis. Since STRIPAK has been shown to bind JNK and Hippo, an important area for future study will be to explore whether STRIPAK acts as a nexus to regulate JNK and Hippo crosstalk. Genetically tractable model organisms should be very valuable in teasing apart pathways upon which both JNK and Hippo signaling impinge.

A second area for future study relates to the role of STRIPAK in trafficking. While roles for trafficking in neurons seem clear, STRIPAK-dependent regulation of trafficking may also be the primary means by which STRIPAK regulates tubulogenesis. One particularly intriguing area for future study relates to the highly spatially resolved targeting of endosomal components in both synaptogenesis and luminal morphogenesis. Which spatially restricted processes are controlled by STRIPAK-dependent targeting of PP2A remains poorly understood. Given the preponderance of spatially polarized events in early embryos, it seems likely that STRIPAK may play roles in such processes during early embryogenesis. This thesis will explore one such process, the targeting of Centralspindlin at the conclusion of cytokinesis (Chapter 2). Another spatially intricate process is the establishment of the ordered array of sarcomeres in skeletal muscle. Chapter 3 will explore the role of STRIPAK in this process. The Strip homologue in *C. elegans* was identified in a screen for enhancers of a hypomorphic allele of *hmp-1*/α-catenin (see Chapter 2). Given the well-known roles of the cadherin complex in regulating cell-cell adhesion at precise cellular boundaries in the *C. elegans* embryo, it will be interesting to determine whether and how STRIPAK modulates this spatial specificity.

A third question regarding STRIPAK that spans all of the biological processes in which STRIPAK is implicated has to do with the dynamics and stoichiometry of the complex *in vivo*. One exciting future endeavor will be to discover a STRIPAK binding motif, similar to that identified in the case of the PP2A-B' regulatory subunit (Wu et al., 2017). Another relates to testing *in vivo* requirements for STRIPAK assembly suggested by the recent cryoEM study described above (Jeong et al., 2021). While this work broke new ground in terms of insight into the biochemical assembly of STRIPAK, the powerful genetic and imaging tools available in model systems should be a powerful complement to biochemical approaches in testing predictions regarding requirements for STRIPAK complex assembly and targeting *in vivo*. Chapter 2 of this thesis begins to test these predictions in the context of the one-cell *C. elegans* zygote. In particular, while a great deal of attention has been focused on Strip and CCM3 orthologues, other STRIPAK components have received relatively little attention. One feature of this thesis is to close this gap. Specifically, whereas Strip and CCM3 have received substantial attention, a common omitted component in *in vivo* analyses of STRIPAK is Striatin. Chapters 2 and 3 stringently test requirements for Striatin in the one-celled zygote and in skeletal muscle cells in *C. elegans*.

It is encouraging that progress is being made on several fronts to understand in detail how STRIPAK regulates important cellular processes. The STRIPAK complex is indeed complex, but its secrets are yielding to experimental analysis. This thesis adds to these efforts.

Introduction to Thesis

The STRIPAK (STRiatin Interacting Phosphatase And Kinase) Complex is an evolutionarily conserved PP2A holoenzyme complex from yeast to humans. A great deal of work has been done *in vitro* to elucidate the biochemical properties of the complex. How the STRIPAK complex functions in living organisms, however, is an emerging area of cell biology. Work in *Drosophila*, zebrafish, *C. elegans*, and mice has shown the STRIPAK complex to be involved in subcellular trafficking and cell division, as well as JNK and Hippo signaling. In this thesis, I further explore the role of the STRIPAK complex in the *C. elegans* embryo and in adult muscle.

In Chapter 1, I review basic structural information regarding the STRIPAK complex, including a recently published cryEM structure that provides guidance for several key experiments in this thesis. I also review previous experiments in genetic model organisms that shed light on *in vivo* roles for the STRIPAK complex.

In Chapter 2, I explore the relationship between the STRIPAK complex and ZEN-4/MKLP-1 (a member of the Centralspindlin complex) after cell division in the one-cell zygote. I show that loss of the STRIPAK backbone (CASH-1/STRN3) or the STRIPAK structural "hub" (FARL-11/STRIP) results in a "bleb" phenotype during cell division, which I show bears a striking resemblance to the phenotype resulting from perturbation of the phosphostatus of ZEN-4. I show that CASH-1 and FARL-11 form a complex, and that FARL-11 can bind to DYN-1/p150glued, potentially linking STRIPAK to the dynein/dynactin complex. Genetically, I show that CASH-1 interacts with ZEN-4 and the downstream Centralspindlin effector ECT-2, suggesting that

CASH-1 works with ZEN-4 to regulate cytokinesis. Lastly, I show that upon loss of CASH-1, ZEN-4 becomes dysregulated after cytokinesis, suggesting that CASH-1 may inactivate ZEN-4, potentially via a STRIPAK-specific PP2A holoenzyme complex.

In Chapter 3, as part of a collaboration with Guy Benian's group at Emory University, I examine the role of the STRIPAK complex in sarcomere assembly. Previously the Benian lab showed that PP2A plays a role in skeletal muscle; in this chapter we expand upon this previous work to show that the STRIPAK complex plays a role in sarcomere assembly. Specifically, we show that both FARL-11 and CASH-1 localize to the sarcomere and that loss of either protein disrupts sarcomere structure, including the sarcoplasmic reticulum.

Chapter 4 briefly provides a possible future framework for studying the STRIPAK complex in *C. elegans*. Here, I discuss potential ways to further elucidate the role of the STRIPAK complex and its potential role in the epidermis, and avenues for future study of STRIPAK interactors.

Appendix 1, a collaboration with Yan Jie's group at the Mechanobiology Institute and the National University of Singapore, presents work examining the effects of applied tension on the M-domain of HMP-1/α-catenin, and measures strength of interaction of HMP-1 and HMP-1/β-catenin, using innovative single-molecule biophysical experiments. I created the expression essential to this work. This work is in review at the *Journal of Biological Chemistry*.

Appendix 2 presents collaborative work I did to create an endogenous knock-in of TES-1/Testin, which I used to perform preliminary imaging during embryogenesis. I also performed a co-IP

experiment to determine if TES-1 interacts with HMP-1/α- catenin in *C. elegans*. The paper reporting this is currently in revision at *Current Biology*.

Appendix 3 is a follow up to the work of Appendix 1, in which I discovered a novel *in vivo* interaction between HMP-1 and SRGP-1/srGAP that is dependent on key salt bridges in the M-domain of HMP-1 /α-catenin. This manuscript is in review at *Development*.

Appendix 4 presents in silico analysis I performed in collaboration with Nathaniel Sharp's group at UW-Madison. I modeled the effects of one of the mutations they discovered in RIF1 to show its potential impact on DNA binding. This work provides a plausible explanation for why this mutant has a phenotype and why two other intramolecular mutations (which were outside the DNA binding domain, and solvent exposed) do not. This manuscript was submitted to *Genetics*.

References

Ahmed, M., Y. Kojima, and I. Masai. 2022. Strip1 regulates retinal ganglion cell survival by suppressing Jun-mediated apoptosis to promote retinal neural circuit formation. *eLife*. 11:e74650. doi:10.7554/eLife.74650.

Bai, S.W., M.T. Herrera-Abreu, J.L. Rohn, V. Racine, V. Tajadura, N. Suryavanshi, S. Bechtel, S. Wiemann, B. Baum, and A.J. Ridley. 2011. Identification and characterization of a set of conserved and new regulators of cytoskeletal organization, cell morphology and migration. *BMC Biology*. 9:54. doi:10.1186/1741-7007-9-54.

Bell, K.R., M.E. Werner, A. Doshi, D.B. Cortes, A. Sattler, T. Vuong-Brender, M. Labouesse, and A.S. Maddox. 2020. Novel cytokinetic ring components drive negative feedback in cortical contractility. *MBoC*. 31:1623–1636. doi:10.1091/mbc.E20-05-0304.

Chen, C., Z. Shi, W. Zhang, M. Chen, F. He, Z. Zhang, Y. Wang, M. Feng, W. Wang, Y. Zhao, J.H. Brown, S. Jiao, and Z. Zhou. 2014. Striatins Contain a Noncanonical Coiled Coil That Binds Protein Phosphatase 2A A Subunit to Form a 2:2 Heterotetrameric Core of Striatin-interacting Phosphatase and Kinase (STRIPAK) Complex. *Journal of Biological Chemistry*. 289:9651–9661. doi:10.1074/jbc.M113.529297.

Chen, H.-W., M.J. Marinissen, S.-W. Oh, X. Chen, M. Melnick, N. Perrimon, J.S. Gutkind, and S.X. Hou. 2002. CKA, a Novel Multidomain Protein, Regulates the JUN N-Terminal Kinase Signal Transduction Pathway in Drosophila. *Mol Cell Biol*. 22:1792–1803. doi:10.1128/MCB.22.6.1792-1803.2002.

De Jamblinne, C.V., B. Decelle, M. Dehghani, M. Joseph, N. Sriskandarajah, K. Leguay, B. Rambaud, S. Lemieux, P.P. Roux, D.R. Hipfner, and S. Carréno. 2020. STRIPAK regulates Slik localization to control mitotic morphogenesis and epithelial integrity. *Journal of Cell Biology*. 219:e201911035. doi:10.1083/jcb.201911035.

Fehon, R.G., A.I. McClatchey, and A. Bretscher. 2010. Organizing the cell cortex: the role of ERM proteins. *Nat Rev Mol Cell Biol*. 11:276–287. doi:10.1038/nrm2866.

Giot, L., J.S. Bader, C. Brouwer, A. Chaudhuri, B. Kuang, Y. Li, Y.L. Hao, C.E. Ooi, B. Godwin, E. Vitols, G. Vijayadamodar, P. Pochart, H. Machineni, M. Welsh, Y. Kong, B. Zerhusen, R. Malcolm, Z. Varrone, A. Collis, M. Minto, S. Burgess, L. McDaniel, E. Stimpson, F. Spriggs, J. Williams, K. Neurath, N. Ioime, M. Agee, E. Voss, K. Furtak, R. Renzulli, N. Aanensen, S. Carrolla, E. Bickelhaupt, Y. Lazovatsky, A. DaSilva, J. Zhong, C.A. Stanyon, R.L. Finley, K.P. White, M. Braverman, T. Jarvie, S. Gold, M. Leach, J. Knight, R.A. Shimkets, M.P. McKenna, J. Chant, and J.M. Rothberg. 2003. A protein interaction map of Drosophila melanogaster. *Science*. 302:1727–1736. doi:10.1126/science.1090289.

Goudreault, M., L.M. D'Ambrosio, M.J. Kean, M.J. Mullin, B.G. Larsen, A. Sanchez, S. Chaudhry, G.I. Chen, F. Sicheri, A.I. Nesvizhskii, R. Aebersold, B. Raught, and A.-C. Gingras. 2009. A PP2A Phosphatase High Density Interaction Network Identifies a Novel Striatin-interacting Phosphatase and Kinase Complex Linked to the Cerebral

Cavernous Malformation 3 (CCM3) Protein. *Molecular & Cellular Proteomics*. 8:157–171. doi:10.1074/mcp.M800266-MCP200.

Harden, N. 2002. Signaling pathways directing the movement and fusion of epithelial sheets: lessons from dorsal closure in Drosophila. *Differentiation*. 70:181–203. doi:10.1046/j.1432-0436.2002.700408.x.

Hipfner, D.R., N. Keller, and S.M. Cohen. 2004. Slik Sterile-20 kinase regulates Moesin activity to promote epithelial integrity during tissue growth. *Genes Dev*. 18:2243–2248. doi:10.1101/gad.303304.

Huang, W., D. Leonard, and D.J. Taylor. 2021. Pack a STRIPAK with hubs inside a hub. *Nat Struct Mol Biol*. 28:232–233. doi:10.1038/s41594-021-00571-z.

Hwang, J., and D.C. Pallas. 2014. STRIPAK complexes: Structure, biological function, and involvement in human diseases. *The International Journal of Biochemistry & Cell Biology*. 47:118–148. doi:10.1016/j.biocel.2013.11.021.

Jeong, B.-C., S.J. Bae, L. Ni, X. Zhang, X. Bai, and X. Luo. 2021. Cryo-EM structure of the Hippo signaling integrator human STRIPAK. *Nat Struct Mol Biol*. 28:290–299. doi:10.1038/s41594-021-00564-y.

La Marca, J.E., S.T. Diepstraten, A. Hodge, H. Wang, A.H. Hart, H.E. Richardson, and W.G. Somers. 2019. Strip and Cka negatively regulate JNK signalling during Drosophila spermatogenesis. *Development*. dev.174292. doi:10.1242/dev.174292.

Lant, B., B. Yu, M. Goudreault, D. Holmyard, J.D.R. Knight, P. Xu, L. Zhao, K. Chin, E. Wallace, M. Zhen, A.-C. Gingras, and W.B. Derry. 2015. CCM-3/STRIPAK promotes seamless tube extension through endocytic recycling. *Nat Commun*. 6:6449. doi:10.1038/ncomms7449.

Liu, B., Y. Zheng, F. Yin, J. Yu, N. Silverman, and D. Pan. 2016. Toll Receptor-Mediated Hippo Signaling Controls Innate Immunity in Drosophila. *Cell*. 164:406–419. doi:10.1016/j.cell.2015.12.029.

Maheshwari, R., K. Pushpa, and K. Subramaniam. 2016. A role for post-transcriptional control of ER dynamics and function in *C. elegans* germline stem cell maintenance. *Development*. dev.134056. doi:10.1242/dev.134056.

Mishra, A.K., V. Sharma, M. Mutsuddi, and A. Mukherjee. 2021. Signaling cross-talk during development: Context-specific networking of Notch, NF-κB and JNK signaling pathways in Drosophila. *Cellular Signalling*. 82:109937. doi:10.1016/j.cellsig.2021.109937.

Moreno, C.S., S. Park, K. Nelson, D. Ashby, F. Hubalek, W.S. Lane, and D.C. Pallas. 2000. WD40 Repeat Proteins Striatin and S/G2 Nuclear Autoantigen Are Members of a Novel Family of Calmodulin-binding Proteins That Associate with Protein Phosphatase 2A. *Journal of Biological Chemistry*. 275:5257–5263. doi:10.1074/jbc.275.8.5257.

Neal, S.J., Q. Zhou, and F. Pignoni. 2020. STRIPAK-PP2A regulates Hippo-Yorkie signaling to suppress retinal fate in the *Drosophila* eye disc peripodial epithelium. *Journal of Cell Science*. jcs.237834. doi:10.1242/jcs.237834.

Neisch, A.L., T.P. Neufeld, and T.S. Hays. 2017. A STRIPAK complex mediates axonal transport of autophagosomes and dense core vesicles through PP2A regulation. *Journal of Cell Biology*. 216:441–461. doi:10.1083/jcb.201606082.

Noselli, S., and F. Agnès. 1999. Roles of the JNK signaling pathway in Drosophila morphogenesis. *Current Opinion in Genetics & Development*. 9:466–472. doi:10.1016/S0959-437X(99)80071-9.

Pal, S., B. Lant, B. Yu, R. Tian, J. Tong, J.R. Krieger, M.F. Moran, A.-C. Gingras, and W.B. Derry. 2017. CCM-3 Promotes *C. elegans* Germline Development by Regulating Vesicle Trafficking Cytokinesis and Polarity. *Current Biology*. 27:868–876. doi:10.1016/j.cub.2017.02.028.

Rehain-Bell, K., A. Love, M.E. Werner, I. MacLeod, J.R. Yates, and A.S. Maddox. 2017. A Sterile 20 Family Kinase and Its Co-factor CCM-3 Regulate Contractile Ring Proteins on Germline Intercellular Bridges. *Current Biology*. 27:860–867. doi:10.1016/j.cub.2017.01.058.

Reynhout, S., and V. Janssens. 2019. Physiologic functions of PP2A: Lessons from genetically modified mice. *Biochimica et Biophysica Acta (BBA) - Molecular Cell Research*. 1866:31–50. doi:10.1016/j.bbamcr.2018.07.010.

Ribeiro, P.S., F. Josué, A. Wepf, M.C. Wehr, O. Rinner, G. Kelly, N. Tapon, and M. Gstaiger. 2010. Combined Functional Genomic and Proteomic Approaches Identify a PP2A Complex as a Negative Regulator of Hippo Signaling. *Molecular Cell*. 39:521–534. doi:10.1016/j.molcel.2010.08.002.

Ríos-Barrera, L.D., and J.R. Riesgo-Escovar. 2013. Regulating cell morphogenesis: The drosophila jun N-terminal kinase pathway. *genesis*. 51:147–162. doi:10.1002/dvg.22354.

Sakuma, C., T. Kawauchi, S. Haraguchi, M. Shikanai, Y. Yamaguchi, V.I. Gelfand, L. Luo, M. Miura, and T. Chihara. 2014. Drosophila Strip serves as a platform for early endosome organization during axon elongation. *Nat Commun*. 5:5180. doi:10.1038/ncomms6180.

Sakuma, C., M. Okumura, T. Umehara, M. Miura, and T. Chihara. 2016a. A STRIPAK component Strip regulates neuronal morphogenesis by affecting microtubule stability. *Sci Rep*. 5:17769. doi:10.1038/srep17769.

Sakuma, C., Y. Saito, T. Umehara, K. Kamimura, N. Maeda, T.J. Mosca, M. Miura, and T. Chihara. 2016b. The Strip-Hippo Pathway Regulates Synaptic Terminal Formation by Modulating Actin Organization at the Drosophila Neuromuscular Synapses. *Cell Reports*. 16:2289–2297. doi:10.1016/j.celrep.2016.07.066.

Sandal, P., C.J. Jong, R.A. Merrill, J. Song, and S. Strack. 2021. Protein phosphatase 2A – structure, function and role in neurodevelopmental disorders. *Journal of Cell Science*. 134:jcs248187. doi:10.1242/jcs.248187.

Shi, Y. 2009. Serine/Threonine Phosphatases: Mechanism through Structure. *Cell*. 139:468–484. doi:10.1016/j.cell.2009.10.006.

Speck, O., S.C. Hughes, N.K. Noren, R.M. Kulikauskas, and R.G. Fehon. 2003. Moesin functions antagonistically to the Rho pathway to maintain epithelial integrity. *Nature*. 421:83–87. doi:10.1038/nature01295.

Suryavanshi, N., J. Furmston, and A.J. Ridley. 2018. The STRIPAK complex components FAM40A and FAM40B regulate endothelial cell contractility via ROCKs. *BMC Cell Biol*. 19:26. doi:10.1186/s12860-018-0175-y.

Uhlirova, M., and D. Bohmann. 2006. JNK- and Fos-regulated Mmp1 expression cooperates with Ras to induce invasive tumors in Drosophila. *EMBO J*. 25:5294–5304. doi:10.1038/sj.emboj.7601401.

Virshup, D.M., and S. Shenolikar. 2009. From Promiscuity to Precision: Protein Phosphatases Get a Makeover. *Molecular Cell*. 33:537–545. doi:10.1016/j.molcel.2009.02.015.

Wagh, V., M.X. Doss, D. Sabour, R. Niemann, K. Meganathan, S. Jagtap, J.A. Gaspar, M.A. Ardestani, S. Papadopoulos, M. Gajewski, J. Winkler, J. Hescheler, and A. Sachinidis. 2014. Fam40b is required for lineage commitment of murine embryonic stem cells. *Cell Death Dis*. 5:e1320–e1320. doi:10.1038/cddis.2014.273.

Wu, C.-G., H. Chen, F. Guo, V.K. Yadav, S.J. Mcilwain, M. Rowse, A. Choudhary, Z. Lin, Y. Li, T. Gu, A. Zheng, Q. Xu, W. Lee, E. Resch, B. Johnson, J. Day, Y. Ge, I.M. Ong, M.E. Burkard, Y. Ivarsson, and Y. Xing. 2017. PP2A-B′ holoenzyme substrate recognition, regulation and role in cytokinesis. *Cell Discov*. 3:17027. doi:10.1038/celldisc.2017.27.

Zheng, Y., B. Liu, L. Wang, H. Lei, K.D. Pulgar Prieto, and D. Pan. 2017. Homeostatic Control of Hpo/MST Kinase Activity through Autophosphorylation-Dependent Recruitment of the STRIPAK PP2A Phosphatase Complex. *Cell Reports*. 21:3612–3623. doi:10.1016/j.celrep.2017.11.076.

Figure 1: Protein Phosphatase 2A Core and Holoenzyme. Schematic summary showing the PP2A core enzyme, composed of the PP2A-structural and PP2A-catalytic subunits (left), which can combine with multiple B regulatory subunits to create a variety of PP2A holoenzymes.

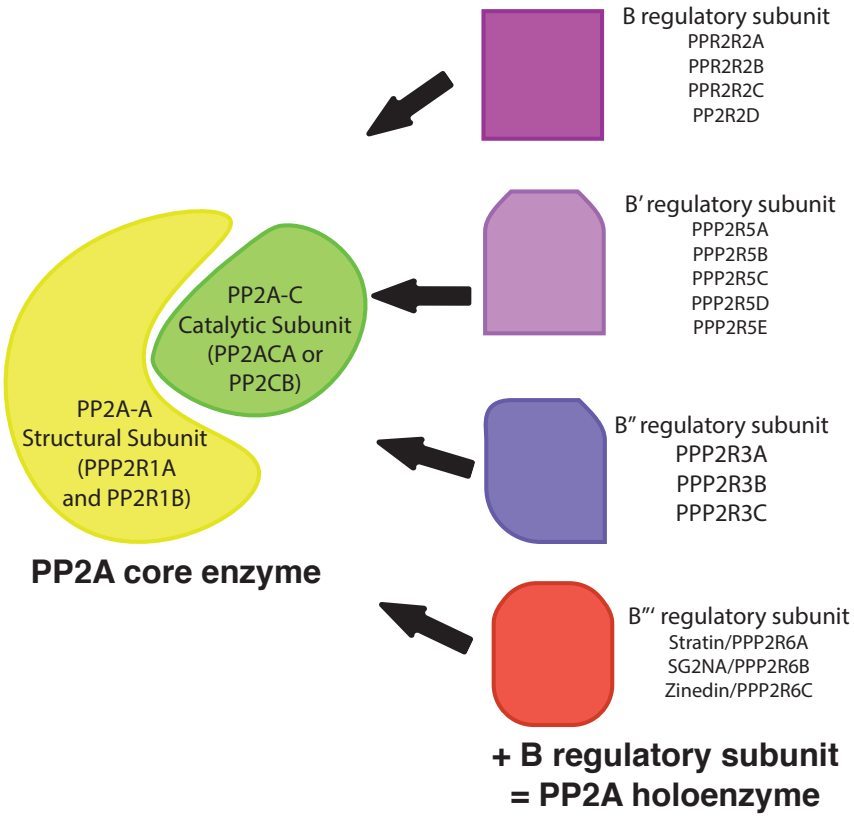
B regulatory subunit
PPR2R2A
PPR2R2B
PPR2R2C
PP2R2D
B′ regulatory subunit
PPP2R5A
PPP2R5B
PPP2R5C
PPP2R5D
PPP2R5E
PP2A-C
Catalytic Subunit
(PP2ACA or
PP2CB)
PP2A-A
Structural Subunit
(PPP2R1A
and PP2R1B)
B″ regulatory subunit
PPP2R3A
PPP2R3B
PPP2R3C
B‴ regulatory subunit
Stratin/PPP2R6A
SG2NA/PPP2R6B
Zinedin/PPP2R6C
PP2A core enzyme
+ B regulatory subunit
= PP2A holoenzyme

Figure 2: Model of the STRIPAK complex. A. Space filling rendering of data from a cryoEM structure of the STRIPAK complex (Jeong et al., 2021). Image was made using Pymol from PDB file 7K36. **B.** Cartoon illustration of the STRIPAK complex, showing all WD40 domains, with *C. elegans* protein names added.

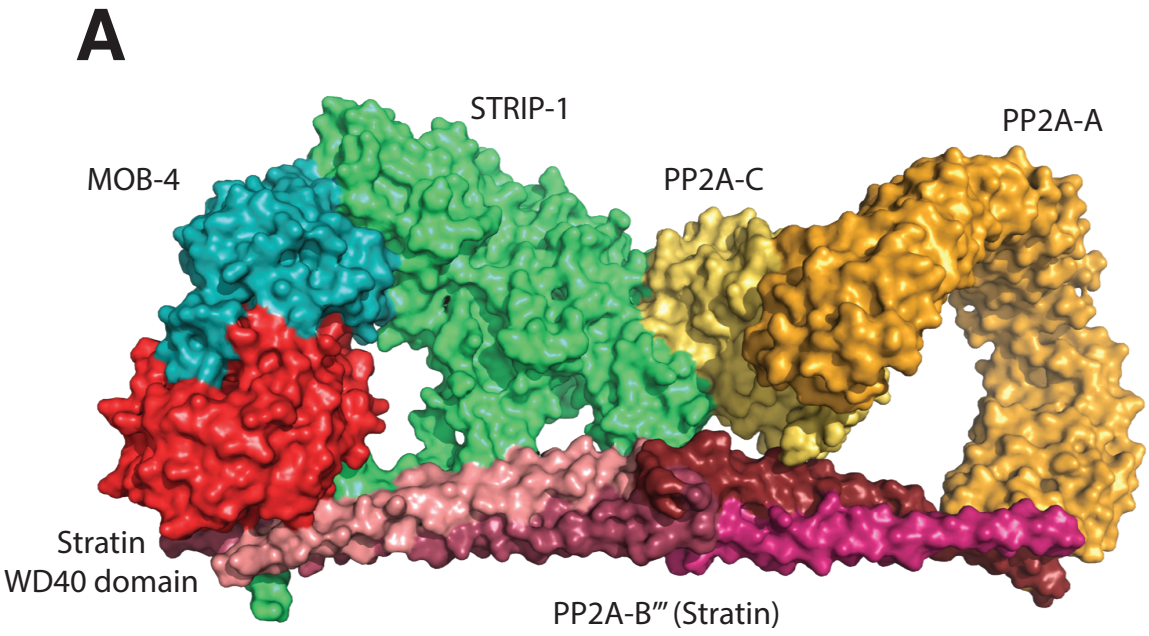
A
STRIP-1
PP2A-A
MOB-4
PP2A-C
Stratin
WD40 domain
PP2A-B‴ (Stratin)

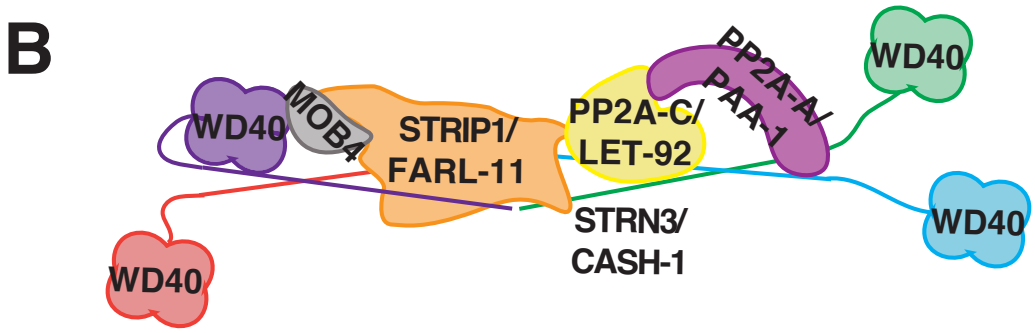
B
WD40
MOB4
STRIP1/
FARL-11
PP2A-C/
LET-92
PP2A-A/
PAA-1
WD40
STRN3/
CASH-1
WD40
WD40

CHAPTER 2:

The STRIPAK complex spatially restricts the Centralspindlin core component ZEN-4/MKLP-1 along the midplane following cytokinesis in the *C. elegans* embryo

This work was prepared for submission to *Current Biology*. The authors are Sterling C.T. Martin and Jeff Hardin.

My contribution to this work include designing, implementing, and analyzing experiments, and writing the draft manuscript

Summary

The STRIPAK (STRiatin-Interacting Phosphatase And Kinase) complex is an evolutionarily conserved complex from yeast to humans. STRIPAK functions in multiple cellular pathways, including the Hippo and MAPK pathways, cytoskeletal rearrangement, trafficking, and cell cycle regulation. Here, we report an *in vivo* functional interaction between the STRIPAK complex (CASH-1/STRN3 and FARL-11/STRIP1) and the cytokinetic regulator, centralspindlin. Centralspindlin is well established as a multiprotein complex essential for cytokinesis, but little is known about how centralspindlin is regulated along the cell-cell contact between the two sister cells at the end of cytokinesis. Using CRISPR/Cas9 we created endogenously tagged knock-ins and mutants to examine the *in vivo* roles of CASH-1 (the backbone of the STRIPAK complex) and FARL-11 during the first cell division of the *C. elegans* zygote. Loss of *cash-1* or *farl-11* function leads to ectopic furrowing and abnormal cytoplasmic extrusions after the first cell division, a phenotype similar to that resulting from ectopic ZEN-4/MKLP1 activation[1]. Dynamic imaging of ZEN-4 in STRIPAK component mutants indicates that STRIPAK plays a role in regulating centralspindlin along the midplane at the conclusion of furrow ingression. As previously reported for *farl-11*[2] loss of *cash-1* function rescues cytokinetic failure in a conditional *dhc-1/dynein heavy chain* mutant. We propose that CASH-1/STRN3, acting via FARL-11/STRIP, regulates dynein/dynactin-dependent removal of centralspindlin along the midplane after the completion of cytokinesis. These results establish a novel role for the STRIPAK complex, in conjunction with DHC-1/Dynein, in regulating trafficking of MKLP1 away from the cell-cell contact between two sister cells following cytokinesis.

Results/Discussion

CASH-1/STRN3 and FARL-11/STRIP1 are expressed and colocalize throughout the first cell division in *C. elegans* embryos

The STRIPAK (STRiatin-Interacting Phosphatase And Kinase) complex is an evolutionarily conserved multiprotein complex, with the Protein Phosphate Complex 2A (PP2A) at its core [3–5]. The backbone of the complex, Striatin/STRN3, is the B''' regulatory subunit of PP2A; it binds one copy of the A-structural and C-catalytic subunits of PP2A and targets the PP2A holoenzyme to subcellular locations. In addition to Striatin, the "core" invariable region of STRIPAK includes Striatin-interacting protein (STRIP1) and a MOB family protein (MOB4). This core region can in turn interact with other STRIPAK interacting proteins, including Cerebral Cavernous Malformation 3 (CCM3) and Germinal Cell Kinase III family proteins (MST3, MST4, or STK25) (Figure 1A). Through these various protein interactions, STRIPAK has been shown to be involved in a variety of cellular events, including cell signaling, cell migration, cell cycle control, apoptosis, vesicular trafficking, and Golgi assembly[6,7]. Previous work has shown that two components of the STRIPAK complex, FARL-11/STRIP1 and CCM-3/CCM3, are expressed and localized during early embryogenesis in *C. elegans*[8,9]. CCM-3 and the GCKIII protein GCK-1 have been implicated in negatively regulating RhoA early in cytokinesis, thereby inhibiting cortical contractility required for cytokinesis[10]. To determine if the backbone of the STRIPAK complex, CASH-1/STRN3, is also expressed in the zygote and early embryo, we endogenously tagged CASH-1 using CRISPR/Cas9 (Figure 1B). We also endogenously tagged FARL-11/STRIP1, as worms overexpressing *farl-11* via extrachromosomal arrays are unhealthy (data not shown). Endogenously tagged *mNG::farl-11* exhibits the same localization and expression as reported for a FARL-11::GFP transgene[8]. CASH-1/STRN3 shows a pattern of

expression similar to FARL-11/STRIP1 (see Figure 2A). To determine if the two proteins are part of a complex *in vivo* we performed coimmunoprecipitation assays and demonstrated that CASH-1 can co-IP with FARL-11 (Figure S1A). These results indicate that the STRIP1 and STRN3 orthologues in *C. elegans* associate physically and colocalize spatially in the zygote and early embryo.

cash-1/STRN3 and *farl-11/STRIP1* mutants display ectopic cytoplastic extrusions along the midplane after first cytokinesis

To determine if CASH-1 and FARL-11 play important functional roles in the early embryo, we also used CRISPR/Cas9 to create various *cash-1* mutants (Figure 1B), and we examined a preexisting *farl-11* allele, *tm6233*, which creates an in-frame fusion of exons 2-6[8]. Interestingly, compared with wild-type embryos (0%, n = 20 embryos), *farl-11* (*tm6233*) (47.4%, significantly different, $p < 0.05$, pairwise proportions test; n = 19 embryos, *cash-1*Δ*wd40* (47.1%, $p < 0.05$, n = 17 embryos) and *cash-1*Δ*n* (75%, $p < 0.001$, n = 16 embryos) embryos all exhibited ectopic cytoplasts at high frequency (Figure 1C,D). We confirmed the timing of cytoplast formation by following the progression of the furrow relative to formation of cytoplasts using a membrane marker in a representative mutant, *cash-1Δwd40* (Figure S1B). Cytoplasts are anuclear based on 4D DIC analysis (Figure 1D) and, in the case of *cash-1*Δ*n,* analysis using a histone marker[11] (Figure S1C). The extrusions vary in diameter from 2.3-14.4 μm where they connect to the cortex of the parent cell (Figure S1D). *cash-1Δn* homozygous embryos are maternal effect lethal; unbalanced P0s generate progeny with an embryonic lethality rate of 87.2% (n = 375 embryos, Figure S1E) and surviving F1s (n = 48) give no progeny.

Significantly, an ectopic extrusion phenotype has been reported in a ZEN-4 S682A phosphomutant, in which excessive clustering of ZEN-4 is thought to occur[1]. We made a similar phosphomutant starting with a strain carrying endogenously tagged *gfp::zen-4*[12], creating *zen-4Δ681/682 (jc66)*. *jc66* homozygous embryos display a 35% cytoplast extrusion rate (n = 20 embryos, Figure 1C,D). That an indistinguishable extrusion phenotype is shared between these mutants suggests that FARL-11/STRIP1, CASH-1/STRN3, and ZEN-4/MKLP1 are part of a functional pathway in the *C. elegans* zygote.

CASH-1/STRN3 is necessary for recruiting FARL-11/STRIP1 to sites of localization in the early embryo

Since CASH-1 forms the backbone of the STRIPAK complex and since the phenotypes of *cash-1* and *farl-11* mutants are so similar, we assessed the functional dependency of CASH-1 and FARL-11 on their mutual localization. After the first division, wild-type CASH-1 and FARL-11 appeared together along the midplane between the two sister cells following furrow ingression (Figure 2A, midplane reslice shown in 2Ab). Using 4d confocal microscopy, we determined the effects of complete deletion of the *cash-1* coding region and *cash-1* domain deletions on CASH-1 and subsequent FARL-11 localization. Interestingly, when we examined an endogenously tagged *cash-1Δwd40* mutant, we saw no localization of CASH-1 surrounding the nucleus (Figure 2B). Surprisingly, when we examined *cash-1ΔN* embryos, CASH-1ΔN tended to localize around the nucleus, but during division also became nuclear (Figure 2C). As expected, in a *cash-1* full deletion (*jc70*), there was no CASH-1 or FARL-11 signal (Figure S1F). In none of the *cash-1* mutants could we detect subcellular localization of FARL-11 (Figure 2B,2C). Taken together, these *in vivo* results indicate that both the N terminus and the WD40 domain are required for

differential functions of CASH-1. The WD40 domain appears to be required for subcellular localization of CASH-1 and FARL-11 recruitment. When CASH-1 lacks the N-terminus (containing its homodimerization domain)[13], it can still localize to sites where full-length CASH-1 localizes, which suggests that a functional WD40 motif is sufficient to localize presumptive CASH-1 protomers *in vivo* in the absence of homodimerization. Because, as was true for *cash-1* full deletion mutants, FARL-11 did not localize correctly in either *cash-1ΔN* or *ΔWD40* mutants, we infer that correct oligomerization of CASH-1 is required for recruitment of FARL-11/STRIP1 to the STRIPAK complex, as previously suggested by a cryoEM structure[4] (see Figure 1A).

The STRIPAK complex interacts functionally and physically with the dynein/dynactin complex

Several temperature-sensitive dynein heavy chain mutants have been identified in *C. elegans* with a wide range of cell division-related defects[2,14]. One allele, *dhc-1*(*or352ts),* is temperature-sensitive, and carries a mutation in the second walker motif, which in orthologues is important for the power stroke, allowing dynein to generate the force to "walk"[15,16]. As reported previously[2], we confirmed that knockdown of *farl-11* via RNAi rescues *dhc-1(or352ts)* mutant embryos raised at the non-permissive temperature. To determine if the *farl-11* rescue of *dhc-1* lethality is STRIPAK dependent, we assessed whether our *cash-1* deletion mutant (*jc70)* could also rescue *dhc-1(or352ts)* temperature-sensitive lethality. *or352ts* homozygous embryos displayed 90.3% embryonic lethality at 20°C (n = 710 embryos, Figure 3A circles), while the *cash-1* deletion displayed 3.24% embryonic lethality (n = 987 embryos, Figure 3A triangles). Loss of *cash-1* function in *cash-1(jc70); dhc-1(or352ts)* double homozygotes resulted in substantial suppression of lethality to 30.9% (n = 110 embryos, Figure 3A squares). Given this

evidence for a genetic interaction between STRIPAK and the dynein/dynactin complex, we performed an unbiased yeast-two-hybrid screen using FARL-11 as bait (Hybrigenics Corporation) and identified a prey construct encoding the C terminus of DNC-1/dynactin (Figure 3D, sequence in Figure S2B). The genetic and physical interactions of CASH-1 and FARL-11 with the dynein/dynactin complex suggest that the STRIPAK complex could be a functionally important regulator of dynein/dynactin-dependent events during or after cytokinesis.

cash-1/STRN3 genetically interacts with the regulators of cytokinesis, *zen-4*/*MKLP1* and its downstream effector *ect-2*

In the early embryo, the molecular connection between centralspindlin and the dynein/dynactin complex remains unclear. In *Drosophila* the MKLP1 orthologue Pavarotti requires p150glued/dynactin for proper targeting[17]. Since our *cash-1* deletion suppresses *dhc-1/dynein heavy chain* temperature-sensitive lethality (see Figure 3A), and *cash-1*, *farl-11* and *zen-4* mutants displayed a strikingly similar cytoplast extrusion phenotype after the first cell division (see Figure 1D), we sought to test whether FARL-11/STRIP1, CASH-1/STRN3, and ZEN-4/MKLP1 are part of a functional pathway in the *C. elegans* zygote, focusing on *zen-4/MKLP1* and its downstream effector, *ect-2/ECT-2*.

First, we assessed a possible genetic interaction between the STRIPAK complex, *zen-4/MKLP1* and *ect-2*, using our endogenously tagged *zen-4Δ681/682* mutant. We crossed our *cash-1Δwd40* mutant into this background, as the WD40 domain of CASH-1 is predicted to be a scaffold for various protein-protein interactions[5,18] In the case of *zen-4Δ681/682* homozygotes, embryonic lethality was 7.7% (n = 1436 embryos, Figure 3B circles), while *cash-1Δwd40* homozygotes displayed 10.6% embryonic lethality (n = 612 embryos, Figure 3B triangles). *zen-*

4Δ681/682; cash-1Δwd40 double homozygotes showed a striking synergistic lethality of 63.7% ($p < 0.001$, n = 1037 embryos, Figure 3B squares). These results suggest that both defective oligomerization of centralspindlin and STRIPAK-dependent processes contribute significantly to regulation of cytokinetic pathways.

We next examined whether the *cash-1Δwd40* mutant showed a similar genetic synergy with *ect-2* loss of function, since ECT-2 is a downstream effector of centralspindlin[19,20]. Using a temperature-sensitive allele, *ect-2(ax751ts)*[21], we created an *ect-2(ax751ts)*; *cash-1Δwd40* double mutant. *ect-2(ax751ts)* embryos displayed 22.9% lethality at 20°C (n = 743 embryos (Figure 3C circles); *cash-1Δwd40* mutants displayed 7.7% lethality (Figure 3C triangles). As with *zen-4Δ681/682; cash-1Δwd40* double mutants, *ect-2(751ts)*; *cash-1Δwd40* double mutants display very comparable synergistic lethality of 61.9% (n = 494 embryos, Figure 3C squares) at 20°C. Taken together, these results suggest that STRIPAK genetically interacts with cytokinetic regulators, and functionally impinges on processes involving ZEN-4/MKLP1.

We also examined the effects of loss of *farl-11* function on CASH-1 localization. If, as our data suggest, FARL-11/STRIP1 links CASH-1/STRN3 and the rest of the STRIPAK complex to the dynein/dynactin machinery, it might be expected that loss of the *farl-11*-dependent linkage between the dynein/dynactin complex and CASH-1 would lead to mistargeting of CASH-1. Indeed, when we examined homozygous *tagRFP::cash-1*; *farl-11 (tm6233)* embryos after cytokinesis we observed CASH-1 puncta at the midplane between the two sister cells (Figure 3E, n = 5 of 5 embryos).

CASH-1/STRN3 regulates ZEN-4/MKLP1 along the midplane after cytokinesis

Centralspindlin clusters (comprised of ZEN-4/MKLP1 and CYK-4/MgcRacGAP[19]) have been proposed to be a crucial molecular complex responsible for RhoA activation, thereby leading to furrowing during cytokinesis (reviewed in[19]). Moreover, in *Drosophila* S2 cells, ectopic targeting of CYK-4/MgcRacGAP (the other member of the centralspindlin complex) to the plasma membrane produces ectopic furrowing[22]. Since *cash-1/STRN3* (this study) and *zen-4/MKLP1* phosphomutants[1] (see Figure 1D) display ectopic cytoplast extrusions after the first cell division and *cash-1* and *zen-4* genetically interact (see Figure 3B), we next determined the effect of *cash-1* mutants on ZEN-4 dynamics along the midplane after cytokinesis (Figure 4A). We analyzed ZEN-4 dynamics at the midplane[1,23] 2 minutes after the completion of furrowing (t = 0 min) and acquired images every 2 minutes (t = 2-8 min) in wild-type, *cash-1* and *zen-4* single mutant, and *cash-1; zen-4* double mutant embryos. We quantified three different features of ZEN-4 dynamics: 1) total ZEN-4 cluster number (TCN), 2) total ZEN-4 cluster area (TCA), and 3) maximal spatial extent of ZEN-4 along the midplane in medial optical sections (MSE).

Since the CASH-1 WD40 domains are thought to "catch and fetch" protein interactors to bring them to the PP2A catalytic core[4], we determined the effect of loss of the CASH-1 WD40 domain on total ZEN-4 clustering (TCN) along the midplane after furrow formation. After the furrow formed in wild-type embryos (t = 2 min) there was consistently a single ZEN-4 cluster (n = 13 embryos). In contrast, in *cash-1Δwd40* mutants there were often multiple clusters (total cluster number = 1.7 ± 0.2; mean ± SEM, n = 11 embryos; one-way ANOVA, statistically different than WT, $p < 0.05$). A comparable increase in cluster number occurred in *zen-4 Δ681/682* mutants (2.5 ± 0.8, n = 6 embryos). In *cash-1Δwd40; zen-4Δ681/682* double mutants we observed a mean cluster number of 4.7 ± 0.8, which was statistically different than wildtype

($p < 0.01$) and *cash-1Δwd40* mutants ($p < 0.05$). Across all subsequent timepoints there was a consistent trend towards increased cluster number in mutant backgrounds (Figure 4B); the increase in cluster number due to mutations in *cash-1* and *zen-4* mutants can be accounted for through additive effects on ZEN-4 clustering along the midplane. We detected a similar trend in total cluster area (TCA), i.e., *cash-1* and *zen-4* mutants were characterized by a larger total area of ZEN-4 accumulation across the period of observation, and these effects appeared additive (Figure 4C). Finally, we assessed the maximal spatial extent of ZEN-4 (MSE) along the midplane between the two sister cells and obtained similar results (Figure 4D). Taken together, these consistent trends suggest that CASH-1-dependent processes and ZEN-4-dependent localization both contribute to efficient, focused clustering of centralspindlin along the midplane, and in turn, reduction of cortical contractility at the conclusion of cytokinesis. Either increased multimerization of ZEN-4 or disruption of STRIPAK function leads to ZEN-4 mislocalization along the midplane after furrow ingression and ectopic cytoplast formation.

To determine if CASH-1 is at the midplane of the cell-cell contact at the same time as ZEN-4, we performed reslices in *tagRFP::cash-1; GFP::zen-4* embryos (Figure 4E, Ea-c) and observed spatial overlap of ZEN-4 signal with CASH-1 at the midplane in 2-cell embryos. Moreover, we observed ZEN-4 along the cytoplast in *cash-1* deletion (*jc70*) embryos (Figure 4F), suggesting that excess ZEN-4 remaining at the midplane promotes cytoplast formation, presumably via ectopic RhoA activation[1,22].

Dynein/dynactin complex function is required for CASH-1/STRN3 and ZEN-4/MKLP1 localization and normal cytokinesis

Work in *Drosophila* implicated the dynein/dynactin complex in targeting of Pavarotti/MKLP1 during cytokinesis[17], but this work did not establish how MKLP1 is targeted by the dynein machinery. Our yeast two-hybrid analysis indicates that FARL-11/STRIP1 and DNC-1/dynactin can physically interact, and our functional analysis indicates that STRIPAK is an upstream regulator of ZEN-4/MKLP1 during cytokinesis. We therefore examined the effects of loss of function of the dynein/dynactin complex on cytokinesis and the resulting effects on STRIPAK localization. We found that amid a wide range of phenotypes, some *dhc-1(or352ts)* embryos imaged at 20°C (Figure 4G, n = 4 of 6 embryos with extrusions) displayed extrusions strikingly similar to those observed in STRIPAK component mutants and phospho-defective *zen-4* mutants. Moreover, when we examined CASH-1 distribution in these embryos we saw widespread mislocalization of CASH-1, including in cytoplasts (Figure 4G, arrowhead). Additionally, when we examined ZEN-4 localization along the midplane in a *dhc-1 (or352ts)* background, not only did we observed extensive mislocalization of ZEN-4, but we also observed ZEN-4 localizing along cytoplasts (Figure 4H, arrowhead).

Our data, combined with previous work in *Drosophila*[24] are consistent with a model in which the dynein/dynactin complex is involved in retrograde trafficking of the STRIPAK complex, which in turn regulates centralspindlin at the midplane following furrow ingression. Specifically, our results suggest that the dynein/dynactin complex, acting via FARL-11/STRIP1, coordinates CASH-1/STRN3 (and hence STRIPAK) localization, which then removes ZEN-4/MKLP1 and other centralspindlin components from the midplane after the completion of cytokinesis (Figure S3). This model accounts for the suppression of cytokinesis defects in *dhc-*

1/dynein heavy chain mutants by loss of STRIPAK components. When dynein/dynactin has reduced function, STRIPAK-tethered cargoes presumably have difficulty moving away from the cell periphery. Severing the connection to the dynein/dynactin complex in this case may actually be beneficial: untethering centralspindlin may allow diffusion or transport via another secondary mechanism. STRIPAK could also regulate accessibility of PP2A to ZEN-4; a previous high-throughput co-immunoprecipitation/mass spectrometry screen identified the structural subunit of PP2A, PAA-1, as a ZEN-4 interactor in the *C. elegans* embryo[25]. While our focus was on amino acid 682 within ZEN-4, which inactivates ZEN-4 clustering when phosphorylated, other residues may be involved in converse regulation. In this case the absence of PP2A recruitment could lead to abnormal maintenance of these activating phosphoresidues. It will be interesting in the future to test these models in detail.

Recently, other non-obligate STRIPAK components (CCM-3 and GCK-1) were shown to act as negative regulators of RhoA after formation of the cytokinetic ring but temporally upstream of the events we have investigated[10].It will be interesting in the future to determine the role of CASH-1/STRN-3 and FARL-11/STRIP1, as core STRIPAK components, not only in targeting of centralspindlin to the cortex, but also as part of this "braking mechanism" as cytokinesis progresses.

Materials and Methods

Worm strains

Worms were maintained on *Escherichia coli* OP50, as previously described[26]. The wild-type strain used in this study was Bristol N2. Maintenance of worms and experiments were performed at 20°C unless otherwise specified. The following genetic lesions were utilized in this study:

SU703 *farl-11 (tm6233)/mIn1 III*-10x outcross

SU912 *cash-1 (jc62[TagRFP::TEV::3xmyc::cash-1 Δ342-678 +Lox2272 + Lox2272*jc60])* V

SU854 *cash-1 (jc60[TagRFP::TEV::3xmyc:::cash-1 +Lox 2272])* V

SU853 *farl-11 (jc61[mNG::TEV::3xflag::farl-11 + LoxP])* III

SU857 *cash-1 (jc60[TagRFP::TEV::3xmyc:::cash-1 +Lox 2272])* V;

(jc61[mNG::TEV::3xflag::farl-11 + LoxP]) III

SU957 *cash-1 (jc70[TagRFP::3xflag::Δ342-678)*V; *zen-4 (lt30 [GFP::loxP::zen-4)]* IV

SU918 *cash-1 (jc63[TagRFP::TEV::3xmyc::cash-1 Δ1-190 + Lox2272])* V/ *tmC12 [egl-9]* V

SU923: *farl-11 (jc61[mNG::TEV::3xflag::farl-11 + LoxP])* III; *cash-1*

(jc63[TagRFP::TEV::3xmyc::cash-1 Δ1-190 + Lox2272]) V/ *tmC12 [egl-9];*

SU929: cash-1 (jc63[TagRFP::TEV::3xmyc::cash-1 Δ1-190 + Lox2272]) V/ *tmC12 [egl-9];*

ruIs32 [pie-1p::GFP::H2B + unc-119(+)] III. zuIs178 [his-72(1kb 5' UTR)::his-

72::SRPVAT::GFP::his-72 (1KB 3' UTR) + 5.7 kb XbaI - HindIII unc-119(+)]

SU940 *zen-4 (zen-4(jc66[gfp::zen-4Δ681/682 *lt30])*IV

SU953 *farl-11 (jc61[mNG::TEV::3xflag::farl-11 + LoxP])* III; *cash-1*

(jc70[TagRFP::3xflag::Δ1-976]) V

SU958 *cash-1 (jc70[TagRFP::3xflag::Δ1-976])*

OD2979 *zen-4 (lt30 [GFP::loxP::zen-4)]* IV (a gift from Karen Ooegma)

SU906 *cash-1 (jc62[TagRFP::TEV::3xmyc::cash-1 Δ342-678 +Lox2272 + Lox2272*jc60])* V;

tSi849 [pKL120; Pmex-5::mCherry::PH(PLC1delta1)::tbb-2 3'UTR; cb-unc-119(+)] I

SU959 *cash-1 (jc60[TagRFP::TEV::3xmyc::cash-1 +Lox 2272])* V; *dhc-1(or352ts)* I

JH3270: *ect-2 (ax751ts)* II

EU1386: *dhc-1 (or352ts)* I

SU957: *cash-1 (jc70[TagRFP::3xflag::Δ1-976]); zen-4 (lt30 [GFP::loxP::zen-4)]* IV

SU1013: *cash-1 (jc60 [TagRFP::TEV::3xmyc::cash-1 + Lox 2272])V; zen-4(lt30[GFP::zen-4 + LoxP])* IV

SU1010: *zen-4(jc66[Δ681/682zen-4 *lt30])* IV; *cash-1 (jc60 [TagRFP::TEV::3xmyc::cash-1 + Lox 2272])* V

SU1011: *farl-11 (jc61[mNG::TEV::3xflag::farl-11 + LoxP])* III; *cash-1(jc62[TagRFP::CASH-1Δ342-678 +Lox2722]*) V

SU1036: *cash-1 (jc62[TagRFP::CASH-1Δ342-678 +Lox2722])* V; *zen-4(zen-4(jc66[gfp::zen-4Δ681/682 *lt30])* IV

SU1032: *cash-1 (jc62[TagRFP::CASH-1Δ342-678 +Lox2722])*V; *ect-2 (ax75 ts)* II

CRISPR/Cas9

To generate endogenous insertions and deletions a self-excising cassette was used[27]. *tagrfp::SEC::CASH-1/+* and *tagRFP::SEC::CASH-1 ΔN/+* were crossed into the *tmC12*[28] balancer to facilitate SEC removal. *mng::SEC::farl-11/+* was crossed into the *mIn1* balancer to facilitate SEC removal. The balanced progeny were heat shocked at 34°C to remove the SEC. Repair template for CASH-1ΔWD40 worms was generated using the SapTrap method and injected into the *jc60* strain[29]. SEC excision and correct knock-in were confirmed by PCR of non-rolling, non-balanced progeny. Worms were outcrossed with N2 a minimum of 4x.

Guide RNA sequences were cloned into the Cas9 containing plasmid (pJW1219).

CASH-1 5’ guide- 5’ -CGGATTCGAGTAGTTACAATGG

CASH-1 ΔN 3' guide: 5'-CCATCCAGTGAACGTCTCAA

CASH-1 ΔWD40 5' guide: 5'-CGAATGCACAACAAGTGAAGNGG

CASH-1 3' guide: 5'CTTGCCAAGGTGTACGTGTC

FARL-11 5' guide: GGCCTGATTCCCATTACATT

Generation of the Δ681/682 *zen-4::GFP* was achieved by using a co-conversion method[30] using a guide previously reported[1].

Imaging

Embryos were isolated from gravid hermaphrodites, mounted on a 10% agarose pad, and were immediately imaged at 20°C. For four-dimensional differential interference contrast microscopy, embryos were imaged using 1 μm slice spacing at 90 sec. intervals using a Nikon Optiphot 2 microscope with a 60×/1.4 NA oiled objective at 20°C using Micro-Manager software[31] (available at https://micro-manager.org). For fluorescence imaging, a Dragonfly 500 spinning disk confocal microscope (Andor Corp.), mounted on a Leica DMi8 microscope, equipped with a Zyla and an iXon camera and controlled by Fusion software (Andor Corp.) was used to collect images of GFP/TagRFP expressing embryos, using 0.5 μm slices at 2 min. intervals with a 63x/1.3 NA glycerol Leica objective at 20°C.

ZEN-4 quantification

ZEN-4 cluster number, length along midplane, and cross-sectional area were scored manually using Fiji[32] (available at https://imagej.net/software/fiji/) after z-projection of 4D images.

Background subtraction of mean fluorescence intensity was performed by drawing a 10 x 10 μm box on an empty portion of the image. For the cross-sectional area, ZEN-4 signal was outlined using the freehand tool. For ZEN-4 length across the midplane, a line was drawn between the two most distant ZEN-4 signals observed along the midplane. ZEN-4 cluster numbers were manually counted.

Yeast two hybrid assay

A FARL-11 Y2H screen was performed by Hybrigenics Services (Paris, France). Full length FARL-11 cDNA was used as the bait while a *C. elegans* Mixed Stage library was used for the prey.

Temperature-sensitive (ts) lethality counts

Temperature-sensitive worms were maintained at 15°C. For lethality counts, L4 worms were singled onto individual plates and allowed to lay for 48 hrs at 20°C. After 48 hrs, the adult worm was removed and total embryos and larvae were counted; 24 hrs later, living larvae were counted.

Coimmunoprecipitation

Coimmunoprecipitation was performed as described[33]. 20 large NGM plates with gravid adults were harvested and frozen in Lysis (-) buffer (50mM HEPES pH7.4, 150mM NaCl, 0.05mM DTT). Worms were lysed by sonication in Lysis (+) buffer (50mM HEPES, pH7.4, 150mM NaCl, 0.05mM DTT, 1%NP-40) and total lysates were centrifuged at 4°C. The soluble fraction was then pre-cleared using Chromotek control magnetic agarose beads (gmab-20) for 30 minutes

at 4°C. Pre-cleared lysates were then incubated with Chromotek RFP-Trap magnetic agarose beads (rtma-20) for 1h at 4°C. Beads were washed 3 times with 1 mL of Lysis (-) buffer, and eluted with 50µL of Lysis (-) buffer at 90°C for 10 min.

Samples were resolved on a 10% Mini-PROTEAN TGX polyacrylamide gel (Bio-rad 456-1036), transferred to Immobilon-FL PVDF membrane (Milipore IPFL00010) using a ThermoFisher Powerblotter (Cat#PB0013), and immunoblotting was performed using a ThermoFisher iBindFlex (Cat#SLF2000). FARL-11 was detected at 1:500 using a rabbit anti-FARL-11 antibody (see below). LiCor 2° Goat anti-Rabbit antibody (925-3211) was used for detection at 1:4000.

FARL-11 antibody construction

Antibody production was performed by Li International (Denver, CO). A 50 amino acid chemically synthesized peptide corresponding to the extreme C-terminus of FARL-11 (aa 929-978 TCAHSVLGANLKLGRHFKKDYEKWLEQEVFNASIDWDKLLIETRGVEDLM) was injected into New Zealand rabbits. Li International performed immunization and provided lyophilized antibody which was resuspended to 1 mg/mL with 1x PBS.

Statistics

A pairwise proportions test with Holm multiple test correction was performed in R-studio (version 4.1.1) for cell extrusions and embryonic lethality measurements. R-studio was used to create stacked bar and scatter plots. For ZEN-4 clustering experiments, a one-way ANOVA with Tukey posthoc analysis was performed and graphed using Prism 9 (GraphPad Corp.).

References

1. Basant, A., Lekomtsev, S., Tse, Y.C., Zhang, D., Longhini, K.M., Petronczki, M., and Glotzer, M. (2015). Aurora B Kinase Promotes Cytokinesis by Inducing Centralspindlin Oligomers that Associate with the Plasma Membrane. Dev Cell *33*, 204–215.

2. O'Rourke, S.M., Dorfman, M.D., Carter, J.C., and Bowerman, B. (2007). Dynein Modifiers in *C. elegans*: Light Chains Suppress Conditional Heavy Chain Mutants. PLoS Genet *3*.

3. Goudreault, M., D'Ambrosio, L.M., Kean, M.J., Mullin, M.J., Larsen, B.G., Sanchez, A., Chaudhry, S., Chen, G.I., Sicheri, F., Nesvizhskii, A.I., et al. (2009). A PP2A Phosphatase High Density Interaction Network Identifies a Novel Striatin-interacting Phosphatase and Kinase Complex Linked to the Cerebral Cavernous Malformation 3 (CCM3) Protein. Molecular & Cellular Proteomics *8*, 157–171.

4. Jeong, B.-C., Bae, S.J., Ni, L., Zhang, X., Bai, X.-C., and Luo, X. (2021). Cryo-EM structure of the Hippo signaling integrator human STRIPAK. Nat Struct Mol Biol *28*, 290–299.

5. Moreno, C.S., Park, S., Nelson, K., Ashby, D., Hubalek, F., Lane, W.S., and Pallas, D.C. (2000). WD40 Repeat Proteins Striatin and S/G2 Nuclear Autoantigen Are Members of a Novel Family of Calmodulin-binding Proteins That Associate with Protein Phosphatase 2A. Journal of Biological Chemistry *275*, 5257–5263.

6. Hwang, J., and Pallas, D.C. (2014). STRIPAK complexes: structure, biological function, and involvement in human diseases. Int J Biochem Cell Biol *47*, 118–148.

7. Pracheil, T., and Liu, Z. (2013). Tiered assembly of the yeast Far3-7-8-9-10-11 complex at the endoplasmic reticulum. J Biol Chem *288*, 16986–16997.

8. Maheshwari, R., Pushpa, K., and Subramaniam, K. (2016). A role for post-transcriptional control of endoplasmic reticulum dynamics and function in *C. elegans* germline stem cell maintenance. Development *143*, 3097–3108.

9. Pal, S., Lant, B., Yu, B., Tian, R., Tong, J., Krieger, J.R., Moran, M.F., Gingras, A.-C., and Derry, W.B. (2017). CCM-3 Promotes *C. elegans* Germline Development by Regulating Vesicle Trafficking Cytokinesis and Polarity. Curr Biol *27*, 868–876.

10. Bell, K.R., Werner, M.E., Doshi, A., Cortes, D.B., Sattler, A., Vuong-Brender, T., Labouesse, M., and Maddox, A.S. (2020). Novel cytokinetic ring components drive negative feedback in cortical contractility. MBoC *31*, 1623–1636.

11. Bao, Z., Murray, J.I., Boyle, T., Ooi, S.L., Sandel, M.J., and Waterston, R.H. (2006). Automated cell lineage tracing in *Caenorhabditis elegans*. Proc. Natl. Acad. Sci. U.S.A. *103*, 2707–2712.

12. Lee, K.-Y., Green, R.A., Gutierrez, E., Gomez-Cavazos, J.S., Kolotuev, I., Wang, S., Desai, A., Groisman, A., and Oegema, K. (2018). CYK-4 functions independently of its centralspindlin partner ZEN-4 to cellularize oocytes in germline syncytia. eLife *7*, e36919.

13. Chen, C., Shi, Z., Zhang, W., Chen, M., He, F., Zhang, Z., Wang, Y., Feng, M., Wang, W., Zhao, Y., et al. (2014). Striatins contain a noncanonical coiled coil that binds protein phosphatase 2A A subunit to form a 2:2 heterotetrameric core of striatin-interacting phosphatase and kinase (STRIPAK) complex. J Biol Chem *289*, 9651–9661.

14. Schmidt, D.J., Rose, D.J., Saxton, W.M., and Strome, S. (2005). Functional Analysis of Cytoplasmic Dynein Heavy Chain in *Caenorhabditis elegans* with Fast-acting Temperature-sensitive Mutations. MBoC *16*, 1200–1212.

15. Cho, C., Reck-Peterson, S.L., and Vale, R.D. (2008). Regulatory ATPase Sites of Cytoplasmic Dynein Affect Processivity and Force Generation. J Biol Chem *283*, 25839–25845.

16. Schmidt, H., Zalyte, R., Urnavicius, L., and Carter, A.P. (2015). Structure of human cytoplasmic dynein-2 primed for its power stroke. Nature *518*, 435–438.

17. Delcros, J.-G., Prigent, C., and Giet, R. (2006). Dynactin targets Pavarotti-KLP to the central spindle during anaphase and facilitates cytokinesis in Drosophila S2 cells. Journal of Cell Science *119*, 4431–4441.

18. Xu, C., and Min, J. (2011). Structure and function of WD40 domain proteins. Protein Cell *2*, 202–214.

19. Basant, A., and Glotzer, M. (2018). Spatiotemporal Regulation of RhoA during Cytokinesis. Current Biology *28*, R570–R580.

20. Nishimura, Y., and Yonemura, S. (2006). Centralspindlin regulates ECT2 and RhoA accumulation at the equatorial cortex during cytokinesis. Journal of Cell Science *119*, 104–114.

21. Zonies, S., Motegi, F., Hao, Y., and Seydoux, G. (2010). Symmetry breaking and polarization of the *C. elegans* zygote by the polarity protein PAR-2. Development *137*, 1669–1677.

22. D'Avino, P.P., and Glover, D.M. (2009). Cytokinesis: mind the GAP. Nat Cell Biol *11*, 112–114.

23. Guse, A., Mishima, M., and Glotzer, M. (2005). Phosphorylation of ZEN-4/MKLP1 by Aurora B Regulates Completion of Cytokinesis. Current Biology *15*, 778–786.

24. Sakuma, C., Kawauchi, T., Haraguchi, S., Shikanai, M., Yamaguchi, Y., Gelfand, V.I., Luo, L., Miura, M., and Chihara, T. (2014). Drosophila Strip serves as a platform for early endosome organization during axon elongation. Nat Commun *5*, 5180.

25. Chen, J.-X., Cipriani, P.G., Mecenas, D., Polanowska, J., Piano, F., Gunsalus, K.C., and Selbach, M. (2016). In Vivo Interaction Proteomics in Caenorhabditis elegans Embryos Provides New Insights into P Granule Dynamics. Molecular & Cellular Proteomics *15*, 1642–1657.

26. Brenner, S. (1974). The genetics of Caenorhabditis elegans. Genetics *77*, 71–94.

27. Dickinson, D.J., Pani, A.M., Heppert, J.K., Higgins, C.D., and Goldstein, B. (2015). Streamlined Genome Engineering with a Self-Excising Drug Selection Cassette. Genetics *200*, 1035–1049.

28. Dejima, K., Hori, S., Iwata, S., Suehiro, Y., Yoshina, S., Motohashi, T., and Mitani, S. (2018). An Aneuploidy-Free and Structurally Defined Balancer Chromosome Toolkit for Caenorhabditis elegans. Cell Reports *22*, 232–241.

29. Schwartz, M.L., and Jorgensen, E.M. (2016). SapTrap, a Toolkit for High-Throughput CRISPR/Cas9 Gene Modification in *Caenorhabditis elegans*. Genetics *202*, 1277–1288.

30. Arribere, J.A., Bell, R.T., Fu, B.X.H., Artiles, K.L., Hartman, P.S., and Fire, A.Z. (2014). Efficient Marker-Free Recovery of Custom Genetic Modifications with CRISPR/Cas9 in *Caenorhabditis elegans*. Genetics *198*, 837–846.

31. Edelstein, A.D., Tsuchida, M.A., Amodaj, N., Pinkard, H., Vale, R.D., and Stuurman, N. (2014). Advanced methods of microscope control using μManager software. J Biol Methods *1*, e10.

32. Schindelin, J., Arganda-Carreras, I., Frise, E., Kaynig, V., Longair, M., Pietzsch, T., Preibisch, S., Rueden, C., Saalfeld, S., Schmid, B., et al. (2012). Fiji: an open-source platform for biological-image analysis. Nat Methods *9*, 676–682.

33. Zaidel-Bar, R., Joyce, M.J., Lynch, A.M., Witte, K., Audhya, A., and Hardin, J. (2010). The F-BAR domain of SRGP-1 facilitates cell–cell adhesion during *C. elegans* morphogenesis. Journal of Cell Biology *191*, 761–769.

Figure 1: Effects of loss of STRIPAK components in *C. elegans* zygotes. A. STRIPAK schematic based on a recently reported cryoEM structure4. B. Protein domain maps of FARL-11 and CASH-1 showing insertion and deletion sites. C. Quantification of cytoplast extrusion frequency in STRIPAK mutants. * = $p < 0.05$, *** = $p < 0.001$, pairwise proportions test). D. DIC images of wildtype (WT), zen-4 Δ681/682, and STRIPAK mutants (cytoplast extrusion denoted with black arrowhead at 7.5 min) after cell division. Times correspond to when nuclei meet (t = 0 min), when zygotes are furrowing (t =4.5 min), furrow formation is complete (t = 6 min), and cytoplasts form (t = 7.5 mins). White arrowhead denotes polar body; black arrowhead denotes extrusion. Scale bar = 10 μm. Asterisks in 1C: *** $p<0.001$, ** = $p < 0.01$, * = $p < 0.05$ (pairwise proportion test with Holm multiple test correction).

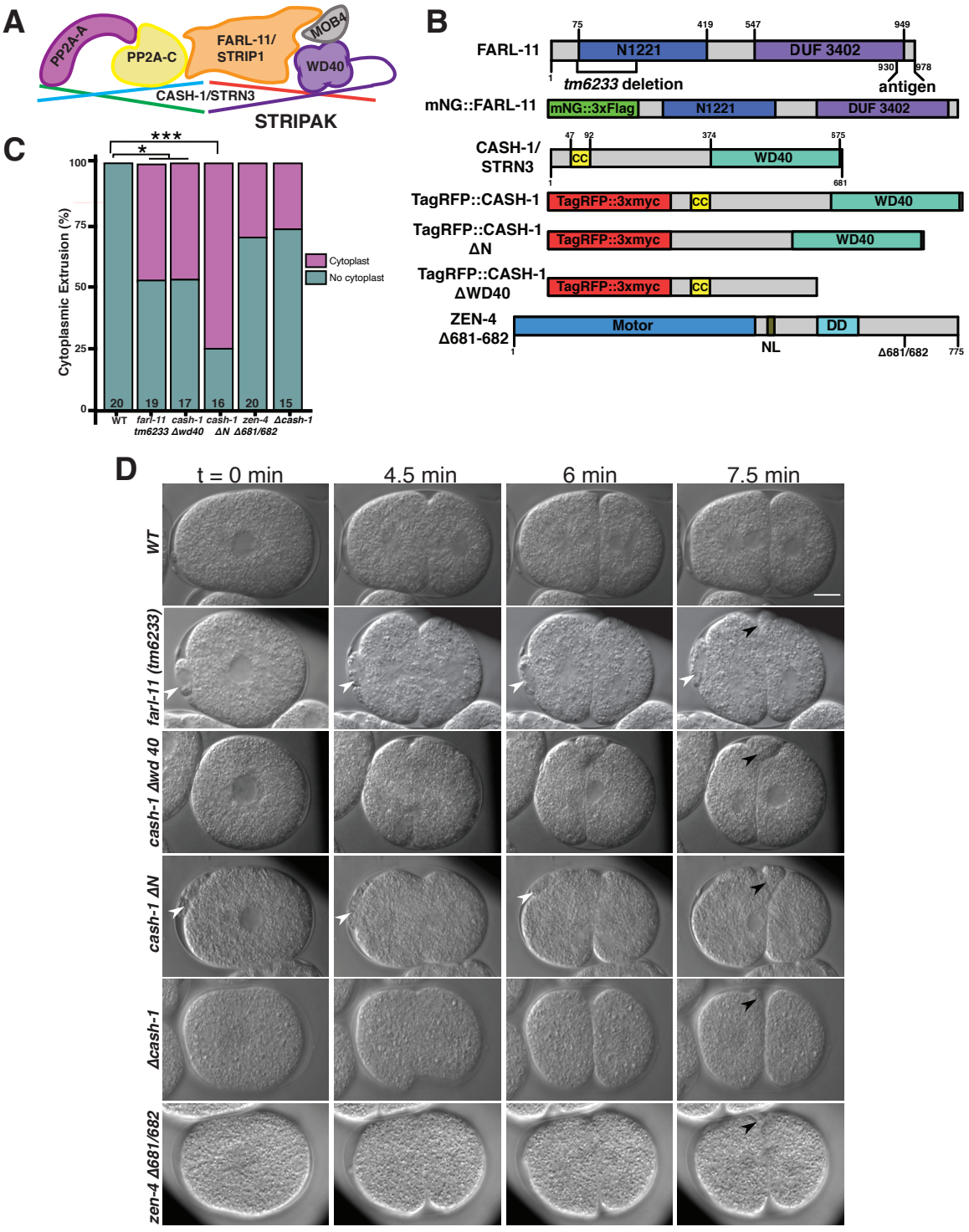
A
PP2A-A
PP2A-C
FARL-11/
STRIP1
MOB4
WD40
CASH-1/STRN3
STRIPAK
B
FARL-11
75
419
547
949
N1221
DUF 3402
1
930
978
tm6233 deletion
antigen
mNG::FARL-11
mNG::3xFlag
N1221
DUF 3402
CASH-1/
STRN3
47
92
374
675
CC
WD40
1
681
TagRFP::CASH-1
TagRFP::3xmyc
CC
WD40
TagRFP::CASH-1
ΔN
TagRFP::3xmyc
WD40
TagRFP::CASH-1
ΔWD40
TagRFP::3xmyc
CC
ZEN-4
Δ681-682
Motor
NL
DD
1
Δ681/682
775
C
***
*
Cytoplasmic Extrusion (%)
100
75
50
25
0
Cytoplast
No cytoplast
20
19
17
16
20
15
WT
farl-11 tm6233
cash-1 Δwd40
cash-1 ΔN
zen-4 Δ681/682
Δcash-1
D
t = 0 min
4.5 min
6 min
7.5 min
WT
farl-11 (tm6233)
cash-1 Δwd 40
cash-1 ΔN
Δcash-1
zen-4 Δ681/682

Figure 2: *In vivo* localization and functional interaction of FARL-11/STRIP1 and CASH-1/STRN3. A. Confocal images of *tagRFP: cash-1;mNG::farl-11* embryos. CASH-1 and FARL-11 localize around the nucleus, and at sites of prominent ER localization (cyan arrowhead, t = 0 min as determined by nuclei meeting in transmitted light images). During furrowing CASH-1 and FARL-11 localize to spindles (t = 4 min); nuclear localization persists in each daughter cell after cytokinesis (t = 6 min) and can be seen in 2-cell embryos (t = 8min). CASH-1 and FARL-11 can be observed at the midplane of the 2-cell embryo in Z reslices (arrowheads). Dotted line indicates site of Z reslicing used in 2Ab. 2Ab: Z reslice at the midplane of a *tagRFP::cash-1;mNG::farl-11* embryo at t = 8 min. Scale bar = 10 μm. **B.** Confocal images of *tagRFP::cash-1Δn;mNG::farl-11* embryos. Cyan arrowhead shows aberrant CASH-1 localization (t = 0 min) compared to the distribution of full-length CASH-1 in A. mNG::FARL-11 localization is not detectable. **C.** Confocal images of *tagRFP::cash-1ΔWD40;mNG::farl-11* embryos. TagRFP::CASH-1ΔWD40 is not seen in the perinuclear region (t = 0 min; compare to images in A). TagRFP::CASH-1ΔWD40 shows no perinuclear localization in later zygotes (t = 10 and 22.5 min), and mNG::FARL-11 localization is absent. White arrowhead denotes nucleus.

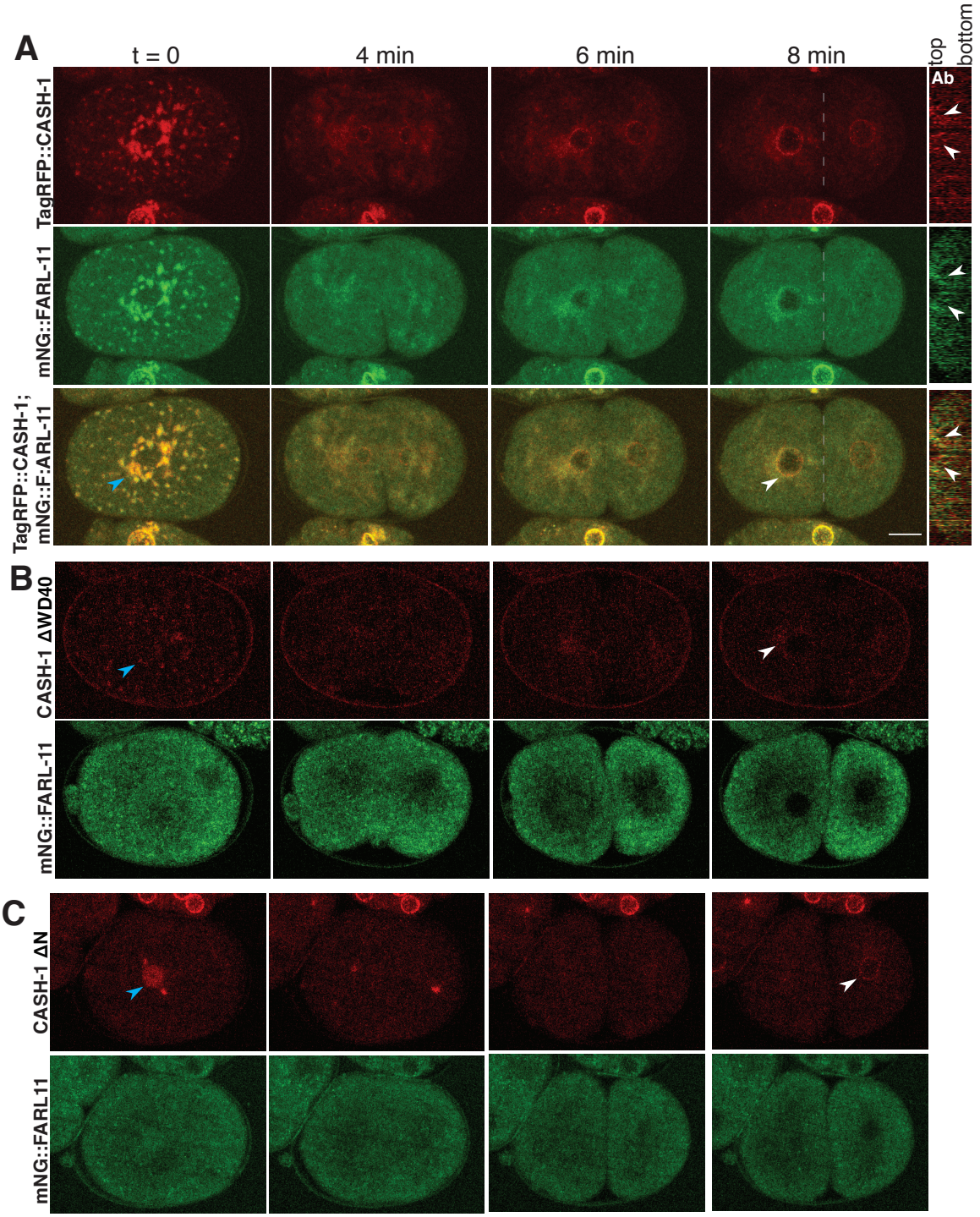
A
t = 0
4 min
6 min
8 min
top
bottom
Ab
TagRFP::CASH-1
mNG::FARL-11
TagRFP::CASH-1;
mNG::F:ARL-11
B
CASH-1 ΔWD40
mNG::FARL-11
C
CASH-1 ΔN
mNG::FARL11

Figure 3: Functional and physical interaction of dynein/dynactin complex components with STRIPAK. A: Embryonic lethality of *dhc-1*(*or352ts*) (circles), *Δcash-1* (triangles), and *dhc-1*(*or352ts*); *Δcash-1* double mutants (squares), showing rescue of *dhc-1*(*or352ts*) lethality at 20°C. (*** = $p < 0.001$; pairwise proportions test). **B.** Embryonic lethality of *zen-4Δ681/682* (circles), *cash-1Δwd40* (triangles), and *cash-1Δwd40,zen-4Δ681/682* double mutants (squares), showing enhancement of lethality at 20°C (* = $p<0.05$, *** = $p < 0.001$; pairwise proportions test) **C.** Embryonic lethality of *ect-2*(*ax751ts*) (circles), *cash-1Δwd40* (triangles), and *ect-2*(*ax751ts*); *cash-1Δwd40* double mutants (squares), showing enhancement of lethality at 20°C. (*** = $p < 0.001$; pairwise proportions test). **D.** Protein domain map of DNC-1/dynactin with predicted FARL-11 binding domain (aa612-1265) based on a yeast-two-hybrid screen; for sequence, see Figure S2B. **E.** Confocal images of a *farl-11(tm6233); tagRFP::cash-1* embryo showing TagRFP::CASH-1 puncta at the midplane in a 2-cell embryo. White arrowhead indicates CASH-1 puncta at midplane. In otherwise wild-type embryos, TagRFP::CASH-1 puncta are never observed at the midplane (compare to Figure 2A). Times correspond to when nuclei meet (t = 0 min), when embryos are furrowing (t =4 min), furrow formation is complete (t = 6 min), and 2 cell embryo (t = 8 mins) Scale bar = 10 μm.

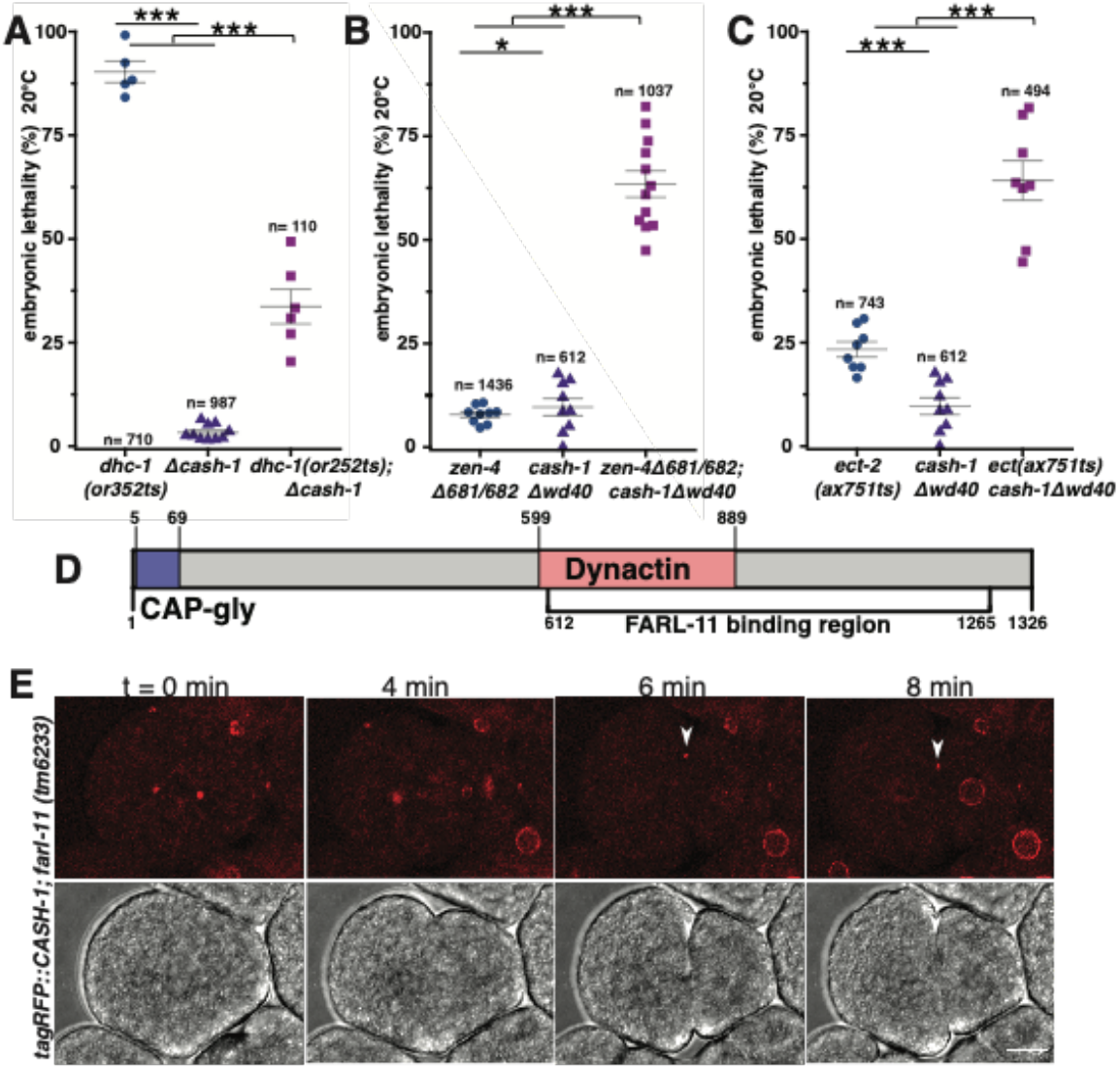
A
B
C
D
E
embryonic lethality (%) 20°C
***
*
n= 710
n= 987
n= 110
n= 1436
n= 612
n= 1037
n= 743
n= 612
n= 494
dhc-1 (or352ts)
Δcash-1
dhc-1(or252ts); Δcash-1
zen-4 Δ681/682
cash-1 Δwd40
zen-4Δ681/682; cash-1Δwd40
ect-2 (ax751ts)
cash-1 Δwd40
ect(ax751ts) cash-1Δwd40
5
69
599
889
1
612
1265
1326
CAP-gly
Dynactin
FARL-11 binding region
t = 0 min
4 min
6 min
8 min
tagRFP::CASH-1; farl-11 (tm6233)

Figure 4: Functional synergy between phosphodefective ZEN-4/MKLP1 and loss of STRIPAK components along the midplane after cytokinesis. A. Confocal images of GFP::ZEN-4 along the midplane after cytokinesis. t = 0 min corresponds to furrowing. At t = 2 mins and beyond *cash-1Δwd40* embryos show broader localization of GFP::ZEN-4 along the midplane, as well as multiple ZEN-4 clusters in the cytoplasm. *zen-4Δ681/682* embryos also show broader distribution of GFP::ZEN-4681/682 along the midplane; multiple clusters can also be observed in the cytoplasm (such puncta have been previously described[1]). *cash-1Δwd40; zen-4Δ681/682* double mutant embryos show broader distribution of GFP::ZEN-4Δ681/682 along the midplane, as well as larger cluster area along the midplane (see panels B-D for quantification). Scale bar = 10 μm. **B.** Quantification of total number of ZEN-4 clusters (TCN) along the midplane after cytokinesis for embryos in panel A. **C.** Quantification of total cluster area (TCA) of ZEN-4 along the midplane after cytokinesis for embryos in panel A. **D.** ZEN-4 maximal spatial extent (MSE) along the midplane after cytokinesis for embryos in panel A. Asterisks in B-D: **** = $p < 0.0001$,*** $p < 0.001$, ** = $p < 0.01$, * = $p < 0.05$, (ANOVA with Tukey posthoc analysis). **E.** Two-cell embryo expressing TagRFP::CASH-1;GFP::ZEN-4 showing localization along the midplane in a 2-cell embryo. Z reslices are shown in Ea, Eb, and Ec; white arrowhead points to ZEN-4 cluster along midplane which indicates site of Z reslicing. GFP::ZEN-4 is at the midplane along with TagRFP::CASH-1 **F.** T= top of embryo, B = bottom of embryo. GFP::ZEN-4 signal in a *cash-1* deletion mutant (*jc70*; left) and corresponding transmitted light image (right). White arrowhead points to GFP::ZEN-4 signal along the forming cytoplast. **G.** Confocal image of a *dhc-1*(*or352ts*); *tagRFP::cash-1* embryo showing TagRFP::CASH-1 localization in a cytoplast at 20°C. White arrowhead points to puncta of TagRFP::CASH-1 in cytoplast. H. Confocal image of a *dhc-1(or352ts); zen-4::GFP* embryo at

20°C. White arrowhead points to a line of GFP::ZEN-4 along the base of a cytoplast. Scale bar = 10 μm.

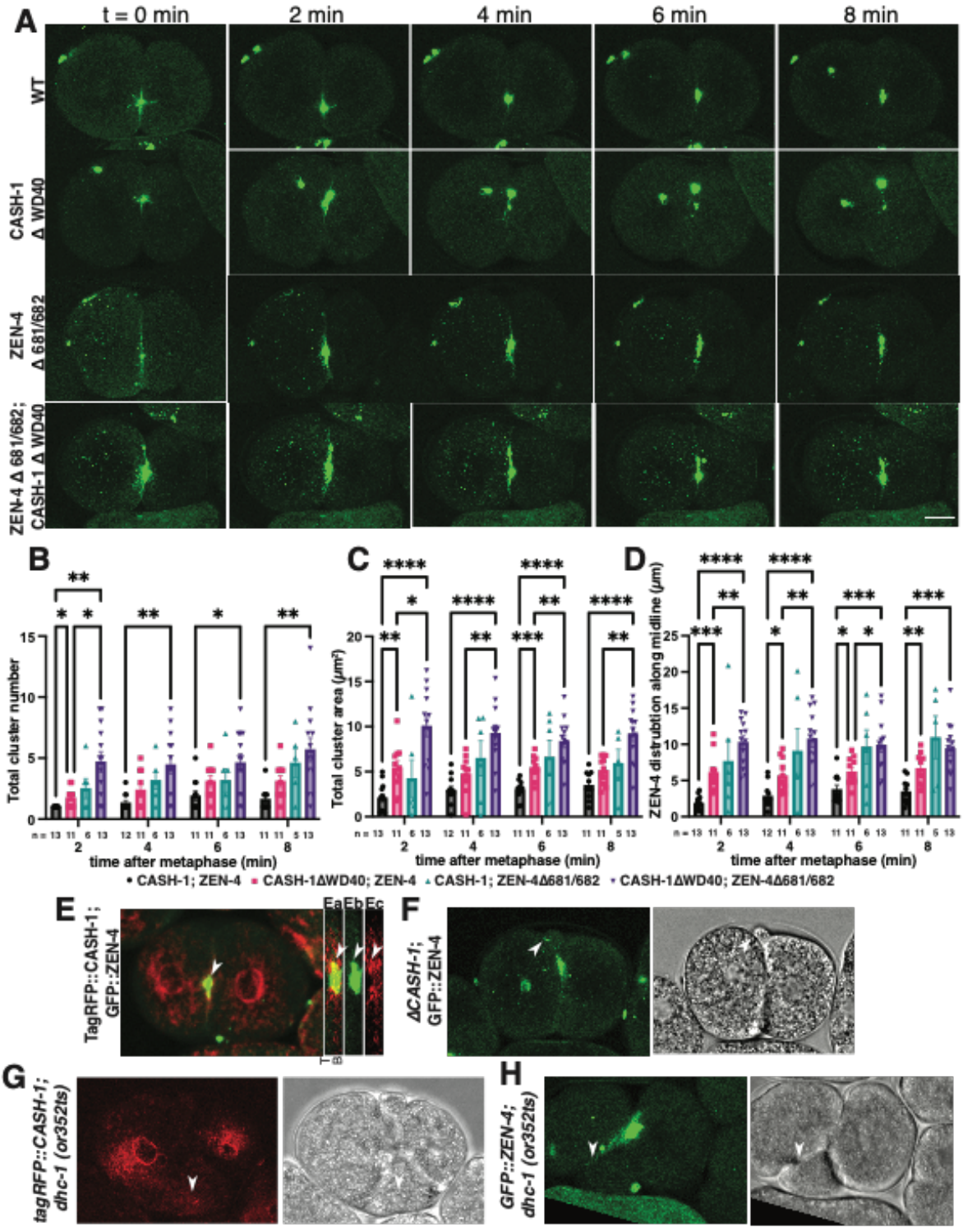
A
t = 0 min
2 min
4 min
6 min
8 min
WT
CASH-1 Δ WD40
ZEN-4 Δ 681/682
ZEN-4 Δ 681/682; CASH-1 Δ WD40
B
Total cluster number
time after metaphase (min)
C
Total cluster area (μm²)
time after metaphase (min)
D
ZEN-4 distribution along midline (μm)
time after metaphase (min)
• CASH-1; ZEN-4 ▪ CASH-1ΔWD40; ZEN-4 ▲ CASH-1; ZEN-4Δ681/682 ▾ CASH-1ΔWD40; ZEN-4Δ681/682
E
TagRFP::CASH-1; GFP::ZEN-4
Ea Eb Ec
F
ΔCASH-1; GFP::ZEN-4
G
tagRFP::CASH-1; dhc-1 (or352ts)
H
GFP::ZEN-4; dhc-1 (or352ts)

Supplemental Figure 1: CASH-1 physically and functionally interacts with FARL-11 and loss of *cash-1* function leads to anucleate cytoplasts. A. Western blot showing coimmunoprecipitation of FARL-11 from *tagRFP::cash-1* lysates. CCL = clarified cell lysate, MA= magnetic agarose, FT = flow through, W = wash. **B.** Confocal and transmitted images showing cytoplast formation in a *cash-1Δwd40; mCherry::PH* embryo. The cytoplast forms after furrow formation. **C.** Confocal image showing that the cytoplast formed in a *cash-1Δn* embryo does not contain nuclear material, based on absence of histone 3.3::GFP. White arrowhead points to the cytoplast, which lacks GFP signal. **D.** Measurement of cytoplast extrusion diameter in various mutant backgrounds corresponding to Figure 1D. **E.** Embryonic lethality in *cash-1Δn* embryos (n = 375 embryos). **F.** Confocal images of a *Δcash-1* embryo showing no detectable or specific CASH-1 or FARL-11 localization. Scale bar = 10 μm.

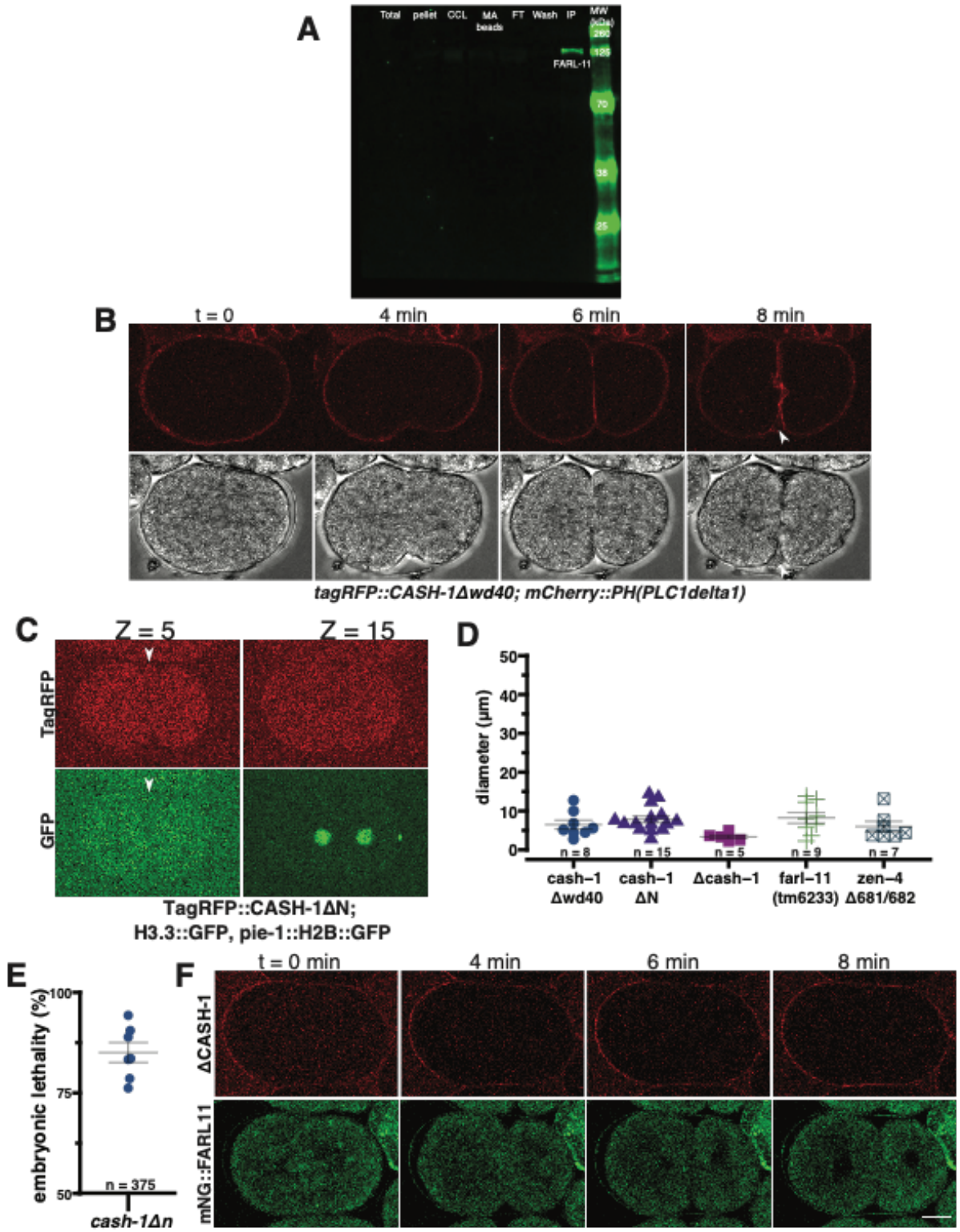
A
Total
pellet
CCL
MA beads
FT
Wash
IP
MW (kDa)
260
135
FARL-11
70
35
25
B
t = 0
4 min
6 min
8 min
tagRFP::CASH-1Δwd40; mCherry::PH(PLC1delta1)
C
Z = 5
Z = 15
TagRFP
GFP
TagRFP::CASH-1ΔN;
H3.3::GFP, pie-1::H2B::GFP
D
diameter (µm)
50
40
30
20
10
0
n = 8
n = 15
n = 5
n = 9
n = 7
cash–1 Δwd40
cash–1 ΔN
Δcash–1
farl–11 (tm6233)
zen–4 Δ681/682
E
embryonic lethality (%)
100
75
50
n = 375
cash-1Δn
F
t = 0 min
4 min
6 min
8 min
ΔCASH-1
mNG::FARL11

Supplemental Figure 2: Predicted FARL-11/STRIP1 binding region within DNC-1/p150Glued. **A.** DNC-1/p150 glued protein domain map. **B.** DNC-1 amino acid sequence identified in a yeast two-hybrid screen using FARL-11 as bait (Hybrigenics Corp.).

A

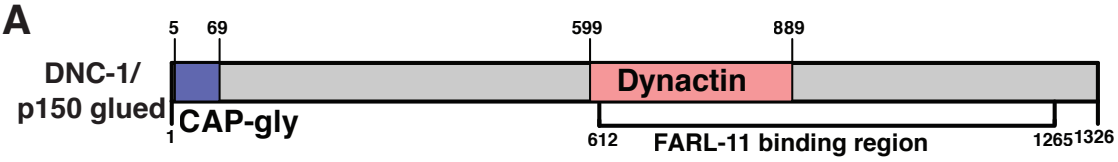

B

DNC-1 Fragment Sequence: KDQVLSLEEQLHGHISVDNDRASMVNQLQISANRNFAEDVERQVNAIEVEFARRQA-
GYLKAFLPDNFSRVGGENDSILLVVMLPRLAAKTKLFASLAAQCFPQVPGGMRREHVTKSHKGEQWAHVARVNYLANSINAAL
GKLESAIGETTVEVLIKLTETYGEMSTHEKTVDQYLELLKKSRFDENTSLDSFVRPLVYFQNMFSLHIGGDGFNAAHWVSEICASL
SAGLAYCRVNTQRISYFLQESITAGEVYNMLQTLNDEFAACESVILKAYRLLPGNVSGSEQKILKLESEFTEDLLNSVVQLDKMVSIL
QEVCANGALSFGGISETEGFDEKRVKEMINAVLGKQDGYIAIDKTFDPIRALIKSLRDSLEKVNSTLESAKMEHSAPEKKSFPPLLD
RAHHRKQAAQEAEGLRWQMEKKDNEMLELRKQMKARIEDVSNYKLRLDMAESRLNSTDKAEGDKVKHLEEKINQMVADHR
RKQIEYDESMDALQREMKEVESDNLELKQRANKISKEALWKNIQSMETRSSGSPSVPMSTSIDEGGASRGEVVFLENQLNKQTN
ARKRAELEVRKLKGELAQAGSKRFSAVPGLISGPITLESQTRQDLLLKLIDNLHDESLRLRREEVNHQAYVPSNPKISTEKMVEEME
IF

Supplemental Figure 3: Model of the interaction of DNC-1/dynactin, DHC-1/dynein heavy chain, STRIPAK, ZEN-4/MKLP1, and the centralspindlin complex. STRIPAK is proposed to bind to DNC-1/DHC-1 via FARL-11/STRN3. STRIPAK in turn is proposed to bind centralspindlin via the CASH-1/STRN3 WD40 domains, which in turn allows removal of centralspindlin from the midplane after cytokinesis. In STRIPAK and ZEN-4 phosphomutants excess ZEN-4 remains at the midplane, leading to cytoplast formation. Red x denotes (*or352ts*) mutation in second Walker motif of DHC-1/Dynein.

CHAPTER 3:

CASH-1/STRN3 and FARL-11/STRIP1/2 Localize to the Sarcoplasmic Reticulum and Are Required for SR and Sarcomere Organization in Striated Muscle

This work is being prepared for submission to *Molecular Biology of the Cell*. The authors are Sterling C.T. Martin, Hiroshi Qadota, Jeff Hardin, Guy M. Benian

My contributions to this work were identifying multiple STRIPAK mutations and creating them using CRIPSR/Cas9 where all the strains used were of my creation.

Summary

CASH-1/STRN3 and FARL-11/STRIP1/2, both core components of the STRIPAK (Jeong et al., 2021)complex have been shown to be important for endoplasmic reticulum homeostasis in the *C. elegans* one-celled zygote. Previously, it has been shown that PP2A components play a role in sarcomere assembly in *C. elegans* muscle. Here we expand upon these results to demonstrate that CASH-1 and FARL-11 are also necessary for sarcomere assembly. We further show that *farl-11* and *cash-1* mutants display disrupted localization of the single SR-associated ryanodine receptor UNC-68 at dense bodies; M localization of UNC-68 is also disrupted in *farl-11* mutants. Our results demonstrate novels roles for the STRIPAK complex in regulation of SR and sarcomeric structure.

Introduction

A major serine-threonine protein phosphatase that is conserved from yeast to humans is protein phosphatase 2A (PP2A; Shi, 2009). PP2A functions in a wide variety of cellular contexts and forms multiple specific protein complexes via different regulatory or targeting subunits. The PP2A core enzyme comprises the catalytic subunit C (PP2AC) and a scaffolding subunit A (PP2AA). This core forms a complex with a variety of regulatory B subunits, with the B subunits mediating subcellular localization and/or substrate recognition. There are four families of regulatory B subunits: B (B55 or PPP2R2), B' (B56 or PPP2R5), B" (B72 or PPP2R3), and B''' (striatins).

The so-called STRIPAK complex is a PP2A complex in which the regulatory subunit is the protein striatin. Recently, the structure of the STRIPAK complex was solved at 3.2 Å resolution using cryo-EM (Jeong et al., 2021). The complex consists of a catalytic subunit (PP2AC), a scaffolding subunit (PP2AA), striatin, striatin interacting protein 1 (STRIP1), and MOB family member 4 (MOB4). The striatin coiled-coil domain forms an elongated scaffold that links the complex together.

In the budding yeast, *Saccharomyces cerevisiae*, the "Far" complex, originally identified as crucial for pheromone-induced cell cycle arrest, is the yeast counterpart of the STRIPAK complex. The Far complex localizes to the endoplasmic reticulum (ER), and it has been shown that the six Far subunits (Far3, 7, 8, 9, 10 and 11) assemble at the ER in a specific sequence (Pracheil and Liu, 2013). Similarly, in *C. elegans*, the nematode ortholog of yeast Far11, called FARL-11 (Far-like 11), is localized to the ER and outer nuclear membrane of early embryos and

the germline (Maheshwari et al., 2016). Moreover, in a *farl-11* loss-of-function mutant, the morphology of the ER is severely disrupted, indicating that FARL-11 protein is required for normal ER morphology. In striated muscle, the sarcoplasmic reticulum (SR) is a highly organized, muscle-specific version of the ER, and is the storage and release depot for Ca^{2+}. In response to an action potential from motor neurons, the calcium release channel of the SR (the ryanodine receptor) is activated and opens to allow flow of Ca^{2+} from the SR into the muscle cell cytoplasm, where Ca^{2+} interacts with components of the sarcomere (usually the troponin/tropomyosin complex) to activate muscle contraction.

The role of STRIPAK in SR function has not been determined. We turned to *C. elegans* as a genetically tractable model organism in which to investigate the function of STRIPAK in muscle function. *C. elegans* is an outstanding system for discovering new conserved aspects of muscle assembly, maintenance and regulation (Gieseler et al., 2017). In a previous study we reported that loss of function of most single components of PP2A results in sarcomere disorganization (Qadota et al., 2018). This includes the catalytic subunit C (LET-92), the scaffolding subunit A (PAA-1), regulatory subunit B (SUR-6), regulatory subunit B' (either PPTR-1 or PPTR-2), regulatory subunit B" (RSA-1) and regulatory subunit B''' (CASH-1). Moreover, we reported that with available antibodies to five of these PP2A components, we were able to localize the components to different and overlapping components of the sarcomere. For example, SUR-6 and PPTR-1 localize to I-bands, PPTR-2 localizes to M-lines and dense bodies (Z-disks), and RSA-1 localizes to M-lines and I-bands (Qadota et al., 2018).

Here we used additional genetic mutants and other reagents generated for a separate study (see Chapter 2), to investigate the role of the STRIPAK complex in adult *C. elegans* muscle. We find that FARL-11 (STRIP1/2) and CASH-1 (STRN3) are localized to the SR, are required for SR morphology, and for sarcomere organization.

Results

Mutations in cash-1/Striatin and farl-11/Strip1 cause mild sarcomeric organizational defects.

To facilitate our studies, we generated antibodies to a C-terminal portion of FARL-11, and also used CRISPR/Cas9 to generate an N-terminal fusion of FARL-11 to mNeonGreen and Flag (strain SU853), and an N-terminal fusion of CASH-1 to TagRFP and myc (strain SU854; Figure 1A). As shown in Figure 1B, anti-FARL-11 rabbit polyclonal antibodies react to a protein of the expected size (~110 kDa) from wildtype, and an appropriately larger fusion protein from the mNG::FARL-11 strain. Antibodies to myc detect an appropriately sized protein (~130 kDa) from the strain that expresses an RFP- and myc-tagged fusion to CASH-1.

In our previous analysis of the PP2A complex in *C. elegans* muscle, we showed that RNAi knockdown of CASH-1/STRN3 results in adults that are slow-moving and sterile; by immunostaining with antibodies to myosin, these animals have disorganized sarcomeric A-bands (Qadota et al., 2018). Inspection of the Million Mutation Project (MMP) collection of mutant strains (Thompson et al., 2013) revealed several strains that have missense mutations in conserved residues of CASH-1, but one of them, *cash-1(gk705529)*, which results in a H121Y mutation, had severe phenotypes: a high percentage of embryonic lethality, and, among the

animals that reach adulthood, greatly reduced motility. We outcrossed this mutant twice to wildtype to remove many of the background mutations, and also re-created the mutation by CRISPR in our RFP- and myc-tagged CASH-1 strain (Figure 2A). We immunostained adults from each strain with antibodies to UNC-89 (obscurin) to assess M-lines, myosin heavy chain A (MHC A) to assess A-bands, and UNC-95 to assess the bases of the M-lines and dense bodies (Z-disks) and muscle cell boundaries. As shown in Figure 2B, each of the mutants display mild disorganization of these structures. The disorganization of A-bands is similar to that previously reported by us using RNAi (Qadota et al., 2018). Also note that the localization of UNC-89 is unusually broad compared to wildtype. In addition, UNC-95 staining is moderately disorganized. To assess to what extent the sarcomeric defect can be attributed to a decreased level of mutant protein vs. a functionally defective protein, we performed quantitative Western blotting to compare the level of RFP/myc-CASH-1 in an otherwise wild-type background to the level of RFP/myc-CASH-1 H121Y. As shown in Figure 2C, H121Y CASH-1 protein levels are not decreased, but rather may be increased.

We selected one *farl-11* MMP allele for analysis, *farl-11(gk437008)*, which has a non-conservative L292 to P change in the N1221 domain. This strain was outcrossed 3X to wildtype. Although we could not create this mutation using CRISPR, we did generate two additional mutations via CRISPR at nearby residues in this same domain: *farl-11(jc93)*, which deletes T281 in-frame, and *farl-11(jc94)*, which deletes P280 in-frame. After outcrossing twice to wildtype and immunostaining, all three mutant alleles show severely disorganized sarcomeres (Figure 3B). Of particular note is the wider distribution of both UNC-89 and myosin, which can be discerned more clearly in the zoomed insets. To assess to what extent the sarcomeric defect is

due to a decreased level of mutant protein vs. a functionally defective mutant protein, we compared the levels of FARL-11 protein from all three *farl-11* mutants to wildtype. Based on Western blot analysis as shown in Figure 3C, we were surprised to find no detectable FARL-11 protein in *farl-11(gk437008)*, a missense mutant. There are no other mutations in the *farl-11* gene in this strain (VC30204), based on a query of the MMP website at Simon Fraser University (http://genome.sfu.ca/mmp/). Both *jc93* and *jc94* display decreased levels of FARL-11: *jc93* expresses 48.9 % of the wild-type level, and *jc94* shows a mean of 64.1% of the wild-type level (mean, n = 4).

CASH-1/STRN3 and FARL-11/STRIP1/2 localize to M-lines and dense bodies

We next sought to determine the localization of CASH-1 and FARL-11 in nematode body wall muscle. To localize CASH-1 we utilized our CRISPR strain, SU854, which expresses a RFP/myc-CASH-1 fusion protein. As shown in Figure 4A, in which CASH-1 was detected with antibodies to myc and M-lines and dense bodies detected with antibodies to UNC-95, CASH-1 is localized between and surrounding dense bodies, i.e., essentially the I-band region. To localize FARL-11 we used antibodies to FARL-11. As indicated in Figure 4B, in which we co-stained with antibodies to PAT-6 (α-parvin), which also localizes to the base of M-lines and dense bodies, FARL-11 localizes between and surrounding dense bodies, but not as broadly as CASH-1. We next asked whether CASH-1 and FARL-11 co-localize. As shown in Figure 4C, in which we used anti-myc to detect RFP/myc-CASH-1 and antibodies to FARL-11, the two proteins colocalize to the same structures.

FARL-11 localizes to the sarcoplasmic reticulum

Transmission electron micrographs have revealed that the SR in *C. elegans* body wall muscle is restricted to thin membranous sacs closely apposed to the dense bodies as well as near the bases of M-lines or the middle of the A-band region (Gieseler et al. 2017). In *C. elegans*, the ryanodine receptor (the calcium release channel of the SR) is encoded by a single gene, *unc-68* (Maryon et al., 1996; Sakube et al., 1997). Using confocal microscopy to image localization of antibodies to UNC-68 and various components of the myofilament lattice (MHC A, MHC B, vinculin, α-actinin), Maryon et al., 1998 concluded that UNC-68 resides primarily in flattened vesicular sacs adjacent to the outer muscle cell membrane in the A-band region. In contrast, Hamada et al., 2002, using antibodies to UNC-68 and either rhodamine-phalloidin or antibodies to the A-band protein paramyosin, concluded that UNC-68 resides in the I-band region. Although these two studies seem to give different localizations for UNC-68, together, the results include both known or suspected locations of the SR (surrounding dense bodies and adjacent to base of M-lines). Unfortunately, the antibodies generated to UNC-68 utilized in these studies are no longer available. A recent report by Piggott et al., 2021 provides the best confocal images of UNC-68 localization in muscle. These authors created a split-GFP knock-in allele for *unc-68* and their confocal images show that GFP::UNC-68 localizes to rows of puncta, some large, some small, but the authors did not co-localize with any sarcomeric markers.

Given that FARL-11 has been localized to the ER of early nematode embryos and that the SR is a muscle-specific type of ER, we used CRISPR/Cas9 to create strain SU980, in which UNC-68 is tagged at its N-terminus with 3xHA. By conventional confocal microscopy, HA-UNC-68 exists in puncta, which are organized in a repeating, striated pattern roughly surrounding both

dense bodies and M-lines (Figure 4D). We next asked whether FARL-11 and UNC-68 might co-localize. As shown in Figure 4E, there is at least some co-localization of the two proteins, suggested by the white puncta created by the overlap of green FARL-11 and magenta HA-UNC-68 signals. Figure 4F likewise shows co-localization of HA-UNC-68 and myc-CASH-1.

To obtain more information about the localization of UNC-68, we used structured illumination microscopy (SIM), which has an ~120 nm resolution in the XY plane. SIM, followed by 3D reconstruction (Figure 5A), shows that HA-UNC-68 localizes to a series of puncta, very similar to the images reported by Piggott et al., 2021. Co-staining with PAT-6 (α-parvin), which localizes to the bases of the M-lines and dense bodies reveals that the HA-UNC-68 puncta localize on either side of the M-lines, and surround the dense bodies, with the larger puncta being closer to the dense bodies. There is also accumulation of HA-UNC-68 at muscle cell boundaries (indicated by yellow arrows in Figure 5B). When viewed in the Z-plane these reconstructions reveal that HA-UNC-68 at the muscle cell boundaries extends more deeply into the muscle cell than does the HA-UNC-68 near the M-lines and dense bodies (Figure 5C). Next, we co-stained using anti-HA, anti-α-actinin (Figure 5D), and anti-UNC-89 (Figure 5E) to determine how deep HA-UNC-68 is localized within the muscle.

Unfortunately, the anti-FARL-11 antibodies did not give a strong enough signal in immunostaining to allow SIM imaging. However, we were able to use confocal microscopy to acquire Z series using anti-FARL-11 and anti-HA to detect HA-UNC-68, starting from the outer muscle cell membrane where the dense bodies are attached to positions deeper into muscle cells (Figure 6). Based on these confocal z-series, UNC-68 extends from the base of the dense bodies

to the deeper parts of the dense bodies (deeper than the known location of UNC-95, which is restricted to the base of dense bodies). FARL-11 also extends along the full depth of dense bodies; interestingly, it is also found at the muscle cell membranes at the boundaries between adjacent spindle-shaped muscle cells. Curiously, HA-UNC-68 only appears at the muscle cell boundaries at the deepest portions of the muscle cell, again consistent with the SIM images. Localization of UNC-68 at the muscle cell boundaries has not previously been reported and its function there is currently unknown. The function of FARL-11 at muscle cell boundaries, particularly throughout the depth of the boundaries of muscle cells, is also unclear. Overall, FARL-11 localization is similar to that of HA-UNC-68 in Z-series, suggesting that FARL-11 is localized to the SR.

In mammalian muscle, the UNC-89 homolog, obscurin, links myofibrils to the surrounding SR, through interaction of obscurin with the SR membrane proteins small ankyrin 1 and 2(Bagnato et al., 2003; Kontrogianni-Konstantopoulos et al., 2003). Moreover, knockout of the mouse obscurin gene results in disorganization of the SR (Lange et al., 2009). This role for obscurin seems to be evolutionarily conserved. In *C. elegans*, there is genetic evidence for an UNC-89-to-SR functional linkage. VAV-1 is a RacGEF that regulates the concentration of intracellular calcium and is expressed in body wall muscle. Overexpression of *vav-1* in muscle results in slow movement; mutagenesis identified suppressor mutations in *egl-19* (an L-type calcium channel) and *unc-89* (Spooner et al., 2012) that allow improved movement. Moreover, in *unc-89* mutants, in addition to disorganization of sarcomeres, there is disorganization of the SR, as probed using transgenics overexpressing MYC-UNC-68 or SERCA-GFP (Spooner et al., 2012). We therefore wondered whether loss of function of *unc-68*, which has been shown to disrupt SR organization

(Maryon et al., 1998) might also disrupt the organization of sarcomeres. As shown in Figure 7, *unc-68(e540)* shows disorganization of major structural components of the sarcomere—the A-bands (MHC A), the M-lines (UNC-89), the bases of M-lines and dense bodies (UNC-95), and the deeper major portions of dense bodies (ATN-1).

If, as our data suggest, FARL-11 and CASH-1 are components of the SR, one straightforward prediction is that in a mutant in which the SR is disrupted, e.g. an *unc-68* mutant, FARL-11 and CASH-1 might be mislocalized. Curiously, however, this is not the case. As shown in Figure 8A, the localization of FARL-11 in *unc-68(e540)* and wildtype are nearly identical. Because *cash-1* and *unc-68* are very close together on the genetic map, we used CRISPR to tag CASH-1 at the N terminus using TagRFP::3xmyc in an *unc-68(e540)* mutant background. As shown in Figure 8B, the localization of CASH-1 in *unc-68(e540)* and wildtype are nearly identical.

We then asked how mutations in *farl-11* and *cash-1* affect the localization of UNC-68, which serves as a proxy for the SR. Interestingly, compared to wildtype (Figure 9A), in the *farl-11 (gk437008)* mutant UNC-68 still localizes between dense bodies, but also displays decreased localization around M-lines (Figure 9B). These analyses place *farl-11* genetically upstream of *unc-68*. To examine HA::UNC-68 in a *cash-1* mutant, we used CRISPR to re-create the H121Y mutation in *cash-1* in the HA::UNC-68 background. To our surprise we saw no difference in localization of UNC-68 compared to wildtype (Figure 9C). Thus, there appears to be a more stringent requirement for FARL-11 compared to CASH-1 for maintenance of SR organization. Alternatively, the *cash-1* point mutation synergizes with other genetic alterations in the Million

Mutation Project strain, and the H121Y alone acts as a weak hypomorph. Further analysis of domain deletions or full cash-1 deletions may be useful in adjudicating this issue.

Discussion

Elucidating the functions of various PP2A holoenzymes in striated muscle in vertebrates is important, given the demonstrated role of PP2A holoenzymes in sarcomere assembly and maintenance. As one example, targeting, expression, and localization of various PP2A holoenzymes in the heart have been shown to be important for proper heart function(Lei et al., 2015; DeGrande et al., 2013). In muscle the release of Ca^{2+} from the sarcoplasmic reticulum (SR) is regulated in part by phosphoregulation of the ryanodine receptor type 2 (RyR2), which has been shown to regulated by PP2A, PP2B, and PP1(Terentyev and Hamilton, 2016), raising the intriguing possibility that PP2A directly regulates RyR2.

Because all the major molecular components of striated muscle sarcomeres are present in *C. elegans* body wall muscle, it is a powerful model for understanding the organization of striated muscle in metazoans(Benian and Epstein, 2011). Previously, we showed that PP2A complex components localize to muscle sarcomeres, and that loss of some PP2A components leads to disorganized muscle (Qadota et al., 2018). This previous work revealed that various PP2A B regulatory subunits are important for sarcomeric structures; however, the lack of available antibodies and translational reporters precluded assessment of the location of various PP2A holoenzymes. Here we have expanded upon that prior work to show that the STRIPAK complex is localized to the sarcomere, and that disruption of STRIPAK causes sarcomere disorganization. Specifically, our analysis of two core members of the STRIPAK complex, FARL-11/STRIP1/2

and CASH-1/STRN3. FARL-11 and CASH-1, reveals that they are both localized within the adult *C. elegans* muscle, and that loss of either of these components results in defects in sarcomeres.

An important result of our analysis is that STRIPAK activity is necessary for normal SR structure in body wall muscle. This is consistent with prior work in the *C. elegans* zygote: a *farl-11* hypomorphic allele causes defects in ER organization (Maheshwari et al., 2016),and the localization of endogenously tagged STRIPAK components (see Chapter 2). Previously, a genetic interaction between *unc-89/obscurin* and *unc-68* was reported (Spooner et al., 2012). In *unc-89* mutants, the organization of UNC-68 (assessed via a transgene) and the sarcoplasmic/endoplasmic reticulum calcium ATPase, SERCA (also via a transgene) were disrupted. Here we have shown that *unc-68 (e540)* mutants have disorganized UNC-89/obscurin localization (Figure 7), which we also observed in *farl-11* mutants. These data suggest that UNC-68 and UNC-89 are mutually dependent on one another for maintenance of their localization. Epistasis testing and colocalization data further suggest that STRIPAK acts upstream of both proteins, and that there may be direct physical association of STRIPAK with UNC-68. Loss of STRIPAK may in turn lead to defects in calcium signaling due to defective SR organization.

Several questions remain. First, is UNC-68 a direct target of the STRIPAK complex? While this is a parsimonious hypothesis based on the data in this chapter, additional; experiments will be required. These include demonstrating that STRIPAK and UNC-68 physically associate *in vivo*. Co-immunoprecipitation experiments are underway to test this idea. While ambitious, reconstitution of the *C. elegans* STRIPAK complex *in vitro* to show that it can catalyze

dephosphorylation of UNC-68 would ultimately be required as well. A second question is whether various STRIPAK components only work via the fully assembled holoenzyme complex. It is possible that individual STRIPAK components have other roles that have yet to be elucidated. We have shown that *C. elegans* is a useful system for beginning to address these and other questions related to this ubiquitous enzymatic complex.

Materials and Methods

C. elegans strains

SU853 *farl-11 (jc61[mNG::TEV::3xflag::farl-11 + LoxP])* III

SU854 *cash-1 (jc60[TagRFP::TEV::3xmyc:::cash-1 +Lox 2272])* V

SU980 *unc-68*(jc78[*3xha::unc-68*]) V

SU1002 *cash-1* (*jc60*[*[TagRFP::TEV::3xmyc:::cash-1 +Lox 2272*]; *unc-68*(jc78[*3xha::unc-68*]) V -2X

SU1047 farl-11 (j*c93* [*farl-11*Δ *T281 *jc61*]) II -2x

SU1048 *farl-11* (*jc94* [*farl-11* Δ*P280 *jc61*]) II

SU1054: *cash-1* (*jc100*[*cash-1 h121y *jc60*]) V-2x

SU1086 *cash-1* (*jc106[3xmyc::cash-1*]); *unc-68* (*e540*)-2x

SU1070 *cash-1* (*jc100*[*cash-1h121y *jc60*]); *unc-68* (*jc78* [*3xha::unc-68*a])-V-2x

CB540 *unc-68 (e540)* V

VC40583 *cash-1* (*gk705529*[*cash-1 h121y*])-V

VC30204 *farl-11* (*gk437008* [*farl-11 l292p*])-II

CRISPR/Cas9

To generate endogenous insertions a self-excising cassette was used as described (Dickinson et al., 2015). *tagrfp::SEC::CASH-1/+* was crossed into the *tmC12* (Dejima et al., 2018) balancer to facilitate SEC removal. *mng::SEC::farl-11/+* was crossed into the *mIn1* balancer to facilitate SEC removal. The balanced progeny were heat shocked at 34°C to remove the SEC. SEC excision and correct knock-in were confirmed by PCR of non-rolling, non-balanced progeny. Worms were outcrossed with N2 a minimum of 2x.

Single point mutants were generated as described (Arribere et al., 2014).

Guide RNA sequences were cloned into the Cas9 containing plasmid (pJW1219).

CASH-1 5' guide- 5' -CGGATTCGAGTAGTTACAATGG

CASH-1 H121Y guide-5' ATTTATGTATGCATCAAGGT

FARL-11-5' guide: - 5'GGCCTGATTCCCATTACATT

FARL-11 L290P guide- 5' ATTTCATTATCAACCATAGT

UNC-68-5'guide-5' TCCTCCCTGCTCCTCCTTGT

Homology searches/protein sequence analysis

CASH-1 and FARL-11 sequences were run through a Hydrophobic Cluster analysis program (mboyle@RPBS) to generate a Hydrophobic Cluster Plot (Neron et al., 2009). Subsequent CRISPR mutants were made at sites of predicted secondary structure (Callebaut et al., 1997).

Generation of antibody to FARL-11

Antibody production was performed by Li International (Denver, CO). A 50 amino acid chemically synthesized peptide corresponding to the extreme C-terminus of FARL-11 (aa 929-978 TCAHSVLGANLKLGRHFKKDYEKWLEQEVFNASIDWDKLLIETRGVEDLM) was injected into New Zealand rabbits. Li International performed immunization and provided lyophilized antibody which was resuspended to 1 mg/mL with 1x PBS.

Western blots

The method of Hannak et al. (2002) was used to prepare total protein lysates from mixed stage populations of wild-type, SU853, SU854, SU1054, SU1047, SU1048, and *farl-11(gk437008)* worms. Equal amounts of total protein were separated on 10% polyacrylamide-SDS-Laemmli gels, transferred to nitrocellulose membranes, reacted with affinity purified, anti-FARL-11 at 1:500 or 1:1000 dilution, and anti-myc (mouse monoclonal clone 9E 10 from the University of Iowa Hybridoma Bank) at 1:300 dilution. Blots were reacted with anti-rabbit (or anti-mouse) immunoglobulin G conjugated to HRP (GE Healthcare) at 1:10,000 dilution, and visualized by ECL. For comparison of protein levels between wildtype and mutants, samples were normalized based on total protein per lane visualized by Ponceau S staining.

Immunostaining, confocal and SIM microscopy of body wall muscle

Adult nematodes were fixed and immunostained using the method described by (Nonet et al., 1993) with further details described in (Wilson et al., 2012). The following primary antibodies were used at 1:200 dilution except as noted: anti-UNC-89 (mouse monoclonal MH42; Benian et al., 1996; Hresko et al., 1994), anti-MHC A (mouse monoclonal 5-6; Miller et al., 1983), anti-

UNC-95 (rabbit polyclonal Benian-13; Qadota et al., 2007), anti-PAT-6 (rat polyclonal; Warner et al., 2013), anti-ATN-1 (mouse monoclonal MH35; Francis and Waterston, 1991), anti-HA (rabbit monoclonal from Cell Signaling Technology Inc., cat. no. 3724S; and mouse monoclonal from Sigma-Aldrich, cat. no. H3663), anti-myc (mouse monoclonal clone 9E 10 from the University of Iowa Hybridoma Bank), and anti-FARL-11 (this study). Secondary antibodies, used at 1:200 dilution, included anti-rabbit Alexa 488, anti-rat Alexa 594, and anti-mouse Alexa 594, all purchased from Invitrogen. Images were captured at room temperature with a Zeiss confocal system (LSM510) equipped with an Axiovert 100M microscope and an Apochromat x63/1.4 numerical aperture oil immersion objective, in 1x and 2.5x zoom mode. Super-resolution microscopy was conducted with a Nikon N-SIM system in 3D structured illumination mode on an Eclipse Ti-E microscope equipped with a 100×/1.49 NA oil immersion objective, 488- and 561-nm solid-state lasers, and an EM-CCD camera (DU-897, Andor Technology). Super-resolution images were reconstructed using the N-SIM module in NIS-Elements software. For all images, confocal and SIM, color balance was adjusted by using Adobe Photoshop (Adobe, San Jose, CA).

References

Arribere, J.A., R.T. Bell, B.X.H. Fu, K.L. Artiles, P.S. Hartman, and A.Z. Fire. 2014. Efficient marker-free recovery of custom genetic modifications with CRISPR/Cas9 in Caenorhabditis elegans. *Genetics*. 198:837–846. doi:10.1534/genetics.114.169730.

Bagnato, P., V. Barone, E. Giacomello, D. Rossi, and V. Sorrentino. 2003. Binding of an ankyrin-1 isoform to obscurin suggests a molecular link between the sarcoplasmic reticulum and myofibrils in striated muscles. *J Cell Biol*. 160:245–253. doi:10.1083/jcb.200208109.

Benian, G.M., and H.F. Epstein. 2011. Caenorhabditis elegans muscle: a genetic and molecular model for protein interactions in the heart. *Circ Res*. 109:1082–1095. doi:10.1161/CIRCRESAHA.110.237685.

Benian, G.M., T.L. Tinley, X. Tang, and M. Borodovsky. 1996. The Caenorhabditis elegans gene unc-89, required fpr muscle M-line assembly, encodes a giant modular protein composed of Ig and signal transduction domains. *J Cell Biol*. 132:835–848. doi:10.1083/jcb.132.5.835.

Callebaut, I., G. Labesse, P. Durand, A. Poupon, L. Canard, J. Chomilier, B. Henrissat, and J.P. Mornon. 1997. Deciphering protein sequence information through hydrophobic cluster analysis (HCA): current status and perspectives. *Cellular and Molecular Life Sciences (CMLS)*. 53:621–645. doi:10.1007/s000180050082.

DeGrande, S.T., S.C. Little, D.J. Nixon, P. Wright, J. Snyder, W. Dun, N. Murphy, A. Kilic, R. Higgins, P.F. Binkley, P.A. Boyden, C.A. Carnes, M.E. Anderson, T.J. Hund, and P.J. Mohler. 2013. Molecular mechanisms underlying cardiac protein phosphatase 2A regulation in heart. *J Biol Chem*. 288:1032–1046. doi:10.1074/jbc.M112.426957.

Dejima, K., S. Hori, S. Iwata, Y. Suehiro, S. Yoshina, T. Motohashi, and S. Mitani. 2018. An Aneuploidy-Free and Structurally Defined Balancer Chromosome Toolkit for Caenorhabditis elegans. *Cell Rep*. 22:232–241. doi:10.1016/j.celrep.2017.12.024.

Dickinson, D.J., A.M. Pani, J.K. Heppert, C.D. Higgins, and B. Goldstein. 2015. Streamlined Genome Engineering with a Self-Excising Drug Selection Cassette. *Genetics*. 200:1035–1049. doi:10.1534/genetics.115.178335.

Francis, R., and R.H. Waterston. 1991. Muscle cell attachment in Caenorhabditis elegans. *J Cell Biol*. 114:465–479. doi:10.1083/jcb.114.3.465.

Hamada, T., Y. Sakube, J. Ahnn, D.H. Kim, and H. Kagawa. 2002. Molecular dissection, tissue localization and Ca2+ binding of the ryanodine receptor of Caenorhabditis elegans. *J Mol Biol*. 324:123–135. doi:10.1016/s0022-2836(02)01032-x.

Hresko, M.C., B.D. Williams, and R.H. Waterston. 1994. Assembly of body wall muscle and muscle cell attachment structures in Caenorhabditis elegans. *J Cell Biol*. 124:491–506. doi:10.1083/jcb.124.4.491.

Jeong, B.-C., S.J. Bae, L. Ni, X. Zhang, X. Bai, and X. Luo. 2021. Cryo-EM structure of the Hippo signaling integrator human STRIPAK. *Nat Struct Mol Biol*. 28:290–299. doi:10.1038/s41594-021-00564-y.

Kontrogianni-Konstantopoulos, A., E.M. Jones, D.B. Van Rossum, and R.J. Bloch. 2003. Obscurin is a ligand for small ankyrin 1 in skeletal muscle. *Mol Biol Cell*. 14:1138–1148. doi:10.1091/mbc.e02-07-0411.

Lange, S., K. Ouyang, G. Meyer, L. Cui, H. Cheng, R.L. Lieber, and J. Chen. 2009. Obscurin determines the architecture of the longitudinal sarcoplasmic reticulum. *J Cell Sci*. 122:2640–2650. doi:10.1242/jcs.046193.

Lei, M., X. Wang, Y. Ke, and R.J. Solaro. 2015. Regulation of Ca(2+) transient by PP2A in normal and failing heart. *Front Physiol*. 6:13. doi:10.3389/fphys.2015.00013.

Maheshwari, R., K. Pushpa, and K. Subramaniam. 2016. A role for post-transcriptional control of endoplasmic reticulum dynamics and function in *C. elegans* germline stem cell maintenance. *Development*. 143:3097–3108. doi:10.1242/dev.134056.

Maryon, E.B., R. Coronado, and P. Anderson. 1996. unc-68 encodes a ryanodine receptor involved in regulating *C. elegans* body-wall muscle contraction. *J Cell Biol*. 134:885–893. doi:10.1083/jcb.134.4.885.

Maryon, E.B., B. Saari, and P. Anderson. 1998. Muscle-specific functions of ryanodine receptor channels in Caenorhabditis elegans. *J Cell Sci*. 111 (Pt 19):2885–2895. doi:10.1242/jcs.111.19.2885.

Miller, D.M., I. Ortiz, G.C. Berliner, and H.F. Epstein. 1983. Differential localization of two myosins within nematode thick filaments. *Cell*. 34:477–490. doi:10.1016/0092-8674(83)90381-1.

Neron, B., H. Menager, C. Maufrais, N. Joly, J. Maupetit, S. Letort, S. Carrere, P. Tuffery, and C. Letondal. 2009. Mobyle: a new full web bioinformatics framework. *Bioinformatics*. 25:3005–3011. doi:10.1093/bioinformatics/btp493.

Nonet, M.L., K. Grundahl, B.J. Meyer, and J.B. Rand. 1993. Synaptic function is impaired but not eliminated in *C. elegans* mutants lacking synaptotagmin. *Cell*. 73:1291–1305. doi:10.1016/0092-8674(93)90357-v.

Piggott, C.A., Z. Wu, S. Nurrish, S. Xu, J.M. Kaplan, A.D. Chisholm, and Y. Jin. 2021. Caenorhabditis elegans junctophilin has tissue-specific functions and regulates neurotransmission with extended-synaptotagmin. *Genetics*. 218:iyab063. doi:10.1093/genetics/iyab063.

Pracheil, T., and Z. Liu. 2013. Tiered assembly of the yeast Far3-7-8-9-10-11 complex at the endoplasmic reticulum. *J Biol Chem*. 288:16986–16997. doi:10.1074/jbc.M113.451674.

Qadota, H., Y. Matsunaga, P. Bagchi, K.I. Lange, K.J. Carrier, W.V. Pols, E. Swartzbaugh, K.J. Wilson, M. Srayko, D.C. Pallas, and G.M. Benian. 2018. Protein phosphatase 2A is crucial for sarcomere organization in *Caenorhabditis elegans* striated muscle. *MBoC*. 29:2084–2097. doi:10.1091/mbc.E18-03-0192.

Qadota, H., K.B. Mercer, R.K. Miller, K. Kaibuchi, and G.M. Benian. 2007. Two LIM domain proteins and UNC-96 link UNC-97/pinch to myosin thick filaments in Caenorhabditis elegans muscle. *Mol Biol Cell*. 18:4317–4326. doi:10.1091/mbc.e07-03-0278.

Sakube, Y., H. Ando, and H. Kagawa. 1997. An abnormal ketamine response in mutants defective in the ryanodine receptor gene ryr-1 (unc-68) of Caenorhabditis elegans. *J Mol Biol*. 267:849–864. doi:10.1006/jmbi.1997.0910.

Shi, Y. 2009. Serine/Threonine Phosphatases: Mechanism through Structure. *Cell*. 139:468–484. doi:10.1016/j.cell.2009.10.006.

Spooner, P.M., J. Bonner, A.V. Maricq, G.M. Benian, and K.R. Norman. 2012. Large isoforms of UNC-89 (obscurin) are required for muscle cell architecture and optimal calcium release in Caenorhabditis elegans. *PLoS One*. 7:e40182. doi:10.1371/journal.pone.0040182.

Terentyev, D., and S. Hamilton. 2016. Regulation of sarcoplasmic reticulum Ca2+ release by serine-threonine phosphatases in the heart. *J Mol Cell Cardiol*. 101:156–164. doi:10.1016/j.yjmcc.2016.08.020.

Thompson, O., M. Edgley, P. Strasbourger, S. Flibotte, B. Ewing, R. Adair, V. Au, I. Chaudhry, L. Fernando, H. Hutter, A. Kieffer, J. Lau, N. Lee, A. Miller, G. Raymant, B. Shen, J. Shendure, J. Taylor, E.H. Turner, L.W. Hillier, D.G. Moerman, and R.H. Waterston. 2013. The million mutation project: a new approach to genetics in Caenorhabditis elegans. *Genome Res*. 23:1749–1762. doi:10.1101/gr.157651.113.

Warner, A., G. Xiong, H. Qadota, T. Rogalski, A.W. Vogl, D.G. Moerman, and G.M. Benian. 2013. CPNA-1, a copine domain protein, is located at integrin adhesion sites and is required for myofilament stability in Caenorhabditis elegans. *Mol Biol Cell*. 24:601–616. doi:10.1091/mbc.E12-06-0478.

Wilson, K.J., H. Qadota, and G.M. Benian. 2012. Immunofluorescent localization of proteins in Caenorhabditis elegans muscle. *Methods Mol Biol*. 798:171–181. doi:10.1007/978-1-61779-343-1_10.

Figure 1: CASH-1 and FARL-11 characterization in *C. elegans*. A. Protein domain map showing FARL-11 and CASH-1 domains; the FARL-11 antibody was raised against the extreme C-terminus. **B.** Western blot of *C. elegans* lysates demonstrating that the anti-FARL-11 antibody binds to a protein of the predicted molecular weight in wildtype, and binds to mNG::FARL-11 in an endogenous knock-in strain (SU853). An anti-myc antibody recognizes the TagRFP::**3xmyc**::CASH-1 protein in endogenous knock-in strain SU854.

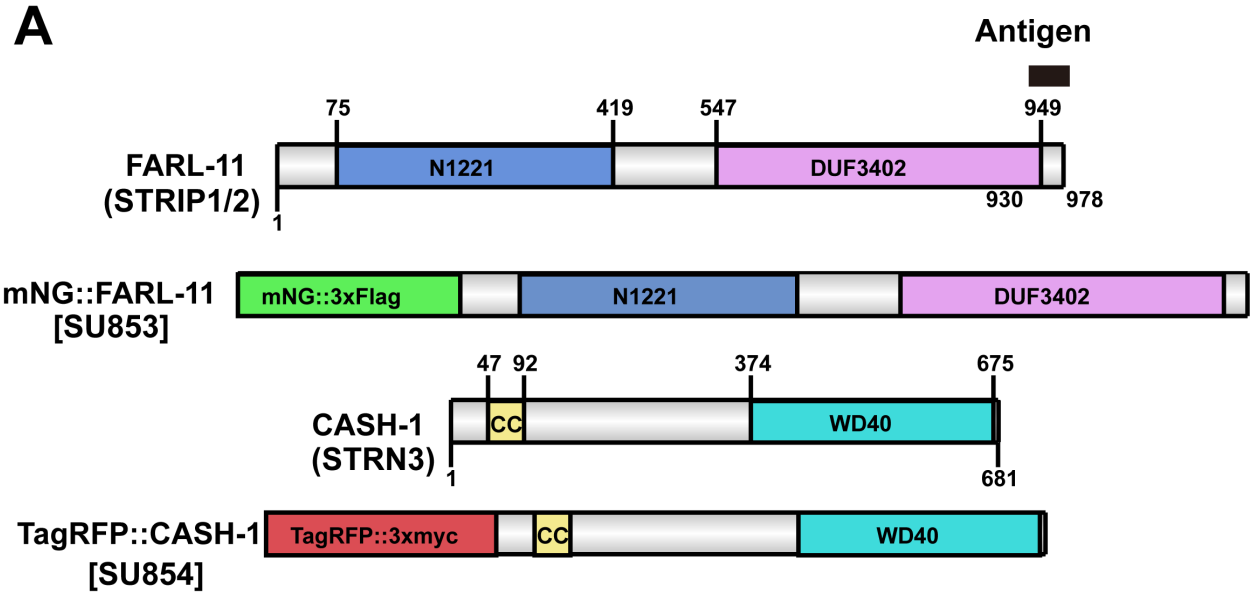
A
Antigen
75
419
547
949
FARL-11
(STRIP1/2)
N1221
DUF3402
1
930
978
mNG::FARL-11
[SU853]
mNG::3xFlag
N1221
DUF3402
47
92
374
675
CASH-1
(STRN3)
CC
WD40
1
681
TagRFP::CASH-1
[SU854]
TagRFP::3xmyc
CC
WD40

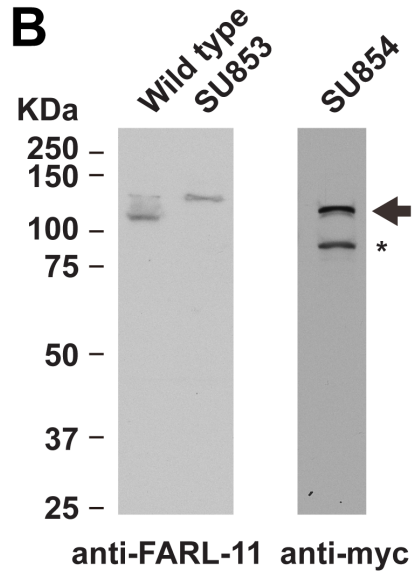
B
Wild type
SU853
SU854
KDa
250
150
100
75
50
37
25
*
anti-FARL-11
anti-myc

Figure 2: CASH-1 localization in the body wall muscle of *C. elegans*. A. Protein domain map of CASH-1, showing location of N-terminal TagRFP::3xmyc (*jc60*) and the H121Y mutation (*gk705529*, recreated in *jc100*). **B.** Both CASH-1 mutants cause mild disorganization of sarcomeric structures. Markers: UNC-89/Obscurin (M-lines), Myosin Heavy Chain/MHC A (A-band), and UNC-95 (base of M-lines and dense bodies). Scale bar = 20 μm. **C.** Western blot showing that the level of CASH-1(H121Y) in *jc100* knock-in worms is not decreased compared to wildtype.

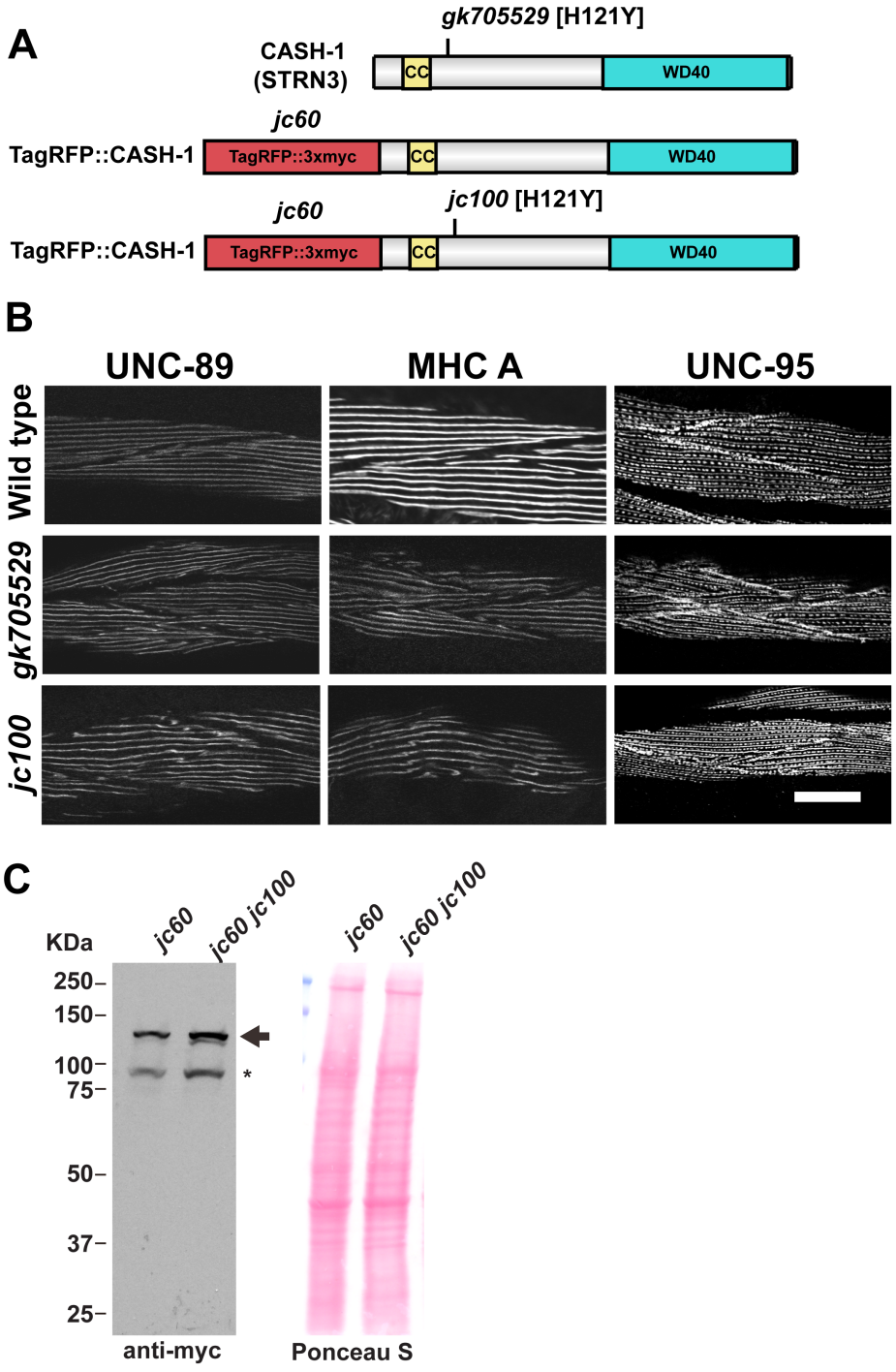
A
gk705529 [H121Y]
CASH-1
(STRN3)
CC
WD40
jc60
TagRFP::CASH-1
TagRFP::3xmyc
CC
WD40
jc60
jc100 [H121Y]
TagRFP::CASH-1
TagRFP::3xmyc
CC
WD40
B
UNC-89
MHC A
UNC-95
Wild type
gk705529
jc100
C
KDa
jc60
jc60 jc100
jc60
jc60 jc100
250
150
100
75
50
37
25
*
anti-myc
Ponceau S

Figure 3: CASH-1 localization in the body wall muscle of *C. elegans*. A. Protein domain map of FARL-11, showing location of the *jc93* (ΔT281), *jc94* (ΔP280), and *gk437008* (L292P) mutations. **B.** Both CASH-1 mutants cause mild disorganization of sarcomeric structures. The following markers were used: UNC-89/obscurin (M-lines), myosin heavy chain/MHC A (A-band), and UNC-95 (base of M-lines and dense bodies). **C.** Western blot showing reduced FARL-11 protein levels in *jc93* (48.9% of wild-type) and *jc94* (64.1% lower than wild-type, average of 4 experiments), while, surprisingly, *gk237008* shows no protein expression. Scale bar = 20 μm.

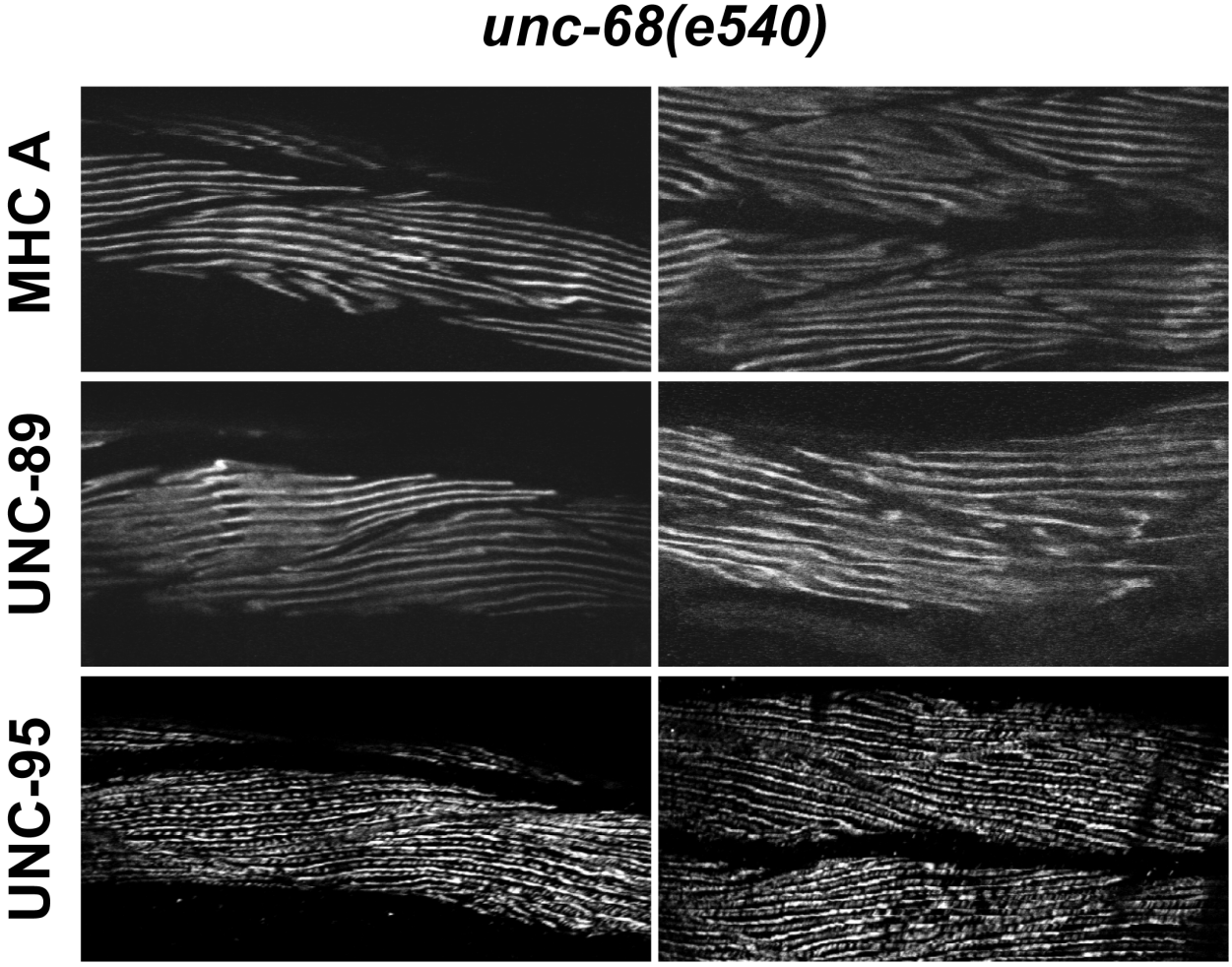
unc-68(e540)
MHC A
UNC-89
UNC-95

Figure 4: CASH-1 and FARL-11 localize to M-lines and dense bodies. A. CASH-1 localizes between M-lines and dense bodies, based on anti-UNC-95 co-staining. **B.** FARL-11 localizes between and surrounding dense bodies, based on co-staining with anti-PAT-6 antibodies. **C.** Co-staining of FARL-11 and CASH-1 shows that they colocalize within muscle. **D.** UNC-68 (the ryanodine receptor of the SR) localizes surrounding both dense bodies and M-lines. **E.** UNC-68 colocalizes with FARL-11. **F.** UNC-68 colocalizes with CASH-1. Scale bar = 10 μm.

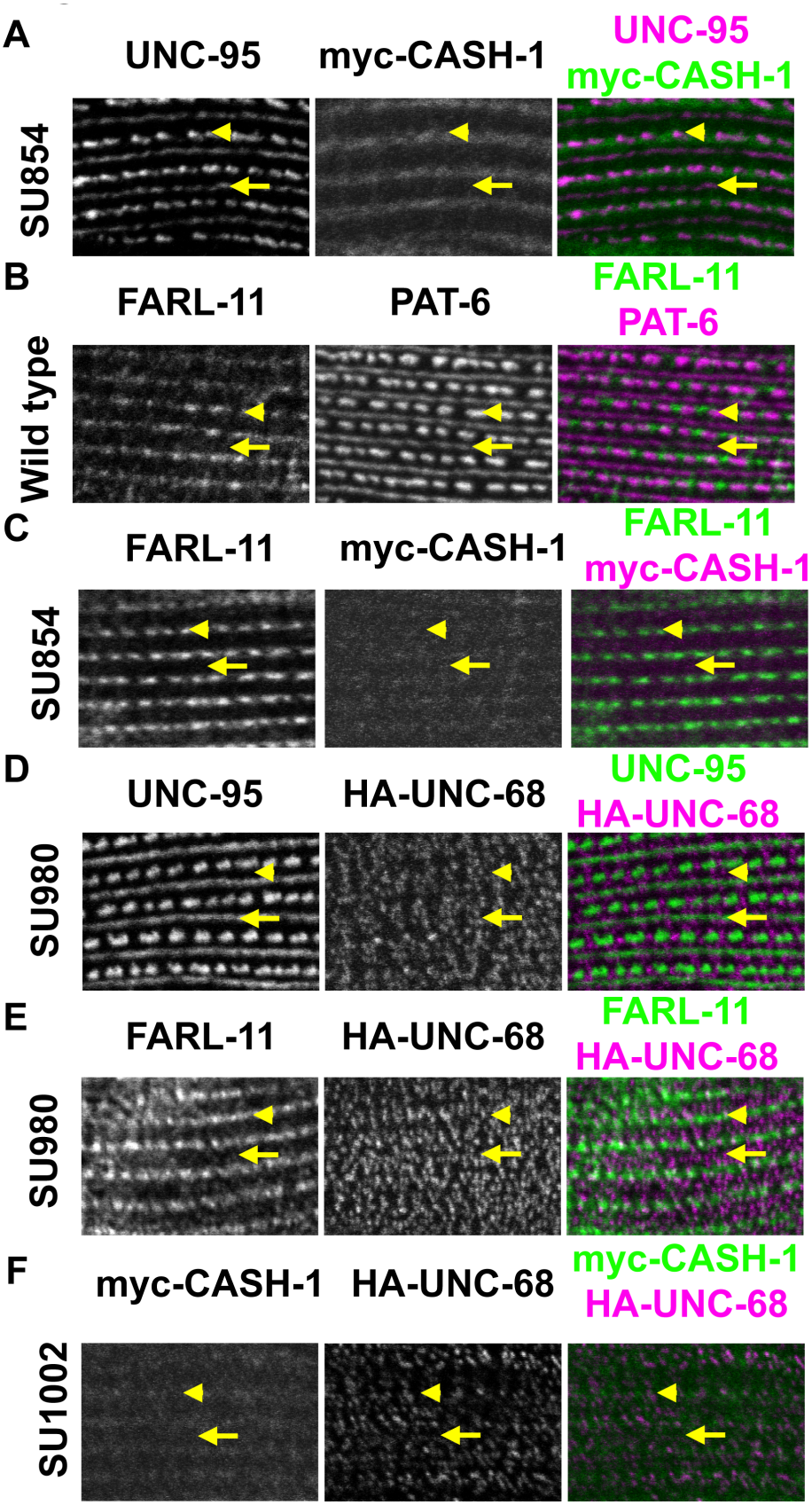
A
UNC-95
myc-CASH-1
UNC-95
myc-CASH-1
SU854
B
FARL-11
PAT-6
FARL-11
PAT-6
Wild type
C
FARL-11
myc-CASH-1
FARL-11
myc-CASH-1
SU854
D
UNC-95
HA-UNC-68
UNC-95
HA-UNC-68
SU980
E
FARL-11
HA-UNC-68
FARL-11
HA-UNC-68
SU980
F
myc-CASH-1
HA-UNC-68
myc-CASH-1
HA-UNC-68
SU1002

Figure 5: Detailed localization of UNC-68 in muscle using SIM. A. Co-staining for UNC-68 and PAT-6 (α -parvin) shows UNC-68 localizes to the bases of the M-lines and dense bodies and reveals that HA-UNC-68 puncta localize on either side of the M-lines and surround dense bodies, with larger puncta closer to dense bodies. **B.** HA-UNC-68 localization at muscle cell boundaries as indicated by yellow arrows. **C.** HA-UNC-68 at the muscle cell boundaries extends more deeply into the muscle cell than does the HA-UNC-68 near the M-lines and dense bodies when viewed in the Z-plane. **D.** Co-staining for HA-UNC-68 and anti- α -actinin (DEB-1); a-actinin is localized to most of the dense body except for the base. HA-UNC-68 localizes predominantly near the outer muscle cell membrane, but UNC-68 signal extends more deeply into muscle cells beyond the dense body and sarcomeric area. **E.** Co-staining for HA-UNC-68 and UNC-89/obscurin to show how deeply into the muscle UNC-68 extends. UNC-89 is located throughout the depth of the M-line, showing that, predominantly, HA-UNC-68 resides near outer muscle cell membranes but also extends deeper into the muscle cell, beyond the sarcomeric area, as in Figure D. Scale bar = 10 μm.

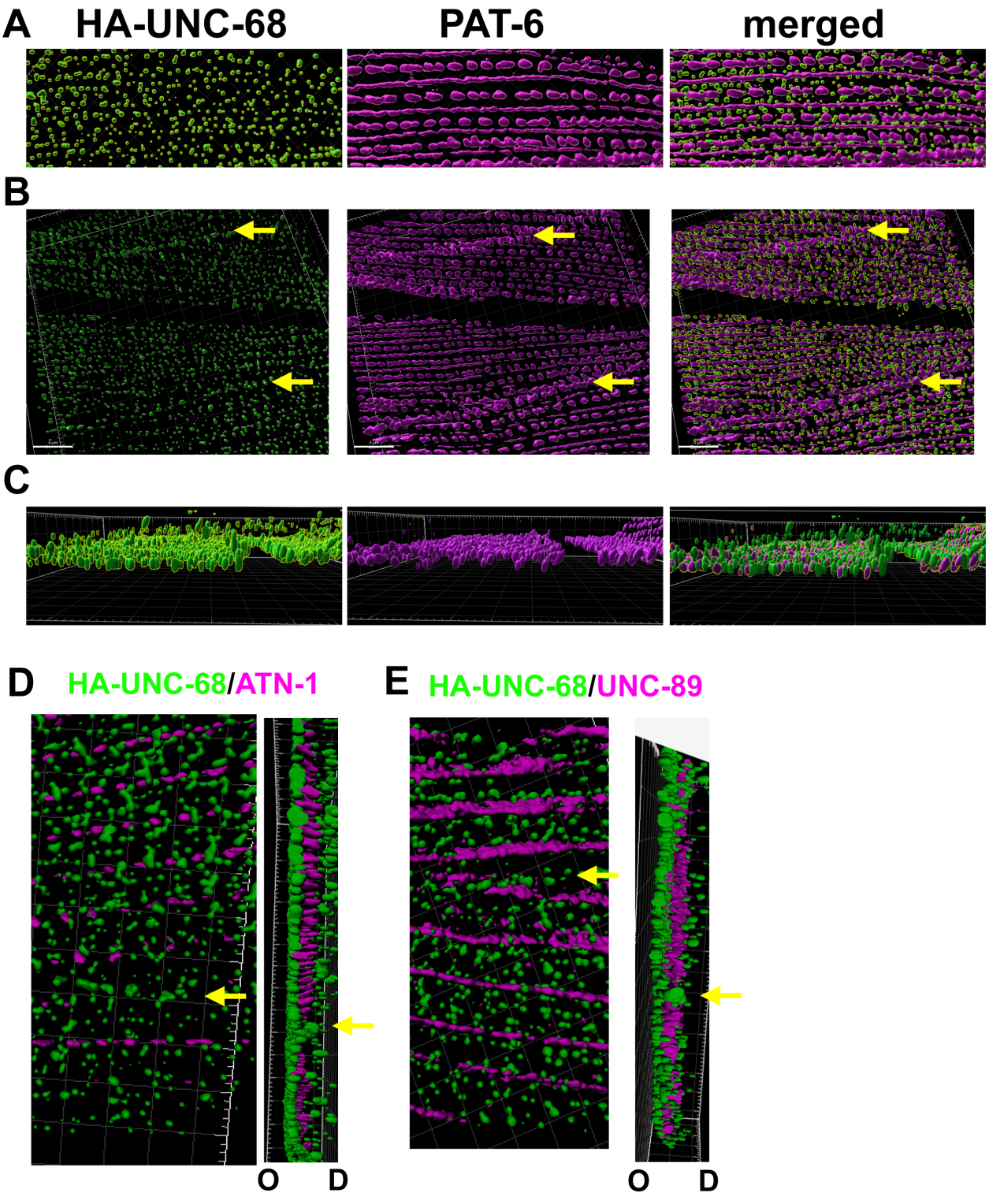
A
HA-UNC-68
PAT-6
merged
B
C
D
HA-UNC-68/ATN-1
O
D
E
HA-UNC-68/UNC-89
O
D

Figure 6: FARL-11 and UNC-68 colocalization within the muscle. FARL-11 localization is similar to that of HA-UNC-68 in Z-series, suggesting that FARL-11 is localized to the SR and extends from the base of dense bodies to the deeper parts of dense bodies. Scale bar = 20 μm.

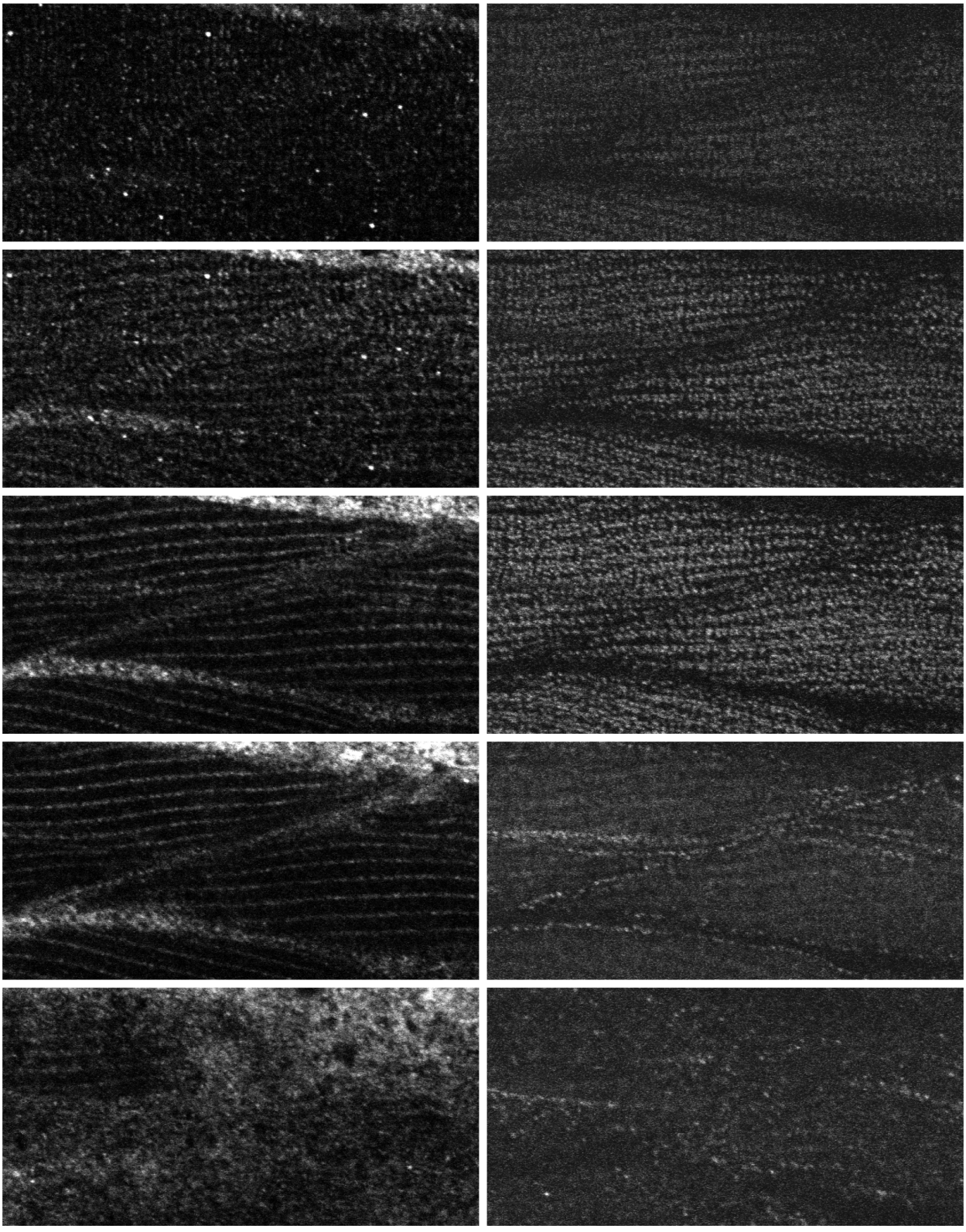
FARL-11
HA-UNC-68

Figure 7: Characterization of *unc-68*(*e540*) defects in the sarcomere. *unc-68(e540)* mutants show disorganization of major structural components of the sarcomere—the A-bands (MHC A), the M-lines (UNC-89), the bases of M-lines and dense bodies (UNC-95), and the deeper major portions of dense bodies (ATN-1). Scale bar = 20 μm.

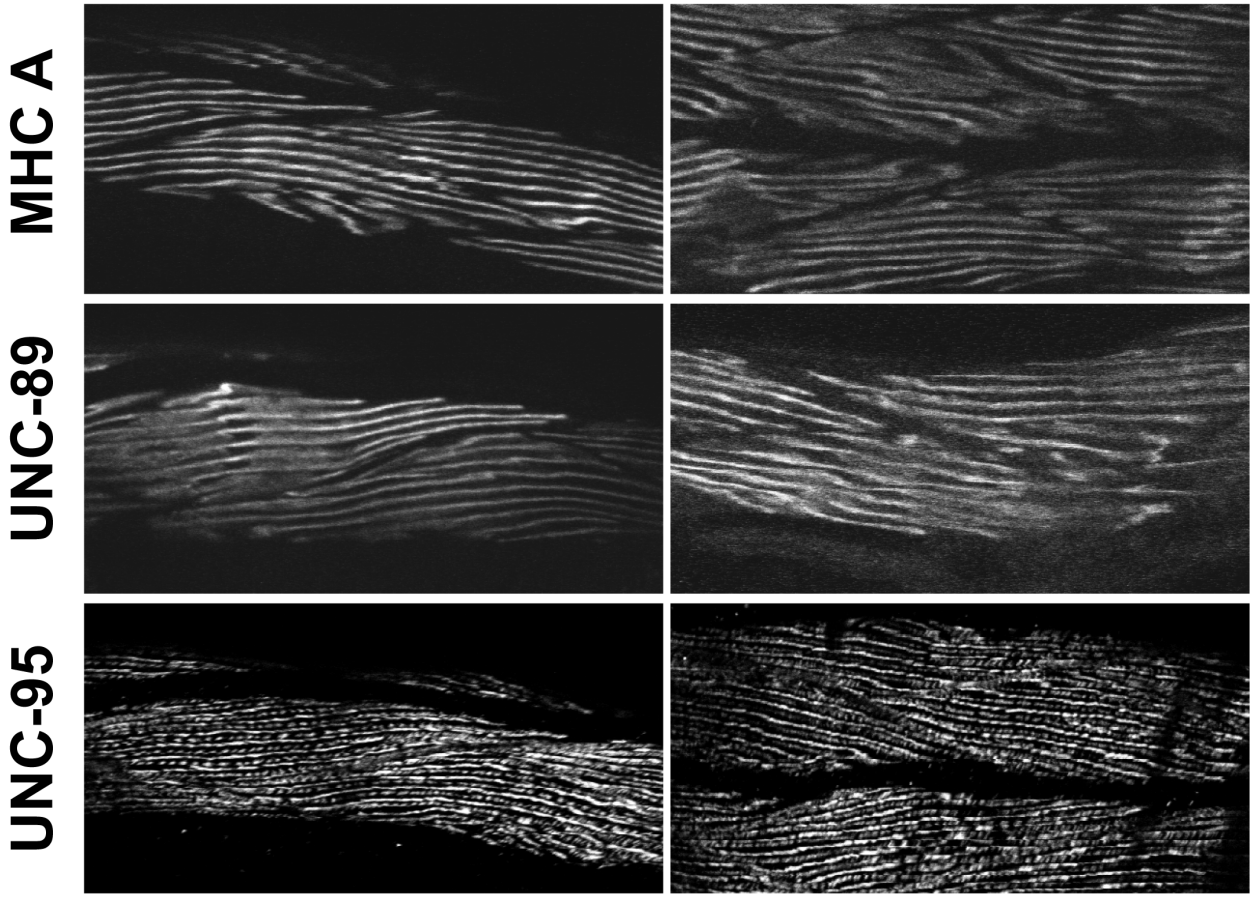
unc-68(e540)
MHC A
UNC-89
UNC-95

Figure 8: Characterization of FARL-11 and CASH-1 localization in *unc-68* (*e540*) mutants. **A.** FARL-11 localization is not disrupted in *unc-68 (e540)* mutants. B. CASH-1 localization is not disrupted in *unc-68 (e540)* mutants. Scale bar = 10 μm.

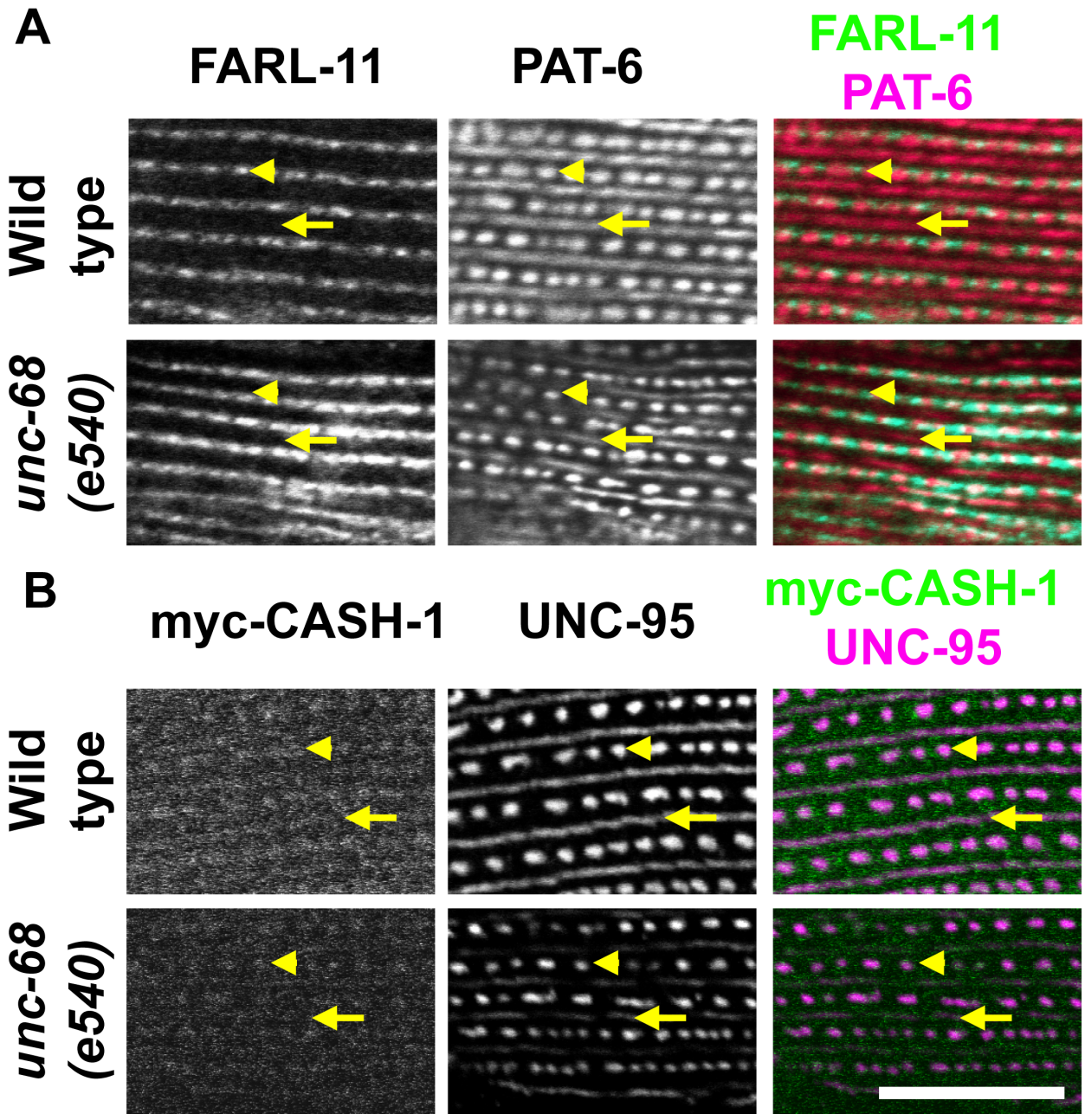
A
FARL-11
PAT-6
FARL-11
PAT-6
Wild type
unc-68 (e540)
B
myc-CASH-1
UNC-95
myc-CASH-1
UNC-95
Wild type
unc-68 (e540)

Figure 9: UNC-68 localization is disrupted in *farl-11*, but not *cash-1* mutants. A. Wild-type UNC-68 localization in muscle. **B.** In *farl-11*(*gk437008*) mutants UNC-68 still localizes between dense bodies, but also exhibits decreased localization around M-lines. **B.** UNC-68 localization is not affected in *cash-1* mutants as compared to A. Scale bar = 10 μm.

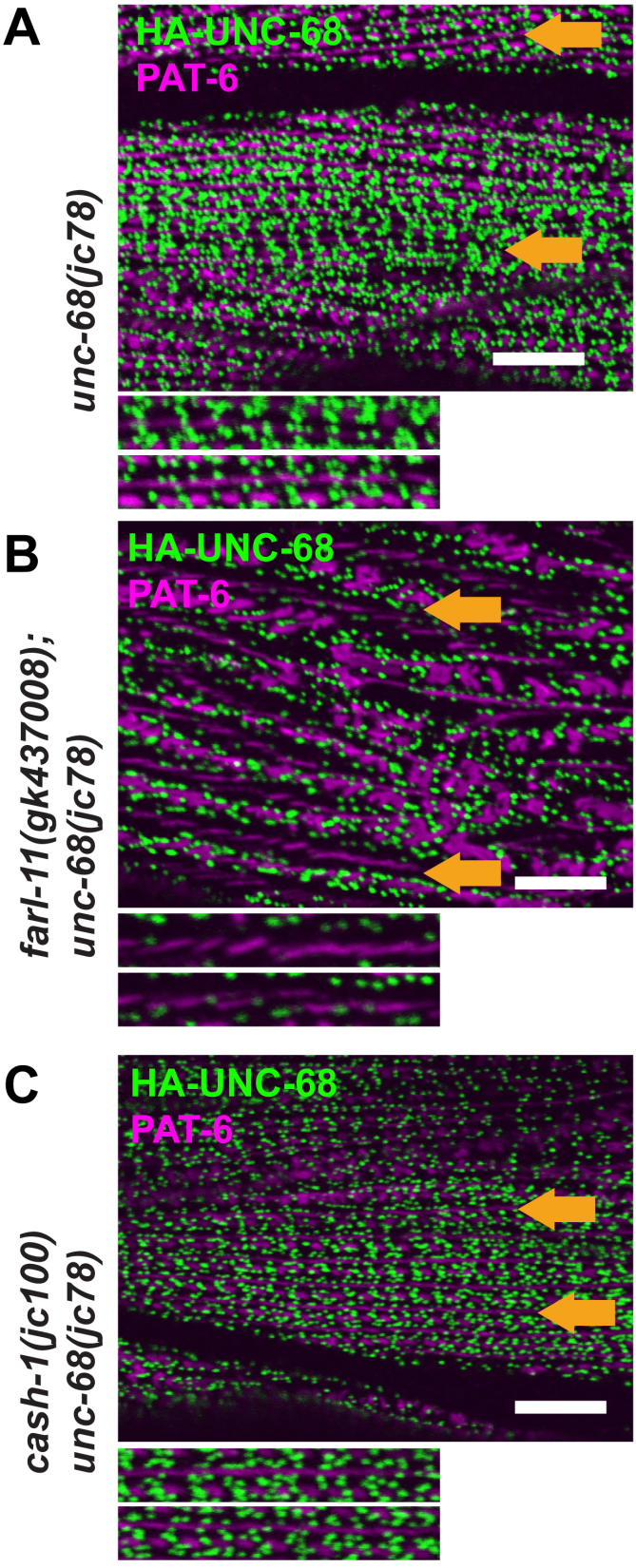
A
HA-UNC-68
PAT-6
unc-68(jc78)
B
HA-UNC-68
PAT-6
farl-11(gk437008);
unc-68(jc78)
C
HA-UNC-68
PAT-6
cash-1(jc100)
unc-68(jc78)

Figure 9 supplemental: UNC-68 localization is disrupted in *farl-11* but not *cash-1* mutants as visualized with UNC-89 as a marker. UNC-68 still localizes between dense bodies, but displays decreased accumulation around M-lines in *farl-11* mutants. Scale bar = 10 μm.

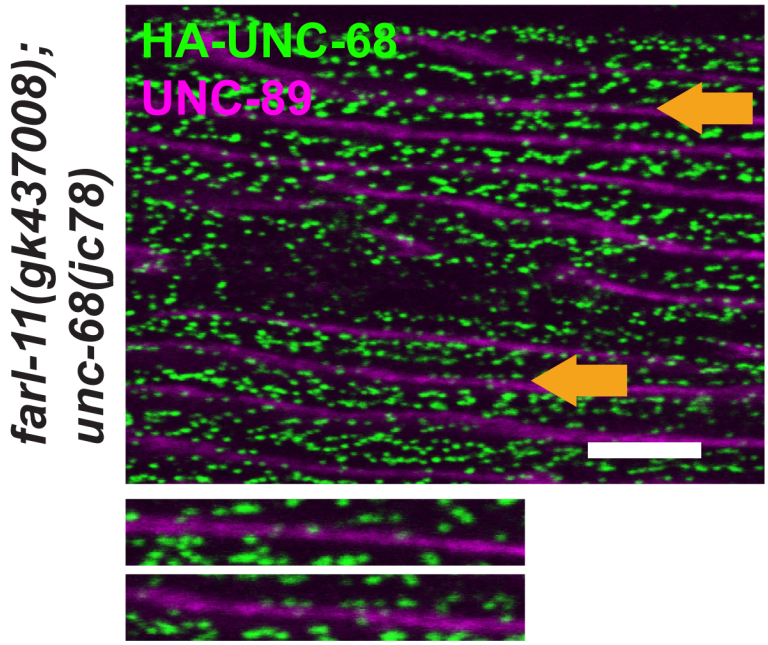
farl-11(gk437008);
unc-68(jc78)
HA-UNC-68
UNC-89

CHAPTER 4:

Future Directions and Conclusions

My Contributions are data in this chapter, entirely generated by me, which are unpublished.

Introduction

In this thesis, I have explored the role of the STRIPAK complex in the nematode, *C. elegans* during cell division (Chapter 2) and in sarcomere assembly in skeletal muscle (Chapter 3). In addition to these roles, there are hints that FARL-11/Strip, and, by extension, the rest of the STRIPAK complex, is active in multiple aspects of the *C. elegans* life cycle. *farl-11* was originally discovered to genetically interact with HMP-1/α-catenin during morphogenesis (Lynch et al., 2012), suggesting that the STRIPAK complex could be playing roles in the postmitotic epidermis. Using the CRISPR/Cas9-generated materials reported in this thesis, there is much more to learn about the STRIPAK complex in various tissues and processes in *C. elegans*.

Future Directions

The role of STRIPAK in the epidermis

There are several future directions suggested by the work in this thesis. *C. elegans* possesses two major epithelial junctional complexes, the cadherin-catenin complex (CCC), and the more basal DLG-1/AJM-1 complex (Lynch and Hardin, 2009) (Figure 1A). Originally, the "hub" of the STRIPAK complex, FARL-11/Strip, was identified in an RNAi enhancer screen, which identified modulators of cadherin-dependent cell adhesion in the hypomorphic *hmp-1(fe4)* background (Lynch et al., 2012, Figure 1). Interestingly, while *farl-11* was originally identified in this screen, none of the other STRIPAK complex components were. I discovered that *cash-1* was not in the Ahringer RNAi library (Kamath, 2003); knockdown of *cash-1* in a *hmp-1(fe4)* background confirmed that *cash-1* is also a potent *hmp-1(fe4)* enhance (Figure 2). CASH-1 knockdown causes cellular debris to escape through the ventral pocket. In a *hmp-1(fe4)* background the loss of function of the two genes synergizes, leading to failure of the ventral

pocket to close resulting in 100% embryonic lethality (Figure 2A-C, model 2D). Interestingly, the *cash-1*Δ*wd40* mutant and *the farl-11 (tm6233)* mutants also result in cellular debris escaping through the ventral pocket (Figure 2A-2C). As both *ccm-3* and *mob-4* are in the Ahringer RNAi library (while *gck-1* is not), determining whether these STRIPAK components are also enhancers of *hmp-1(fe4)* is warranted. It is possible that *ccm-3* and *mob-4* were not identified in the *hmp-1 (fe4)* enhancer screen due to low knockdown efficacy (Kamath et al., 2000). Knockdown by injection RNAi is consistently more efficient in our hands, so injecting double-stranded RNAs (dsRNAs) for each of these STRIPAK complex components into *hmp-1(fe4)* adults and assaying for enhancement of lethality may reveal that they, too, genetically interact with cadherin-based adhesion. If the other members of the STRIPAK complex are not enhancers of *hmp-1(fe4)* this could indicate a specific role for FARL-11/CASH-1 in the epidermis, independent of the rest of the STRIPAK complex. Functional distinctions among STRIPAK complex components would be a novel and interesting finding.

I have performed a preliminary set of investigations of the expression of STRIPAK components in the embryonic epidermis as a prelude to further analysis in the future. Upon further examination of the *cash-1*Δ*n* embryos, there are embryos that display subtle dorsal bulges that are not as severe but are similar to those in *hmp-1(fe4)* embryos (Figure 3A). To determine if CASH-1 or FARL-11 are expressed during this stage of embryonic development, I examined endogenously tagged TagRFP::CASH-1 and mNG::FARL-11 I had previously produced (for details regarding the relevant strains, see Chapter 2). Both proteins localize to sites of cell-cell contact during embryonic elongation (Figure 3B). CASH-1 does not colocalize with the cadherin-catenin complex (CCC) (Figure 3C), nor does it appear to coIP with HMP-2/β-catenin

(Figure 3E). Interestingly, TagRFP::CASH-1 appears to colocalize with DLG-1::mNG (Figure 3D) and knockdown of the DLG-1/AJM-1 complex leads to loss of CASH-1 at junctions (Figure 4A and 4B), suggesting that CASH-1 and FARL-11 may be interacting with apical junctions subapically to the CCC, and that this interaction is dependent on the WD40 domain of CASH-1 (Figure 4C). Knockdown of *dlg-1* or *ajm-1* did not affect TagRFP::CASH-1 localization to the nucleus, suggesting recruitment to this site via a different means. In contrast, recruitment of TagRFP::CASH-1 is not dependent on HMP-1 or HMP-2, since knockdown of either does not obviously affect TagRFP::CASH-1 localization at junctions (Figure 4D and 4E), nor is TagRFP::CASH-1 localization affected when MAGI-1, a protein that localizes between the CCC and the DLG-1/AJM-1 complex (Lynch et al., 2012), is depleted via RNAi (Figure 4F). Knockdown of *cash-1* does not obviously affect steady-state levels of junctional DLG-1::mNG, HMP-1::eGFP, or HMP-2::eGFP (Figure 4G-I). This suggests that CASH-1, if it has functional roles at this stage of development, acts downstream of key junctional organizing proteins. It is possible that CASH-1 and FARL-11 affect dynamics of the DLG-1/AJM-1 complex, which could be assessed via fluorescence recovery after photobleaching (FRAP) or other technologies. Clearly further work is needed to identify what functional roles STRIPAK might be playing and how it might contribute to junctional stability. As there are already CRISPR knock-ins for GCK-1 and CCM-3 (Pal et al., 2017; Bell et al., 2020), it would also be of interest to see if these components of STRIPAK localize to junctions during morphogenesis.

CASH-1, FARL-11, and ER homeostasis

Prior to my work, FARL-11/Strip and CASH-1/Striatin had been shown to be important for endoplasmic reticulum (ER) homeostasis; a hypermorphic *farl-11* allele and *cash-1* knockdown

perturb the structure of the ER in the embryo (Maheshwari et al., 2016). This perturbation of the ER causes disruption of RME-2 trafficking in the early embryo (Maheshwari et al., 2016) and GLP-1 trafficking in the gonad (Pal et al., 2017). My work adds to this story by showing that the specialized ER of skeletal muscle, the sarcoplasmic reticulum (SR), is also mislocalized in STRIPAK mutant backgrounds (see Chapter 3). Determining how both *farl-11* and *cash-1* contribute to ER homeostasis would be of significant interest, given the ubiquitous and essential roles of the ER in myriad cellular processes. From data shown in Chapter 2, CASH-1ΔN appears to localize correctly (possibly via its intact WD40 domain), while CASH-1ΔWD40 does not. CASH-1ΔWD40 forms puncta; these puncta may correspond to patches of ER. Such patches of ER were also reported in *farl-11(kp35)* hypomorphs and *cash-1* knockdown (Maheshwari et al., 2016). To understand how CASH-1 and FARL-11 are interacting with the ER at higher spatial resolution, one fruitful approach would be to use cryoEM in serial section from single embryos (Yi et al., 2019) to understand how CASH-1 and FARL-11 associate with the ER in wildtype and in *cash-1ΔWD40* mutants. Another unresolved issue is to which portions of the ER STRIPAK components localize. Colocalizing STRIPAK components with markers for different regions of the ER, such as TRAM, which marks the rough ER, PIS (phosphatidylinositol synthase), which marks the smooth ER, and emerin, which marks the nuclear envelope (Rolls et al., 2002) could provide insights into the question.

The complete STRIPAK interactome

As CASH-1/Striatin is the B''' regulatory subunit of PP2A and FARL-11/Strip is presumably a structural "hub" for STRIPAK complex assembly, identifying additional physical or genetic interactors with either protein could identify additional, presumably non-obligate, members of

the STRIPAK complex, or potential targets of PP2A phosphoregulation. To identify CASH-1 interactors, one could take a two-pronged approach, using both genetics and mass spectrometry. Using *cash-1ΔWD40* mutants, which have low-level lethality, one could perform a genome-wide RNAi screen to determine additional genes, which when knocked down, lead to enhancement of lethality in this sensitized background. Any "hits" could then be followed up and examined via microscopy to determine what is the nature of the lethality and if they have any effect on CASH-1 or FARL-11 localization, prior to endogenous tagging to assess subcellular localization. Conversely, *cash-1Δn* and *farl-11(tm6233)* mutants are both homozygote lethal, so one could perform EMS mutagenesis screens in heterozygous mothers to identify suppressor mutations that rescue homozygous lethality. Either of these approaches could help to determine additional genes involved in activating or suppressing STRIPAK function, or genes that act in parallel to STRIPAK.

Another approach to mapping the STRIPAK interactome would be coIP/mass spectrometry using the endogenous TagRFP::CASH-1 and mNG::FARL-11 knock-ins. Previous mass spectrometry experiments were focused on other members of the STRIPAK complex, such as the PP2A catalytic subunit (Goudreault et al., 2009), or GCK-1 (Pal et al., 2017). Using other members of the complex to pull down additional potential interactors may identify new STRIPAK-associated components. Any hits could be validated using RNAi to determine if knockdown has any effect on CASH-1 or FARL-11 localization, or if knockdown in the *cash-1* and *farl-11* mutants leads to enhancement or suppression of phenotypes. Furthermore, any proteins that are identified from mass spectrometry could be followed up to determine if they directly bind with CASH-1 using standard pulldown assays. This is of interest as currently there

is no known “STRIPAK motif” common to STRIPAK interacting proteins; any proteins that are shown to bind directly to CASH-1 could be used to identify a potential STRIPAK binding domain that would aid in helping identify substrates of the STRIPAK complex.

The role of Germinal Center Kinase-1 (GCK-1) in the STRIPAK complex

Although not the focus of this thesis, the "K″ in STRIPAK represents the kinase, GCK-1. What potential role(s) GCK-1 could be playing in the STRIPAK complex is an open question. Lant et al 2015 showed that GCK-1 binds to CCM-3 and that CCM-3 links the two proteins to CASH-1. GCK-1 was also shown to be involved in cytokinesis (Bell et al., 2020). Furthermore, a kinase dead GCK-1 K62R/T186A transgene failed to rescue canal cell extension in a *ccm-3* mutant, suggesting that kinase function is necessary for canal extension (Lant et al., 2015). What function the kinase domain could be playing in other tissues is of interest and could be preliminarily examined using CRISPR/Cas9 to create an endogenous K62R/T186R *gck-1* mutant. This kinase-dead GCK-1 could then be crossed into the CASH-1ΔWD40 mutant to dissect GCK-1 functions that depend upon or are independent of the STRIPAK complex. As GCK-1 has been shown to be involved in cytokinesis, one could test if the kinase function is involved in cytokinesis and assay for any blebs (as in Chapter 2) or embryos that fail during cytokinesis. Furthermore, since CASH-1 and STRIPAK are enhancers of *hmp-1(fe4),* one could test to see if loss of function of the kinase domain of GCK-1 enhances *hmp-1(fe4)* lethality. This is an interesting possibility, our group, in collaboration with the Audhya group, showed that FARL-11 and PAA-1 (the structural subunit of PP2A) were revealed to be interactors in a screen for HMP-1/α-catenin and HMP-2/β-catenin interactors (Callaci et al., 2015).

Conclusions

C. elegans is a powerful model organism for elucidating assembly of and additional roles for the STRIPAK complex *in vivo*. During early embryogenesis I showed that STRIPAK plays a role in organizing ZEN-4/MKLP-1 after cytokinesis and that later, during morphogenesis, STRIPAK localizes to epidermal cell-cell junctions. In work with the Benian group I also showed that both CASH-1 and FARL-11 play roles in sarcomere assembly and organization in adult body wall muscle. The future directions sketched here will hopefully help to elucidate the functions of the STRIPAK complex during embryogenesis and in specific tissues in an intact organism. Given the high degree of conservation of key proteins in the STRIPAK complex from nematodes to humans, these results can then be used as a stepping stone to further studies in vertebrates.

References

Bell, K.R., M.E. Werner, A. Doshi, D.B. Cortes, A. Sattler, T. Vuong-Brender, M. Labouesse, and A.S. Maddox. 2020. Novel cytokinetic ring components drive negative feedback in cortical contractility. *MBoC*. 31:1623–1636. doi:10.1091/mbc.E20-05-0304.

Callaci, S., K. Morrison, X. Shao, A.L. Schuh, Y. Wang, J.R. Yates, J. Hardin, and A. Audhya. 2015. Phosphoregulation of the *C. elegans* cadherin–catenin complex. *Biochemical Journal*. 472:339–352. doi:10.1042/BJ20150410.

Goudreault, M., L.M. D'Ambrosio, M.J. Kean, M.J. Mullin, B.G. Larsen, A. Sanchez, S. Chaudhry, G.I. Chen, F. Sicheri, A.I. Nesvizhskii, R. Aebersold, B. Raught, and A.-C. Gingras. 2009. A PP2A Phosphatase High Density Interaction Network Identifies a Novel Striatin-interacting Phosphatase and Kinase Complex Linked to the Cerebral Cavernous Malformation 3 (CCM3) Protein. *Molecular & Cellular Proteomics*. 8:157–171. doi:10.1074/mcp.M800266-MCP200.

Kamath, R. 2003. Genome-wide RNAi screening in Caenorhabditis elegans. *Methods*. 30:313–321. doi:10.1016/S1046-2023(03)00050-1.

Kamath, R.S., M. Martinez-Campos, P. Zipperlen, A.G. Fraser, and J. Ahringer. 2000. Effectiveness of specific RNA-mediated interference through ingested double-stranded RNA in Caenorhabditis elegans. *Genome Biol*. 2:research0002.1. doi:10.1186/gb-2000-2-1-research0002.

Lant, B., B. Yu, M. Goudreault, D. Holmyard, J.D.R. Knight, P. Xu, L. Zhao, K. Chin, E. Wallace, M. Zhen, A.-C. Gingras, and W.B. Derry. 2015. CCM-3/STRIPAK promotes seamless tube extension through endocytic recycling. *Nat Commun*. 6:6449. doi:10.1038/ncomms7449.

Lynch, A.M., T. Grana, E. Cox-Paulson, A. Couthier, M. Cameron, I. Chin-Sang, J. Pettitt, and J. Hardin. 2012. A Genome-wide Functional Screen Shows MAGI-1 Is an L1CAM-Dependent Stabilizer of Apical Junctions in *C. elegans*. *Current Biology*. 22:1891–1899. doi:10.1016/j.cub.2012.08.024.

Lynch, A.M., and J. Hardin. 2009. The assembly and maintenance of epithelial junctions in *C. elegans*. *Frontiers in Bioscience-Landmark*. 14:1414–1432. doi:10.2741/3316.

Maheshwari, R., K. Pushpa, and K. Subramaniam. 2016. A role for post-transcriptional control of endoplasmic reticulum dynamics and function in *C. elegans* germline stem cell maintenance. *Development*. 143:3097–3108. doi:10.1242/dev.134056.

Pal, S., B. Lant, B. Yu, R. Tian, J. Tong, J.R. Krieger, M.F. Moran, A.-C. Gingras, and W.B. Derry. 2017. CCM-3 Promotes *C. elegans* Germline Development by Regulating Vesicle Trafficking Cytokinesis and Polarity. *Current Biology*. 27:868–876. doi:10.1016/j.cub.2017.02.028.

Rolls, M.M., D.H. Hall, M. Victor, E.H.K. Stelzer, and T.A. Rapoport. 2002. Targeting of Rough Endoplasmic Reticulum Membrane Proteins and Ribosomes in Invertebrate Neurons. *MBoC*. 13:1778–1791. doi:10.1091/mbc.01-10-0514.

Yi, X., E.J. Verbeke, Y. Chang, D.J. Dickinson, and D.W. Taylor. 2019. Electron microscopy snapshots of single particles from single cells. *Journal of Biological Chemistry*. 294:1602–1608. doi:10.1074/jbc.RA118.006686.

Figure 1: *C. elegans* epithelial junctional complexes and identification of lethal enhancers of *hmp-1 (fe4).* **A.** Schematic of the two major epithelial junctional complexes in *C. elegans*. The cadherin-catenin complex (CCC), which contains HMR-1/cadherin, HMP-2/β-catenin, and HMP-1/α-catenin, lies apical to the DLG-1/AJM-1 complex. **B.** Pie chart showing classes of lethal enhancers of *hmp-1*(*fe4*) from a genome-wide feeding RNAi screen, updated from Lynch et al (2012).

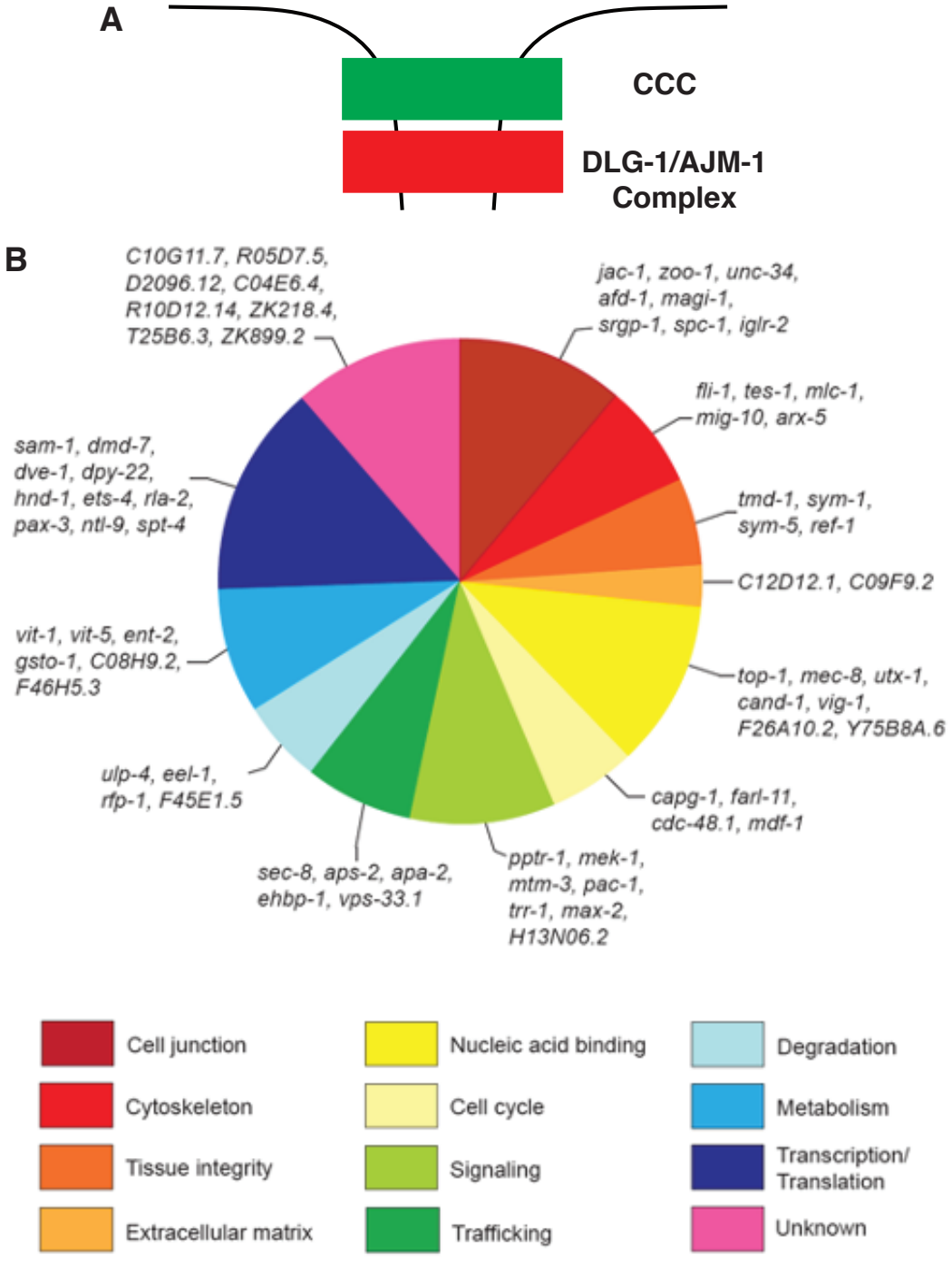
A
CCC
DLG-1/AJM-1
Complex
B
C10G11.7, R05D7.5,
D2096.12, C04E6.4,
R10D12.14, ZK218.4,
T25B6.3, ZK899.2
jac-1, zoo-1, unc-34,
afd-1, magi-1,
srgp-1, spc-1, iglr-2
fli-1, tes-1, mlc-1,
mig-10, arx-5
tmd-1, sym-1,
sym-5, ref-1
C12D12.1, C09F9.2
top-1, mec-8, utx-1,
cand-1, vig-1,
F26A10.2, Y75B8A.6
capg-1, farl-11,
cdc-48.1, mdf-1
pptr-1, mek-1,
mtm-3, pac-1,
trr-1, max-2,
H13N06.2
sec-8, aps-2, apa-2,
ehbp-1, vps-33.1
ulp-4, eel-1,
rfp-1, F45E1.5
vit-1, vit-5, ent-2,
gsto-1, C08H9.2,
F46H5.3
sam-1, dmd-7,
dve-1, dpy-22,
hnd-1, ets-4, rla-2,
pax-3, ntl-9, spt-4
Cell junction
Cytoskeleton
Tissue integrity
Extracellular matrix
Nucleic acid binding
Cell cycle
Signaling
Trafficking
Degradation
Metabolism
Transcription/
Translation
Unknown

Figure 2: STRIPAK mutants display ectopic blebs at the ventral midline and synergize with *hmp-1*(*fe4*) during ventral enclosure. A. At t = 0 min, a bleb (arrow) can be seen at the ventral midline in *cash*-1 RNAi and *cash-1*(RNAi); *hmp-1*(*fe4*) background (arrows), but not in *hmp-1*(*fe4*) embryos. Similar ventral midline debris can also be seen in *cash-1*Δ*wd40* and *farl-11*(*tm6233*) mutants (arrows). In single STRIPAK loss-of-function backgrounds this debris persists at subsequent time points. **B.** At t = 10 min, *cash-1* (RNAi); *hmp-1*(*fe4*) embryos begin to eject non-epidermal cells at the ventral midline as ventral enclosure begins to fail (arrowhead). **C.** At t = 20 min, further ejection of cells at the ventral midline occurs in *cash-1*(RNAi); *hmp-1*(*fe4*) embryos as they begin to explode. **D.** Model suggesting how ventral midline debris in STRIPAK loss-of-function backgrounds may synergistically interfere with ventral enclosure in *hmp-1*(*fe4*) embryos, in which adherens junctions are already weakened. Scale bar = 10 μm.

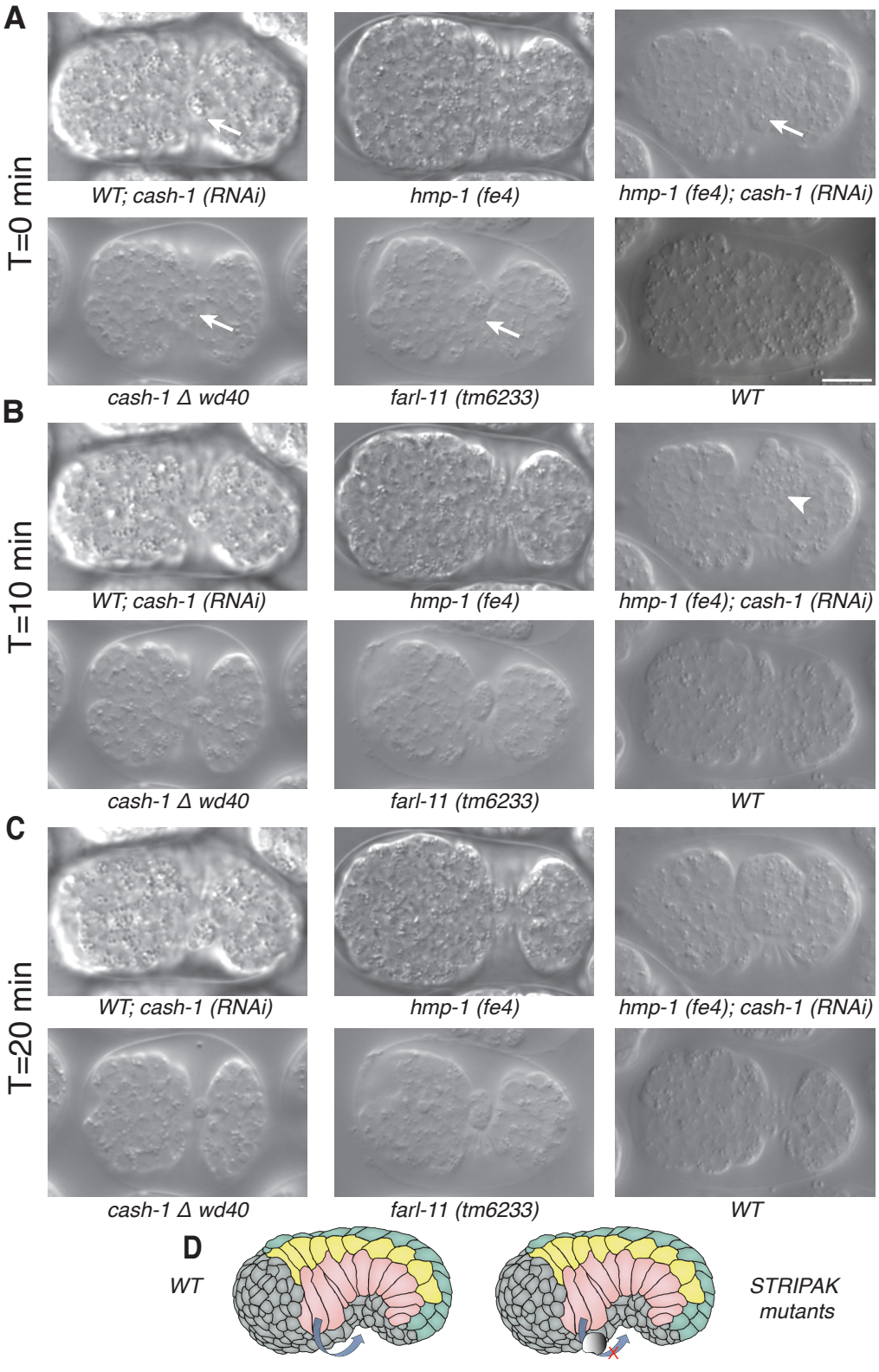
A
T=0 min
WT; cash-1 (RNAi)
hmp-1 (fe4)
hmp-1 (fe4); cash-1 (RNAi)
cash-1 Δ wd40
farl-11 (tm6233)
WT
B
T=10 min
WT; cash-1 (RNAi)
hmp-1 (fe4)
hmp-1 (fe4); cash-1 (RNAi)
cash-1 Δ wd40
farl-11 (tm6233)
WT
C
T=20 min
WT; cash-1 (RNAi)
hmp-1 (fe4)
hmp-1 (fe4); cash-1 (RNAi)
cash-1 Δ wd40
farl-11 (tm6233)
WT
D
WT
STRIPAK mutants

Figure 3: CASH-1 and FARL-11 localize to cell junctions during elongation. A. *cash-1*Δ*N* mutants can exhibit subtle dorsal bulges (arrow), which are superficially similar to those in *hmp-1*(*fe4*) embryos (arrow). **B.** mNG:FARL-11/Strip and TagRFP::CASH-1/Striatin localization during morphogenesis. Both localize to epidermal junctions (arrows). **C.** TagRFP::CASH-1 colocalizes with DLG-1::mNG during elongation. **D.** TagRFP::CASH-1 does not colocalize with HMP-2::eGFP during elongation. **E.** Western blot showing that HMP-2 does not coIP with TagRFP::CASH-1. Proteins in association with CASH-1 were co-immunoprecipitated using anti-RFP magnetic agarose beads. Resulting proteins were resolved via SDS-PAGE and blotted for HMP-2 via rabbit anti-HMP-2. No co-immunoprecipitated HMP-2 was detected in the IP fraction, but an unknown protein band running higher than HMP-2 molecular weight was detected. Scale bar = 10 μm.

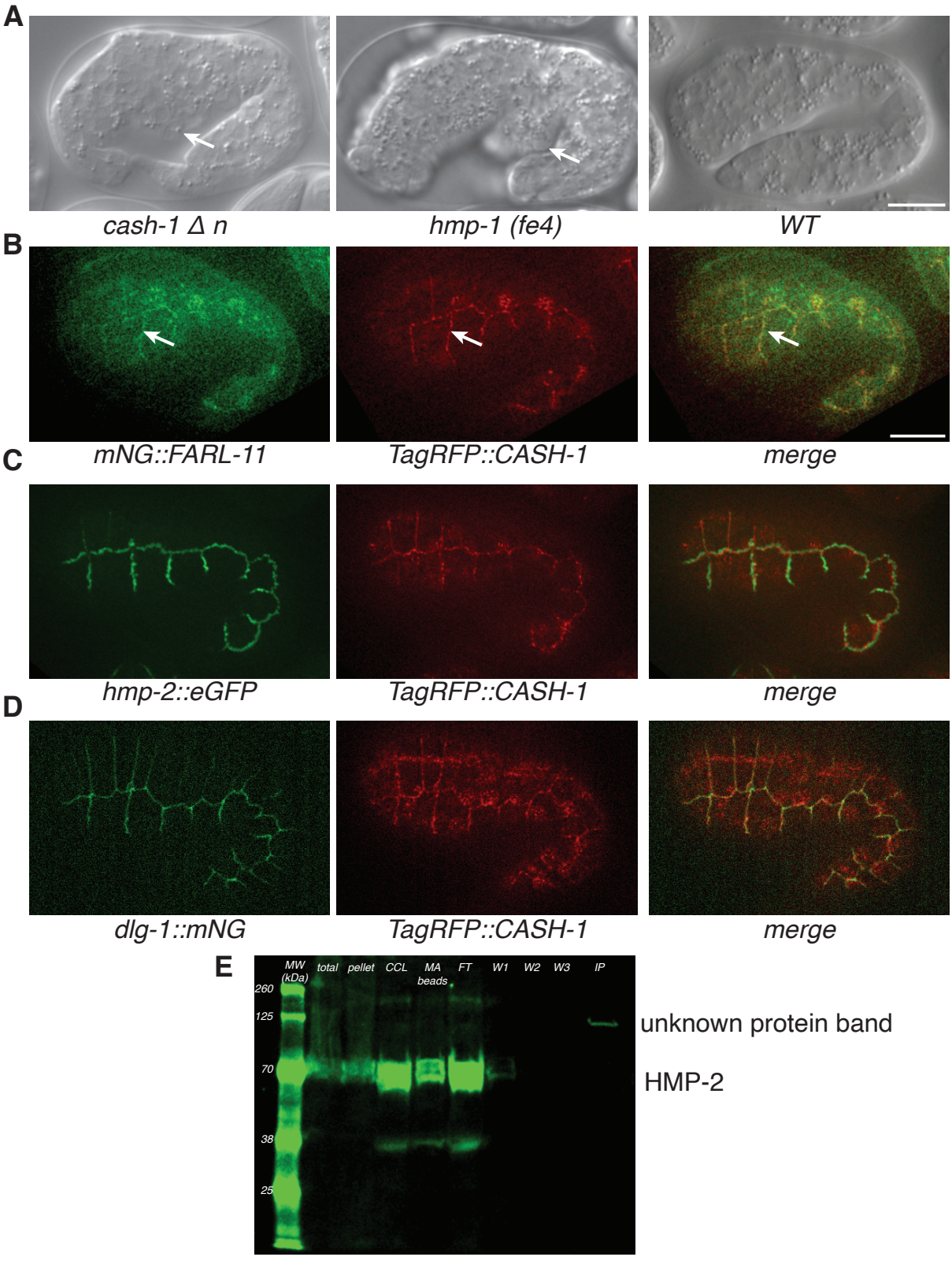
A
cash-1 Δ n
hmp-1 (fe4)
WT
B
mNG::FARL-11
TagRFP::CASH-1
merge
C
hmp-2::eGFP
TagRFP::CASH-1
merge
D
dlg-1::mNG
TagRFP::CASH-1
merge
E
MW (kDa)
total
pellet
CCL
MA beads
FT
W1
W2
W3
IP
260
125
70
38
25
unknown protein band
HMP-2

Figure 4: Recruitment of TagRFP::CASH-1 to junctions is dependent on the DLG-1/AJM-1 complex. A. *dlg-1* knockdown abolishes TagRFP::CASH-1 recruitment to junctions, but does not prevent TagRFP::CASH-1 from localizing to the nuclear region (arrowhead). **B.** *ajm-1* knockdown similarly abolishes TagRFP::CASH-1 recruitment to junctions, but does not prevent TagRFP::CASH-1 from localizing to the nuclear region. **C.** TagRFP::CASH-1ΔWD40 fails to be recruited to junctions. **D.** In contrast to DLG-1/AJM-1 components, *hmp-1* knockdown does not affect TagRFP::CASH-1 localization at junctions (arrow). **E.** *hmp-2* knockdown likewise does not affect TagRFP::CASH-1 localization at junctions (arrow). **F.** *magi-1* knockdown does not affect TagRFP::CASH-1 localization at junctions (arrow). **G-I.** *cash-1* knockdown does not affect DLG-1::mNG (G), HMP-1::eGFP (H), or HMP-2::eGFP localization to junctions. Scale bar = 10 μm.

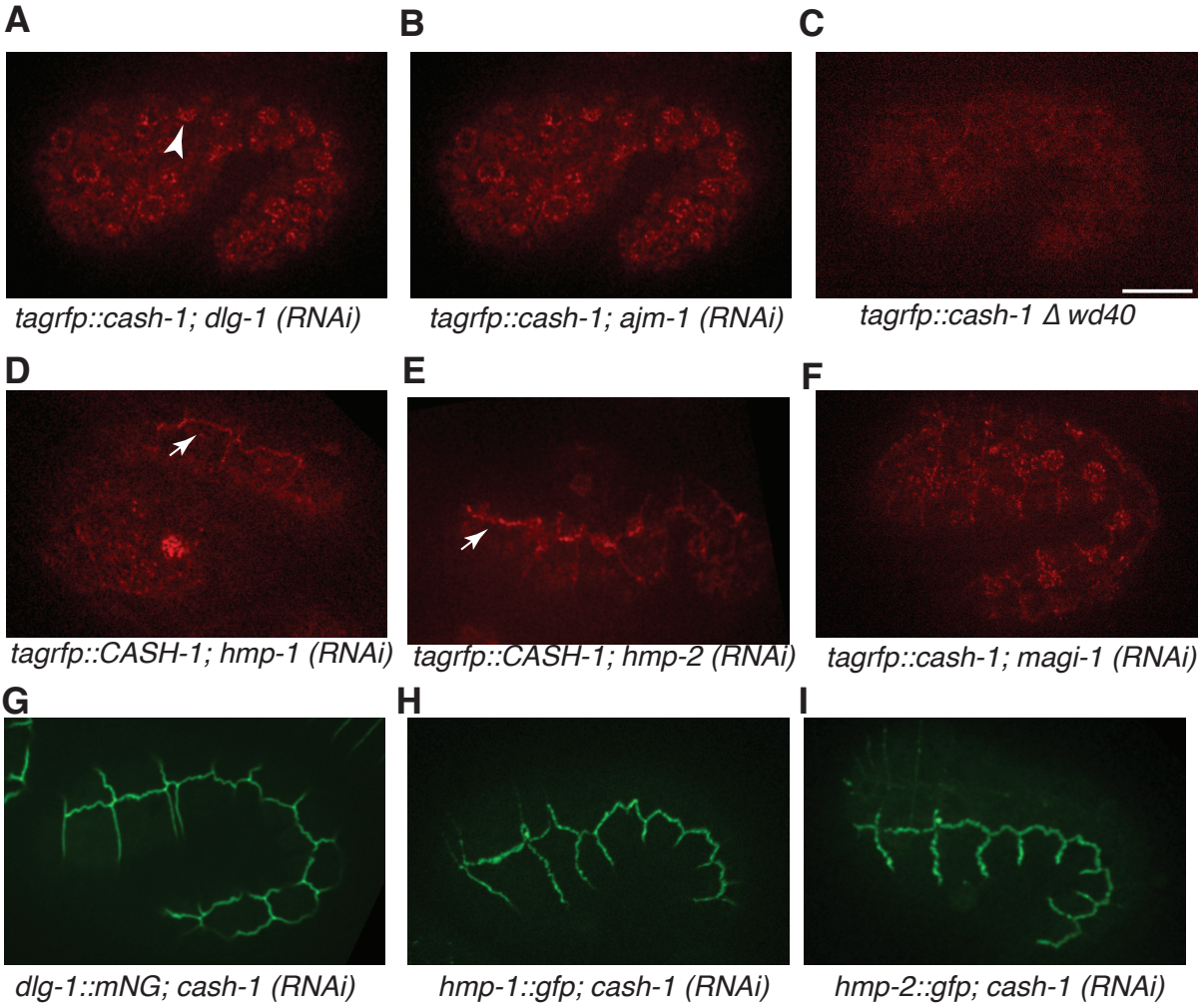
A
B
C
tagrfp::cash-1; dlg-1 (RNAi)
tagrfp::cash-1; ajm-1 (RNAi)
tagrfp::cash-1 Δ wd40
D
E
F
tagrfp::CASH-1; hmp-1 (RNAi)
tagrfp::CASH-1; hmp-2 (RNAi)
tagrfp::cash-1; magi-1 (RNAi)
G
H
I
dlg-1::mNG; cash-1 (RNAi)
hmp-1::gfp; cash-1 (RNAi)
hmp-2::gfp; cash-1 (RNAi)

APPENDIX 1:

Mechano-biochemical regulation of the *C. elegans* HMP-1–HMP-2 protein complex

This work is in review at the *Journal of Biological Chemistry*. The authors are Shimin Le , Miao Yu, Sterling Martin, Jeff Hardin, Jie Yan

My contributions to this work include cloning the protein expression constructs that were essential to this work.

Summary

The HMP-1–HMP-2 protein complex, a counterpart of the α-catenin–β-catenin complex in *C. elegans*, mediates the tension transmission between HMR-1 (cadherin) and the actin cytoskeleton and serves as a critical mechanosensor at the cell–cell adherens junction. The complex has been shown to play critical roles in embryonic development and tissue integrity in *C. elegans*. The complex is subject to tension due to internal actomyosin contractility and external mechanical micro-environmental perturbations. However, how tension regulates the stability and interactions of the HMP-1–HMP-2 complex has yet to be investigated. Here, we directly quantify the mechanical stability of full-length HMP-1 and its force-bearing modulation domains (M1-M3), and show that they unfold within physiological levels of tension (pico-newton scale). The inter-domain interactions within the modulation domain lead to strong mechanical stabilization of M1 in HMP-1, resulting in a significantly stronger force threshold to expose the buried vinculin binding site compared to the M1 domain in α-catenins. Moreover, we also quantify the mechanical stability of the inter-molecular HMP- 1–HMP-2 interface and show that it is mechanically stable enough to support the tension-transmission and tension-sensing of the HMP-1 modulation domains. Further, we show that single-residue phosphomimetic mutation (Y69E) in HMP-2 weakens the mechanical stability of the HMP-1–HMP-2 interface and thus weakens the force-transmission molecular linkage and its associated mechanosensing functions. Together, these results provide a mechano-biochemical understanding of the role of *C. elegans* HMP-1–HMP-2 protein complex in mechanotransduction, and reveal that the mechanical switch mechanism for activating the vinculin signalling protein binding is evolutionarily conserved.

Introduction

Cell–cell adhesions play crucial roles in embryonic development and tissue integrity. These adhesions are formed and regulated by a variety of force-bearing proteins that are assembled into supramolecular physical linkages. The force-bearing proteins within the linkages interact with numerous signalling proteins in a manner sensitive to mechanical cues, forming the physical basis for mechanotransduction [1]. For instance, the classic cadherin-based adherens junction is linked to the actin cytoskeleton through a core supramolecular physical linkage comprising a linear array of cadherin, β-catenin, α-catenin and F-actin. The tension in the linkage has been estimated to be in the order of several piconewtons (pN) by molecular tension sensors [2–4]. Signalling proteins interact with mechanosensing proteins in the linkage in a force-dependent manner (e.g., vinculin–α-catenin interaction), regulating the strength of the adherens junction and converting the mechanical cues into a cascade of downstream biochemical signalling events [5–12]. While the mechano- biochemical regulation of the mammalian adherens junction has been intensively investigated over recent years [4, 6–12], its counterpart in *C. elegans*, an important model system for development and aging, is more poorly understood [2–4]. It remains unclear about whether the mechano-biochemical regulations of adherens junctions are evolutionarily conserved for nematode.

In *C. elegans*, the adherens junction is linked to the actin cytoskeleton through a core HMR-1(cadherin)– HMP-2(β-catenin)–HMP-1(α-catenin)–F-actin supramolecular linkage [13–20]. The extracellular domains of HMR-1 on one cell dimerize with the HMR-1 on the neighboring cells. This supramolecular linkage is subject to tensile forces due to internal actomyosin contraction and external mechanical microenvironmental perturbations, and is believed to play

crucial mechanotransduction functions within cells in tissues [14, 17, 21]. However, how these core proteins respond to physiological level of tension, is still unknown. Furthermore, the mechanical stability of the protein-protein interfaces in the linkage, which determines the integrity of the tension-transmission supramolecular linkage, has yet to be investigated.

In this study, we focused on the mechano-biochemical regulation of the HMP-1 protein, and the protein–protein interface it forms with HMP-2. By single-protein manipulation using magnetic tweezer [22–24], we directly quantified the mechanical stability of full-length HMP-1 and its force-bearing modulation domains (M1-M3), as well as the HMP-1–HMP-2 interface. We show that the HMP-1 force-bearing domains unfold within pico-newton (pN) scale tensions. Interestingly and importantly, the inter-domain interaction between M1 and M2-M3 leads to strong mechanical stabilization of the M1 domain in HMP-1, preventing high affinity binding of vinculin to the cryptic vinculin binding site (VBS) in the M1 domain during short exposure to low tensions (< 15 pN), in sharp contrast to mammalian α-catenins where the VBSs are readily

exposed at tension slightly above 5 pN [6, 12]. Furthermore, our results show that the HMP-1–HMP-2 interface has an average lifetime of tens of seconds to tens of minutes within a physiologically relevant tension range. Finally, a phosphotyrosine-mimetic mutation (Y69E) in HMP-2 was shown to significantly weaken the mechanical stability of the HMP-1–HMP-2 interface. Together, these results reveal an intricate interplay between the mechanical and biochemical regulation of HMR-1–HMP-2–HMP-1 mediated force transmission and tension-dependent interactions, providing deeper insights into the molecular mechanisms underlying mechanotransduction at the adherens junction of *C. elegans*.

Results

Mechanical stability of full-length HMP-1

In order to probe the mechanical stability of full-length HMP-1, we prepared a single-molecule construct where full-length HMP-1 is inserted between four well characterized titin Ig 27th domains (I27, two repeats at each end) acting as a molecular spacer [25–27]. The N- and C-termini of the construct contain a biotinylated AviTag and a SpyTag [26, 28], respectively, for specific tethering (Figure 1a). Furthermore, there is a 572-bp DNA handle added between the single-molecule construct and the super-paramagnetic bead as an additional spacer to avoid non-specific interaction between the bead and surface [26, 27, 29]. A magnetic-tweezer setup was implemented to apply well-controlled force on the tethered molecule via the bead and record the bead height in real time [22–24]. Due to force balance, the tension in the molecule is the same as the applied force. More details of the single-molecule construct can be found in Supplementary Text S1.

Figure 1b shows the typical force–height curves of full-length HMP-1 during linear force-increase scans with a force-loading rate of 1 pN s-1 from ~ 1 pN up to 30 pN. During each force-increase scan, six unfolding events were clearly observed, indicated by six step-wise bead height jumps (black arrows in Figure 1b). Such stepwise bead height change equals the extension change of the tethered molecule due to structural changes [22, 30]. The I27 domain is highly mechanically stable, and unfolds with a slow rate of approximately 10-3 s-1 over the force range at lab room temperatures [25, 31]. Therefore, these six unfolding events correspond to the unfolding of the six structured domains in full-length HMP-1, i.e., two N-terminal domains (N1, and N2), three modulation domains (M1, M2 and M3), and the C-terminal F-actin binding

domain. These unfolded domains could refold at forces <6 pN during force-decrease scans (inset of Figure 1b, with a loading rate of -0.1 pN -1), allowing repeating the force scans for multiple cycles on one tethered molecule.

Performing over 30 force-increase scans, we obtained the force-step size graph of the unfolding events (Figure 1c) and the corresponding unfolding force distributions (Figure 1d). Clearly, mechanical unfolding of the six domains can be roughly categorized into three mechanical groups: three domains unfold at a force range of 3-10 pN, two domains unfold at 10-15 pN, and one domain unfolds at 16-22 pN. In addition, occasionally, two domains unfolded concurrently (within our temporal resolution: 10 ms), indicated by a single unfolding event associated with a step size that corresponds to the sum of the step size of two individual domains. The results from the mechanical unfolding of the full-length HMP-1 suggest that all the functional domains of HMP-1 respond to physiological levels of forces [2–4].

Mechanical stability of modulation domains of HMP-1

As the modulation domains contain key binding sites for signalling proteins such as vinculin[18], we sought to probe the mechanical stability of the tension-bearing modulation domain of HMP-1. Similar to the full-length HMP-1 construct, we prepared a single-molecule construct "HMP-1-M123" that contains the three modulation domains (Figure 2a). Figure 2b shows the typical force–height curves of the HMP-1-M123 during force-increase scans with a force loading rate of 1 pN s-1, where three unfolding events of the three modulation domains were observed. Repeating such force-increase scans over 100 times, we obtained the 2D graph of force-dependent step sizes (Figure 2c) and the unfolding force distributions of the three modulation

domains (Figure 2d). Two of the domains unfolded almost concurrently at about 10-15 pN, while the other unfolded at a higher force of 15-20 pN. Comparing to the unfolding signals obtained from full-length HMP-1 (Figure 1), the unfolding of modulation domains fall into the second and third mechanical groups of the full-length HMP-1. Hence, the two N-terminal domains (N1, and N2) and C-terminal domain of HMP-1 should belong to the first mechanical group that unfold within 3-10 pN (with a loading rate of 1 pN s-1). Together with results in next sections, this allows the assignment of the first two unfolding events to M1 and another domain from M2 or M3, and the third unfolding event to M2 or M3. The three unfolded modulation domains could refold in a stepwise manner during force-decrease scans at forces of ~ 4 pN, 3 pN and below 2 pN, respectively, at a force loading rate of -0.1 pN s-1 (Figure 2e).

Unexpectedly, the M1 domain of HMP-1 exhibits a much higher mechanical stability than its mammalian counterparts, where rapid unfolding of the M1 domain occurs at forces slightly above ~ 5 pN at similar forceloading rates [6, 12]. This significantly higher mechanical stability of the HMP-1-M1 domain indicates either a stronger intrinsic mechanical stability of the M1 domain, or mechanical stabilization due to an interaction with its neighbouring domains. Our data suggest that it is due to an interaction with its neighbouring domains, as isolated M1 domain unfolded at forces below 5 pN under the same force loading rate (Figure S1).

Tension-induced unfolding of the HMP-1 modulation domains activates high-affinity vinculin binding

Similar to mammalian α-catenin, there is a single conserved vinculin binding site (VBS) buried inside the HMP-1-M1 domain, which has been shown to bind to DEB-1 (vinculin counterpart in

C. elegans), as well as mammalian vinculin[18]. Previous ITC (Isothermal titration calorimetry) experiments reported that the D1 domain of vinculin and DEB-1 bind to HMP-1-M123 domain with a low affinity – the vinculin-D1 binding was associated with a high dissociation constant of Kd ~ 600 nM, whereas the DEB-1-D1 binding was not detectable [18]. On the other hand, both D1 domains bind to the HMP-1-M1 domain alone with a much higher affinity, indicated by Kd of ~ 3 nM for vinculin-D1 and ~ 150 nM for DEB-1-D1 [18]. These results suggest that the inter-domain interaction of M1–M23 greatly suppresses the binding of the D1 domain of vinculin or DEB-1 to the VBS in the HMP-1-M1 domain. Since HMP-1 modulation domain lies in a tension transmission supramolecular linkage, it is reasonable to postulate that tension-induced disruption of the M1–M23 interaction could release the auto-inhibitory inter-domain interaction, which in turn activates high-affinity binding of vinculin/DEB-1 to HMP-1-M1.

To test this hypothesis, we first stretched the single-molecule construct of HMP-1-M123 with multiple linear force-increase scans (1 pN s-1) followed by force-decrease scans (-0.1 pN s-1), and observed the characteristic cooperative unfolding of two modulation domains, one of which is M1 at 10-15 pN, and the unfolding of the other modulation domain (M2 or M3) at 15-20 pN (Figure 3a, dark gray curves), as well as the characteristic refolding of the domains at lower forces < 5 pN (Figure 3e). We then introduced 10 nM vinculin-D1 (the vinculin-D1 domain, the binding domain for the VBS in M1) at low forces of ~ 1 pN (to ensure that the domains were folded during solution exchange), and repeated the force-increase and force-decrease scans (Figure 3a, magenta and orange curves). During several initial force-increase scans, the characteristic unfolding signals of the three M domains were still observed (magenta curves),

followed by loss of the unfolding signature of one of the domains at 10-15 pN (orange curve in Figure 3b and red curve Figure 3c).

The observation of vinculin-D1 binding at 10 nM under force is in sharp contrast to the Kd ≈ 600 nM measured between vinculin-D1 and HMP-1-M12 in the absence of force, consistent with the hypothesis that the force-induced unfolding of HMP-1 modulation domains exposes the buried VBS for high-affinity vinculin- D1 binding. The high-affinity vinculin-D1 binding then suppresses the refolding of the M1 domain during the force-decrease scans. At a higher concentration (200 nM) of vinculin-D1, the binding of vinculin-D1 was observed after the unfolding of the M domains in the first force-increase scan, indicating faster binding at the higher concentration (Figure 3c). Figure 3d-e show the resulting force-dependent step sizes and transition forces of the remaining M2 and M3 domain unfolding events in the presence of 200 nM vinculin-D1 in solution. The unfolding force histogram shows two major mechanical groups spread over 10-15 pN and 15-50 pN force ranges, respectively. Compared to the unfolding force distribution in the absence of vinculin-D1 (Figure2 c&d), the HMP-1-M1 refolding is suppressed by vinculin-D1 binding, while the refolding and unfolding signatures of HMP-1-M2 and HMP-1-M3 were largely unaffected. There is a minor mechanical group with unfolding forces less than 10 pN, which might be due to an altered refolding of the modulation domains due to vinculin-D1 binding.

In addition, in mammals the vinculin-D1 binding to VBS is known to induce an α-helical structure of the VBS peptide associated with a different force-dependent extension from the randomly coiled conformation [6, 12, 26], which implies that the applied force can tune the

binding/unbinding dynamics of the vinculin-D1 to VBS. Indeed, when the force on the HMP-1 was increased to a range of 27−30 pN in the presence of 200 nM vinculin-D1, dynamic transitions between two distinct extension levels were observed, associated with an extension difference of ~ 4 nm (Figure 3f-g), which is the expected extension difference between the α-helical and randomly coiled conformations of the VBS peptide over this force range [6, 12, 26]. This result suggests that the bound complex of HMP-1-VBS–vinculin-D1 can be rapidly destabilized at forces greater than this force range.

HMP-1–HMP-2 interface provides sufficient mechanical stability for supporting tension transmission

We have shown that the tension-induced rapid unfolding of modulation domains involves tensions in the range of 10-15 pN. Tension-dependent activation of trans-binding of signalling proteins requires that the tension-transmission HMR-1–HMP-2–HMP-1–F-actin supramolecular linkage can withstand this tension range over a sufficient lifetime to support tension-dependent interactions. As the integrity of the tension-transmission pathway is dependent on the mechanical stability of protein–protein interfaces in the linkage, it is important to measure the mechanical stability of protein–protein interfaces in the tension transmission linkage. The HMP-1–HMP-2 interface is a critical protein–protein interface in the linkage, which comprises the N-terminal tail peptide of HMP-2 (Nt) and the N-terminal domain of HMP-1 (N12) (Figure 4a) [19]. We sought to quantify the mechanical stability of this interface.

We utilized a single-molecule construct that converts a protein–protein interaction into an intra-molecular interaction (Figure 4a) [10, 11, 26, 32–34]. Briefly, the construct of the HMP-1–HMP-

2 interface consists of the N12 domain of HMP-1, the Nt peptide of HMP-2, and a long flexible unstructured peptide linker in between. The construct is flanked by two repeats of I27 domains at each side. An AviTag and a SpyTag are fused at each end of the construct for specific tethering (Figure 4a, and Text S1). At sufficiently low forces, N12 and Nt can interact with each other to recreate the HMP-1–HMP-2 interface, looping the long linker as they do so. In contrast, a sufficiently high force can destabilize the interface, and the resulting rupturing of the interface leads to the release of the long linker. Such rupturing event leads to an abrupt extension increase of the construct, which is indicated by a stepwise large bead height increase of the same amount as the extension increase [30].

Figure 4b shows the typical force–height curves of the HMP-1–HMP-2 interface construct during force increase scans with a loading rate of 1 pN s-1. Clearly, during each scan, a single bead height jump of 110.9 Å ± 8.4 nm (N=178) was observed at 16.6 Å ± 1.7 pN (N=178). The size of the bead height increases at these forces are consistent with the extension of the linker and unfolding of the domain N12 domain, suggesting concurrent rupturing of the interface and the unfolding of the N12 domain. Similar force-increase scans were repeated for over 50 times at three force-loading rates: 0.2 pN s-1, 1 pN s-1, 5 pN s-1, and the resulting force-dependent step sizes of the rupturing events are shown in Figure 4c. The normalized histograms of rupturing forces at the three loading rates show that the interface ruptures at 15.9Å ± 1.9 pN (N=56), 16.58Å ± 7 pN (N=178), and 19.1Å ± 3.1 pN (N=106), respectively. These forces are greater than the unfolding forces of the first and second modulation domains at the corresponding loading rates, suggesting that the HMP-1– HMP-2 interface provides mechanical stability that is

sufficient to support the mechanotransduction of the modulation domains, which require mechanical destabilization of the M1 domain for high-affinity vinculin binding.

To directly quantify the tension-dependent lifetime of the HMP-1–HMP-2 interface, we implemented a force-clamp assay. Briefly, the construct was first held at a force of ~ 0.5 pN for 30 sec to allow the formation of the interface, and then held at a targeting force of 12-16 pN and the dwell time was recorded until the interface ruptured. Repeating the procedure for multiple cycles (N> 50), the average lifetime of the interface at this force was obtained by exponential fitting to the histogram of the dwell times (Methods). The forcedependent lifetimes of the interface were obtained by performing such measurement at different targeting forces (Figure 4e-f). The force-dependent lifetime of the interface consistently shows that the interface is more mechanically stable than the M1. For an example, at the force of ~ 14 pN the HMP-1–HMP-2 interface can last over tens of seconds, while at the same force the M1 domain unfolds almost immediately.

In addition, the construct also allowed us to quantify the mechanical responses of the N12 domains of HMP-1. Consistent with the data from full-length HMP-1 unfolding experiments, the N1 and N2 domain unfolded at forces of 3-9 pN during force-increase scans at 1 pN s-1 loading rate (Figure 4g). The equilibrium unfolding/refolding dynamics of the N1 and N2 domains can be observed at constant forces around 4 pN (Figure 4h).

Single-residue phosphorylation-mimetic mutations on HMP-2 weaken the mechanical stability of the HMP-1–HMP-2 interface

The HMP-2 N-terminus peptide contains two phosphorylation residues, i.e., the 69th tyrosine (Y69) and 47th serine (S47) residues, which lies within the HMP-1–HMP-2 interface. It was previously observed that a Y69E or S47E mutation in the HMP-2 led to cell–cell adhesion disruptions [19]. This led to the hypothesis that the phosphorylation of these residues could weaken the stability of the HMP-1–HMP-2 interface, which has yet to be tested [19]. In this section, we quantify the effects of these mutations on the mechanical stability of the HMP-1–HMP-2 interface. For this purpose, we prepared two single-molecule constructs of the HMP-1–HMP-2 interface that carry 1) the Y69E mutation, or 2) the S47E mutation (Figure 5a).

Figure 5b shows typical force–height curves of the HMP-1–HMP-2Y69E interface construct during force increase scans with a force loading rate of 1 pN s-1. Repeating similar force-increase scans for three force loading rates (0.2 pN s-1, 1 pN s-1, 5 pN s-1), we obtained the resulting force-dependent step sizes of interface rupturing (corresponding to the first stepwise bead height increase) and domain unfolding transitions (Figure 5c), and the corresponding interface rupturing force distributions at three force-loading rates (Figure 5d). Interestingly, a two-peak distribution of the interface rupturing force was observed. For instance, at 1 pN s-1, one peak was observed at 14.1Å ± 1.4 pN (N=188), and the other peak was observed at 5.7Å ± 1.5 pN (N=86), which is in sharp contrast to the single-peaked rupturing force distribution (peak force at 16.58Å ± 1.7 pN for 1 pN s-1, Figure 4) observed from the wild-type interface. Similar experiments performed on the HMP-1–HMP- 2S47E interface show a single-peak distribution (peak force at 14.3Å ± 2.2 pN, N=32), which is slightly lower than the peak force of the wild-

type interface (Figure 5e-g). These results demonstrate that the phosphorylation of one or two of the residues leads to impaired mechanical stability of the HMP-1–HMP-2 interfaces. Between the two, the results suggest that the Y69E mutations could cause a more severe weakening effect on the mechanical stability of the interface. Consistently, the lifetimes of the HMP-1–HMP-2Y69E interface were within 200 seconds at forces of 1-2 pN, while the HMP-1–HMP-2S47E interface remained stable over thousands of seconds at a slightly higher force of ~ 3 pN.

Discussion

In this work, we sought to provide insights into the molecular mechanisms underlying the mechanobiochemicial regulation of the HMP-1–HMP-2 mediated cell–cell adhesions of *C. elegans*. We have systematically investigated 1) the mechanical stability of full-length HMP-1 protein, particularly the functional modulation domains within physiological force range; 2) the force-dependent binding of vinculin to HMP-1;3) the mechanical stability of the HMP-1–HMP-2 interface, including its dependence on the phosphorylation of specific HMP-2 residues within the interface.

Our results revealed that the five domains within HMP-1 can be unfolded when subjected to physiological levels of force less than 20 pN. An interesting finding is that, despite the high-degree of structural and domain organization similarities between HMP-1 and its mammalian counterpart α-catenins, we observed significant differences in the mechanical stability of the modulation domains. Importantly, the unfolding force of the critical VBS-bearing M1 domain is shifted from ~ 5 pN for mammalian α-catenins to ~ 14 pN for HMP-1, revealing a significantly greater autoinhibition of M1 unfolding, and hence its binding to vinculin, by its inter-domain interaction between M1 and M2-M3.

We show that the force-induced release of the inter-domain interactions within the modulation domain, which leads to unfolding of the M1, is required for activation of high-affinity vinculin binding. Force-induced exposure of VBSs for high-affinity vinculin binding has been observed for other VBS-containing force-bearing mechanosensing proteins, such as talin, α-actinin [6, 26]. Therefore, force-activated binding of vinculin seems a conserved strategy utilized by cells in different organisms.

Importantly, we show that the HMP-1–HMP-2 interface has a significantly greater mechanical stability than that of M1 and M2 domains, suggesting that this interface is mechanically stable enough to support the force-dependent interaction between the modulation domains and signaling factors such as vinculin. We also demonstrated that the mechanical stability of the HMP-1–HMP-2 interface is weakened by single phosphomimetic (Y69E, S47E) mutations of HMP-2, implying destabilization of the tension-transmission supramolecular linkage and thus suppression of the activation of the modulation domains for their respective interactors. These results suggest the existence of an intricate interplay between mechanical and biochemical regulations of HMP-1–HMP-2 mediated mechanosensing at cell-cell adhesions in *C. elegans*, which is consistent with the previous observation that phosphomimetic mutation on HMP-2 leads to adherens junction disruption *in vivo* [19]. The stronger HMP-1–HMP-2 interface and the greater forces required to release the autoinhibited M1 domain raise an interesting question of whether *C. elegans* experience higher inter-cellular tension than that of mammalian cells, which requires a more stable force-transmission pathway and higher force-activation threshold for vinculin binding.

Another interesting question is raised regarding the molecular mechanisms that confer the HMP-1–HMP-2 interface the high mechanical stability. The structure of the HMP-1–HMP-2 interface reveals that the interface is formed by interactions between a single α-helix from the N-terminus of HMP-2 and the N-terminal 4-α-helical bundle (N1 domain) of HMP-1, leading to a 5-α-helical bundle in the complex. Actomyosin contraction generates tensile forces in the tension-transmission linkage, as a result the HMP-1–HMP-2 interface is under a shear-force pulling geometry (i.e., the force direction is nearly parallel to the interacting interface). Such protein-protein interface arrangement and force pulling geometry have also been found in several other critical force-bearing interfaces, such as the vinculin–talin, vinculin–α-catenin, β-catenin–α-catenin, which lie in different tension-transmission supramolecular linkages playing critical mechanotransduction roles at focal adhesion and cell-cell adhesions [1]. Together, these results suggest that protein-protein interfaces formed between a peptide and a rigid structural domain under a shear-force pulling geometry could also be a evolutionarily conserved key mechanism to provide high mechanical stability to these tension-bearing interfaces [1].

Materials and Methods

Plasmids constructs and protein expression.

Six plasmids were prepared for expression of the protein constructs for single-molecule stretching experiments: 1). pET151-Avi-(I27)2-(full length HMP-1)-(I27)2-Spy, 2) pET151-Avi-(I27)2-(HMP-1-M123)-(I27)2-Spy, 3) pET151-Avi-(I27)2-(HMP-1-M1)-(I27)2-Spy, 4) pET151-Avi-(I27)2-(HMP-1-N12)-(long flexible linker)-(HMP-2-Nt)-(I27)2-Spy, 5) pET151-Avi-(I27)2-(HMP-1-N12)- (long flexible linker)-(HMP-2-NtY69E)-(I27)2-Spy, 6) pET151-Avi-(I27)2-(HMP-1-N12)-(long flexible linker)- (HMP-2-NtS47E)-(I27)2-Spy. Briefly, the DNA fragments

encoding HMP-1 domains were amplified by PCR the template sequence [18, 19]. The long flexible linker and other DNA fragments were synthesized by geneArt/IDTgblock. The DNA fragments were then assembled into a pET151-avi-(I27)2-(inset)-(I27)2-spy plasmid template [26] by HiFi DNA Assembly (NEB) and sequencing-confirmed (1st BASE). Each plasmid was co-transformed with a BirA plasmid and expressed in Escherichia coli BL21 (DE3) cultured in LB-media with D-Biotin (Sigma Aldrich), and affinity purified through 6His-tag. Detailed sequence information of the plasmids can be found in Text S1.

Single-protein manipulation and analysis.

A vertical magnetic tweezers setup was combined with a disturbance-free, rapid solution-exchange flow channel for conducting in vitro protein stretching experiments [22–24]. All in vitro protein stretching experiments were performed in solution containing: 1X PBS, 1% BSA, 2 mM DTT, 10 mM sodium L-ascorbate at 22 Å ± 1oC. The force calibration of the magnetic tweezers setup has a 10% uncertainty due to the heterogeneity of the diameter of paramagnetic beads [22] and the bead height determination of the magnetic tweezers setup has a ~ 2-5 nm uncertainty due to the thermal fluctuation of the tethered bead and the resolution of the camera [10].

Supplementary Text S1: Plasmids construct and protein expression.

Six plasmids were prepared for expression of the protein constructs for single-molecule stretching experiments: 1). pET151-Avi-(I27)2-(full length HMP1)-(I27)2-Spy, 2) pET151- Avi-(I27)2-(HMP1-M123)-(I27)2-Spy, 3) pET151-Avi-(I27)2-(HMP1-M1)-(I27)2-Spy, 4). pET151-Avi-(I27)2-(HMP1-N12)-(long flexible linker)-(HMP2-Nt)-(I27)2-Spy, 5). pET151-Avi-(I27)2-(HMP1-N12)-(long flexible linker)-(HMP2-NtY69E)-(I27)2-Spy, 6). pET151-Avi-(I27)2-(HMP1- N12)-(long flexible linker)-(HMP2-NtS47E)-(I27)2-Spy. Briefly, the DNA fragments

encoding HMP1 domains were amplified by PCR the template sequence [1, 2]. The long flexible linker and other DNA fragments were synthesized by geneArt/IDTgblock. The DNA fragments were then assembled into a pET151-avi-(I27)2-(inset)-(I27)2-spy plasmid template [3] by HiFi DNA Assembly (NEB) and sequencing-confirmed (1st BASE). Each plasmid was co-transformed with a BirA plasmid and expressed in Escherichia coli BL21 (DE3) cultured in LB-media with D-Biotin (Sigma Aldrich), and affinity purified through 6His-tag (at N-terminus). Detailed sequence information of the plasmids are listed below:

1). Avi-$(I27)_2$-(full length HMP1)-$(I27)_2$-Spy:

HHHHHHGKPIPNPLLGLDSTENLYFQGIDPFTGLNDIFEAQKIEWHEGGGSGLIEV
EKPLYGVEVFVGETAHFEIELSEPDVHGQWKLKGQPLAASPDAEIIEDGKKHILILH
NAQLGMTGEVSFQAANTKSAANLKVKELGGGSGLIEVEKPLYGVEVFVGETAHFE
IELSEPDVHGQWKLKGQPLAASPDAEIIEDGKKHILILHNAQLGMTGEVSFQAANTK
SAANLKVKELGGGSGKLMPANGNSHAYFNIDEVRSKNVLKQITQLINEVTNITETFP
LKPGQTTEGLVATLDAAVANFLQTGSFAISKCPIANSDPRAIDLLHEALGAVQDTGQ
VMIQTGRDFVRDSTSTNKRAIATNSGRNLLTAVAKFLILADSIDVKVIVDKVDEVRE
TAHQMIEADTKIKVDDLYNLLISQIEELDITVRRRAIDLVKPNQRDDLLAARSALRQT
APLLYTSTRTFVRHPEHEEARRNRDYTADEMHSALNALESVLNGQQPKVTFSEYG
RIGDLINEIDTFQNRIEIDPAHYRRGTDRPDLEGHCERIVSGSASIADAESTRENRKQ
KIVAECNNLRQALQELLTEYEKSTGRRDDNDDIPLGIAEVHKRTKDLRRHLRRAIVD
HISDAFLDTRTPLILLIEAAKEGHEENTRYRSKMFQEHANEIVSVARLSCQLSSDVES
VSVIQHTAAQLEKLAPQVAQAAILLCHQPTSKTAQENMETYKNAWFDKVRLLTTA
LDNITTLDDFLAVSEAHIVEDCERGIKGITANASTPDENAANCETVDCAAGSIRGRA
LRVCDVVDAEMDFLQNSEYTETVKQAVRILKTQRVDQFAERASALANRQEAHGLT

WDPKTKEEEMNEFINACTLVHDAVKDIRHALLMNRSMNDVDSDVEYEADGVGAA
NADANRTISEQENQQNLMRRLPEEEKKKIQAQIDIFKVTQTRFEREVAKWDETGND
IISLANNMCKIMMSMTEFTRGCGPLKTTMDVIRAAQEISLNGSKLNALARQIGEESA
DSQTKKDLLAYLSQITLYCQQLNICSKVKADVTQVGNELVVSALDSAMSLIQTARNL
LTAVVQTVKAAYIASTKFRRPNANSVRVEWRMAPPKKQPLIRPQKNNAIIRRASER
RPLQPAKVLAEFTRNEIETGRDSDDEELDRRHQQRINGRLLEGGGSGLIEVEKPLYG
VEVFVGETAHFEIELSEPDVHGQWKLKGQPLAASPDAEIIEDGKKHILILHNAQLGM
TGEVSFQAANTKSAANLKVKELGGGSGLIEVEKPLYGVEVFVGETAHFEIELSEPDV
HGQWKLKGQPLAASPDAEIIEDGKKHILILHNAQLGMTGEVSFQAANTKSAANLKV
KELGGGSGAHIVMVDAYKPTK*

2). Avi-$(I27)_2$-(HMP1-M123)-$(I27)_2$-Spy:

HHHHHHGKPIPNPLLGLDSTENLYFQGIDPFTGLNDIFEAQKIEWHEGGGSGLIEV
EKPLYGVEVFVGETAHFEIELSEPDVHGQWKLKGQPLAASPDAEIIEDGKKHILILH
NAQLGMTGEVSFQAANTKSAANLKVKELGGGSGLIEVEKPLYGVEVFVGETAHFE
IELSEPDVHGQWKLKGQPLAASPDAEIIEDGKKHILILHNAQLGMTGEVSFQAANTK
SAANLKVKELGGGSGKLGQQPKVTFSEYGRIGDLINEIDTFQNRIEIDPAHYRRGTD
RPDLEGHCERIVSGSASIADAESTRENRKQKIVAECNNLRQALQELLTEYEKSTGRR
DDNDDIPLGIAEVHKRTKDLRRHLRRAIVDHISDAFLDTRTPLILLIEAAKEGHEENT
RYRSKMFQEHANEIVSVARLSCQLSSDVESVSVIQHTAAQLEKLAPQVAQAAILLCH
QPTSKTAQENMETYKNAWFDKVRLLTTALDNITTLDDFLAVSEAHIVEDCERGIKG
ITANASTPDENAANCETVDCAAGSIRGRALRVCDVVDAEMDFLQNSEYTETVKQA
VRILKTQRVDQFAERASALANRQEAHGLTWDPKTKEEEMNEFINACTLVHDAVKD
IRHALLMNRSMNDVDSDVEYEADGVGAANADANRTISEQLEGGGSGLIEVEKPLYG

VEVFVGETAHFEIELSEPDVHGQWKLKGQPLAASPDAEIIEDGKKHILILHNAQLGM

TGEVSFQAANTKSAANLKVKELGGGSGLIEVEKPLYGVEVFVGETAHFEIELSEPDV

HGQWKLKGQPLAASPDAEIIEDGKKHILILHNAQLGMTGEVSFQAANTKSAANLKV

KELGGGSGAHIVMVDAYKPTK*

3). Avi-$(I27)_2$-(HMP1-M1)-$(I27)_2$-Spy:

HHHHHHGKPIPNPLLGLDSTENLYFQGIDPFTGLNDIFEAQKIEWHEGGGSGLIEV

EKPLYGVEVFVGETAHFEIELSEPDVHGQWKLKGQPLAASPDAEIIEDGKKHILILH

NAQLGMTGEVSFQAANTKSAANLKVKELGGGSGLIEVEKPLYGVEVFVGETAHFE

IELSEPDVHGQWKLKGQPLAASPDAEIIEDGKKHILILHNAQLGMTGEVSFQAANT

KSAANLKVKELGGGSGKLGQQPKVTFSEYGRIGDLINEIDTFQNRIEIDPAHYRRGT

DRPDLEGHCERIVSGSASIADAESTRENRKQKIVAECNNLRQALQELLTEYEKSTGR

RDDNDDIPLGIAEVHKRTKDLRRHLRRAILEGGGSGLIEVEKPLYGVEVFVGETAH

FEIELSEPDVHGQWKLKGQPLAASPDAEIIEDGKKHILILHNAQLGMTGEVSFQAAN

TKSAANLKVKELGGGSGLIEVEKPLYGVEVFVGETAHFEIELSEPDVHGQWKLKG

QPLAASPDAEIIEDGKKHILILHNAQLGMTGEVSFQAANTKSAANLKVKELGGGSG

AHIVMVDAYKPTK*

4). Avi-$(I27)_2$-(HMP1-N12)-(Long Linker)-(HMP2-Nt)-$(I27)_2$-Spy:

HHHHHHGKPIPNPLLGLDSTENLYFQGIDPFTGLNDIFEAQKIEWHEGGGSGLIEV

EKPLYGVEVFVGETAHFEIELSEPDVHGQWKLKGQPLAASPDAEIIEDGKKHILILH

NAQLGMTGEVSFQAANTKSAANLKVKELGGGSGLIEVEKPLYGVEVFVGETAHFE

IELSEPDVHGQWKLKGQPLAASPDAEIIEDGKKHILILHNAQLGMTGEVSFQAANTK

SAANLKVKELGGGSGKLMPANGNSHAYFNIDEVRSKNVLKQITQLINEVTNITETFP

LKPGQTTEGLVATLDAAVANFLQTGSFAISKCPIANSDPRAIDLLHEALGAVQDTGQ

VMIQTGRDFVRDSTSTNKRAIATNSGRNLLTAVAKFLILADSIDVKVIVDKVDEVRE

TAHQMIEADTKIKVDDLYNLLISQIEELDITVRRRAIDLVKPNQRDDLLAARSALRQT

APLLYTSTRTFVRHPEHEEARRNRDYTADEMHSALNALESVLNGGGSGLKGGGSG

VPGGEKKVRKLLPERKPEPKEEVVLKSVLRKRPEEEEPKVEPKKPKPEAEVKTIKP

PPVEPEPTPIAAPVTVPVVGKKAEAKAPKEEAAKPKGPIKGVPKKTPSPIEAERRK

LRPGSGGEKPPDEASSSPPGSGGGSGGGGSGKLGDIEFIKVNKGGGGSGGGGSGTS

AAEATNSTTSIVEMMQMPTQQLKQSVMDLLTYEGSNDMSGLSGGGSGGGGSLEGG

GSGLIEVEKPLYGVEVFVGETAHFEIELSEPDVHGQWKLKGQPLAASPDAEIIEDGK

KHILILHNAQLGMTGEVSFQAANTKSAANLKVKELGGGSGLIEVEKPLYGVEVFVG

ETAHFEIELSEPDVHGQWKLKGQPLAASPDAEIIEDGKKHILILHNAQLGMTGEVSF

QAANTKSAANLKVKELGGGSGAHIVMVDAYKPTK*

5). Avi-$(I27)_2$-(HMP1-N12)-(Long Linker)-(HMP2-Nt^{Y69E})-$(I27)_2$-Spy: Replace the TSA AEATNSTTSIVEMMQMPTQQLKQSVMDLLTYEGSNDMSGLS in 3). to be TSAAEA TNSTTSIVEMMQMPTQQLKQSVMDLLTEEGSNDMSGLS.

6). Avi-$(I27)_2$-(HMP1-N12)-(Long Linker)-(HMP2-Nt^{S47E})-$(I27)_2$-Spy: Replace the TSA AEATNSTTSIVEMMQMPTQQLKQSVMDLLTYEGSNDMSGLS in 3). to be TSAAEA TNSTTEIVEMMQMPTQQLKQSVMDLLTYEGSNDMSGLS.

References

1. Le, S., Yu, M., Yan, J.. Mechanical regulation of tension-transmission supramolecular linkages. Current Opinion in Solid State and Materials Science 2021;25(1):100895.

2. Borghi, N., Sorokina, M., Shcherbakova, O.G., Weis, W.I., Pruitt, B.L., Nelson, W.J., Dunn, A.R.. E-cadherin is under constitutive actomyosin-generated tension that is increased at cell-cell contacts upon externally applied stretch. Proc Natl Acad Sci U S A 2012;109(31):12568–73.

3. Charras, G., Yap, A.S.. Tensile forces and mechanotransduction at cell–cell junctions. Current Biology 2018;28(8):R445–R457.

4. Hirano, Y., Amano, Y., Yonemura, S., Hakoshima, T.. The force-sensing device region of α-catenin is an intrinsically disordered segment in the absence of intramolecular stabilization of the autoinhibitory form. Genes Cells 2018;23(5):370–385.

5. Pokutta, S., Weis, W.I.. Structure of the dimerization and beta-catenin-binding region of alpha-catenin. Mol Cell 2000;5(3):533–43.

6. Yao, M., Qiu, W., Liu, R., Efremov, A.K., Cong, P., Seddiki, R., Payre, M., Lim, C.T., Ladoux, B., M.ge, R.M., Yan, J.. Force-dependent conformational switch of α-catenin controls vinculin binding. Nat Commun 2014;5:4525.

7. Buckley, C.D., Tan, J., Anderson, K.L., Hanein, D., Volkmann, N., Weis, W.I., Nelson, W.J., Dunn, A.R.. Cell adhesion. the minimal cadherin-catenin complex binds to actin filaments under force. Science 2014;346(6209):1254211.

8. Huang, D.L., Bax, N.A., Buckley, C.D., Weis, W.I., Dunn, A.R.. Vinculin forms a directionally asymmetric catch bond with f-actin. Science 2017;357(6352):703–706.

9. Ladoux, B., M.ge, R.M.. Mechanobiology of collective cell behaviours. Nat Rev Mol Cell Biol 2017;18(12):743–757.

10. Le, S., Yu, M., Yan, J.. Phosphorylation reduces the mechanical stability of the α-catenin/ β-catenin complex. Angew Chem Int Ed Engl 2019;58(51):18663–18669.

11. Le, S., Yu, M., Yan, J.. Direct single-molecule quantification reveals unexpectedly high mechanical stability of vinculin-talin–alpha-catenin linkages. Science Advances 2019;5(eaav2720).

12. Pang, S.M., Le, S., Kwiatkowski, A.V., Yan, J.. Mechanical stability of αT-catenin and its activation by force for vinculin binding. Mol Biol Cell 2019;30(16):1930–1937.

13. Simske, J.S., K.ppen, M., Sims, P., Hodgkin, J., Yonkof, A., Hardin, J.. The cell junction protein vab-9 regulates adhesion and epidermal morphology in *C. elegans*. Nat Cell Biol 2003;5(7):619–25.

14. Cox, E.A., Hardin, J.. Sticky worms: adhesion complexes in *C. elegans*. J Cell Sci 2004;117(Pt 10):1885–97.

15. Neukomm, L.J., Frei, A.P., Cabello, J., Kinchen, J.M., Zaidel-Bar, R., Ma, Z., Haney, L.B., Hardin, J., Ravichandran, K.S., Moreno, S., Hengartner, M.O.. Loss of the rhogap srgp-1 promotes the clearance of dead and injured cells in caenorhabditis elegans. Nat Cell Biol 2011;13(1):79–86.

16. Zaidel-Bar, R., Joyce, M.J., Lynch, A.M., Witte, K., Audhya, A., Hardin, J.. The f-bar domain of srgp-1 facilitates cell-cell adhesion during *C. elegans* morphogenesis. J Cell Biol 2010;191(4):761–9.

17. Hardin, J., Lynch, A., Loveless, T., Pettitt, J.. Cadherins and their partners in the nematode worm caenorhabditis elegans. Prog Mol Biol Transl Sci 2013;116:239–62.

18. Kang, H., Bang, I., Jin, K.S., Lee, B., Lee, J., Shao, X., Heier, J.A., Kwiatkowski, A.V., Nelson, W.J., Hardin, J., Weis, W.I., Choi, H.J.. Structural and functional characterization of caenorhabditis elegans α-catenin reveals constitutive binding to β-catenin and f-actin. J Biol Chem 2017;292(17):7077–7086.

19. Shao, X., Kang, H., Loveless, T., Lee, G.R., Seok, C., Weis, W.I., Choi, H.J., Hardin, J.. Cell-cell adhesion in metazoans relies on evolutionarily conserved features of the α-catenin . β-catenin-binding interface. J Biol Chem 2017;292(40):16477–16490.

20. Shao, X., Lucas, B., Strauch, J., Hardin, J.. The adhesion modulation domain of caenorhabditis elegans α-catenin regulates actin binding during morphogenesis. Mol Biol Cell 2019;30(17):2115–2123.

21. Vuong-Brender, T.T.K., Boutillon, A., Rodriguez, D., Lavilley, V., Labouesse, M.. Hmp-1/α-catenin promotes junctional mechanical integrity during morphogenesis. PLoS One 2018;13(2):e0193279.

22. Chen, H., Fu, H., Zhu, X., Cong, P., Nakamura, F., Yan, J.. Improved high-force magnetic tweezers for stretching and refolding of proteins and short DNA. Biophysical Journal 2011;100(2):517–523.

23. Le, S., Yao, M., Chen, J., Efremov, A.K., Azimi, S., Yan, J.. Disturbance-free rapid solution exchange for magnetic tweezers single-molecule studies. Nucleic Acids Research 2015;43(17):e113–e113.

24. Le, S., Liu, R., Lim, C.T., Yan, J.. Uncovering mechanosensing mechanisms at the single protein level using magnetic tweezers. Methods 2016;94:13–18.

25. Yuan, G., Le, S., Yao, M., Qian, H., Zhou, X., Yan, J., Chen, H.. Elasticity of the transition state leading to an unexpected mechanical stabilization of titin immunoglobulin domains. Angew Chem Int Ed Engl 2017;56(20):5490–5493.

26. Le, S., Hu, X., Yao, M., Chen, H., Yu, M., Xu, X., Nakazawa, N., Margadant, F.M., Sheetz, M.P., Yan, J.. Mechanotransmission and mechanosensing of human alpha-actinin 1. Cell Rep 2017;21(10):2714–2723.

27. Le, S., Yu, M., Hovan, L., Zhao, Z., Ervasti, J., Yan, J.. Dystrophin as a molecular shock absorber. ACS Nano 2018;12(12):12140–12148.

28. Zakeri, B., Fierer, J.O., Celik, E., Chittock, E.C., Schwarz-Linek, U., Moy, V.T., Howarth, M.. Peptide tag forming a rapid covalent bond to a protein, through engineering a bacterial adhesin. Proc Natl Acad Sci U S A 2012;109(12):E690–7.

29. Le, S., Chen, H., Zhang, X., Chen, J., Patil, K.N., Muniyappa, K., Yan, J.. Mechanical force antagonizes the inhibitory effects of recx on reca filament formation in mycobacterium tuberculosis. Nucleic Acids Res 2014;42(19):11992–9.

30. Zhao, X., Zeng, X., Lu, C., Yan, J.. Studying the mechanical responses of proteins using magnetic tweezers. Nanotechnology 2017;28(41):414002.

31. Yu, M., Lu, J.H., Le, S., Yan, J.. Unexpected low mechanical stability of titin i27 domain at physiologically relevant temperature. The Journal of Physical Chemistry Letters 2021;12(33):7914–7920.

32. Spadaro, D., Le, S., Laroche, T., Mean, I., Jond, L., Yan, J., Citi, S.. Tension-dependent stretching activates zo-1 to control the junctional localization of its interactors. Curr Biol 2017;27(24):3783–3795.e8.

33. Yu, M., Le, S., Ammon, Y.C., Goult, B.T., Akhmanova, A., Yan, J.. Force-dependent regulation of talin-kank1 complex at focal adhesions. Nano Lett 2019;19(9):5982–5990.

34. Wang, Y., Barnett, S.F.H., Le, S., Guo, Z., Zhong, X., Kanchanawong, P., Yan, J.. Label-free single-molecule quantification of rapamycin-induced fkbp-frb dimerization for direct control of cellular mechanotransduction. Nano Lett 2019;19(10):7514–7525.

Figure 1: Mechanical stability of full-length HMP-1: A. Sketches of the single-molecule construct and the experimental design. Top panel shows the domain map of the construct: AviTag, two repeats of I27 domain $(I27)_2$, full-length HMP-1, $(I27)_2$, SpyTag. The bottom panel shows a single-molecule tether between a SpyCather-coated coverslip surface and a biotin-DNAcoated super-paramagnetic bead (via streptavidin). Structural changes of the domains in the tether lead to extension changes of the molecule, which can be detected by the corresponding bead height changes. **B.** Four representative force–height curves of a full-length HMP-1 tether during force-increase scans at a loading rate of 1 pN s^{-1}. The coloured curves are obtained by 10-point FFT (fast Fourier transformation) smooth of the raw data (gray). The arrows indicate the unfolding events of the six domains in HMP-1. The inset shows the refolding events during force-decrease scans at a loading rate of -0.1 pN s^{-1}. **C-D.** The resulting force-dependent unfolding step sizes and the normalized force histogram obtained over 30 repeats of scans from three independent tethers. *N* in panel (d) indicates the total number of unfolding events.

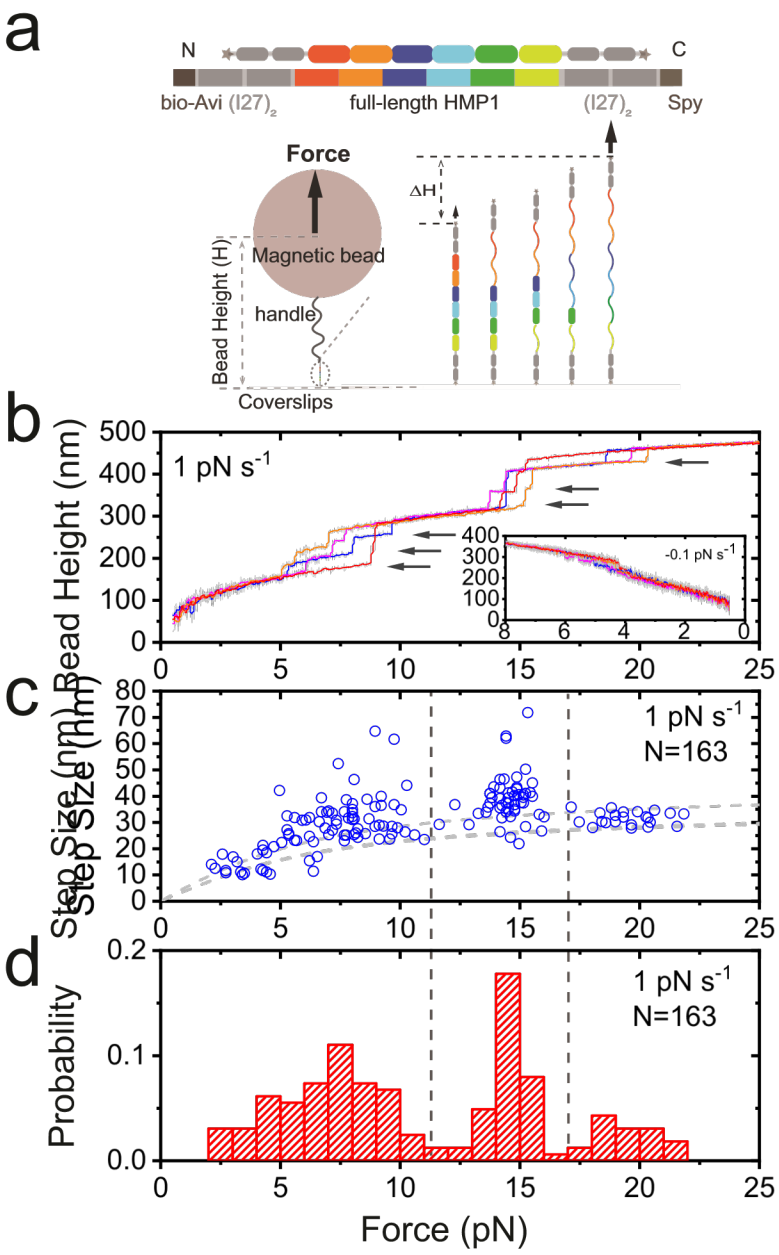
a
N
C
bio-Avi (I27)2
full-length HMP1
(I27)2
Spy
Force
ΔH
Magnetic bead
handle
Bead Height (H)
Coverslips
b
1 pN s-1
-0.1 pN s-1
Bead Height (nm)
c
1 pN s-1
N=163
Step Size (nm)
d
1 pN s-1
N=163
Probability
Force (pN)

Figure 2: Mechanical stability of the HMP-1 modulation domains. A. Sketches of the single-molecule construct and the experimental design. Top panel shows the domain map of the construct, and the structure of the modulation domains (PDB:5H5M) [18]. The bottom panel shows a single-molecule tether under force. **B.** Five representative force–height curves of the HMP-1 modulation domains during force-increase scans at a loading rate of 1 pN s^{-1}. **C-D.** The resulting force-dependent step sizes and the normalized force histogram of the unfolding events obtained over 165 repeats of scans from five tethers. The unfolding events are divided into three groups based on unfolding forces and step sizes. The number of unflding events (*N*) in each group and the corresponding average unfolding forces and step sizes are indicated (panel (**c**)). The blue curve in panel **D** is the double-Gaussion fitting to the normalized unfolding force histogram. The peak forces are indicated. The area ratio (0.66:0.26) of the two groups is also indicated. **E.** Three representative force–height curves (colored curves) of HMP-1 modulation domains during force-decrease scans with a loading rate of -0.1 pN s^{-1} started from fully unfolded conformation. As a comparison, the force–height curves of the HMP-1 modulation domain with all three subdomains folded (gray curves) are also plotted

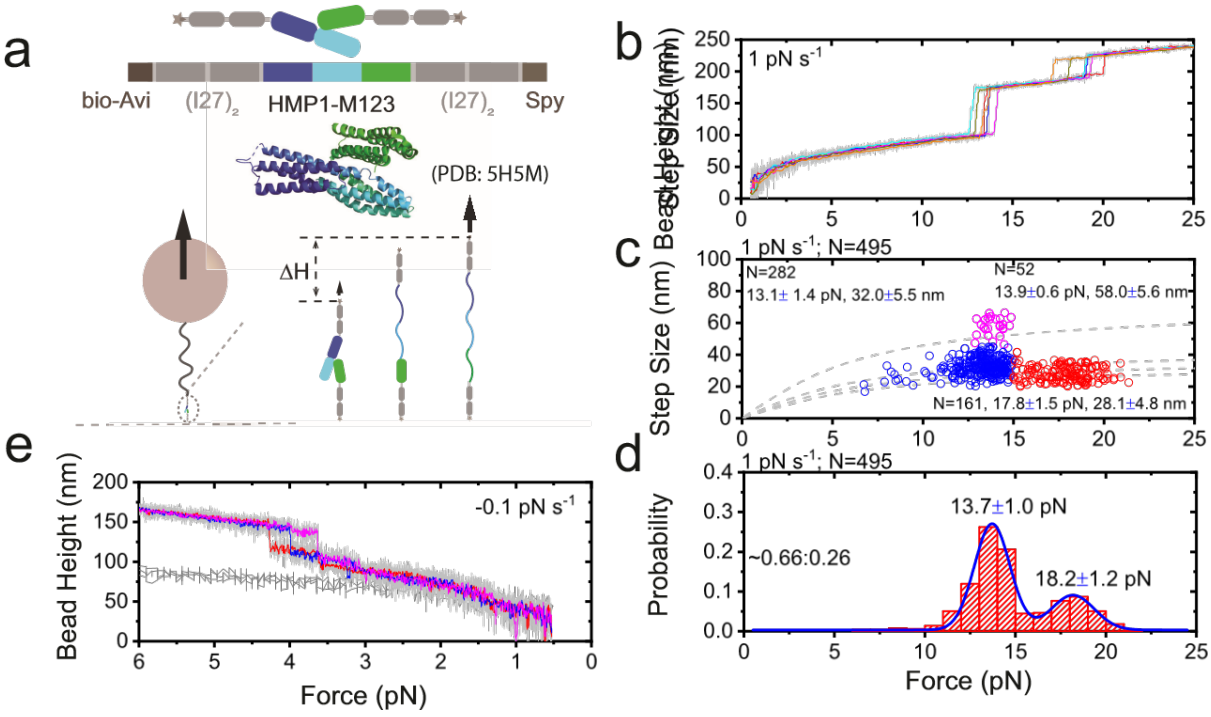
a
bio-Avi
(I27)2
HMP1-M123
(I27)2
Spy
(PDB: 5H5M)
ΔH
b
1 pN s-1
Step Size (nm)
Bead Height (nm)
c
1 pN s-1; N=495
N=282
13.1± 1.4 pN, 32.0±5.5 nm
N=52
13.9±0.6 pN, 58.0±5.6 nm
N=161, 17.8±1.5 pN, 28.1±4.8 nm
Step Size (nm)
d
1 pN s-1; N=495
13.7±1.0 pN
~0.66:0.26
18.2±1.2 pN
Probability
Force (pN)
e
-0.1 pN s-1
Bead Height (nm)
Force (pN)

Figure 3: Mechanical activation of HMP-1 modulation domains for vinculin binding. A. The Left panel shows the domain map of the HMP-1 modulation domain, and the sequence alignment of the conserved vinculin binding sites among the HMP-1 and mammalian α-catenins. The right panel shows a single-molecule tether under force. **B.** Representative force–height curves during force-increase scans in the absence of vinculin-D1 (dark gray curves) and in the presence of 10 nM vinculin-D1 (magenta and orange curves). **C.** Representative force–height curves during force-increase scans in the absence of vinculin-D1 (dark gray curves) and in the presence of 200 nM vinculin-D1 (magenta and red curves). **D-E.** The resulting force-dependent step sizes and the normalized unfolding force histogram obtained over 150 repeats of scans from five tethers in 200 nM vinculin-D1. The unfolding events are divided into three groups based on unfolding forces. The number of unfolding events (N) in each group and the corresponding average unfolding forces and step sizes are indicated (panel **D**). The blue curve in panel **E** is the triple-Gaussion fitting to the normalized unfolding force histogram. The peak forces and the area ratio (0.08:0.52:0.40) of the three groups areindicated. **F** Representative force–height curves of the tether at indicated constant forces. Dynamic binding or unbinding events of vinculin-D1 were indicated by 3-5 nm bead height changes, as shown in the resulting normalized histograms of bead height **G**.

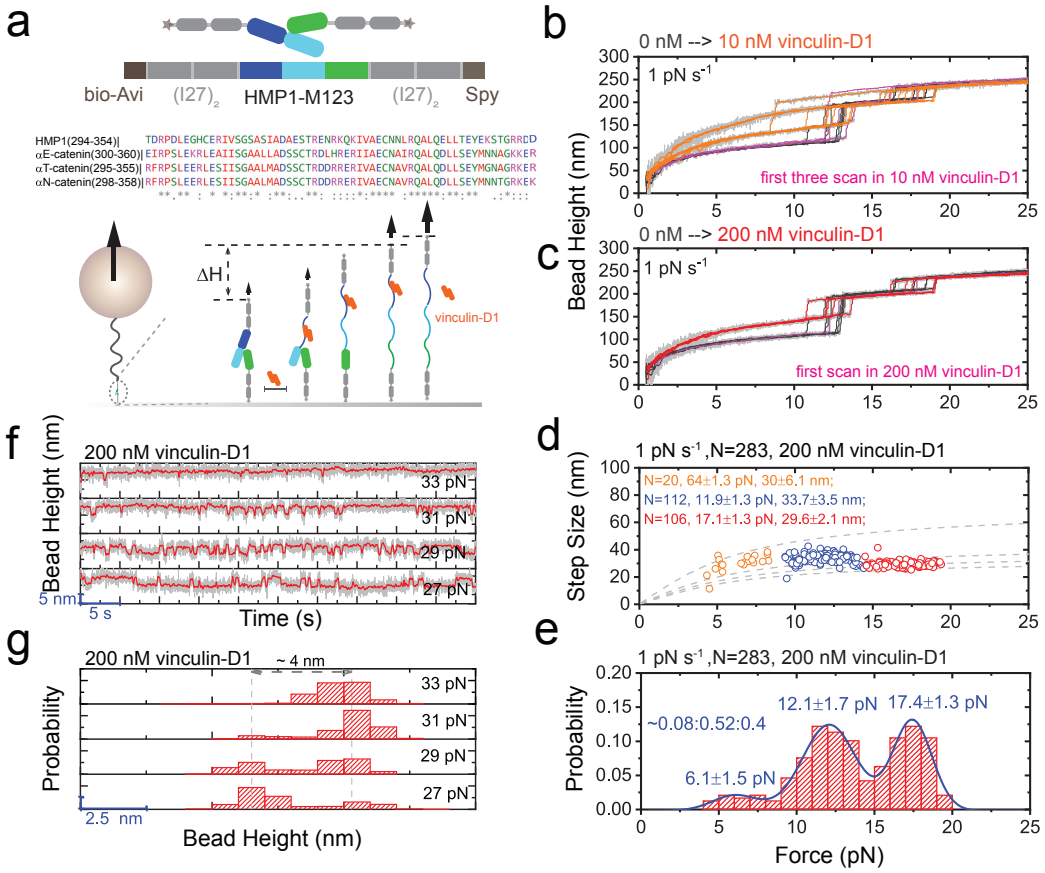
a
bio-Avi
(I27)2
HMP1-M123
(I27)2
Spy
HMP1(294-354)| TDRPDLEGHCERIVSGSASIADAESTRENRKQKIVAECNNLRQALQELLTEYEKSTGRRDD
αE-catenin(300-360)| EIRPSLEKRLEAIISGAALLADSSCTRDLHRERIIAECNAIRQALQDLLSEYMNNAGKKER
αT-catenin(295-355)| RFRPSLEERLESIISGAALMADSSCTRDDRRERIVAECNAVRQALQDLLSEYMGNAGRKER
αN-catenin(298-358)| RFRPSLEERLESIISGAALMADSSCTRDDRRERIVAECNAVRQALQDLLSEYMNNTGRKEK
ΔH
vinculin-D1
b
0 nM --> 10 nM vinculin-D1
1 pN s-1
first three scan in 10 nM vinculin-D1
Bead Height (nm)
c
0 nM --> 200 nM vinculin-D1
1 pN s-1
first scan in 200 nM vinculin-D1
d
1 pN s-1 ,N=283, 200 nM vinculin-D1
N=20, 64±1.3 pN, 30±6.1 nm;
N=112, 11.9±1.3 pN, 33.7±3.5 nm;
N=106, 17.1±1.3 pN, 29.6±2.1 nm;
Step Size (nm)
e
1 pN s-1 ,N=283, 200 nM vinculin-D1
12.1±1.7 pN
17.4±1.3 pN
~0.08:0.52:0.4
6.1±1.5 pN
Probability
Force (pN)
f
200 nM vinculin-D1
33 pN
31 pN
29 pN
27 pN
Bead Height (nm)
5 nm
5 s
Time (s)
g
200 nM vinculin-D1
~ 4 nm
33 pN
31 pN
29 pN
27 pN
Probability
2.5 nm
Bead Height (nm)

Figure 4: Mechanical stability of the HMP-1–HMP-2 interface. A. The single-molecule construct, the domain map, the structure of the HMP-1–HMP-2 interface (PDB:5XA5) [19], and the single-molecule tether under force. **B**. Representative force–height curves of a tether during force-increase scans at a loading rate of 1 pN s-1. **C-D.** The resulting force-dependent step sizes and the normalized rupturing force histograms obtained over 50 repeats of scans for five tethers at three indicated force loading rates. The number of rupturing events, the average forces and the average step sizes at corresponding loading rates are N=56, F=15.9 ±1.9 pN, ΔH=115.4 ±12.2 nm (0.2 pN s-1); N=178, F=16.58 ±1.7 pN, ΔH=110.9±8.4 nm (1 pN s-1); N=106, F=19.1 ±3.1 pN, ΔH=112.6 ±14.2 nm (5 pN s-1). **E.** Representative force–height curves of a tether during force-clamp at 14.0 pN. The stepwise bead height jumps indicate the rupturing of the HMP-1–HMP-2 interface. **F.** The resulting force dependent average lifetime τ(F) of the HMP-1–HMP-2 interface obtained from such force-clamp experiments, which can be well fitted with Bell's model, $\tau(F) = k{-}10\ e{-}F\Delta kBT$, where Δ is the transition distance and k0 is the extrapolated zero-force rupturing rate. **G.** Representative force–height curves of the tether during force-decrease scans with a loading rate of -0.1 pN s-1. Gray arrows indicate the refolding of N1 and N2 domains, black arrow indicates the re-formation of the interface. **H.** Representative time traces of the bead height at indicated constant forces, before the re-formation of the interface. Dynamic unfolding and refolding of the N1 and N2 domain were observed. **I.** Representative force–height curves of the tether during force-increase scans at the indicated loading rate starting from a conformation in which the HMP-1–HMP-2 interface was not re-formed, whereas the N1 and N2 domains were refolded. **J.** The resulting normalized unfolding force histogram during the force-increase scans.

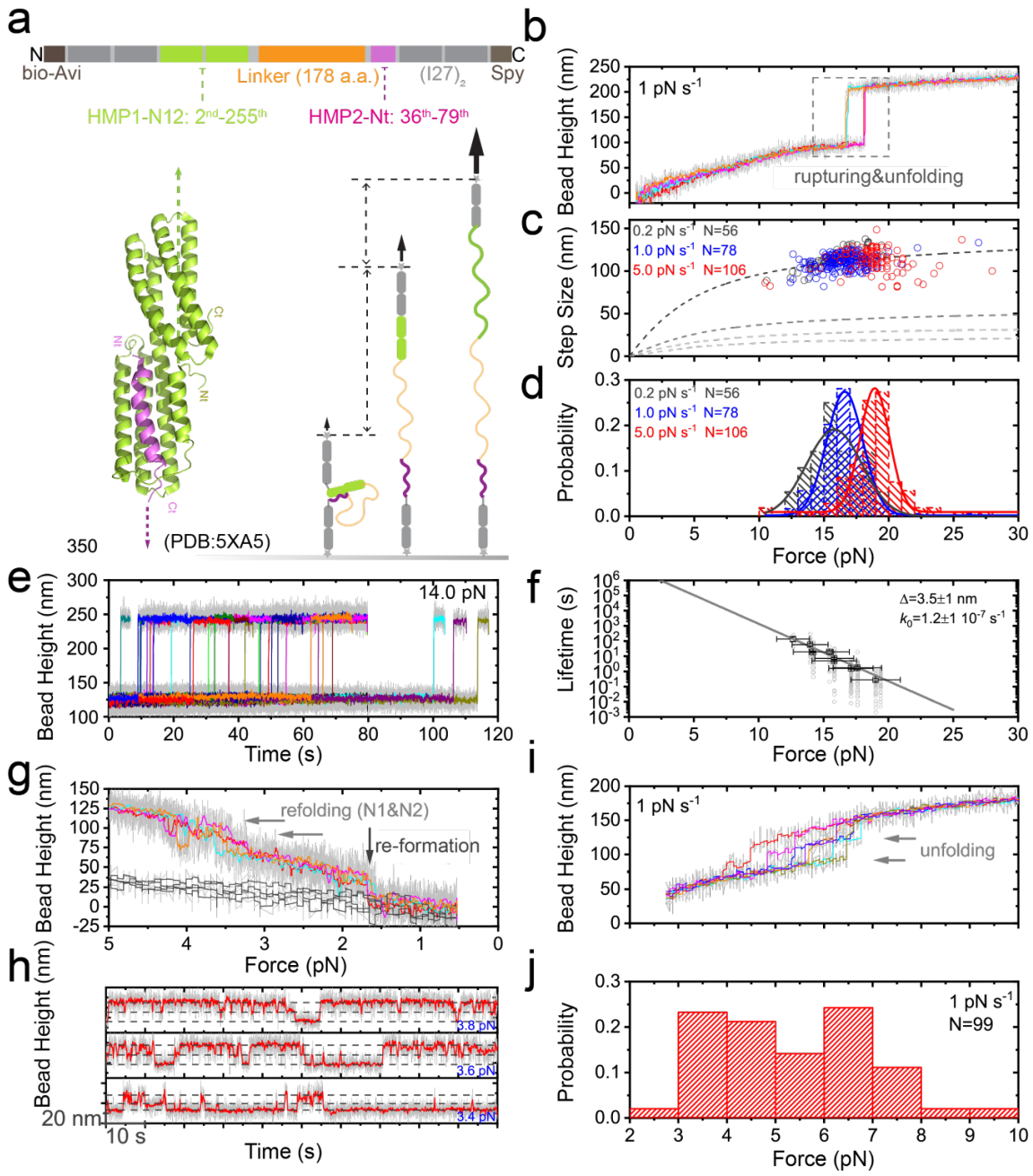
a
N
C
bio-Avi
Linker (178 a.a.)
(I27)2
Spy
HMP1-N12: 2nd-255th
HMP2-Nt: 36th-79th
(PDB:5XA5)
350
b
1 pN s-1
rupturing&unfolding
Bead Height (nm)
c
0.2 pN s-1 N=56
1.0 pN s-1 N=78
5.0 pN s-1 N=106
Step Size (nm)
d
Probability
Force (pN)
e
14.0 pN
Bead Height (nm)
Time (s)
f
Δ=3.5±1 nm
k0=1.2±1 10-7 s-1
Lifetime (s)
Force (pN)
g
refolding (N1&N2)
re-formation
Bead Height (nm)
Force (pN)
h
3.8 pN
3.6 pN
3.4 pN
20 nm
10 s
Bead Height (nm)
Time (s)
i
1 pN s-1
unfolding
Bead Height (nm)
j
1 pN s-1
N=99
Probability
Force (pN)

Figure 5: Mechanical stability of the HMP-1–HMP-2 interface with Y69E or S47E mutation on HMP-2. A. Sketches of the domain map and sequences of HMP-2-Nt. **B.** Representative force–height curves of a HMP-1–HMP-2Y69E interface tether during force-increase scans at 1 pN s-1. **C-D.** The resulting force-dependent step sizes and the normalized rupturing force histograms obtained at the three indicated loading rates. The number of rupturing events, the average forces and the average step sizes at corresponding loading rates are N=12, F=4.7±0.9 pN, ΔH=38.2±4.5 nm; N=2, F=12.6±0.7 pN, ΔH=100.4±16.1 nm (0.2 pN s-1, two groups); N=86, F=5.7±1.5 pN, ΔH=44.5±9.3 nm; N=188, F=14.1±1.4 pN, ΔH=105.8±14.3 nm (1.0 pN s-1, two groups); N=221, F= 7.4±2.1 pN, ΔH=39.9±7.3 nm; N=441, F= 14.7±2.5 pN, ΔH=91.5±33.8 nm (5.0 pN s-1, two groups); **E.** Representative time traces of the bead height of a HMP-1–HMP-2Y69E interface tether at indicated constant forces, where dynamic formation and rupturing of the interface were observed. **F.** Representative force–height curves of a HMP-1–HMP-2S47E interface tether during force-increase scans at 1 pN s-1. **G-H.** The resulting force-dependent step sizes and the normalized rupturing force histograms obtained at the three indicated loading rates. The number of rupturing events, the average forces and the average step sizes at corresponding loading rates are:N=108, F= 13.6±1.2 pN, ΔH=107.4±9.2 nm (0.2 pN s-1); N=32, F= 14.3±2.2 pN, ΔH=112.4±14.7 nm (1.0 pN s-1); N=67, F= 16.3±1.7 pN, ΔH=117.3±10.9 nm (5.0 pN s-1); **I.** Representative time traces of the bead height of a HMP-1–HMP-2S47E tether at a constant force of 3 pN for over 4000 sec where the interface remained stable, followed by a force-increase scan (after the break sign) to rupture the interface.

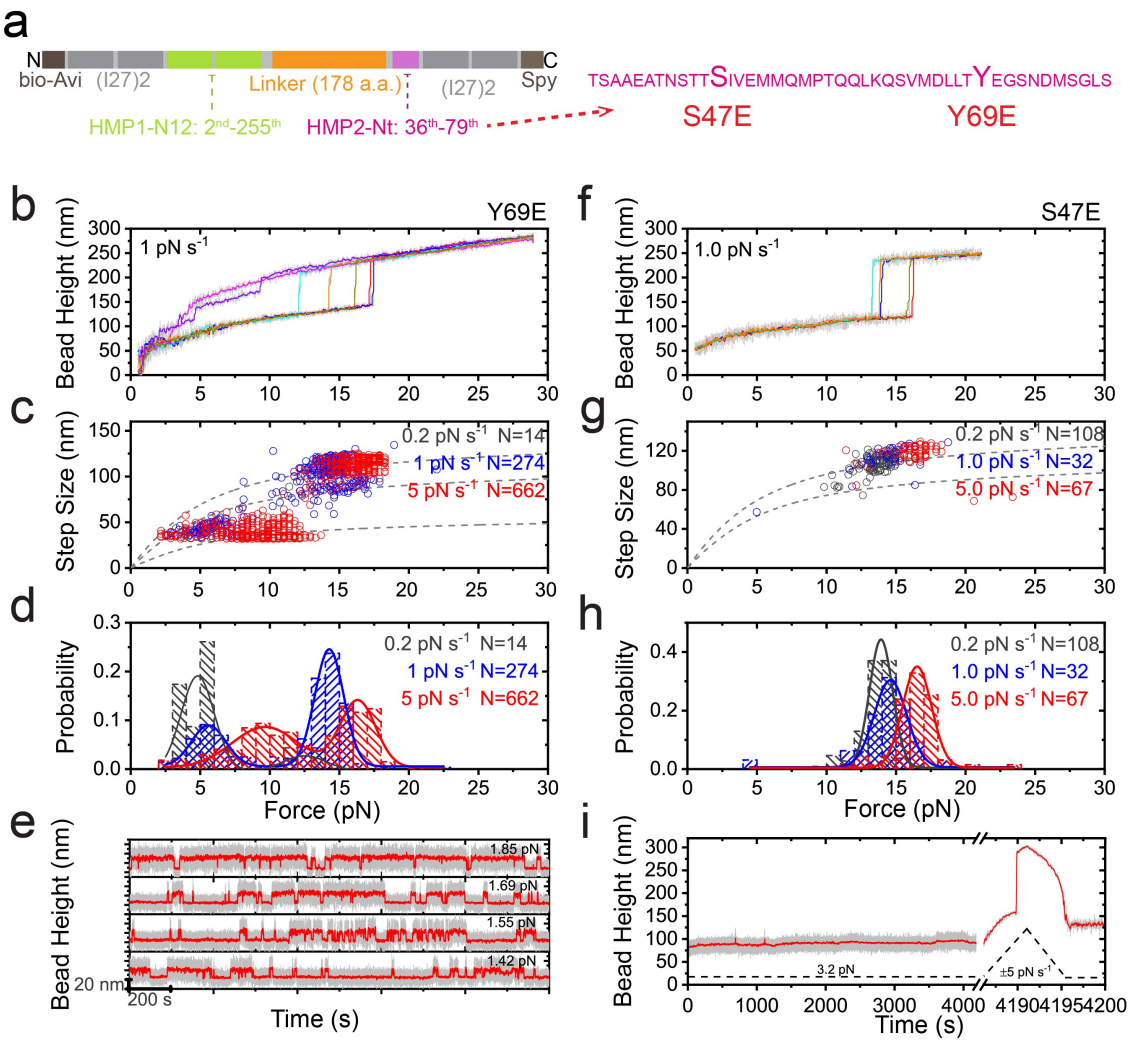
a
N
bio-Avi
(I27)2
Linker (178 a.a.)
(I27)2
Spy
C
HMP1-N12: 2nd-255th
HMP2-Nt: 36th-79th
TSAAEATNSTTSIVEMMQMPTQQLKQSVMDLLTYEGSNDMSGLS
S47E
Y69E
b
Y69E
1 pN s-1
Bead Height (nm)
c
Step Size (nm)
0.2 pN s-1 N=14
1 pN s-1 N=274
5 pN s-1 N=662
d
Probability
Force (pN)
e
Bead Height (nm)
1.85 pN
1.69 pN
1.55 pN
1.42 pN
20 nm
200 s
Time (s)
f
S47E
1.0 pN s-1
Bead Height (nm)
g
Step Size (nm)
0.2 pN s-1 N=108
1.0 pN s-1 N=32
5.0 pN s-1 N=67
h
Probability
Force (pN)
i
Bead Height (nm)
3.2 pN
±5 pN s-1
Time (s)

Supplementary Figure S1. Force-responses of HMP1-M1 domain. A. Representative force–bead height curves of the HMP1-M1 domain at a loading rate of ~ 1 pN s−1 . **B.** representative bead height fluctuations of HMP1-M1 domain at constant forces of ~ 2 pN. Colored lines are 10-point FFT (Fast Fourier Transform) smoothing of the raw data in grey.

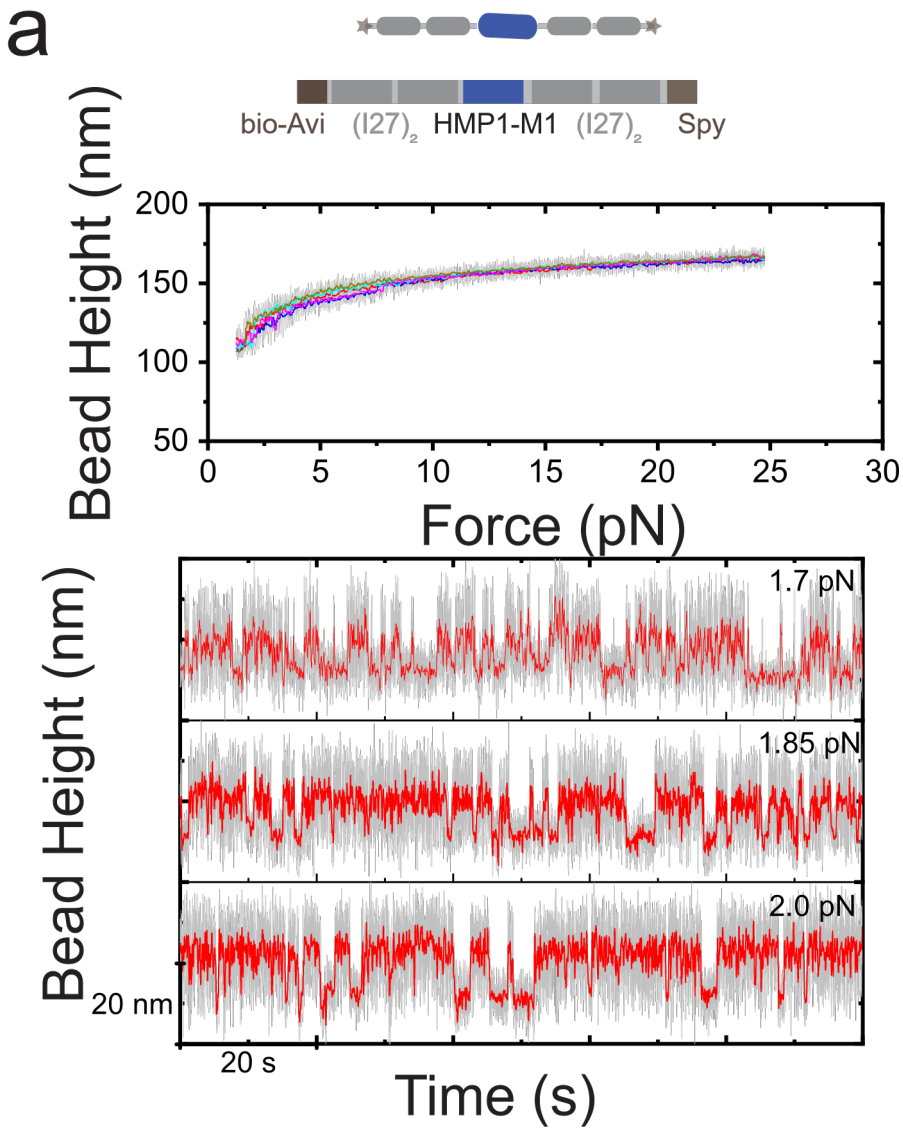
a
bio-Avi
(I27)2
HMP1-M1
(I27)2
Spy
Bead Height (nm)
200
150
100
50
0
5
10
15
20
25
30
Force (pN)
Bead Height (nm)
1.7 pN
1.85 pN
2.0 pN
20 nm
20 s
Time (s)

APPENDIX 2

TES-1/Tes protects junctional actin networks under tension from self-injury during epidermal morphogenesis in the *C. elegans* embryo

This work is in revision at *Current Biology*. The authors are Allison M. Lynch, Yuyun Zhu, Bethany G. Lucas, Jonathan D. Winkelman, Sterling C.T. Martin, Samuel D. Block, Anjon Audhya, Margaret L. Gardel, and Jeff Hardin

My contributions to this work include creation an endogenous knock-in of TES-1/Testin, which I used to perform preliminary imaging during embryogenesis. I also performed a co-IP experiment to determine if TES-1 interacts with HMP-1/α-catenin in *C. elegans*

Summary

During embryonic morphogenesis, the integrity of epithelial tissues depends on the ability of cells in tissue sheets to undergo rapid changes in cell shape while preventing self-injury to junctional actin networks. LIM domain-containing repeat (LCR) proteins are recruited to sites of strained actin filaments in cultured cells [1-3], and are therefore promising candidates for mediating self-healing of actin networks, but whether they play similar roles in living organisms has not been determined. Here, we establish roles for *Caenorhabditis elegans* TES-1/Tes, an actin-binding LCR protein present at apical junctions, during epithelial morphogenesis. TES1**::**GFP is recruited to apical junctions during embryonic elongation, when junctions are under tension; in embryos in which stochastic failure of cell elongation occurs, TES-1 is only strongly recruited to junctions in cells that successfully elongate, and recruitment is severely compromised in genetic backgrounds in which cell shape changes do not successfully occur. *tes1* mutant embryos display junctional F-actin defects, and loss of TES-1 strongly enhances tension-dependent injury of junctional actin networks in hypomorphic mutant backgrounds for CCC components, suggesting that TES-1 helps to prevent self-injury of junctional actin networks during rapid cell shape change. Consistent with such role, a fragment of TES-1 containing its LIM domains localizes to stress fiber strain sites (SFSS) in cultured vertebrate cells. Together, these data establish TES-1 as a tension-sensitive stabilizer of the junctional actin cytoskeleton during embryonic morphogenesis.

Introduction

Embryonic tissues require epithelial cell-cell adhesions that are both dynamic and strong. On the one hand, they must be dynamic, as cells rearrange and change shape to allow for the complex processes of morphogenesis, but on the other, cell-cell adhesions must be able to withstand contractile forces that threaten tissue integrity [4-7]. Thus, identifying factors that modulate junctional integrity is important for understanding embryonic morphogenesis. Here, we describe a novel modulatory role for the *C. elegans* Testin/Tes ortholog, TES-1, at cell-cell junctions.

Vertebrate Tes/testin (hereafter Tes) has an N-terminal CR domain , a PET (Prickle, Espinas and Testin) domain, and three C-terminal LIM (Lin11, Isl-1 & Mec-3) domains. Biochemical and structure-function analyses have suggested that the N terminus of Tes allows association with the actin cytoskeleton [8, 9]. The LIM domains appear to allow association with heterologous binding partners [10, 11], may be involved in mediating intracellular inhibition of Tes [12] and the PET domain may allow homodimerization of Tes via interaction with the LIM1-2 region [13].

Tes has been implicated in several actin-dependent processes. In cultured cells, Tes localizes to focal adhesions, integrin-based attachment sites linking intracellular actin stress fibers to sites of attachment to the extracellular matrix (ECM) [1, 8, 9, 14]. Tes also appears to associate with cell-cell adhesions. Tes localizes to spot-like cell-cell contacts [10, 15], where it colocalizes with cadherin/catenin complex (CCC) components [10]. Vertebrate zyxin can interact with Tes in vitro [9, 11] and also localizes to adherens junctions [8, 9, 15-22]. Zyxin and other LIM domain proteins preferentially localize to natural rupture sites in bundled F-actin networks in cultured cells subjected to tension, where they are thought to allow rapid healing of

ruptured bundles [23-25]; reviewed in [1]. In cultured cells the LIM domains of zyxin, Tes, and other LIM domain proteins are sufficient for this response [2].

While previous work has examined the role of Tes in establishing and maintaining actin networks under stress in cultured cells, particularly at sites of cell-ECM attachment, roles for Tes have not been established at sites of epithelial cell-cell adhesion in an intact, developing organism. *C. elegans* epidermal morphogenesis provides a convenient system for studying the roles of proteins that modulate epithelial cell-cell adhesion. Epidermal morphogenetic movements that require the CCC include (1) ventral enclosure, during which the embryo is encased in an epidermal monolayer [26] and new epidermal cell-cell junctions are formed [27]; and (2) the early phase of elongation, which involves a coordinated actomyosin-mediated contraction of the embryo, primarily driven by lateral (seam) epidermal cells [28, 29]; reviewed in [30, 31]. These contractile forces exert substantial tension on cell-cell junctions; the forces of contraction are transmitted via circumferential filament bundles (CFBs), large bundles of F-actin anchored at epidermal cell-cell junctions [28, 32]. Anchorage of CFBs depends on the core components of the CCC: HMR-1/cadherin, HMP-2/β-catenin, and HMP-1/α-catenin [27]. Reduced function of core CCC components coupled with removal of other adherens junctional proteins leads to catastrophic morphogenetic failure, predominantly during embryonic elongation [33-36]. Here, we describe the roles of TES-1/Tes, in preventing "self-injury" of the junctional proximal actin network that maintains the connection between the CCC and CFBs during periods of mechanical stress in the developing *C. elegans* epidermis.

Results and Discussion

We previously conducted a genome-wide RNAi screen in a sensitized HMP-1/α-catenin background, *hmp-1(fe4)*, and uncovered modulators of cell adhesion in *C. elegans* during

morphogenesis [35]. In our initial screen, we identified a gene on chromosome IV, which when knocked down, potently enhanced the penetrance and severity of the *hmp-1(fe4)* phenotype [35] (Supplemental Video 1). Previously named TAG-224 (Temporarily Assigned Gene 224), we renamed the protein TES-1 because of its significant homology to the vertebrate protein Tes after examination of the predicted protein sequence using BLAST and ClustalW. ClustalW analysis indicates that the two proteins are approximately 35% identical and 64% similar. Pfam analysis shows both proteins have a similar domain structure: an N-terminal PET domain followed by three C-terminal LIM domains (Fig. 1A).

TES-1 functionally interacts with hmp-1/α-catenin at the *C. elegans* apical junction

All *hmp-1(fe4); tes-1*(RNAi) embryos arrest during the elongation stage of morphogenesis with junctional actin defects that suggest a requirement for TES-1 during developmental stages requiring strong cell-cell adhesions (Fig. 1B-D). In 26 % of *hmp-1(fe4); tes-1*(RNAi) embryos (6 of 23 embryos examined via 4d microscopy) individual cells leaked out of the ventral midline, compared with 0% of *hmp-1(fe4)* homozygotes (0 of 22 embryos examined; significantly different, Fisher's exact test, $p = 0.02$), suggesting that nascent junctions also have a more stringent requirement for TES-1 in this sensitized background (Fig. 1D, arrow). Phalloidin staining demonstrated that *tes-1(RNAi)* exacerbated junctional proximal actin defects in a *hmp-1(fe4)* background (Fig. 1E-G). We confirmed the efficacy of *tes-1* RNAi and the synergistic lethality resulting from TES-1 depletion in *hmp-1(fe4)* embryos by crossing a deletion allele, *tes-1(ok1036),* into *hmp-1(fe4)* worms: double homozygotes exhibit 93.7% lethality and elongation arrest (n = 516 embryos examined).

We next confirmed that, like vertebrate Tes [8, 9], TES-1 directly binds F-actin by performing actin cosedimentation assays using recombinant TES-1 protein and found that TES-1

cosediments with F-actin (Fig. 1H). The extent of cosedimentation of TES-1 with F-actin is statistically indistinguishable from another well characterized junctional actin-binding protein in *C. elegans*, HMP-1/α-catenin [37] (Fig. 1I).

TES-1 localizes to apical junctions in the embryonic epidermis

To assess the expression pattern and subcellular localization of TES-1, we constructed a translational fusion protein containing the entire genomic sequence of *tes-1* fused to GFP driven by its endogenous promoter (Fig. 2). In early embryos, TES-1::GFP is visible in epidermal cells, where its location is exclusively cytoplasmic. At the 2-fold stage of elongation, TES-1::GFP puncta begin to accumulate at sites of cell-cell contact (Fig. 2B). These clusters expand and become more evenly distributed along cell borders as elongation continues (Fig. 2C); junctional TES-1 signal likewise increases significantly after the two-fold stage of elongation (Fig. 2H). Strikingly, TES-1::GFP is maintained at seam-dorsal and seam-ventral, but not seam-seam borders (Fig. 2D). Importantly, TES-1::GFP rescues lethality seen in *ok1036/+; fe4* embryos. *ok1036/+;fe4/fe4* worms are extremely difficult to maintain due to *fe4* maternal effect; progeny of such worms exhibit 80% lethality (n = 20 embryos scored) and the addition of extrachromosomal TES-1::GFP reduces this lethality to 38% (n = 92 embryos scored). Significantly, *ok1036/ok1036;fe4/fe4* worms can develop to adulthood, but only if they express *tes-1::gfp*, indicating the GFP is functional.

To determine whether TES-1::GFP colocalizes with adhesion complexes, we performed immunostaining experiments on embryos expressing TES-1::GFP. The apicobasal distribution of TES-1 indicates that it colocalizes predominatly with the cadherin/catenin complex vs. the DLG-1/AJM-1 complex. Embryos co-immunostained for HMR-1/cadherin and GFP display substantial overlap of HMR-1 and TES-1::GFP (Fig. 2C), wheras there is much less overlap with

AJM-1, a component of the DLG-1 (Discs Large)/AJM-1 complex, which is basal to the CCC (Fig. 2D). Partial localization of Tes with the CCC has likewise previously been reported in cultured vertebrate cells [10]. Although one study has reported that vertebrate α-catenin and Tes can be coimmunoprecipitated [38], we have been unable to coimmunoprecipitate TES with *C. elegans* CCC components in a generalized proteomics approach [39] or in directed coIP experiments (Fig. S2), suggesting that the interaction of TES-1 with the *C. elegans* CCC is indirect.

To address the role of junctional components in localizing Tes in living embryos, we performed knockdown experiments in *tes-1::gfp* transgenic embryos followed by confocal microscopy. *ajm-1*(RNAi) in embryos expressing TES-1::GFP does not prevent localization of TES-1::GFP to junctions (Fig. 2E). In these embryos, however, TES-1::GFP foci do not spread to form a continuous, intense band, which may reflect the failure of *ajm-1(RNAi)* embryos to elongate successfully (see below). In contrast, the effects of loss of function of *hmr-1*/cadherin on TES-1::GFP localization were more severe. In *hmr-1*(RNAi) embryos TES-1::GFP failed to be recruited to junctions (Fig. 2F).

Based on previous studies of vertebrate homologues [9, 11], we next assessed the effects of loss of ZYX-1/zyxin on TES-1::GFP junctional localization, since ZYX-1 translational fusions have previously been reported to be weakly expressed in epidermal cells in embryos [40]. While vertebrate Tes can physically interact with zyxin [9, 11] and we were able to coIP TES-1 and ZTX-1 (Fig. S3A), we were only able to detect a very weak, substoichiometric interaction between TES-1 and ZYX-1 via coIP and pulldown of bacterial expressed proteins (Fig. S3B). When we crossed the strain expressing *tes-1::gfp* into *zyx-1(gk190)* worms, we occasionally saw TES-1::GFP localized to seam-seam junctions in addition to seam-dorsal and

seam-ventral junctions in resulting progeny at the 3-4-fold stage (Fig. 2G; 4/13 embryos examined; 0/8 embryos examined displayed seam:seam localization in the transgenic strain alone; not significant, Fisher's Exact test, $p = 0.27$), suggesting that ZYX-1 contributes weakly at best to the restriction of TES-1 to seam-dorsal and seam-ventral boundaries. This result is consistent with experiments in vertebrates, which show that while depletion of Zyxin can reduce the amount of Tes at focal adhesions [9], Tes can still localize independently of Zyxin [11].

TES-1 requires its PET and LIM2-3 domains

To our knowledge, the roles of specific regions of a Tes family member have not been assessed in a living organism. To identify which subdomains are required for junctional targeting and function of TES-1 we analyzed the expression pattern of GFP deletion constructs and analyzed the ability of each construct to rescue embryonic viability in offspring from *hmp-1(fe4)/+; tes-1(ok1036)/+* mothers (Fig. 3). Unlike full-length TES-1::GFP, TES-1ΔPET::GFP localized along all seam cell borders in the epidermis, including seam-seam borders, as well as CFBs (Fig. 3B). Deletion of LIM1 (Fig. 3C) or LIM2 (Fig. 3D) both perturbed junctional localization similarly: each localized sporadically to epidermal junctions, including some seam-seam junctions. However, there was also localization at what appeared to be actin-containing structures in epidermal cells. Deletion of LIM3 rendered the GFP entirely cytoplasmic (Fig. 3E). Deletion of all three LIM domains simultaneously resulted in GFP localization along structures that appear to be CFBs (Fig. S3F). This result is consistent with work on vertebrate Tes, which can co-immunoprecipitate actin [9] and localize via its N terminus [13, 38]. Because full-length TES-1::GFP localizes to cell-cell junctions, this result suggests that the latent ability of TES-1 to bind to CFBs is not normally manifest when other subdomains of TES-1 can bind their normal targets.

Due to maternal effects and gonadal defects, assessing synergistic lethality of *tes-1::gfp* deletion constructs in *hmp-1(fe4)* homozygous mothers proved challenging. We therefore tested for the ability of subdomains of TES-1 to rescue synergistic lethality in *ok1036/ok1036; hmp-1(fe4)/+* embryos (Fig. 3G). TES-1ΔPET could rescue some embryonic lethality in this genetic background, but progeny had numerous defects, including germline malformations, protruding vulvae, and sterility. TES-1ΔLIM1-3, TES-1ΔLIM2, and TES-1ΔLIM2 were unable to rescue the 39% lethality observed among progeny of *ok1036/ok1036; hmp-1(fe4)/+* mothers. among progeny of *tes-1(ok1036); hmp-1(fe4)* embryos. Interestingly, while lines harboring *tes-1ΔLIM1::GFP* could not be obtained, occasional *tes-1(ok1036); hmp-1(fe4); tes-1ΔLIM1::GFP* embryos were able to grow to adulthood, but these adults were sterile. Overall, these results indicate that the LIM domains of TES-1 are crucial for *tes-1* function during morphogenesis, but that LIM1 may be less important, and are consistent with the observation that the distribution of TES-1ΔPET::GFP and TES-1ΔLIM1::GFP appears most similar to full-length TES-1::GFP.

While overall the deletion analysis indicates that the LIM domains are crucial for junctional targeting of TES-1, the difference in localization pattern of the ΔLIM3 and ΔLIM1-3 is curious. Recently, it has been suggested that the LIM1-2 domain of vertebrate TES can engage in both heterophilic binding to proteins such as zyxin and homophilic dimerization via interaction with the PET domain of Tes [38]. Homodimerization of αE-catenin drives it away from adherens junctions [41, 42]. While it is not currently known if homodimeric Tes is sequestered away from cell adhesion sites in a similar way, if it is this might explain the cytoplasmic accumulation of TES-1ΔLIM3::GFP in *C. elegans*. Deletion of LIM3 might favor homodimerization over heterophilic interactions of TES-1 with other binding partners.

TES-1 localizes to junctions in a tension-dependent manner

Tes is required for the maintenance of stress fibers in cultured vertebrate cells [43], and accumulates at "focal adherens junctions", spot-like foci of cell-cell adhesion, in human vascular endothelial cells [10]. These data suggest that Tes might play tension-dependent roles in organizing the actin network at adherens junctions in epithelia during embryonic morphogenesis. During elongation of the *C. elegans* embryo, a coordinated change in the shape of epidermal cells drives elongation of the embryo to approximately 4-fold its original length [28]. The CCC anchors CFBs at junctions – specifically seam-ventral and seam-dorsal junctions – during this time, when the contractile forces driving elongation result in elevated tension at these junctional boundaries [27, 32, 44-46]. Given the localization of TES-1, it is a good candidate to stabilize junctional actin networks during embryonic elongation.

Because *hmr-1*/cadherin, *hmp-1*/*α-catenin*, and *hmp-2/β-catenin* homozygous null mutant embryos fail to progress past the two-fold stage of elongation, we could not assess whether disruption of TES-1::GFP recruitment to junctions is due primarily to physical absence of CCC components or because of the pre-elongation death of the embryos. In order to adjudicate between these possibilities we examined *hmp-1(fe4)* embryos expressing TES-1::GFP. The *fe4* lesion causes weaker binding of F-actin by HMP-1 and leads to less stable junctions [47]. *hmp-1(fe4)* embryos display a variable phenotype (Fig. 4A); while some embryos fail to elongate appreciably, other embryos extend to the 2-fold stage of elongation (Fig. 4B). We found that TES-1::GFP did not localize to junctions in *hmp-1(fe4)* embryos that failed to elongate past 1.5-fold (5 of 5 embryos imaged via spinning disc confocal microscopy), even in embryos that survived and hatched. However, TES-1::GFP did localize to junctions in *hmp-1(fe4)* embryos that elongated to at least 2-fold their original length (3 of 3 embryos examined; significantly

different; Fisher's exact test, p = 0.018). The correlation between the extent of elongation of *fe4* embryos and the normal TES-1::GFP localization patterns identified previously suggests that TES-1 is only recruited to junctions that resemble those in normal embryos at the 2-fold stage.

To examine whether junctional tension affects the ability of TES-1::GFP to localize, we introduced the full-length TES-1::GFP into *let-502(sb118)* worms (Fig. 4C-D). Loss of LET-502/Rho kinase reduces actomyosin contractility in the epidermis and prevents elongation of *C. elegans* embryos. *let-502(sb118)* is a temperature-sensitive allele; when *let-502(sb1180); tes-1::gfp* embryos were imaged at permissive temperatures, TES-1::GFP localized to junctions in a wild-type manner (Fig. 4C). However, when these embryos were reared at the restrictive temperature (25°C), TES-1::GFP remained entirely cytoplasmic in embryos that failed to elongate (Fig. 3D). We also attempted the converse experiment: loss of MEL-11/myosin phosphatase function results in excessively elongated embryos due to greater than normal epidermal contractility [45, 46]. However, adhesion complexes undergo changes in morphology that make this converse experiment difficult to interpret. In MEL-11-depleted embryos, the initially continuous distribution of junctional TES-1::GFP was progressively lost, as TES-1::GFP became fragmented and pulled away from junctions into linear arrays (Fig. 4E,F). One possibility consistent with this result is that the excessive tension that develops in a *mel-11* loss-of-function background leads to collapse of junctional proximal actin around CFB insertion sites, including associated TES-1.

TES-1 regulates actin networks during elongation

We next assessed why loss of TES-1 might enhance the *hmp-1(fe4)* phenotype. LIM domains proteins, including Tes and zyxin, are recruited to "stress fiber strain sites", bundled F-actin networks in cultured cells subjected to strain, where they are thought to allow rapid healing

of damaged bundles [2, 23-25]. We reasoned that since under normal circumstances TES-1 colocalizes with the CCC, TES-1 could similarly help to stabilize junctional-proximal actin subject to strain during periods of mechanical stress at adherens junctions during elongation. Consistent with this possibility, when we examined F-actin organization in *tes-1(ok1036)* homozygous embryos via phalloidin staining, we found defects not present in wild-type embryos (Fig. 5C-F). As seen in Fig. 5D, the majority of *tes-1(ok1036)* embryos display decreased junctional-proximal actin. Additionally, we also observed more severe phenotypes, including gaps between CFBs, CFB collapse, and complete loss of preserved junctional-proximal actin (Fig. 5E). These defects are consistent with TES-1 preventing damage to junctional actin networks subjected to high strain during embryonic elongation.

Mammalian LIM domain proteins are recruited to strained actin networks via their LIM domain-containing region [2, 3, 24]. Since removal of the LIM domains of TES-1 results in loss of recruitment to junctional actin networks in the epidermis, we tested whether the LCR of TES-1 behaves similarly. When transfected into mouse embryonic fibroblasts, TES-1(LIM1-3)::mCherry is recruited to damaged actin bundles, indicating that it behaves in a manner similar to other LIM domain proteins in this assay. Compared with the LCR of *M. musculus* zyxin in the same assay, recruitment is less pronounced, but significant (Fig. 5G), as is true for vertebrate Tes

.

Taken together, our results are consistent with a model in which actomyosin-mediated tension generated in elongating embryos leads to strain-dependent recruitment of TES-1 to junctions during elongation, stabilizing them against the rigors of mechanical stress during morphogenesis. In this sense, elongating epidermal cells in the *C. elegans* embryo are subject to "self-injury", as they must remodel their junctional-proximal actin networks during the dramatic

change in shape that these cells undergo. It is likely that LIM-domain dependent stabilization of junctional proximal actin filaments is only one component of an apparatus that stabilizes and repairs such filaments. For example, our previous experiments indicated that UNC-94/tropmodulin is recruited to the same junctions, where it presumably protects minus ends of F-actin filaments from subunit loss [33]. Recruitment of TES-1 to these same junctions could stabilize CCC-dependent actin networks by allowing strained F-actin at the CCC to self-heal, by recruiting additional F-actin to these networks, or both.

Materials and Methods

Nematode Strains and Genetics

C. elegans strains were maintained using standard methods [48]. Bristol N2 was used as wildtype. The following alleles were utilized in this study. LGI: *hmp-2(qm39); let-502(sb118);* LGII: *zyx-1(gk190); mel-11(it26);* LGIV: *tes-1(ok1036);* LGV: *hmp-1(fe4).* The following transgenic arrays were made for this study: *tes-1::gfp*, *tes-1ΔPET::gfp*, *tes-1ΔLIM1::gfp*, *tes-1ΔLIM2::gfp*, *tes-1ΔLIM3::gfp*, *tes-1ΔLIM1-3::gfp*. Each of the *tes-1* constructs contained 5kb of endogenous promoter.

Plasmids

A ~5kb genomic sequence containing 2kb promoter and entire genomic region of *tes-1* was PCR amplified using Phusion polymerase (NEB). The primers used were: 5' GCGTCGACGAGTTTTTGTCAAGAGTAAGAC and 3' GCCCCGGGATCAACTGATCATCCGGATTCG. The PCR product was digested with *SalI* and *SmaI* and ligated into a similarly digested Fire lab vector pPD95.75, which contains the GFP

sequence. A frameshift was repaired via PCR to generate a *Ptes-1(2kb)::tes-1::gfp* construct (pAML224). To generate *Ptes-1(5kb)::tes-1::gfp*, additional promoter sequence was PCR amplified using Phusion polymerase. The primers used were:
5' GCCTGCAGGAAGACAACGCTTGTCAAGAAT and
3' GCGTCGACATTTTGCCCTCGAAATGCAATAC. The PCR product and pAML224 were digested using *PstI* and *SalI* and ligated together to generate pAML224v2. The identity of pAML224v2 was confirmed via sequencing. Domain deletions were performed using circle PCR as described previously [35].

Microinjection

DNA was microinjected into worms as described previously [49]. Briefly, injection mixes consisting of 5ng/µl of transgenic *tes-1* DNA constructs, 20 ng/µl of junk DNA (F35D3) and 75 ng/µl of *rol-6(su1006)* transgenic marker DNA were microinjected into both gonads of hermaphrodites. Progeny were screened for the presence of *rol-6(su1006)*, and stable lines were established by passaging of worms.

Injection RNA interference was performed as described previously [50]. dsRNA was generated using an Ambion T7 and/or T3 Megascript kits; templates included yk662b10 (*hmr-1*), yk285a2 (*ajm-1*), yk1054c06 (*zyx-1*), yk282d2 (*zoo-1*) (NEXTDB, http://nematode.lab.nig.ac.jp/).

Antibody and Phalloidin Staining

Immunostaining was performed using freeze-cracking [51]. Staining was performed as described previously [52]. Embryos were mounted onto poly-L-lysine-coated ring slides and incubated with primary antibodies in PBST and 5% non-fat dry milk overnight at 4°C. Embryos were then

incubated with secondary antibodies in PBST and 5% non-fat dry milk for approximately three hours at room temperature. The following primary antibodies were used: 1:1000 mouse-anti-GFP (Invitrogen), 1:1000 rabbit-anti-GFP, 1:4000 polyclonal rabbit-anti-HMP-1, 1:4000 polyclonal rabbit-anti-HMR-1 and 1:200 monoclonal mouse-anti-AJM-1 (MH27). The following secondary antibodies were used: 1:50 anti-rabbit IgG Texas Red, 1:50 anti-rabbit FITC, 1:50 anti-mouse Texas Red and 1:50 anti-mouse FITC.

Phalloidin staining of mutant and wild-type embryos was used to visualize actin in fixed embryos [27]. Embryos were mounted on poly-L-lysine-coated ring slides and fixed using the following: 4% paraformaldehyde, 0.1 mg/mL lysolecithin, 48 mM Pipes pH 6.8, 25 mM Hepes pH 6.8, 2 mM $MgCl_2$, and 10 mM EGTA for 20 minutes at room temperature. 1:20 Phalloidin-488 was incubated with embryos at room temperature for 90 minutes. Images of stained embryos were acquired as described below.

For co-immunostaining and phalloidin staining, embryos were gathered in a 1.5 mL Eppendorf tube and permeabilized with a solution of 4% paraformaldehyde, 10% Triton-X-100, 48 mM Pipes pH 6.8, 25 mM Hepes pH 6.8, 2 mM $MgCl_2$ and 10mM EGTA for 20 minutes at room temperature. Embryos were incubated overnight in PBST+5% dry milk+1:1000 rabbit-anti-GFP at 4C on a nutator. Secondary antibodies (1:10 Phalloidin-666 and 1:50 anti-rabbit FITC) were incubated for 2 hours at room temperature. Images of stained embryos were acquired as described below.

Confocal Microscopy

Spinning-disc confocal images were acquired with a Z-slice spacing of 0.2μm for imaging of actin, 0.3 μm for embryos stained for both GFP and actin, and 0.5μm for all other imaging using either Perkin Elmer Ultraview or Micromanager software [53, 54] and a Nikon Eclipse E600 microscope connected to a Yokogawa CSU10 spinning disk scanhead and a Hamamatsu ORCA-ER charge-coupled device (CCD) camera. Junctional/cytoplasmic signal measurements were performed as described previously [55]. Fisher's exact test calculations were performed online at https://www.socscistatistics.com/tests/fisher/default2.aspx; other statistical analyses were performed using GraphPad Prism v. 9.0 software (GraphPad Software, San Diego, California USA, www.graphpad.com).

DIC Imaging

Four dimensional DIC movies were gathered on either a Nikon Optiphot-2 connected to a QImaging camera or an Olympus BX5 connected to a Scion camera. Mounts were made as previously described (Raich et al., 1999). ImageJ plugins (http://worms.zoology.wisc.edu/research/4d/4d.html) were used to compress and view movies.

Protein Expression and Purification

GST- and SUMO-His-tagged proteins were expressed in BL21-Gold(DE3) *Escherichia coli* cells and purified as described [47, 56]. Cells were induced with 0.1mM IPTG at 18°C for 16 hours. Wash and elution buffers were as follows: GST wash (1X PBS, 500mM NaCl, 0.1% Tween-20, and 1mM DTT), GST elution (50mM Tris pH 8.0, 0.3% glutathione, 150mM NaCl), His wash (50mM Na-Phosphate pH 8.0, 300mM NaCl, 0.1% Tween-20, 10mM Imidazole), and His elution (250mM Imidazole, 100mM NaCl, 10% glycerol, 50mM Hepes pH 7.6). For actin-

pelleting assays, the GST tag was cleaved from GST-TES-1 using ProTEV Plus (Promega), according to manufacturer's instructions.

Directed Yeast Two-Hybrid Assays

Yeast two-hybrid assays were performed as in [35]. Either full-length HMP-1 or HMP-2 yeast two-hybrid plasmid [57] was transformed into Y2H Gold yeast singly or with a plasmid encoding full-length ZYX-1 [58]. Positive single transformants were tested for autoactivation, and double transformants were patched onto SD/-Leu/-Trp/X-α–gal/AurA plates. Colonies that grew and turned blue were considered positive for a direct interaction.

Actin-Pelleting Assays

Actin co-sedimentation assays were performed as described previously [47]. Briefly, 5μM purified, cleaved proteins (quantified via a Bradford Assay) were incubated at room temperature for one hour with 0 or 5μM polymerized chicken F-actin (Cytoskeleton, Inc.). BSA was used a negative control, and SUMO-His-HMP-1 [39] was used as a positive control. Samples were then centrifuged at 100,000 rpm for 20 min at 4°C in a TLA-120.1 rotor using a Beckman Optima tabletop ultracentrifuge. Samples were run on 12% SDS-PAGE gels, stained with Coomassie Brilliant Blue, and bands were quantified using ImageJ.

Co-immunoprecipitations and Western Blots

C. elegans expressing TES-1::GFP were grown in liquid culture as previously described [59]. Co-immunoprecipitations were completed as in [33]. Western blots were performed as described previously [60], using rabbit anti-GFP, rabbit anti-HMP-1 [39] and mouse anti-ZYX-1 [58] primary antibodies and Li-COR IRDye® secondary antibodies to detect proteins.

Stress fiber strain site assay

A *tes-1 LCR::mCherry* construct was designed and expressed using the procedures described in detail in [2]. Briefly, a synthetic gBlock DNA encoding a mammalian codon-optimized version of the LIM1-3 domain of TES-1 was ordered from IDT (Coralville, Iowa) and cloned into a CMV-driven expression vector that fused the C-terminus of LCR(Tes) to mCherry, and used to transfect zyxin $^{-/-}$ mouse embryo fibroblast cells (MEFs) rescued with stably integrated GFP-zyxin. Transfected MEFs were imaged on an inverted Nikon Ti-E microscope (Nikon, Melville, NY) with a Yokogawa CSU-X confocal scanhead and Zyla 4.2 sCMOS Camera (Andor, Belfast, UK). A 405 nm laser coupled to a Mosaic digital micromirror device (Andor) was used to locally damage stress fibers. Kymography of TES-1(LIM1-3)::GFP was performed using ImageJ as described in [2].

References

1. Smith, M.A., Hoffman, L.M., and Beckerle, M.C. (2014). LIM proteins in actin cytoskeleton mechanoresponse. Trends Cell Biol *24*, 575-583.

2. Winkelman, J.D., Anderson, C.A., Suarez, C., Kovar, D.R., and Gardel, M.L. (2020). Evolutionarily diverse LIM domain-containing proteins bind stressed actin filaments through a conserved mechanism. Proc Natl Acad Sci U S A.

3. Sun, X., Phua, D.Y.Z., Axiotakis, L., Jr., Smith, M.A., Blankman, E., Gong, R., Cail, R.C., Espinosa de Los Reyes, S., Beckerle, M.C., Waterman, C.M., et al. (2020). Mechanosensing through Direct Binding of Tensed F-Actin by LIM Domains. Dev Cell *55*, 468-482 e467.

4. Charras, G., and Yap, A.S. (2018). Tensile Forces and Mechanotransduction at Cell-Cell Junctions. Curr Biol *28*, R445-R457.

5. Mege, R.M., and Ishiyama, N. (2017). Integration of Cadherin Adhesion and Cytoskeleton at Adherens Junctions. Cold Spring Harb Perspect Biol *9*.

6. Pinheiro, D., and Bellaiche, Y. (2018). Mechanical Force-Driven Adherens Junction Remodeling and Epithelial Dynamics. Dev Cell *47*, 3-19.

7. Wickstrom, S.A., and Niessen, C.M. (2018). Cell adhesion and mechanics as drivers of tissue organization and differentiation: local cues for large scale organization. Curr Opin Cell Biol *54*, 89-97.

8. Coutts, A.S., MacKenzie, E., Griffith, E., and Black, D.M. (2003). TES is a novel focal adhesion protein with a role in cell spreading. J Cell Sci *116*, 897-906.

9. Garvalov, B.K., Higgins, T.E., Sutherland, J.D., Zettl, M., Scaplehorn, N., Köcher, T., Piddini, E., Griffiths, G., and Way, M. (2003). The conformational state of Tes regulates its zyxin-dependent recruitment to focal adhesions. J Cell Biol *161*, 33-39.

10. Oldenburg, J., van der Krogt, G., Twiss, F., Bongaarts, A., Habani, Y., Slotman, J.A., Houtsmuller, A., Huveneers, S., and de Rooij, J. (2015). VASP, zyxin and TES are tension-dependent members of Focal Adherens Junctions independent of the α-catenin-vinculin module. Sci Rep *5*, 17225.

11. Hadzic, E., Catillon, M., Halavatyi, A., Medves, S., Van Troys, M., Moes, M., Baird, M.A., Davidson, M.W., Schaffner-Reckinger, E., Ampe, C., et al. (2015). Delineating the Tes Interaction Site in Zyxin and Studying Cellular Effects of Its Disruption. PLoS One *10*, e0140511.

12. Zhong, Y., Zhu, J., Wang, Y., Zhou, J., Ren, K., Ding, X., and Zhang, J. (2009). LIM domain protein TES changes its conformational states in different cellular compartments. Mol Cell Biochem *320*, 85-92.

13. Sala, S., Catillon, M., Hadzic, E., Schaffner-Reckinger, E., Van Troys, M., and Ampe, C. (2017). The PET and LIM1-2 domains of testin contribute to intramolecular and homodimeric interactions. PLoS One *12*, e0177879.

14. Griffith, E., Coutts, A.S., and Black, D.M. (2004). Characterisation of chicken TES and its role in cell spreading and motility. Cell Motil Cytoskeleton *57*, 133-142.

15. Ren, D.D., Kelly, M., Kim, S.M., Grimsley-Myers, C.M., Chi, F.L., and Chen, P. (2013). Testin interacts with vangl2 genetically to regulate inner ear sensory cell orientation and the normal development of the female reproductive tract in mice. Dev Dyn *242*, 1454-1465.

16. Beckerle, M.C. (1986). Identification of a new protein localized at sites of cell-substrate adhesion. J Cell Biol *103*, 1679-1687.

17. Crawford, A.W., and Beckerle, M.C. (1991). Purification and characterization of zyxin, an 82,000-dalton component of adherens junctions. J Biol Chem *266*, 5847-5853.

18. Hansen, M.D., and Beckerle, M.C. (2006). Opposing roles of zyxin/LPP ACTA repeats and the LIM domain region in cell-cell adhesion. J Biol Chem *281*, 16178-16188.

19. Lee, N.P., Mruk, D.D., Conway, A.M., and Cheng, C.Y. (2004). Zyxin, axin, and Wiskott-Aldrich syndrome protein are adaptors that link the cadherin/catenin protein complex to the cytoskeleton at adherens junctions in the seminiferous epithelium of the rat testis. J Androl *25*, 200-215.

20. Macalma, T., Otte, J., Hensler, M.E., Bockholt, S.M., Louis, H.A., Kalff-Suske, M., Grzeschik, K.H., von der Ahe, D., and Beckerle, M.C. (1996). Molecular characterization of human zyxin. J Biol Chem *271*, 31470-31478.

21. Nguyen, T.N., Uemura, A., Shih, W., and Yamada, S. (2010). Zyxin-mediated actin assembly is required for efficient wound closure. J Biol Chem *285*, 35439-35445.

22. Vasioukhin, V., Bauer, C., Yin, M., and Fuchs, E. (2000). Directed actin polymerization is the driving force for epithelial cell-cell adhesion. Cell *100*, 209-219.

23. Smith, M.A., Blankman, E., Deakin, N.O., Hoffman, L.M., Jensen, C.C., Turner, C.E., and Beckerle, M.C. (2013). LIM domains target actin regulators paxillin and zyxin to sites of stress fiber strain. PLoS One *8*, e69378.

24. Smith, M.A., Blankman, E., Gardel, M.L., Luettjohann, L., Waterman, C.M., and Beckerle, M.C. (2010). A zyxin-mediated mechanism for actin stress fiber maintenance and repair. Dev Cell *19*, 365-376.

25. Yoshigi, M., Hoffman, L.M., Jensen, C.C., Yost, H.J., and Beckerle, M.C. (2005). Mechanical force mobilizes zyxin from focal adhesions to actin filaments and regulates cytoskeletal reinforcement. J Cell Biol *171*, 209-215.

26. Williams-Masson, E.M., Malik, A.N., and Hardin, J. (1997). An actin-mediated two-step mechanism is required for ventral enclosure of the *C. elegans* hypodermis. Development *124*, 2889-2901.

27. Costa, M., Raich, W., Agbunag, C., Leung, B., Hardin, J., and Priess, J.R. (1998). A putative catenin-cadherin system mediates morphogenesis of the Caenorhabditis elegans embryo. J Cell Biol *141*, 297-308.

28. Priess, J.R., and Hirsh, D.I. (1986). Caenorhabditis elegans morphogenesis: the role of the cytoskeleton in elongation of the embryo. Dev Biol *117*, 156-173.

29. Gally, C., Wissler, F., Zahreddine, H., Quintin, S., Landmann, F., and Labouesse, M. (2009). Myosin II regulation during *C. elegans* embryonic elongation: LET-502/ROCK, MRCK-1 and PAK-1, three kinases with different roles. Development *136*, 3109-3119.

30. Chisholm, A.D., and Hardin, J. (2005). Epidermal morphogenesis. WormBook, 1-22.

31. Vuong-Brender, T.T., Yang, X., and Labouesse, M. (2016). *C. elegans* Embryonic Morphogenesis. Curr Top Dev Biol *116*, 597-616.

32. Vuong-Brender, T.T., Ben Amar, M., Pontabry, J., and Labouesse, M. (2017). The interplay of stiffness and force anisotropies drives embryo elongation. Elife *6*.

33. Cox-Paulson, E.A., Walck-Shannon, E., Lynch, A.M., Yamashiro, S., Zaidel-Bar, R., Eno, C.C., Ono, S., and Hardin, J. (2012). Tropomodulin protects alpha-catenin-dependent junctional-actin networks under stress during epithelial morphogenesis. Curr Biol *22*, 1500-1505.

34. Lockwood, C., Zaidel-Bar, R., and Hardin, J. (2008). The *C. elegans* zonula occludens ortholog cooperates with the cadherin complex to recruit actin during morphogenesis. Curr Biol *18*, 1333-1337.

35. Lynch, A.M., Grana, T., Cox-Paulson, E., Couthier, A., Cameron, M., Chin-Sang, I., Pettitt, J., and Hardin, J. (2012). A Genome-wide Functional Screen Shows MAGI-1 Is an L1CAM-Dependent Stabilizer of Apical Junctions in *C. elegans*. Curr Biol *22*, 1891-1899.

36. Zaidel-Bar, R., Joyce, M.J., Lynch, A.M., Witte, K., Audhya, A., and Hardin, J. (2010). The F-BAR domain of SRGP-1 facilitates cell-cell adhesion during *C. elegans* morphogenesis. J Cell Biol *191*, 761-769.

37. Kang, H., Bang, I., Weis, W.I., and Choi, H.J. (2016). Purification, crystallization and initial crystallographic analysis of the α-catenin homologue HMP-1 from Caenorhabditis elegans. Acta Crystallogr F Struct Biol Commun *72*, 234-239.

38. Sala, S., Van Troys, M., Medves, S., Catillon, M., Timmerman, E., Staes, A., Schaffner-Reckinger, E., Gevaert, K., and Ampe, C. (2017). Expanding the Interactome of TES by

Exploiting TES Modules with Different Subcellular Localizations. J Proteome Res *16*, 2054-2071.

39. Callaci, S., Morrison, K., Shao, X., Schuh, A.L., Wang, Y., Yates, J.R., Hardin, J., and Audhya, A. (2015). Phosphoregulation of the *C. elegans* cadherin-catenin complex. Biochem J *472*, 339-352.

40. Luo, S., Schaefer, A.M., Dour, S., and Nonet, M.L. (2014). The conserved LIM domain-containing focal adhesion protein ZYX-1 regulates synapse maintenance in Caenorhabditis elegans. Development *141*, 3922-3933.

41. Benjamin, J.M., Kwiatkowski, A.V., Yang, C., Korobova, F., Pokutta, S., Svitkina, T., Weis, W.I., and Nelson, W.J. (2010). AlphaE-catenin regulates actin dynamics independently of cadherin-mediated cell-cell adhesion. J Cell Biol *189*, 339-352.

42. Drees, F., Pokutta, S., Yamada, S., Nelson, W.J., and Weis, W.I. (2005). Alpha-catenin is a molecular switch that binds E-cadherin-beta-catenin and regulates actin-filament assembly. Cell *123*, 903-915.

43. Griffith, E., Coutts, A.S., and Black, D.M. (2005). RNAi knockdown of the focal adhesion protein TES reveals its role in actin stress fibre organisation. Cell Motil Cytoskeleton *60*, 140-152.

44. Piekny, A.J., Johnson, J.L., Cham, G.D., and Mains, P.E. (2003). The Caenorhabditis elegans nonmuscle myosin genes nmy-1 and nmy-2 function as redundant components of the let-502/Rho-binding kinase and mel-11/myosin phosphatase pathway during embryonic morphogenesis. Development *130*, 5695-5704.

45. Wissmann, A., Ingles, J., and Mains, P.E. (1999). The Caenorhabditis elegans mel-11 myosin phosphatase regulatory subunit affects tissue contraction in the somatic gonad and the embryonic epidermis and genetically interacts with the Rac signaling pathway. Dev Biol *209*, 111-127.

46. Wissmann, A., Ingles, J., McGhee, J.D., and Mains, P.E. (1997). Caenorhabditis elegans LET-502 is related to Rho-binding kinases and human myotonic dystrophy kinase and interacts genetically with a homolog of the regulatory subunit of smooth muscle myosin phosphatase to affect cell shape. Genes Dev *11*, 409-422.

47. Maiden, S.L., Harrison, N., Keegan, J., Cain, B., Lynch, A.M., Pettitt, J., and Hardin, J. (2013). Specific conserved C-terminal amino acids of Caenorhabditis elegans HMP-1/α-catenin modulate F-actin binding independently of vinculin. J Biol Chem *288*, 5694-5706.

48. Brenner, S. (1974). The genetics of Caenorhabditis elegans. Genetics *77*, 71-94.

49. Mello, C., and Fire, A. (1995). Chapter 19 DNA Transformation. In Cuenorhubditis elegans: Modern Biologcal Analysis of an Organism. (Elsevier BV), pp. 451-482.

50. Walston, T., Tuskey, C., Edgar, L., Hawkins, N., Ellis, G., Bowerman, B., Wood, W., and Hardin, J. (2004). Multiple Wnt signaling pathways converge to orient the mitotic spindle in early *C. elegans* embryos. Dev Cell *7*, 831-841.

51. Albertson, D.G. (1984). Formation of the first cleavage spindle in nematode embryos. Developmental Biology *101*, 61-72.

52. Leung, B., Hermann, G.J., and Priess, J.R. (1999). Organogenesis of the Caenorhabditis elegans Intestine. Developmental Biology *216*, 114-134.

53. Edelstein, A., Amodaj, N., Hoover, K., Vale, R., and Stuurman, N. (2010). Computer Control of Microscopes Using μManager. In Current Protocols in Molecular Biology. (Wiley-Blackwell).

54. Edelstein, A.D., Tsuchida, M.A., Amodaj, N., Pinkard, H., Vale, R.D., and Stuurman, N. (2014). Advanced methods of microscope control using μManager software. Journal of Biological Methods *1*, 10.

55. Shao, X., Lucas, B., Strauch, J., and Hardin, J. (2019). The adhesion modulation domain of Caenorhabditis elegans alpha-catenin regulates actin binding during morphogenesis. Mol Biol Cell *30*, 2115-2123.

56. Mayers, J.R., Fyfe, I., Schuh, A.L., Chapman, E.R., Edwardson, J.M., and Audhya, A. (2011). ESCRT-0 assembles as a heterotetrameric complex on membranes and binds multiple ubiquitinylated cargoes simultaneously. J Biol Chem *286*, 9636-9645.

57. Kwiatkowski, A.V., Maiden, S.L., Pokutta, S., Choi, H.J., Benjamin, J.M., Lynch, A.M., Nelson, W.J., Weis, W.I., and Hardin, J. (2010). In vitro and in vivo reconstitution of the cadherin-catenin-actin complex from Caenorhabditis elegans. Proc Natl Acad Sci U S A *107*, 14591-14596.

58. Lecroisey, C., Brouilly, N., Qadota, H., Mariol, M.C., Rochette, N.C., Martin, E., Benian, G.M., Ségalat, L., Mounier, N., and Gieseler, K. (2013). ZYX-1, the unique zyxin protein of Caenorhabditis elegans, is involved in dystrophin-dependent muscle degeneration. Mol Biol Cell *24*, 1232-1249.

59. Stiernagle, T. (2006). Maintenance of *C. elegans*. WormBook, 1-11.

60. Zhang, Y., Wang, X., Matakatsu, H., Fehon, R., and Blair, S.S. (2016). The novel SH3 domain protein Dlish/CG10933 mediates fat signaling in Drosophila by binding and regulating Dachs. Elife *5*.

Figure 1: TES-1 loss enhances phenotypes in hypomorphic CCC backgrounds. A. Protein domain maps of *C. elegans* TES-1 and human Tes. TES-1 and Tes both contain N-terminal Prickle, Espinas, Testin (PET) domains and three C-terminal Lin-11, Isl-1, Mec-3 (LIM) domains. The *tes-1*(*ok1036*) allele removes LIM1-2 along with some intronic sequence and introduces a frameshift into the remainder of the coding region. **B-D.** *tes-1*(RNAi) enhances the severity of morphogenetic defects in *hmp-1*(*fe4*) embryos. **B.** Wild-type embryo imaged using Nomarski microscopy. **C.** *hmp-1*(*fe4*) embryo; bulges become apparent during embryonic elongation (t = 3 hr). **D.** In *hmp-1*(*fe4*);*tes-1*(RNAi) embryos, cells leak out of the ventral midline (t = 1 hr), and all embryos die with sever elongation defects (t = 3 hr). **E-G.** *tes-1*(RNAi) enhances the severity of actin defects in *hmp-1*(*fe4*) embryos. **E.** Wild-type embryos maintain a population of junctional proximal actin along cell borders (white arrow) and dorsal and ventral epidermal cells in elongated embryos contain circumferential actin filament bundles (CFBs) that are evenly spaced. Bright signal is muscle, denoted by yellow arrowheads. **F.** *hmp-1*(*fe4*) embryos also typically maintain junctional proximal actin (white arrow); however, their CFBs are less evenly spaced, and sometimes clump together (white arrowhead). **G.** *hmp-1*(*fe4*); *tes-1*(RNAi) embryos display clumping of CFBs, and also a complete lack of junctional proximal actin. CFBs appear to have been torn away from the junction, leaving bare zones devoid of F-actin (white arrow). Scale bar = 5 μm. **H.** TES-1 binds to F-actin in an actin co-sedimentation assay. Full-length TES-1 remains in the supernatant fraction (S) when incubated without F-actin. However, TES-1 is detected in the pellet fraction (P) when incubated with 5 mM F-actin. **I.** Quantification of TES-1 found in the pellet after incubation with F-actin. Bovine Serum Albumin (BSA) served as a negative control and SUMO:HMP-1 as a positive control. TES-1 bound to F-actin significantly more than did BSA (two replicates; **p < = 0.01, unpaired Student's T test).

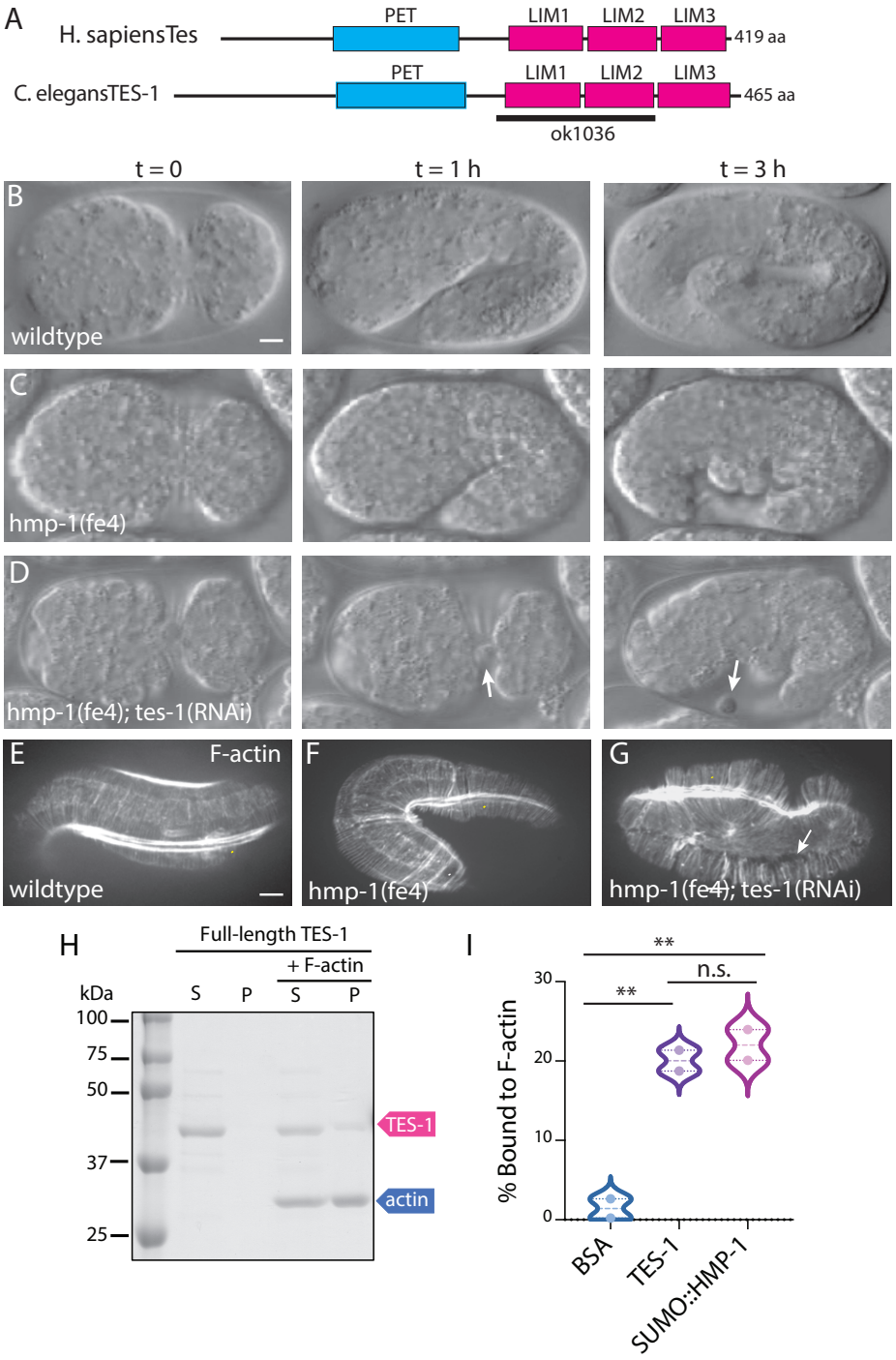
A
H. sapiensTes
PET
LIM1
LIM2
LIM3
419 aa
C. elegansTES-1
465 aa
ok1036
t = 0
t = 1 h
t = 3 h
B
wildtype
C
hmp-1(fe4)
D
hmp-1(fe4); tes-1(RNAi)
E
F-actin
wildtype
F
hmp-1(fe4)
G
hmp-1(fe4); tes-1(RNAi)
H
Full-length TES-1
+ F-actin
kDa
S
P
S
P
100
75
50
37
25
TES-1
actin
I
**
n.s.
**
30
20
10
0
% Bound to F-actin
BSA
TES-1
SUMO::HMP-1

Figure 2: TES-1 localizes to sites of cell-cell attachment during embryonic elongation.

A. Schematic of the full-length TES-1::GFP used in this study, along with TES-1::GFP is driven by its full-length endogenous promoter and contains a C-terminal GFP. **B.** Expression of TES-1::GFP is initially cytoplasmic, but as elongation proceeds, TES-1::GFP localizes to cell-cell junctions, first in puncta and then strongly to seam-dorsal and seam-ventral boundaries. Scale bar = 5 μm. **C-D.** TES-1::GFP co-localizes with HMR-1 but not AJM-1. Insets show magnifications of boxed regions. While HMR-1 and TES-1::GFP largely co-localize, TES-1::GFP and AJM-1 do not. **E.** *ajm-1* (RNAi) does not influence the ability of TES-1::GFP to localize to junctions (arrows). Scale bar = 5 μm. **F.** *hmr-1*(RNAi) completely prevents TES-1::GFP localization at junctions (arrow); however, the embryos never elongate to the point at which TES-1::GFP normally localizes. **G.** *zyx-1*(*gk190*); *tes-1::gfp* embryos show persistent seam-seam junctional localization in addition to the normal seam-dorsal and seam-ventral localization (arrow). **H.** TES-1 is recruited to junctions during elongation. Junctional/cytoplasmic ratio of TES-1::GFP at 1.5-fold and >=2.5-fold. *, $p < 0.05$ (Mann-Whitney U

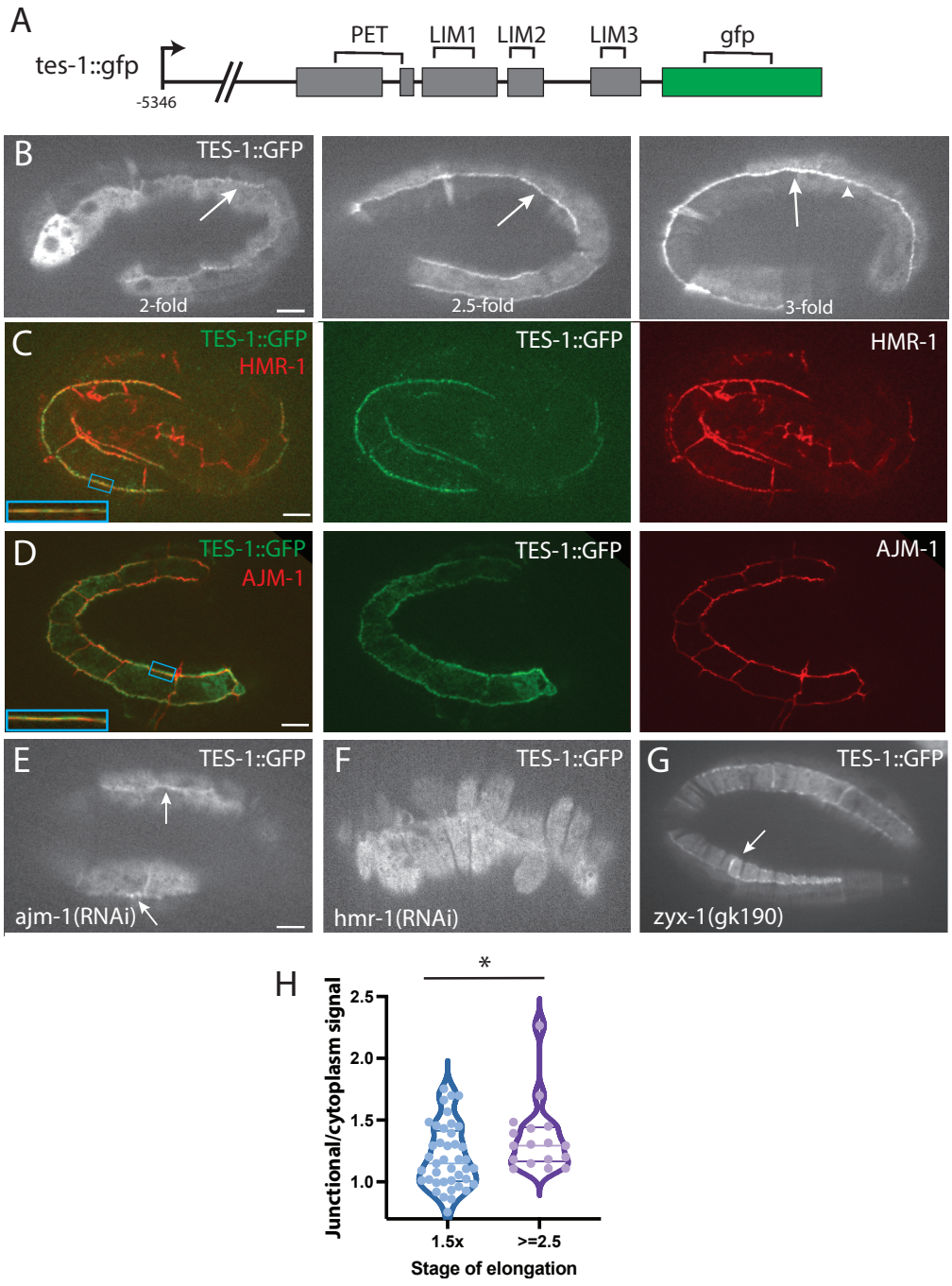
A
tes-1::gfp
-5346
PET
LIM1
LIM2
LIM3
gfp
B
TES-1::GFP
2-fold
2.5-fold
3-fold
C
TES-1::GFP
HMR-1
TES-1::GFP
HMR-1
D
TES-1::GFP
AJM-1
TES-1::GFP
AJM-1
E
TES-1::GFP
ajm-1(RNAi)
F
TES-1::GFP
hmr-1(RNAi)
G
TES-1::GFP
zyx-1(gk190)
H
*
Junctional/cytoplasm signal
2.5
2.0
1.5
1.0
1.5x
>=2.5
Stage of elongation

Figure 3: TES-1 localization requires its PET and LIM2-3 domains. For relevant domains of TES-1, see **Figure 1A**. **A.** Full-length TES-1::GFP localizes to dorsal:seam and ventral:seam cell boundaries in the epidermis (arrow). **B.** Unlike full-length TES-1**::**GFP, TES-1DPET::GFP localizes along all seam cell borders in the epidermis, including seam-seam borders (arrows). Deletion of LIM1 **C** or LIM2 **D** both perturb junctional localization similarly: each localizes sporadically to epidermal junctions, including some seam-seam junctions. However, there is also localization at what appeared to be actin-containing structures in epidermal cells. **E.** Deletion of LIM3 rendered the GFP entirely cytoplasmic. **F.** Deletion of all three LIM domains simultaneously resulted in GFP localization along structures that appear to be CFBs. **G.** Rescue of embryonic lethality in progeny of *tes-1(ok1036)/+;hmp-1(fe4)/hmp-1(fe4)* hermaphrodites. ***** = significantly different from non-transgenic animals ($p < 0.05$, Fisher's exact test).

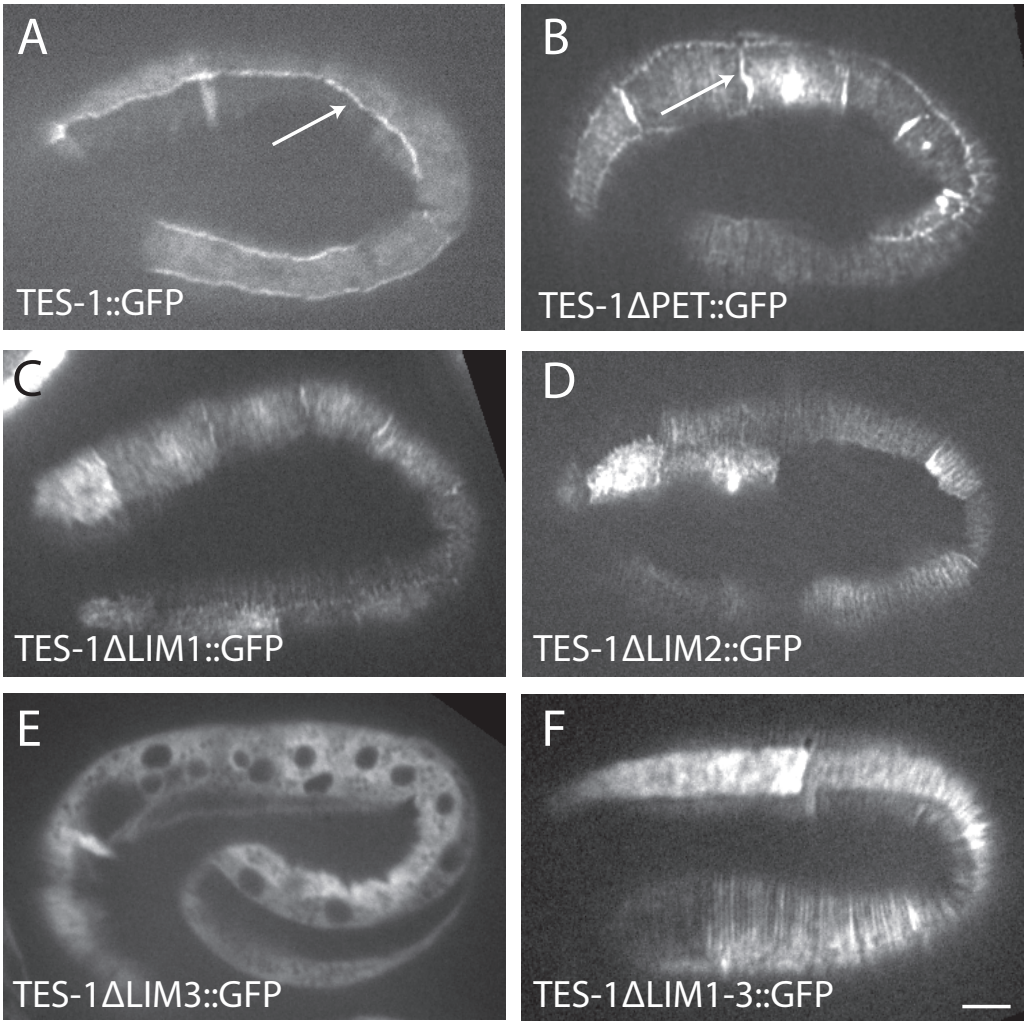

G

Transgene*	Dead embryos	Larvae	% dead
ok1036/+;fe4	30	46	39.5
+ ΔPET	24	98	19.7**
+ ΔLIM1-3	23	46	33.3
+ ΔLIM2	27	54	33.3
+ ΔLIM3	58	110	34.5

*Stable lines could not be recovered for ΔLIM1; see Results
**Significantly different, $p < 0.05$, Fisher's Exact Test

Figure 4: TES-1::GFP localizes to junctions in a tension-dependent manner. A. In *hmp-1(fe4)* embryos that successfully elongate to two-fold, TES-1::GFP accumulates along seam cell junctions (white arrow). **B.** In *hmp-1(fe4)* embryos that do not elongate past 1.5-fold before failing, TES-1::GFP does not localize to junctions, instead remaining entirely cytoplasmic. **C.** In *let-502(sb118ts); tes-1::gfp* embryos reared at the permissive temperature ("unshifted"), development is normal and TES-1::GFP localizes to junctions as in wildtype. **D.** In temperature-shifted embryos, the LET-502 protein is inactivated, embryos fail to elongate, and TES-1::GFP never accumulates along epidermal junctions. **E.** In *mel-11(RNAi); tes-1::gfp* embryos, the embryos elongate normally, and TES-1::GFP junctional localization is not impacted. **F.** Upon depletion of *mel-11*, the worms elongate past their normal four-fold length. TES-1::GFP localizes to junctions, however it appears as though it is being pulled away from junctions in long extensions from epidermal cell borders. Scale bars = 5 μm.

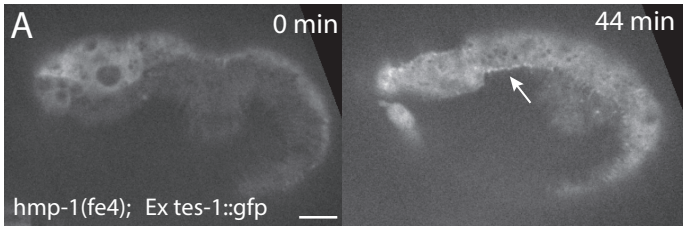
A
0 min
44 min
hmp-1(fe4); Ex tes-1::gfp

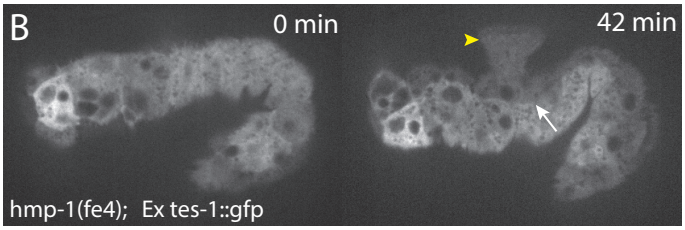
B
0 min
42 min
hmp-1(fe4); Ex tes-1::gfp

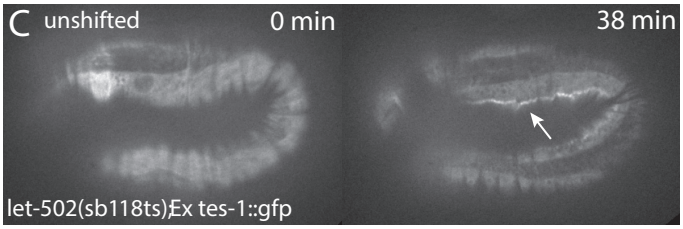
C unshifted
0 min
38 min
let-502(sb118ts)Ex tes-1::gfp

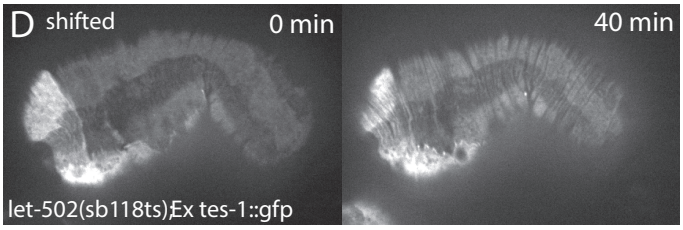
D shifted
0 min
40 min
let-502(sb118ts)Ex tes-1::gfp

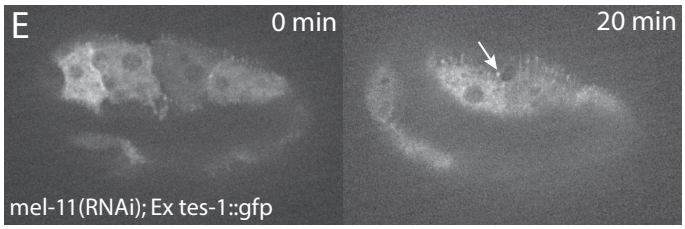
E
0 min
20 min
mel-11(RNAi); Ex tes-1::gfp

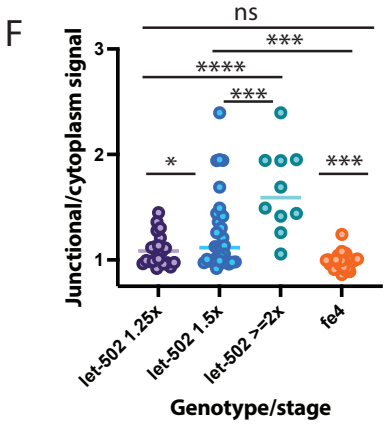
F
ns
***
****
***
*
***
Junctional/cytoplasm signal
3
2
1
let-502 1.25x
let-502 1.5x
let-502 >=2x
fe4
Genotype/stage

Figure 5: TES-1 regulates actin networks *in vivo* and is recruited to strained actin filaments. **A-D.** Fixed and phalloidin stained embryos. Bright staining is muscle (arrowhead). Scale bar is 5 μm.**A.** Wild-type embryos exhibit parallel circumferential filament bundles (CFBs, blue box inset) and retain junctional-proximal actin (green box inset). **B.** Approximately half the *tes-1(ok1036)* embryos exhibit reduced junctional-proximal actin although CFB organization looks normal. **C.** *ok1036* embryos also exhibit more severe phenotypes including gaps and clumping of CFBs (blue box) and a complete loss of junctional-proximal actin (green box). **D.** Quantification of phalloidin staining phenotypes. Class 1 embryos have normal CFBs and junctional-proximal actin. Class 2 embryos have reduced junctional-proximal actin. Class 3 embryos have reduced junctional-proximal actin and CFB organization defects and Class 4 embryos have no retained junctional-proximal actin and CFB organization defects. **E-H.** Recruitment of the TES-1 LCR::mCherry to stress fiber strain sites (SFSS) in transfected mouse embryonic fibroblasts. **E.** Schematic of the experiment (adapted from [2]). Irradiated stress fibers under strain recruit LCR proteins, which are visible as a zone of recruitment in kymographs. **F.** Representative kymographs of laser-induced recruitment of the TES-1 LCR::mCherry and mouse GFP ::Zyxin to SFSS. White dashed and gray solid lines indicate where fluorescence and distance were measured . Dashed gray vertical line indicates t_0, when strain is first observed **H.** Quantification of GFP and mCherry accumulation over time in the kymograph from **G**. **H.** LCR mCherry/GFP ratio for MmZyx (red) and TES-1 LCR (green). TES-1 LCR accumulates markedly ($p=0.23$, $n>10$; Student's T-test, equal variance not assumed) but to a lesser extent than MmZyx; error bars indicate 95% confidence intervals.

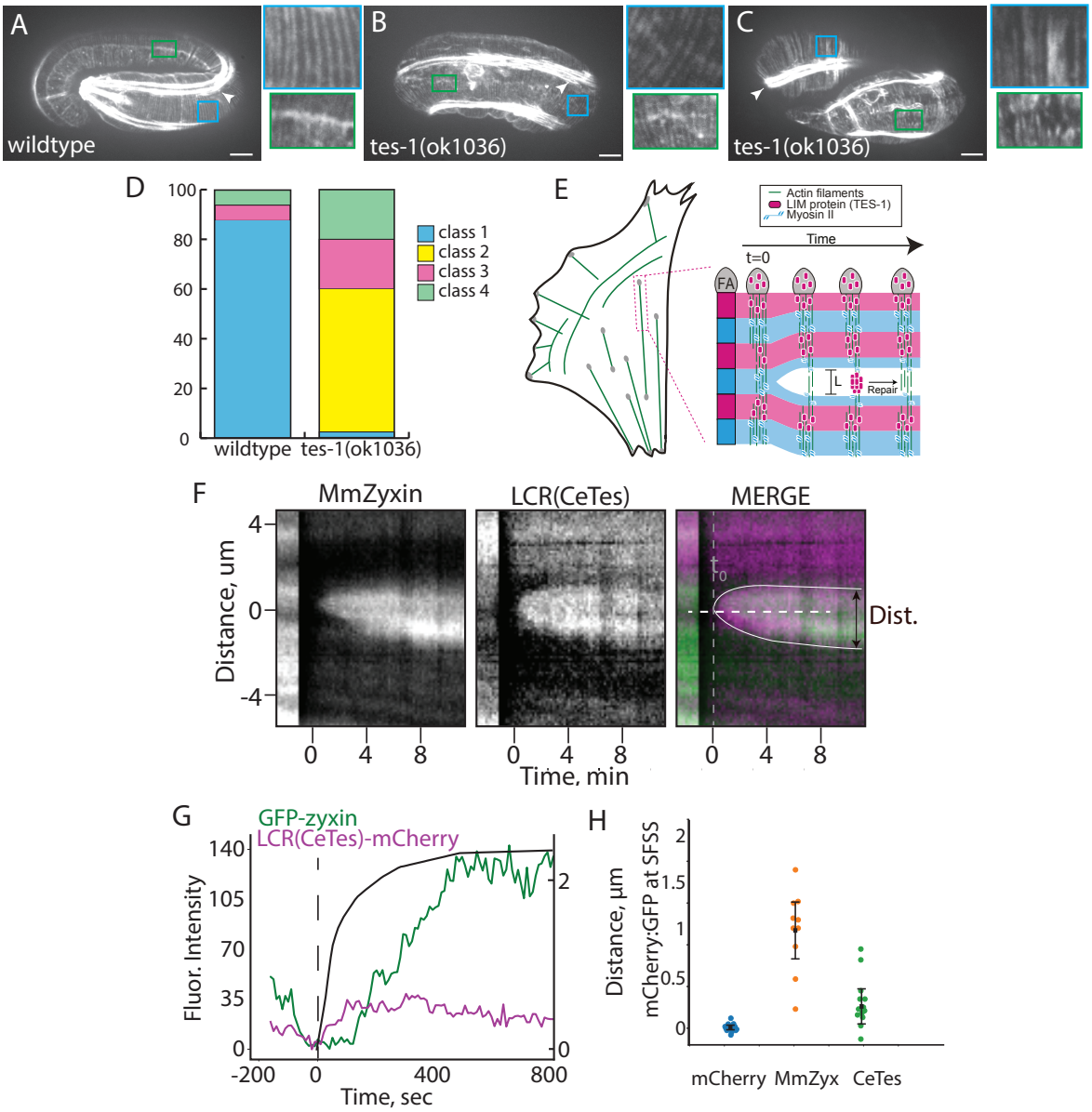
A
wildtype
B
tes-1(ok1036)
C
tes-1(ok1036)
D
100
80
60
40
20
0
wildtype
tes-1(ok1036)
class 1
class 2
class 3
class 4
E
Actin filaments
LIM protein (TES-1)
Myosin II
Time
t=0
FA
L
Repair
F
MmZyxin
LCR(CeTes)
MERGE
Distance, um
4
0
-4
0
4
8
Time, min
Dist.
G
GFP-zyxin
LCR(CeTes)-mCherry
Fluor. Intensity
140
105
70
35
0
2
0
-200
0
400
800
Time, sec
H
Distance, µm
mCherry:GFP at SFSS
2
1.5
1
0.5
0
mCherry
MmZyx
CeTes

Supplemental Figure 1. Depletion of TES-1 enhances defects in a *hmp-2* hypomorph. Top. *hmp-2(qm39)* embryos are viable and display subtle body morphology defects. **Bottom.** In *hmp-2(qm39);tes-1(RNAi)* embryos, cells leak out of the ventral midline in terminally arrested embryos (right panel, arrow).

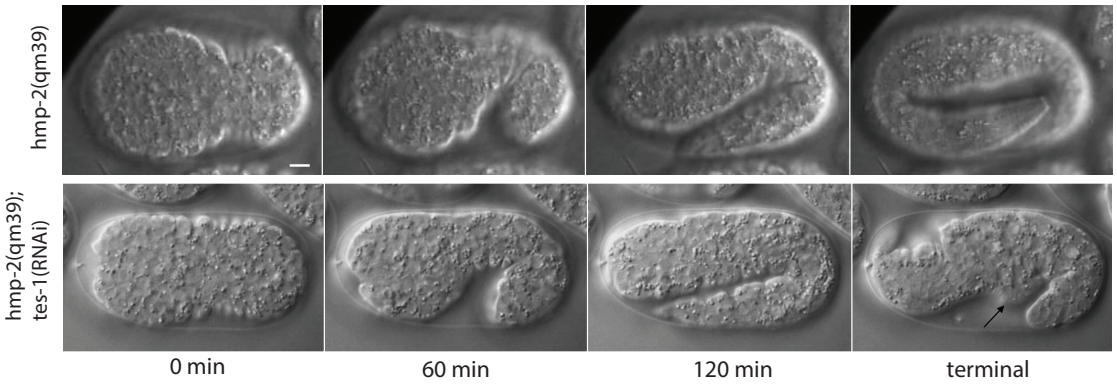
hmp-2(qm39)
hmp-2(qm39); tes-1(RNAi)
0 min
60 min
120 min
terminal

Supplemental Figure 2. TES-1 cannot coimmunoprecipitate HMP-1/a-catenin. TES-1::GFP was immunoprecipitated from an extract of mixed stage embryos, and the resulting proteins were blotted and probed with anti-GFP and anti-HMP-1 antibodies. TES-1::GFP is substantially enriched in the IP fraction **A**, demonstrating that anti-GFP antibodies can coIP TES-1::GFP. Although in a parallel preparation HMP-1 can be detected in the total lysate, pellet and wash fractions, it is undetectable in the IP fraction **B**.

A

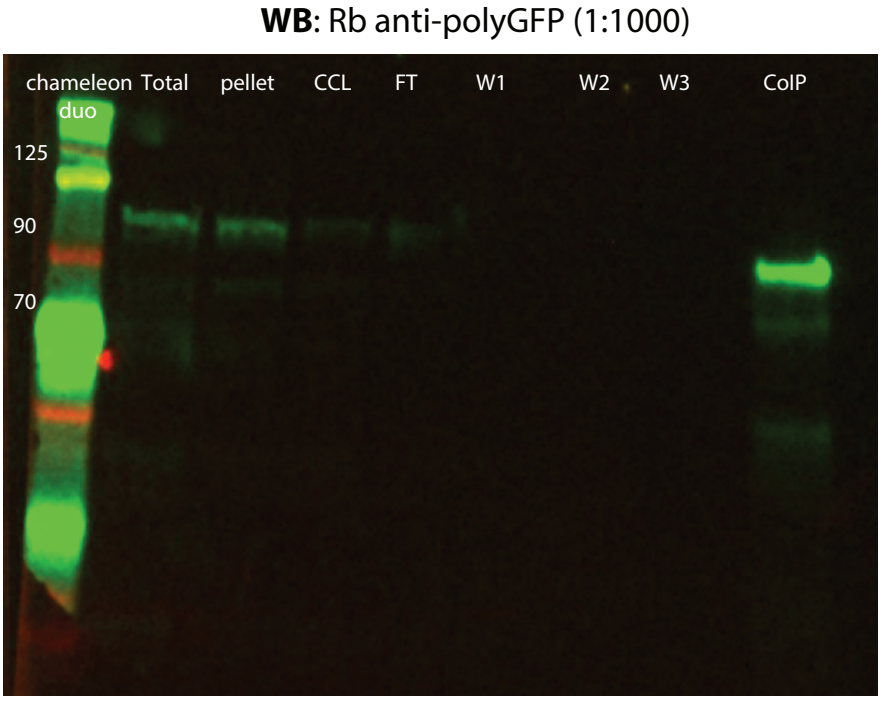
WB: Rb anti-polyGFP (1:1000)
chameleon duo
Total
pellet
CCL
FT
W1
W2
W3
CoIP
125
90
70
TES-1::GFP

B

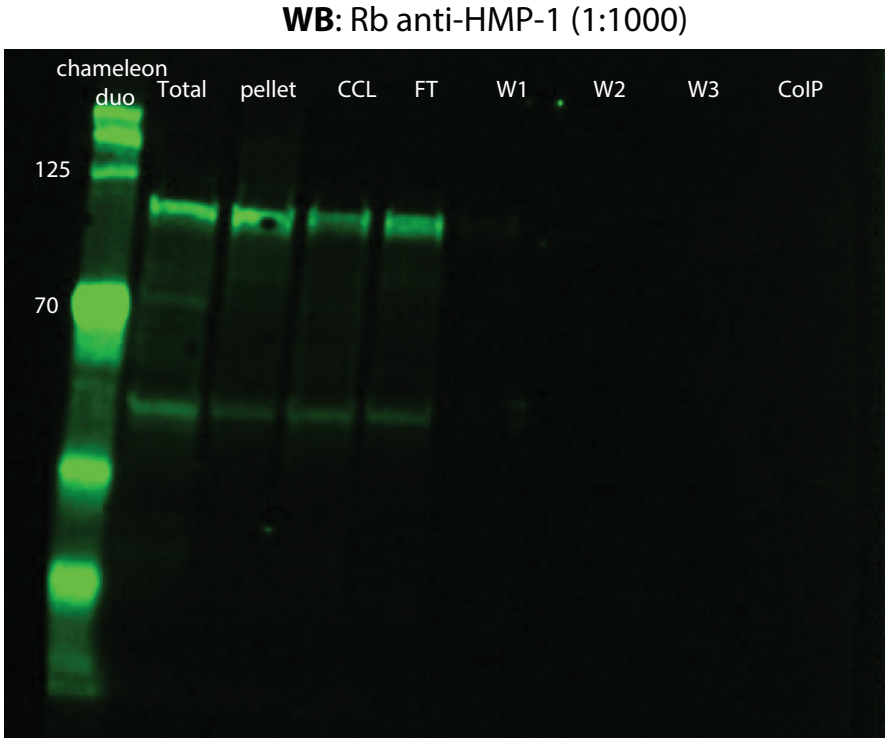
WB: Rb anti-HMP-1 (1:1000)
chameleon duo
Total
pellet
CCL
FT
W1
W2
W3
CoIP
125
70
HMP-1

Supplemental Figure 3: TES-1 only weakly binds ZYX-1/zyxin. **A**. Co-immunoprecipitation of TES-1 and ZYX-1. TES-1::GFP was immunoprecipitated from an extract of mixed stage embryos, and the resulting protein was blotted and probed with anti-GFP and anti-ZYX-1 antibodies. ZYX-1 is substantially enriched in the IP fraction. **B**. Pulldown using recombinant ZYX-1/zyxin and TES-1/Tes. Extracts of bacteria expressing ZYX-1-MBP were incubated with either GST or GST-TES-1. The resulting mixture was purified using glutathione beads, blotted, and probed using anti-MBP antibodies. MBP-ZYX-1 and TES-1GST weakly interact at substoichiometric levels

A

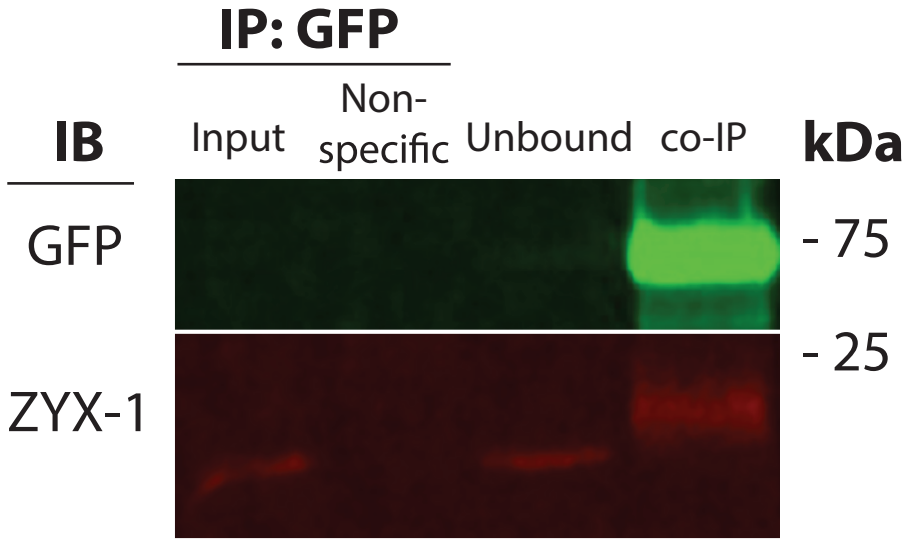
IP: GFP
IB
Input
Non-specific
Unbound
co-IP
kDa
GFP
ZYX-1
- 75
- 25

B

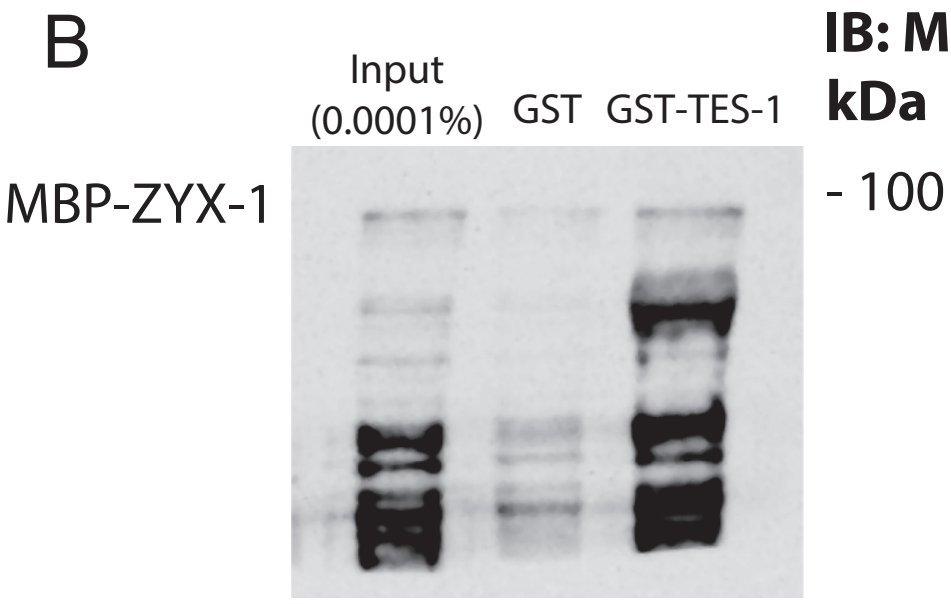
IB: MBP
kDa
Input (0.0001%)
GST
GST-TES-1
MBP-ZYX-1
- 100

APPENDIX 3
A *C. elegans* srGAP is a novel α-catenin M domain-binding protein that strengthens cadherin-dependent adhesion during morphogenesis

This work is in review at *Development*. The authors are Joel M. Serre, Bethany Lucas, Sterling C. T. Martin, Xiangqiang Shao, and Jeff Hardin

My contributions to this work are that I discovered a novel *in vivo* interaction between HMP-1 and SRGP-1/srGAP that is dependent on key salt bridges in the M-domain of HMP-1/α-catenin. These results are included in Figure 3 This manuscript is in review at *Development*

Summary

The cadherin-catenin complex (CCC) is central to embryonic development and tissue repair, yet how CCC binding partners function alongside core CCC components remains poorly understood. Here we establish a novel role for an evolutionarily conserved protein, the slit-robo GTPase-activating protein SRGP-1/srGAP, in cadherin-dependent morphogenetic processes in the *Caenorhabditis elegans* embryo. SRGP-1 binds to the M domain of the core CCC component, HMP-1/α-catenin, via its C terminus. The SRGP-1 C terminus is sufficient to target it to adherens junctions, but only during later embryonic morphogenesis, when junctional tension is known to increase. Surprisingly, mutations that disrupt stabilizing salt bridges in the M domain block this recruitment. Loss of SRGP-1 leads to an increase in mobility and decrease of junctional HMP-1. In sensitized genetic backgrounds with weakened adherens junctions, loss of SRGP-1 leads to late embryonic failure. Rescue of these phenotypes requires the C-terminus of SRGP-1 but also other domains of the protein. Taken together, these data establish a novel role for an srGAP in stabilizing and organizing the CCC during epithelial morphogenesis by binding to a partially closed conformation of α-catenin at junctions.

Introduction:

Embryonic morphogenesis poses a fundamental challenge to epithelial tissues. As cells rearrange and change shape during morphogenesis, adhesions between cells must be dynamically formed, broken, and reformed (Pinheiro and Bellaiotache, 2018; Takeichi, 2014; Walck-Shannon and Hardin, 2014) yet they must also withstand tensile forces, which threaten tissue integrity (Charras and Yap, 2018; Guillot and Lecuit, 2013; Leckband and de Rooij, 2014; Lecuit and Yap, 2015; Pannekoek et al., 2019; Priya and Yap, 2015). Central to meeting this fundamental challenge is the cadherin-catenin complex (CCC) (Harris and Tepass, 2010; Leckband and de Rooij, 2014; Lecuit and Yap, 2015; Niessen et al., 2011; Takeichi, 2014). The CCC mediates intercellular adhesion at adherens junctions (AJs) through the homophilic interactions of transmembrane cadherins. β-catenin binds the C-terminus of cadherins, while the N terminus binds the N terminus of α-catenins (Pokutta and Weis, 2007). The C terminus of α-catenin binds F-actin, linking the CCC to the cytoskeleton (Buckley et al., 2014; Maiden and Hardin, 2011; Mege and Ishiyama, 2017).

The CCC must respond to differing tension states (Charras and Yap, 2018; Guillot and Lecuit, 2013; Huveneers and de Rooij, 2013; Leckband and de Rooij, 2014; Lecuit et al., 2011; Lecuit and Yap, 2015; Mege and Ishiyama, 2017). α-catenin is one locus for such regulation. Imaging (Kim et al., 2015), molecular dynamics simulations (Barrick et al., 2018; Ishiyama et al., 2018; Li et al., 2015), crystallographic data (Choi et al., 2012; Ishiyama et al., 2018; Ishiyama et al., 2013; Kang et al., 2017), and single-molecule tweezing (Pang et al., 2019; Yao et al., 2014) suggest that the middle (M) domain of α-catenins can undergo reversible distension under tension. Tension unmasks the binding site for vinculin in vertebrate αE-catenin (Yonemura et al., 2010). Disruption of vinculin binding sites in αE-catenin leads to weak effects

in cultured cells, however (Huveneers et al., 2012), suggesting that additional tension-sensitive α-catenin binding partners may act cooperatively to strengthen the CCC.

A useful system for identifying functionally relevant, novel interactors with the CCC is the embryonic epidermis of the *C. elegans* embryo. The epidermis is born on the dorsal side of the embryo and spreads ventrally during ventral enclosure (Williams-Masson et al., 1997). After enclosure, actomyosin-mediated constriction of epidermal cells squeezes the embryo into a vermiform shape (Chisholm and Hardin, 2005; Marston and Goldstein, 2006; Vuong-Brender et al., 2016). In *C. elegans*, the core CCC is composed of HMR-1/cadherin, HMP-1/α-catenin, and HMP-2/β-catenin. Maternal loss of CCC components leads to ventral enclosure failure; zygotic loss results in failure of elongation due to defects in the junctional proximal actin network (Costa et al., 1998; Kwiatkowski et al., 2010; Maiden et al., 2013; Vuong-Brender et al., 2018).

We previously used a weak loss-of-function allele of *hmp-1*/α-catenin to look for synergistic, lethal enhancers of morphogenetic defects during embryonic morphogenesis (Cox-Paulson et al., 2012; Lynch et al., 2012). One of these is the single *C. elegans* slit-robo GTPase activating protein (srGAP) homolog, SRGP-1 (Zaidel-Bar et al., 2010). srGAPs have an N-terminal lipid-binding, extended F-BAR domain (Coutinho-Budd et al., 2012; Guez-Haddad et al., 2015; Sporny et al., 2017); a GTPase activating protein (GAP) domain that can downregulate Rho family GTPases (Foletta et al., 2002; Guerrier et al., 2009; Mason et al., 2011; Soderling et al., 2002; Waltereit et al., 2012; Wong et al., 2001; Yamazaki et al., 2013; Yang et al., 2006); and a C-terminal SH3 domain that binds F-actin regulators (Carlson et al., 2011; Endris et al., 2011).

Here, we use a combination of genetic, biochemical, and imaging approaches in *C. elegans* to demonstrate a novel role for an srGAP in binding a closed conformation of the α-

catenin M domain to stabilize adherens junctions under mechanical tension during embryonic morphogenesis.

Results and Discussion

SRGP-1/srGAP binds HMP-1/α-catenin

SRGP-1 is a *bona fide* srGAP based on homology and structure-function analyses ((Neukomm et al., 2011; Zaidel-Bar et al., 2010); see Figure S1). Our previous work showed that SRGP-1 colocalizes with the CCC and that when SRGP-1::GFP is overexpressed, outward membrane bends form that contain CCC proteins but not DLG/AJM complex proteins (Zaidel-Bar et al., 2010). We sought to determine if SRGP-1 directly binds HMP-1/α-catenin, since we previously identified SRGP-1 in a HMP-1 co-immunoprecipitation/mass spectrometry screen (Callaci et al., 2015). We verified this result (Figure 1A) and next used a yeast two-hybrid assay to show that full-length SRGP-1 can interact directly with full-length HMP-1 but not HMP-2/β-catenin (Figure 1B). We confirmed this novel interaction via protein pull-down assays using His-SUMO-HMP-1 (Callaci et al., 2015) and GST-SRGP-1 in bacteria. Using a series of deletions (for domain maps, see Figures S1A, B) we found that the HMP-1 M domain appears responsible for the interaction with amino acids 685-1059 of SRGP-1 (hereafter the "C terminus"; Figures 1C and S2).

SRGP-1 is maintained at the junction during morphogenesis through its C terminus

We next assessed the necessity of the SRGP-1 C terminus for SRGP-1 colocalization with HMP-1/α-catenin *in vivo*. SRGP-1(ΔC)::GFP exhibits a marked increase in cytoplasmic vs. junctional signal compared to full-length SRGP-1 (Figure 1D,E). Both proteins contain an intact F-BAR domain, and so as expected readily associate with and follow the curvature of the membrane. Full-length SRGP-1::GFP and HMP-1::mScarlet-I closely followed the curvature of

the membrane at junctions. In contrast, HMP-1 frequently no longer followed SRGP-1(ΔC)::GFP into membrane bends (Figure 1E, insets), as reflected in a change in overlap at junction (Manders overlap coefficient M2 with thresholding, GFP overlap with mScarlet-I = 0.82 for SRGP-1::GFP, n = 57 junctions; M2 = 0.46 for SRGP-1(ΔC)::GFP, n = 36). These data indicate that the SRGP-1 C-terminus is necessary for restricting it to junctions and for normal association with HMP-1. Because some SRGP-1ΔC can localize to junctions, we infer that additional interactions outside the C terminus also promote accumulation of SRGP-1 at junctions.

We next determined whether the C terminus alone is sufficient to target SRGP-1 to the CCC. Full-length SRGP-1::GFP expressed in the *srgp-1(gk441841)* null background was robustly targeted to cell-cell junctions throughout morphogenesis (Figure 2A). In contrast, SRGP-1(C term)::GFP failed to localize in the early embryo, and SRGP-1(C term)::GFP remained much more cytoplasmic in later embryos (Figure 1D). During ventral enclosure and elongation, however, SRGP-1(C term)::GFP localized to junctions (Figure 2B, yellow arrows).

We next assessed effects of HMP-1 depletion on SRGP-1 junctional recruitment. SRGP-1::GFP was not depleted from induced membrane tubulations in *hmp-1(RNAi)* embryos (Figure 2C, right, yellow arrowheads), but junctional SRGP-1 was greatly reduced (see Figure 2E for quantification). In contrast, *hmp-1(RNAi)* led to complete loss of junctional SRGP-1(C term) at all stages (Figure 2D, E), indicating that HMP-1 is required for normal junctional recruitment of SRGP-1 during ventral enclosure and elongation, and that interaction of the SRGP-1 C terminus with the CCC has a stringent requirement for HMP-1.

The HMP-1 M domain is required for normal SRGP-1 recruitment

Our previous work showed that overexpression of a construct lacking most of the HMP-1 M domain (HMP-1(ΔVH2)::GFP) can rescue viability, albeit weakly, in embryos carrying a C-terminal HMP-1 truncation, *hmp-1(zu278)* (Maiden et al., 2013). It remained possible, however, that other parts of the HMP-1 M domain retained in *zu278* mutants recruit other interactors. We confirmed that the same M domain deletion can partially rescue *hmp-1* CRISPR null (*jc48*) homozygotes (Shao et al., 2019) from 100% to 35.3% embryonic lethality (Figure 2G), although some rescued embryos develop body morphology defects (data not shown). We conclude that the M domain is necessary for full function of HMP-1 in the absence of other HMP-1 truncations.

We next examined effects of deletion of the HMP-1 M domain on SRGP-1 recruitment. *srgp-1::mScarlet-I; hmp-1(jc48); Ex[hmp-1(ΔVH2)::gfp]* embryos retain detectable membrane-localized SRGP-1::mScarlet-I in lateral epidermal cells (seam cells) during elongation but at greatly reduced levels (Figure 2F, H). Thus, the HMP-1 M domain appears important for recruiting or maintaining SRGP-1 at the CCC during embryonic elongation.

Recruitment of the SRGP-1 C terminus depends on the conformation of the HMP-1 M domain

Our previous structural work (Kang et al., 2017) demonstrated that HMP-1 possesses conserved salt bridges that are structural analogues of salt bridges in mammalian αE-catenin (Barrick et al., 2018; Li et al., 2015). Two arginines (R551 and R554) are predicted to stabilize the internal structure of the HMP-1 M domain, resisting its complete extension. We used CRISPR/Cas9 mutagenesis to mutate these residues to alanines. *hmp-1(R551/554A)::mScarlet-I* mutants are viable and do not display overt morphological defects under laboratory conditions.

We then constructed *srgp-1(gk441841);hmp-1(R551/554A)::mScarlet-I* strains expressing *srgp-1::gfp* constructs. Whereas full-length HMP-1::mScarlet-I colocalized precisely with full-length SRGP-1::GFP (Figure 3A, top), HMP-1(R551/554A) did not (Fig. 3A, second row), reflected in a statistically significant decrease in colocalization at junctions (Pearson's r = 0.53 for HMP-1::mScarlet-I vs. SRGP-1::GFP pixels above threshold, n = 25 junctions; r = 0.49 for HMP-1(R551/554A)::mScarlet-I vs. SRGP-1::GFP, n = 25; significantly different, $p < 0.0001$, unpaired Student's t-test). Strikingly, junctional enrichment of SRGP-1(C term)::GFP was completely abrogated in *hmp-1(R551/554A)::mScarlet-I* embryos (Figure 3A bottom row; quantified in Figure 3B). These results indicate that junctional recruitment of the SRGP-1 C terminus requires that the HMP-1 M domain be in a partially closed conformation.

Normal levels and mobility of HMP-1 at junctions require SRGP-1 function

We next examined whether SRGP-1 is required for normal junctional morphology. We could not detect a statistically significant effect on junctional tortuosity ratio of total path length/Feret length in *srgp-1(gk441841)* embryos (data not shown). We did find, however, that in *srgp-1*(*gk441841*) mutants average junctional intensity of an endogenous HMP-1::GFP knock-in (Marston et al., 2016) was measurably decreased compared to wildtype (Figure 3C). HMP-1(R551/554A)::GFP showed a similar decrease in junctional intensity (Figure 3C). We next analyzed mobility of HMP-1 at junctions using fluorescence recovery after photobleaching (FRAP; Figure 3D). Loss of SRGP-1 led to a statistically significant decrease in recovery half-life ($t_{1/2}$ for wildtype = 25.0 sec; $t_{1/2}$ for *srgp-1* = 30.5 sec; $p < 0.04$, Student's t-test, n = 1 for each), indicating increased mobility of HMP-1 in the absence of SRGP-1. These results suggest a role for SRGP-1 in organizing and stabilizing HMP-1 at junctions.

The SRGP-1 C terminus is required in CCC-sensitized backgrounds

srgp-1(RNAi) in the *hmp-1* weak loss-of-function mutant, *hmp-1(fe4)*, causes many embryos to arrest with defects in gastrulation cleft closure and subsequent ventral enclosure (Zaidel-Bar et al., 2010). We analyzed the remaining *hmp-1(fe4); srgp-1(RNAi)* embryos that survived beyond ventral enclosure. *hmp-1(fe4); srgp-1(RNAi)* embryos arrested as they approached the 2-fold stage of elongation with pronounced dorsal folds (100% of embryos, n = 21 embryos; see Figure 3E); thus SRGP-1 also plays key roles during the early stages of embryonic elongation.

We were unable to create *srgp-1(gk441841); hmp-1(fe4)* double mutants for rescue experiments, so instead used homozygotes for a hypomorphic allele of *hmp-2*/β-catenin, *hmp-2(qm39)* (Lockwood et al., 2008; Zaidel-Bar et al., 2010) as a sensitized background. *hmp-2(qm39)* embryos appear largely wildtype during embryonic development but later develop slight body morphology defects that resolve during cuticle molts (Figure 4A). In contrast, double homozygous *srgp-1(gk441841); hmp-2(qm39)* embryos displayed 57.1% embryonic lethality, arresting with dorsal humps during elongation (Figure 4B).

We next performed rescue experiments using SRGP-1 fragments in *srgp-1(gk441841); hmp-2(qm39)* embryos. SRGP-1(full-length)::GFP and SRGP-1(ΔGAP)::GFP were capable of strong rescue, although full-length SRGP-1::GFP rescued more effectively (Figure 4C, D, G). Importantly, *srgp-1(gk441841); hmp-2(qm39); Ex[srgp-1(ΔC)::gfp]* embryos were indistinguishable from *srgp-1(gk441841); hmp-2(qm39)* alone (Figure 4E, G), indicating that the C terminus of SRGP-1 is functionally important during elongation. The C terminus alone was not sufficient to rescue lethality, however (Figure 4F, G). Taken together with its inability to

support normal junctional localization (see Figures 1, 2), these data suggest that a key functional role for the SRGP-1 C terminus is to target to and maintain SRGP-1 at the CCC.

SRGP-1 stabilizes cadherin-dependent adhesion during epidermal morphogenesis

Although roles for srGAPs outside of neural tissues are beginning to be recognized (Fritz et al., 2015; Lahoz and Hall, 2013; Ye et al., 2010), roles of srGAPs during epithelial morphogenesis are not understood. Here we demonstrated the importance of the SRGP-1 C terminus in binding the HMP-1/α-catenin M domain, and, unexpectedly, that a partially closed conformation of the M domain is necessary for junctional maintenance of SRGP-1 mediated via its C terminus. Junctional SRGP-1 is in turn crucial for epidermal morphogenesis in sensitized backgrounds. A parsimonious model for SRGP-1 recruitment to the CCC during embryonic elongation is via direct HMP-1 binding. Given the timing of recruitment of C-terminal fragments of SRGP-1::GFP, increased interaction of the SRGP-1 C terminus with HMP-1 appears to occur at a time when adherens junctions are under increased tension (Figure 4H). That the SRGP-1 C terminus is capable of being recruited to junctions starting at ventral enclosure indicates that HMP-1-dependent recruitment of SRGP-1 at the junction can occur at this time in the absence of a lipid-interacting domain.

There is a well-known precedent for tension-regulated recruitment of proteins to the CCC via α-catenin. Vinculin is recruited to the CCC via α-catenin under tension by exposing a binding site within α-catenin normally buried within its M domain (Choi et al., 2012; Huveneers and de Rooij, 2013; Yonemura et al., 2010). Maximal vinculin binding to mammalian αE-catenin is favored by complete unfurling of the αE-catenin M domain (Yao et al., 2014); salt bridge mutations in the M domain of αE-catenin thus activate it for vinculin binding (Choi et al.,

2012; Huveneers et al., 2012; Ishiyama et al., 2013; Yonemura et al., 2010). The mechanism of recruitment of SRGP-1 to HMP-1 appears quite different from the vinculin/αE-catenin paradigm: destabilizing mutations predicted to maintain the HMP-1 M domain in a constitutively extended state lead to loss of SRGP-1 junctional recruitment via its C terminus. SRGP-1 may therefore require the HMP-1 M domain to adopt an intermediate conformation under tension that precedes complete unfurling of its M domain. Rigorous testing of such a mechanism awaits further biophysical experiments.

Notably, loss of HMP-1 (Figure 2C, D) or the HMP-1 M domain (Figure 2H) leads to loss of junctional SRGP-1, whereas destabilizing salt bridge mutations only strongly affect recruitment of the SRGP-1 C-terminus (Figure 3A). Since significant junctional SRGP-1 is retained even when the SRGP-1 C-terminus is deleted (Figure 1E), multiple domains of SRGP-1 may recognize multiple conformational states of the HMP-1 M domain. Alternatively, another protein may be recruited when the HMP-1 M domain is extended, thereby recruiting SRGP-1 in a manner independent of the SRGP-1 C terminus.

In summary, our results identify novel roles for an srGAP during cadherin-dependent epithelial morphogenetic events. It will be interesting to determine if vertebrate srGAPs can interact similarly with a component of the CCC. Future experiments should continue to clarify how this multifunctional family of proteins contributes to cadherin-dependent adhesion during morphogenesis.

Materials and Methods

Nematode Strains and Genetics

C. elegans strains were maintained using standard methods (Brenner, 1974). Bristol N2 was used as wildtype. Ten outcrosses to N2 were performed to remove background mutations from the

Million Mutation Project strain, VC30226, which carries the *srgp-1(gk441841)* allele (Thompson et al., 2013).

DIC Imaging

Four dimensional DIC movies were collected on either a Nikon Optiphot-2 connected to a QiCAM camera (QImaging) or an Olympus BX50 connected to a Scion CFW-1512M camera (Scion Corp.) using Micro-Manager software (v. 1.42) (Edelstein et al., 2010; Edelstein et al., 2014). ImageJ plugins (https://worms.zoology.wisc.edu/research/4d/4d.html) were used to compress and view movies.

Confocal imaging

SRGP-1::GFP;HMP-1::mScarlet-I embryos were dissected from adult hermaphrodites and mounted onto 10% agar pads in M9 solution and imaged essentially as described (Zaidel-Bar et al., 2010). For fluorescence imaging, a Dragonfly 500 spinning disc confocal microscope (Andor Corp.), mounted on a Leica DMi8 microscope, equipped with a Zyla camera and controlled by Fusion software (Andor Corp.) was used to collect images using 0.5 μm slices with a 63×/1.3 NA glycerol Leica objective at 20°C.

FRAP

FRAP analysis was conducted on Z-projections of 4D confocal movies composed of 4 z-positions spaced 0.18um apart. 4D movies were generated by photobleaching a ROI for 3 seconds and images were collected at 2 second intervals thereafter. Photobleaching was performed using an Andor Mosaic DMD (Andor Corp., Oxford, England) and imaging was performed on a Leica Dmi8 microscope with a Dragonfly spinning disk (Andor Corp.). Images were collected on a Zyla CMOS camera using Fusion software (Andor Corp.). Recovery curves

were analyzed via single-exponential curve fitting using custom Jython scripts written for Fiji. Scripts are available at https://worms.zoology.wisc.edu/research/microscopy/4d.html

Intensity Analyses

To compare intensity, mean HMP-1 junctional signal was measured by tracing HMP-1::GFP junctional signal on Z-projections of 4 focal planes spaced 0.18 µm apart. Intensity profiles were collected by drawing a 1 pixel wide line between nuclei during elongation. Colocalization of HMP-1 and SRGP-1 was performed in Fiji using Just Another Colocalization Plugin (JACoP; https://imagej.nih.gov/ij/plugins/track/jacop.html) (Bolte and Cordelieres, 2006). Four focal planes from 25 junctional segments were combined into single stacks for each genotype. Maximum intensity Z projections were obtained, and automated Costes thresholding within JACoP was visually confirmed in each case.

CRISPR

HMP-1::mScarlet-I and SRGP-1::mScarlet-I worms were generated via plasmid-based CRISPR/Cas9 (Dickinson et al., 2015) using repair templates cloned using SapTrap cloning (Schwartz and Jorgensen, 2016). Small substitution mutations were made via marker-free genome editing (Arribere et al., 2014). Guides, homology arms primers, and single-stranded repair templates for all CRISPR/Cas9 editing can be found in Supplementary Table 1.

Microinjection

For transgenic lines, 10 ng/μL of the transgene of interest, in addition to 20 ng/μL non-coding DNA (F35D3) and 80 ng/μL *rol-6(su1006),* was injected into the gonads of *srgp-1(gk441841)* young adults, as described previously (Mello and Fire, 1995).

Injection RNA interference was performed as previously described (Walston et al., 2004). dsRNA was generated using an Ambion T7 and/or T3 Megascript kit; the template used was the *srgp-1* feeding clone from a feeding library (Kamath et al., 2003), while the template used for *hmp-1* (yk1315a06) was obtained from Dr. Yuji Kohara (NEXTDB, http://nematode.lab.nig.ac.jp/). "Weak" injection RNAi was accomplished by injecting young adults with 1 μg/μL dsRNA into the pseudocoelom and imaging embryos 18 hours after injection.

Protein Expression and Purification

GST- and SUMO-His-tagged proteins were expressed in BL21-Gold(DE3) *Escherichia coli* cells and purified as described (Maiden et al., 2013; Mayers et al., 2011). Cells were induced with 0.1mM IPTG at 18°C for 16 hours. Wash and elution buffers were as follows: GST wash (1X PBS, 500 mM NaCl, 0.1% Tween-20, and 1mM DTT), GST elution (50 mM Tris pH 8.0, 0.3% glutathione, 150 mM NaCl), His wash (50 mM Na-Phosphate pH 8.0, 300 mM NaCl, 0.1% Tween-20, 10 mM Imidazole), and His elution (250 mM Imidazole, 100 mM NaCl, 10% glycerol, 50 mM Hepes pH 7.6).

Directed Yeast Two-Hybrid Assays

Yeast two-hybrid assays were performed as described previously (Lynch et al., 2012). Either full-length HMP-1 or HMP-2 yeast two-hybrid plasmids (Kwiatkowski et al., 2010) were transformed into Y2H Gold yeast singly or with a plasmid encoding full-length SRGP-1 that was cloned into the pGBKT7 vector (Clontech). Positive single transformants were tested for autoactivation, and double transformants were patched onto SD/-Leu/-Trp/X-α–gal/AurA plates. Colonies that grew and turned blue were considered positive for a direct interaction.

Actin Cosedimentation Assays

Actin cosedimentation assays were performed as described previously (Maiden et al., 2013) . Briefly, 5μM purified proteins (quantified via a Bradford Assay) were incubated at room temperature for one hour with 0 μM, 2 μM, or 10 μM polymerized chicken F-actin (Cytoskeleton, Inc.). These samples were then centrifuged at 100,000 rpm for 20 min at 4°C in TLA-120.1 rotor. Samples were run on 12% SDS-PAGE gels, stained with Coomassie Brilliant Blue, and bands were quantified using ImageJ.

Co-immunoprecipitation

C. elegans used for co-immunoprecipitations were grown in liquid culture as previously described (Stiernagle, 2006). Co-immunoprecipitations were completed as previously described (Cox-Paulson et al., 2012). HMP-1 and HMP-2 were co-immunoprecipitated using a rabbit anti-HMP-1 antibody (Zaidel-Bar et al, 2010) as a control. Western blots were performed as described below. Western blots were performed as described previously (Zhang et al., 2016),

blotting with rabbit anti-GFP or rabbit anti-HMP-1 antibodies and using chemiluminescence to detect proteins using an Odyssey Fc imaging system (Li-COR Biosciences).

Statistical Analysis

Fisher's Exact Test (http://www.graphpad.com/quickcalcs/contingency1/) was used to determine significance between rescue groups. Differences in cytoplasmic fluorescence levels were determined using Student's t-tests after measuring average junctional and cytoplasmic signals in ImageJ. Significant difference in Pearson's R for colocalizations was assessed using the online Z calculator available at https://www.calculator.net/z-score-calculator.html.

References

Arribere, J. A., Bell, R. T., Fu, B. X., Artiles, K. L., Hartman, P. S. and Fire, A. Z. (2014). Efficient marker-free recovery of custom genetic modifications with CRISPR/Cas9 in Caenorhabditis elegans. *Genetics* 198, 837-846.

Barrick, S., Li, J., Kong, X., Ray, A., Tajkhorshid, E. and Leckband, D. (2018). Salt bridges gate alpha-catenin activation at intercellular junctions. *Molecular Biology of the Cell* 29, 111-122.

Bolte, S. and Cordelieres, F. P. (2006). A guided tour into subcellular colocalization analysis in light microscopy. *J Microsc* 224, 213-232.

Brenner, S. (1974). The genetics of *Caenorhabditis elegans*. *Genetics* 77, 71-94.

Buckley, C. D., Tan, J., Anderson, K. L., Hanein, D., Volkmann, N., Weis, W. I., Nelson, W. J. and Dunn, A. R. (2014). Cell adhesion. The minimal cadherin-catenin complex binds to actin filaments under force. *Science* 346, 1254211.

Callaci, S., Morrison, K., Shao, X., Schuh, A. L., Wang, Y., Yates, J. R., Hardin, J. and Audhya, A. (2015). Phosphoregulation of the *C. elegans* cadherin-catenin complex. *Biochem J* 472, 339-352.

Carlson, B. R., Lloyd, K. E., Kruszewski, A., Kim, I. H., Rodriguiz, R. M., Heindel, C., Faytell, M., Dudek, S. M., Wetsel, W. C. and Soderling, S. H. (2011). WRP/srGAP3 facilitates the initiation of spine development by an inverse F-BAR domain, and its loss impairs long-term memory. *J Neurosci* 31, 2447-2460.

Charras, G. and Yap, A. S. (2018). Tensile Forces and Mechanotransduction at Cell-Cell Junctions. *Current biology : CB* 28, R445-R457.

Chisholm, A. D. and Hardin, J. (2005). Epidermal morphogenesis. *WormBook : the online review of C. elegans biology*, 1-22.

Choi, H. J., Pokutta, S., Cadwell, G. W., Bobkov, A. A., Bankston, L. A., Liddington, R. C. and Weis, W. I. (2012). αE-catenin is an autoinhibited molecule that coactivates vinculin. *Proceedings of the National Academy of Sciences of the United States of America* 109, 8576-8581.

Costa, M., Raich, W., Agbunag, C., Leung, B., Hardin, J. and Priess, J. R. (1998). A putative catenin-cadherin system mediates morphogenesis of the *Caenorhabditis elegans* embryo. *The Journal of cell biology* 141, 297-308.

Coutinho-Budd, J., Ghukasyan, V., Zylka, M. J. and Polleux, F. (2012). The F-BAR domains from srGAP1, srGAP2 and srGAP3 regulate membrane deformation differently. *Journal of Cell Science* 125, 3390-3401.

Cox-Paulson, E. A., Walck-Shannon, E., Lynch, A. M., Yamashiro, S., Zaidel-Bar, R., Eno, C. C., Ono, S. and Hardin, J. (2012). Tropomodulin protects alpha-catenin-dependent junctional-actin networks under stress during epithelial morphogenesis. *Current biology : CB* 22, 1500-1505.

Dickinson, D. J., Pani, A. M., Heppert, J. K., Higgins, C. D. and Goldstein, B. (2015). Streamlined Genome Engineering with a Self-Excising Drug Selection Cassette. *Genetics* 200, 1035-1049.

Edelstein, A., Amodaj, N., Hoover, K., Vale, R. and Stuurman, N. (2010). Computer control of microscopes using microManager. *Curr Protoc Mol Biol* Chapter 14, Unit14 20.

Edelstein, A. D., Tsuchida, M. A., Amodaj, N., Pinkard, H., Vale, R. D. and Stuurman, N. (2014). Advanced methods of microscope control using μManager software. *Journal of Biological Methods* 1, 10.

Endris, V., Haussmann, L., Buss, E., Bacon, C., Bartsch, D. and Rappold, G. (2011). SrGAP3 interacts with lamellipodin at the cell membrane and regulates Rac-dependent cellular protrusions. *Journal of cell science* 124, 3941-3955.

Foletta, V. C., Brown, F. D. and Young, W. S. (2002). Cloning of rat ARHGAP4/C1, a RhoGAP family member expressed in the nervous system that colocalizes with the Golgi complex and microtubules. *Brain Res Mol Brain Res* 107, 65-79.

Fritz, R. D., Menshykau, D., Martin, K., Reimann, A., Pontelli, V. and Pertz, O. (2015). SrGAP2-Dependent integration of membrane geometry and slit-robo-repulsive cues regulates fibroblast contact inhibition of locomotion. *Developmental Cell* 35, 78-92.

Guerrier, S., Coutinho-Budd, J., Sassa, T., Gresset, A., Jordan, N. V., Chen, K., Jin, W. L., Frost, A. and Polleux, F. (2009). The F-BAR domain of srGAP2 induces membrane protrusions required for neuronal migration and morphogenesis. *Cell* 138, 990-1004.

Guez-Haddad, J., Sporny, M., Sasson, Y., Gevorkyan-Airapetov, L., Lahav-Mankovski, N., Margulies, D., Radzimanowski, J. and Opatowsky, Y. (2015). The neuronal migration factor srGAP2 achieves specificity in ligand binding through a two-component molecular mechanism. *Structure* 23, 1989-2000.

Guillot, C. and Lecuit, T. (2013). Mechanics of epithelial tissue homeostasis and morphogenesis. *Science* 340, 1185-1189.

Harris, T. J. and Tepass, U. (2010). Adherens junctions: from molecules to morphogenesis. *Nat Rev Mol Cell Biol* 11, 502-514.

Huveneers, S. and de Rooij, J. (2013). Mechanosensitive systems at the cadherin-F-actin interface. *Journal of cell science* 126, 403-413.

Huveneers, S., Oldenburg, J., Spanjaard, E., van der Krogt, G., Grigoriev, I., Akhmanova, A., Rehmann, H. and de Rooij, J. (2012). Vinculin associates with endothelial VE-cadherin

junctions to control force-dependent remodeling. *The Journal of Cell Biology* 196, 641-652.

Ishiyama, N., Sarpal, R., Wood, M. N., Barrick, S. K., Nishikawa, T., Hayashi, H., Kobb, A. B., Flozak, A. S., Yemelyanov, A., Fernandez-Gonzalez, R., et al. (2018). Force-dependent allostery of the alpha-catenin actin-binding domain controls adherens junction dynamics and functions. *Nat Commun* 9, 5121.

Ishiyama, N., Tanaka, N., Abe, K., Yang, Y. J., Abbas, Y. M., Umitsu, M., Nagar, B., Bueler, S. A., Rubinstein, J. L., Takeichi, M., et al. (2013). An autoinhibited structure of alpha-catenin and its implications for vinculin recruitment to adherens junctions. *J Biol Chem* 288, 15913-15925.

Kamath, R. S., Fraser, A. G., Dong, Y., Poulin, G., Durbin, R., Gotta, M., Kanapin, A., Le Bot, N., Moreno, S., Sohrmann, M., et al. (2003). Systematic functional analysis of the Caenorhabditis elegans genome using RNAi. *Nature* 421, 231-237.

Kang, H., Bang, I., Jin, K. S., Lee, B., Lee, J., Shao, X., Heier, J. A., Kwiatkowski, A. V., Nelson, W. J., Hardin, J., et al. (2017). Structural and functional characterization of Caenorhabditis elegans alpha-catenin reveals constitutive binding to beta-catenin and F-actin. *J Biol Chem* 292, 7077-7086.

Kim, T. J., Zheng, S., Sun, J., Muhamed, I., Wu, J., Lei, L., Kong, X., Leckband, D. E. and Wang, Y. (2015). Dynamic visualization of alpha-catenin reveals rapid, reversible conformation switching between tension states. *Current Biology : CB* 25, 218-224.

Kwiatkowski, A. V., Maiden, S. L., Pokutta, S., Choi, H. J., Benjamin, J. M., Lynch, A. M., Nelson, W. J., Weis, W. I. and Hardin, J. (2010). In vitro and in vivo reconstitution of the cadherin-catenin-actin complex from *Caenorhabditis elegans*. *Proceedings of the National Academy of Sciences of the United States of America* 107, 14591-14596.

Lahoz, A. and Hall, A. (2013). A tumor suppressor role for srGAP3 in mammary epithelial cells. *Oncogene* 32, 4854-4860.

Leckband, D. E. and de Rooij, J. (2014). Cadherin adhesion and mechanotransduction. *Annu Rev Cell Dev Biol* 30, 291-315.

Lecuit, T., Lenne, P. F. and Munro, E. (2011). Force generation, transmission, and integration during cell and tissue morphogenesis. *Annu Rev Cell Dev Biol* 27, 157-184.

Lecuit, T. and Yap, A. S. (2015). E-cadherin junctions as active mechanical integrators in tissue dynamics. *Nature Cell Biology* 17, 533-539.

Li, J., Newhall, J., Ishiyama, N., Gottardi, C., Ikura, M., Leckband, D. E. and Tajkhorshid, E. (2015). Structural determinants of the mechanical stability of alpha-catenin. *J Biol Chem* 290, 18890-18903.

Lockwood, C., Zaidel-Bar, R. and Hardin, J. (2008). The *C. elegans* zonula occludens ortholog cooperates with the cadherin complex to recruit actin during morphogenesis. *Current Biology : CB* 18, 1333-1337.

Lynch, A. M., Grana, T., Cox-Paulson, E., Couthier, A., Cameron, M., Chin-Sang, I., Pettitt, J. and Hardin, J. (2012). A genome-wide functional screen shows MAGI-1 is an L1cam-dependent stabilizer of apical junctions in *C. elegans*. *Current biology : CB* 22, 1891-1899.

Maiden, S. L. and Hardin, J. (2011). The secret life of alpha-catenin: moonlighting in morphogenesis. *The Journal of Cell Biology* 195, 543-552.

Maiden, S. L., Harrison, N., Keegan, J., Cain, B., Lynch, A. M., Pettitt, J. and Hardin, J. (2013). Specific conserved C-terminal amino acids of *Caenorhabditis elegans* HMP-1/α-catenin modulate F-actin binding independently of vinculin. *J Biol Chem* 288, 5694-5706.

Marston, D. J. and Goldstein, B. (2006). Actin-based forces driving embryonic morphogenesis in Caenorhabditis elegans. *Current Opinion in Genetics & Development* 16, 392-398.

Marston, D. J., Higgins, C. D., Peters, K. A., Cupp, T. D., Dickinson, D. J., Pani, A. M., Moore, R. P., Cox, A. H., Kiehart, D. P. and Goldstein, B. (2016). MRCK-1 drives apical constriction in *C. elegans* by linking developmental patterning to force generation. *Current Biology : CB* 26, 2079-2089.

Mason, F. M., Heimsath, E. G., Higgs, H. N. and Soderling, S. H. (2011). Bi-modal regulation of a formin by srGAP2. *J Biol Chem* 286, 6577-6586.

Mayers, J. R., Fyfe, I., Schuh, A. L., Chapman, E. R., Edwardson, J. M. and Audhya, A. (2011). ESCRT-0 assembles as a heterotetrameric complex on membranes and binds multiple ubiquitinylated cargoes simultaneously. *J Biol Chem* 286, 9636-9645.

Mege, R. M. and Ishiyama, N. (2017). Integration of cadherin adhesion and cytoskeleton at adherens junctions. *Cold Spring Harb Perspect Biol* 9.

Mello, C. and Fire, A. (1995). Chapter 19 DNA Transformation. In *Caenorhabditis elegans: Modern Biologcal Analysis of an Organism*, pp. 451-482: Elsevier BV.

Neukomm, L. J., Frei, A. P., Cabello, J., Kinchen, J. M., Zaidel-Bar, R., Ma, Z., Haney, L. B., Hardin, J., Ravichandran, K. S., Moreno, S., et al. (2011). Loss of the RhoGAP SRGP-1 promotes the clearance of dead and injured cells in Caenorhabditis elegans. *Nature Cell Biology* 13, 79-86.

Niessen, C. M., Leckband, D. and Yap, A. S. (2011). Tissue organization by cadherin adhesion molecules: dynamic molecular and cellular mechanisms of morphogenetic regulation. *Physiological Reviews* 91, 691-731.

Pang, S. M., Le, S., Kwiatkowski, A. V. and Yan, J. (2019). Mechanical stability of alphaT-catenin and its activation by force for vinculin binding. *Molecular Biology of the Cell* 30, 1930-1937.

Pannekoek, W. J., de Rooij, J. and Gloerich, M. (2019). Force transduction by cadherin adhesions in morphogenesis. *F1000Res* 8.

Pinheiro, D. and Bellaiotache, Y. (2018). Mechanical force-driven adherens junction remodeling and epithelial dynamics. *Developmental Cell* 47, 391.

Pokutta, S. and Weis, W. I. (2007). Structure and mechanism of cadherins and catenins in cell-cell contacts. *Annu Rev Cell Dev Biol*.

Priya, R. and Yap, A. S. (2015). Active tension: the role of cadherin adhesion and signaling in generating junctional contractility. *Curr Top Dev Biol* 112, 65-102.

Schwartz, M. L. and Jorgensen, E. M. (2016). SapTrap, a toolkit for high-throughput CRISPR/Cas9 gene modification in *Caenorhabditis elegans*. *Genetics* 202, 1277-1288.

Shao, X., Lucas, B., Strauch, J. and Hardin, J. (2019). The adhesion modulation domain of *Caenorhabditis elegans* alpha-catenin regulates actin binding during morphogenesis. *Molecular Biology of the Cell* 30, 2115-2123.

Soderling, S. H., Binns, K. L., Wayman, G. A., Davee, S. M., Ong, S. H., Pawson, T. and Scott, J. D. (2002). The WRP component of the WAVE-1 complex attenuates Rac-mediated signalling. *Nature Cell Biology* 4, 970-975.

Sporny, M., Guez-Haddad, J., Kreusch, A., Shakartzi, S., Neznansky, A., Cross, A., Isupov, M. N., Qualmann, B., Kessels, M. M. and Opatowsky, Y. (2017). Structural History of Human SRGAP2 Proteins. *Mol Biol Evol* 34, 1463-1478.

Stiernagle, T. (2006). Maintenance of *C. elegans*. *WormBook : the online review of C. elegans biology*, 1-11.

Takeichi, M. (2014). Dynamic contacts: rearranging adherens junctions to drive epithelial remodelling. *Nat Rev Mol Cell Biol* 15, 397-410.

Thompson, O., Edgley, M., Strasbourger, P., Flibotte, S., Ewing, B., Adair, R., Au, V., Chaudhry, I., Fernando, L., Hutter, H., et al. (2013). The million mutation project: a new approach to genetics in *Caenorhabditis elegans*. *Genome Res* 23, 1749-1762.

Vuong-Brender, T. T., Yang, X. and Labouesse, M. (2016). *C. elegans* Embryonic Morphogenesis. *Curr Top Dev Biol* 116, 597-616.

Vuong-Brender, T. T. K., Boutillon, A., Rodriguez, D., Lavilley, V. and Labouesse, M. (2018). HMP-1/alpha-catenin promotes junctional mechanical integrity during morphogenesis. *PloS one* 13, e0193279.

Walck-Shannon, E. and Hardin, J. (2014). Cell intercalation from top to bottom. *Nat Rev Mol Cell Biol* 15, 34-48.

Walston, T., Tuskey, C., Edgar, L., Hawkins, N., Ellis, G., Bowerman, B., Wood, W. and Hardin, J. (2004). Multiple Wnt signaling pathways converge to orient the mitotic spindle in early *C. elegans* embryos. *Developmental Cell* 7, 831-841.

Waltereit, R., Leimer, U., Halbach, O. V. U., Panke, J., Holter, S. M., Garrett, L., Wittig, K., Schneider, M., Schmitt, C., Calzada-Wack, J., et al. (2012). Srgap3(-/-) mice present a neurodevelopmental disorder with schizophrenia-related intermediate phenotypes. *FASEB Journal* 26, 4418-4428.

Williams-Masson, E. M., Malik, A. N. and Hardin, J. (1997). An actin-mediated two-step mechanism is required for ventral enclosure of the *C. elegans* hypodermis. *Development* 124, 2889-2901.

Wong, K., Ren, X. R., Huang, Y. Z., Xie, Y., Liu, G., Saito, H., Tang, H., Wen, L., Brady-Kalnay, S. M., Mei, L., et al. (2001). Signal transduction in neuronal migration: roles of GTPase activating proteins and the small GTPase Cdc42 in the Slit-Robo pathway. *Cell* 107, 209-221.

Yamazaki, D., Itoh, T., Miki, H. and Takenawa, T. (2013). srGAP1 regulates lamellipodial dynamics and cell migratory behavior by modulating Rac1 activity. *Molecular Biology of the Cell* 24, 3393-3405.

Yang, Y., Marcello, M., Endris, V., Saffrich, R., Fischer, R., Trendelenburg, M. F., Sprengel, R. and Rappold, G. (2006). MEGAP impedes cell migration via regulating actin and microtubule dynamics and focal complex formation. *Exp Cell Res* 312, 2379-2393.

Yao, M., Qiu, W., Liu, R., Efremov, A. K., Cong, P., Seddiki, R., Payre, M., Lim, C. T., Ladoux, B., Mege, R. M., et al. (2014). Force-dependent conformational switch of alpha-catenin controls vinculin binding. *Nat Commun* 5, 4525.

Ye, B. Q., Geng, Z. H., Ma, L. and Geng, J. G. (2010). Slit2 regulates attractive eosinophil and repulsive neutrophil chemotaxis through differential srGAP1 expression during lung inflammation. *J Immunol* 185, 6294-6305.

Yonemura, S., Wada, Y., Watanabe, T., Nagafuchi, A. and Shibata, M. (2010). alpha-Catenin as a tension transducer that induces adherens junction development. *Nature Cell Biology* 12, 533-542.

Zaidel-Bar, R., Joyce, M. J., Lynch, A. M., Witte, K., Audhya, A. and Hardin, J. (2010). The F-BAR domain of SRGP-1 facilitates cell-cell adhesion during *C. elegans* morphogenesis. *The Journal of Cell Biology* 191, 761-769.

Zhang, Y., Wang, X., Matakatsu, H., Fehon, R. and Blair, S. S. (2016). The novel SH3 domain protein Dlish/CG10933 mediates fat signaling in *Drosophila* by binding and regulating Dachs. *Elife* 5, e16624.

Figure 1: SRGP-1 and HMP-1 interact *in vitro* and *in vivo*. A. Co-immunoprecipitation of HMP-1 and SRGP-1::GFP from mixed-stage embryos, larvae, and adults. "Non-specific" = lysate bound to protein-G agarose beads without antibody present; "unbound" = protein that did not immunoprecipitate. **B.** Yeast two-hybrid assay showing direct interaction between full-length HMP-1 and full-length SRGP-1 (blue) but not between full-length HMP-2 and full-length SRGP-1 (brown). Brown color indicates no autoactivation in yeast transformed with single constructs. **C.** Protein pull-down between full-length SUMO-HMP-1 (purple arrowhead) or SUMO-HMP-1(ΔVH2) (purple arrow) and GST-SRGP-1(C term) (blue arrow). GST-SRGP-1(C term) interacts with full-length HMP-1, but not SUMO-HMP-1(ΔVH2). Additional pull-downs with deletions are shown in Supplemental Figure 2. **D.** Cytoplasmic vs. junctional localization of SRGP-1 expression constructs used in this study. **E.** SRGP-1::GFP deletions lacking the C-terminus do not retain normal colocalization with HMP-1 at sites of membrane bending. Top row: full-length SRGP-1::GFP (green), HMP-1::mScarlet-I (red), and merge. Insets show higher magnification views of a junction between a seam (lateral) and dorsal epidermal cell. Colocalization of HMP-1 and SRGP-1 occurs in SRGP-1-induced membrane bends. Bottom row: SRGP-1(ΔC)::GFP (green), HMP-1::mScarlet-I (red), and merge. Insets show higher magnification views. HMP-1 no longer consistently colocalizes with SRGP-1::GFP(ΔC) in membrane bends. Scale bar = 10 μm.

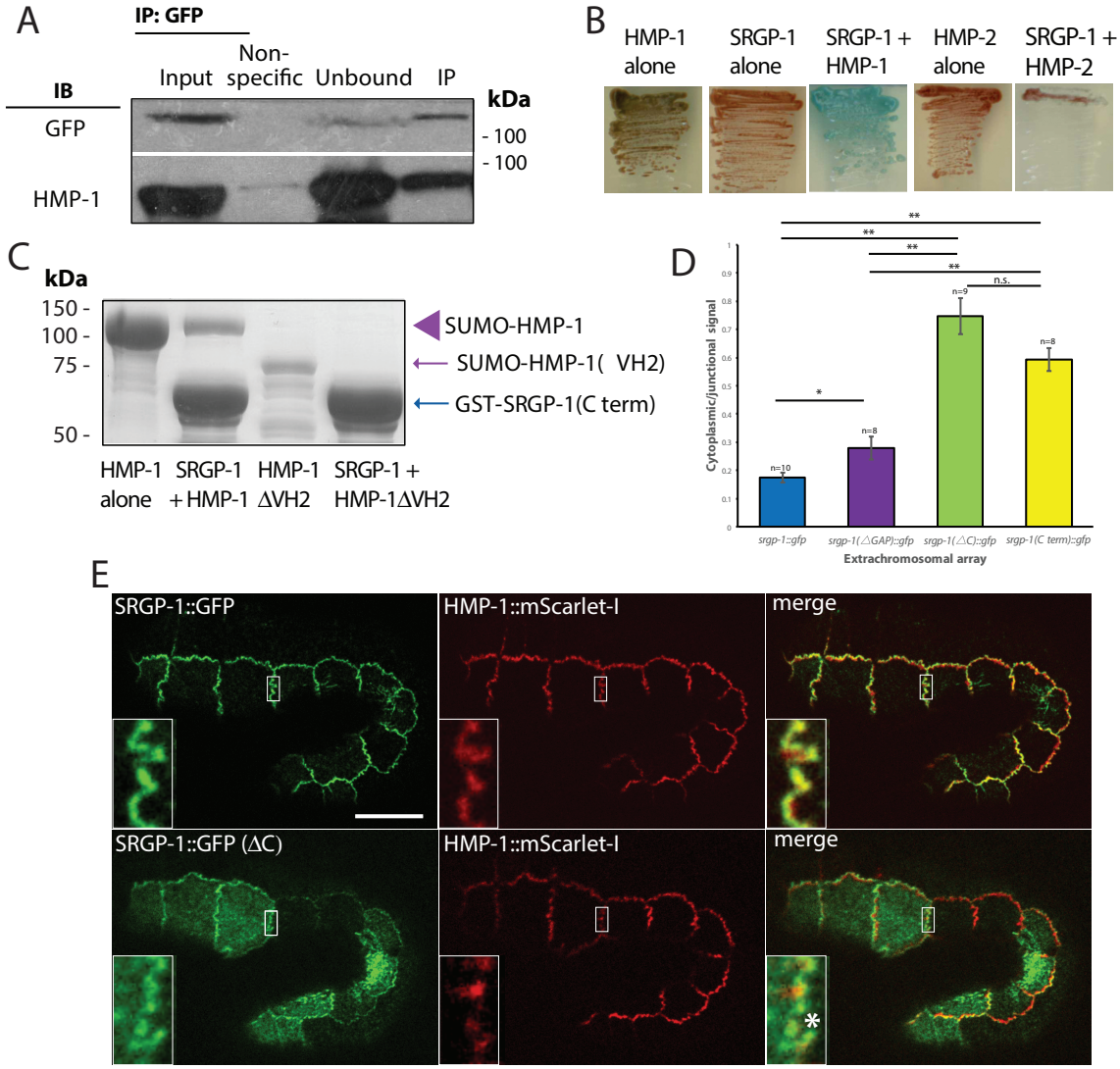
A
IP: GFP
Non-
Input specific Unbound IP
IB
kDa
GFP
HMP-1
- 100
- 100
B
HMP-1 alone
SRGP-1 alone
SRGP-1 + HMP-1
HMP-2 alone
SRGP-1 + HMP-2
C
kDa
150 -
100 -
75 -
50 -
SUMO-HMP-1
SUMO-HMP-1(VH2)
GST-SRGP-1(C term)
HMP-1 alone
SRGP-1 + HMP-1
HMP-1 ΔVH2
SRGP-1 + HMP-1ΔVH2
D
Cytoplasmic/junctional signal
n=10
n=8
n=9
n=8
*
**
**
**
**
n.s.
srgp-1::gfp
srgp-1(△GAP)::gfp
srgp-1(△C)::gfp
srgp-1(C term)::gfp
Extrachromosomal array
E
SRGP-1::GFP
HMP-1::mScarlet-I
merge
SRGP-1::GFP (ΔC)
HMP-1::mScarlet-I
merge
*

Figure 2: Junctional maintenance of SRGP-1 requires HMP-1. A. SRGP-1(full-length)::GFP expression in mutants lacking endogenous SRGP-1. Scale bar = 10 μm. **B.** SRGP-1(C term)::GFP expression in mutants lacking endogenous SRGP-1. During ventral enclosure, SRGP-1(C term)::GFP is not localized to cell-cell junctions, nor at the leading edge (white arrows). As the ventral midline seals and the embryo begins elongation, SRGP-1(C term)::GFP localizes to junctions (20 and 30 min., yellow arrows, respectively). Scale bar = 10 μm. **C.** (Left). Overexpression of SRGP-1::GFP in a wild-type background leads to strong junctional expression (red arrowhead) and junction-associated membrane extensions (yellow arrowheads). (Right) Depletion of HMP-1 via injection RNAi dramatically reduces junctional localization of SRGP-1 but does not deplete full-length SRGP-1::GFP from apical membrane extensions (yellow arrowheads). **D.** (Left) SRGP-1(C term)::GFP expressed in a wild-type embryo localizes to cell-cell junctions during elongation (white arrow). (Right) SRGP-1(C term)::GFP is no longer recruited and/or maintained at the junction in *hmp-1(RNAi)* embryos (red arrow). **E.** Intensity profiles showing SRGP-1::GFP intensity along a 5 μm line centered on the junction (red line in panel B indicates an example site of measurement) in control (purple) and *hmp-1* RNAi (orange) backgrounds for full-length SRGP-1 and C-term only. Dark lines indicate mean value; light envelope indicates S.D. SRGP-1(FL)::GFP control: n=9 measurements, *hmp-1* RNAi: n=16. SRGP-1(C)::GFP control: n=7, *hmp-1* RNAi: n=14. **F.** In *srgp-1::mScarlet-I* embryos, SRGP-1::mScarlet-I accumulates at junctions during elongation. Scale bar = 10 μm. **G.** *hmp-1(jc48); Ex[hmp-1(ΔVH2)::gfp)]* embryos are viable and can appear largely wildtype. **H.** SRGP-1::mScarlet-I; *hmp-1(jc48); Ex[hmp-1(ΔVH2)::gfp)]* embryos show reduced SRGP-1::mScarlet-I junctional accumulation, although small amounts of SRGP-1::mScarlet-I can still accumulate at sites of cell-cell contact during elongation (white arrowheads).

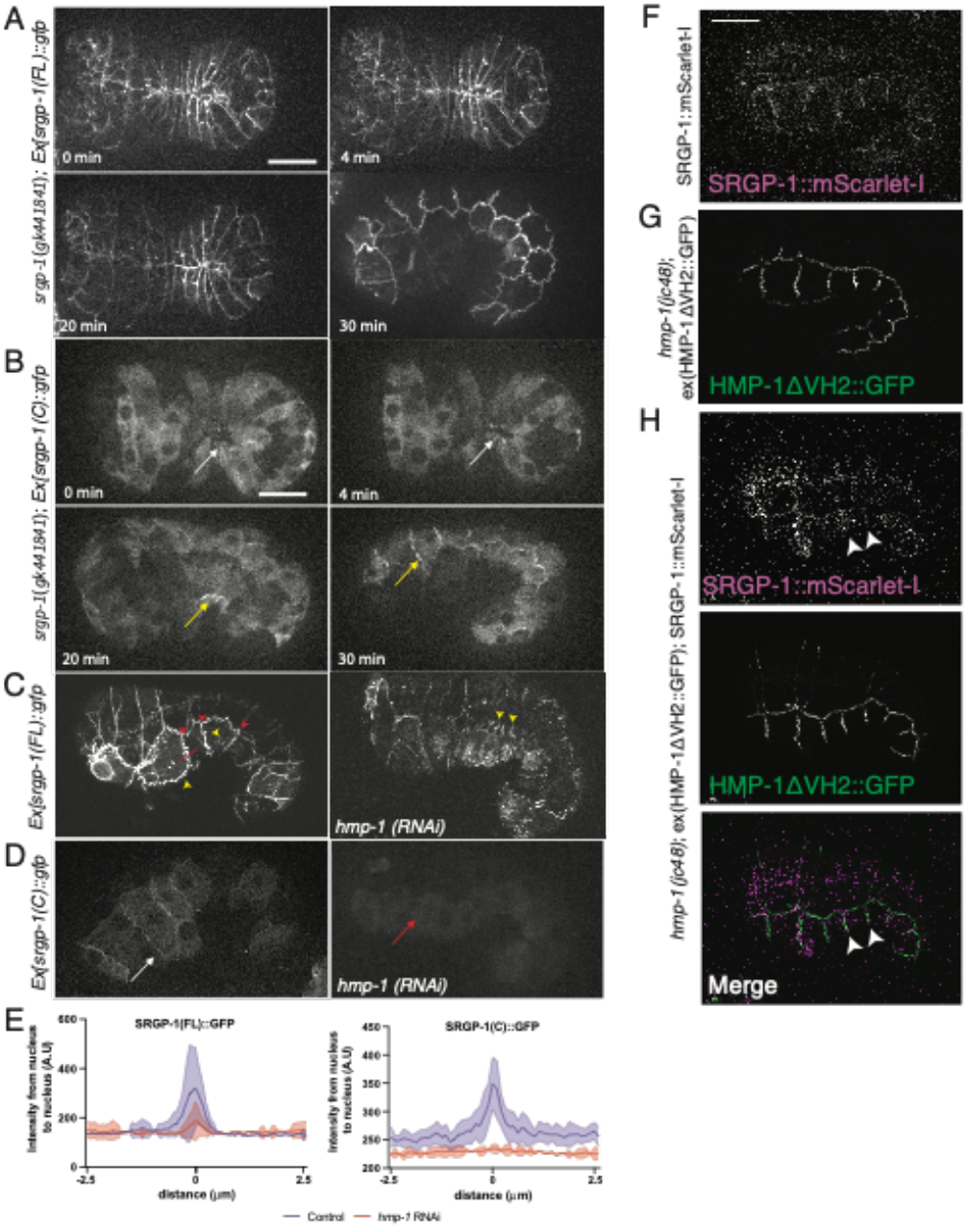
A
srgp-1(gk441841); Ex[srgp-1(FL)::gfp
0 min
4 min
20 min
30 min
B
srgp-1(gk441841); Ex[srgp-1(C)::gfp
0 min
4 min
20 min
30 min
C
Ex[srgp-1(FL)::gfp
hmp-1 (RNAi)
D
Ex[srgp-1(C)::gfp
hmp-1 (RNAi)
E
SRGP-1(FL)::GFP
SRGP-1(C)::GFP
Intensity from nucleus to nucleus (A.U)
distance (µm)
Control
hmp-1 RNAi
F
SRGP-1::mScarlet-I
SRGP-1::mScarlet-I
G
hmp-1(jc48); ex(HMP-1ΔVH2::GFP)
HMP-1ΔVH2::GFP
H
hmp-1(jc48); ex(HMP-1ΔVH2::GFP); SRGP-1::mScarlet-I
SRGP-1::mScarlet-I
HMP-1ΔVH2::GFP
Merge

Figure 3. Salt bridges within the HMP-1 M domain are required for recruitment of the SRGP-1 C terminus. A. Top Row: SRGP-1::GFP colocalization with HMP-1::mScarlet-I. Scale bar = 10 μm. Second Row: SRGP-1::GFP colocalization with HMP-1$^{R551/554A}$::mScarlet-I. Insets in the first and second row are zoomed images of junctions indicated by boxes. Third Row: SRGP-1(C-term)::GFP colocalization with HMP-1::mScarlet-I. Bottom Row: SRGP-1(C-term)::GFP localization with HMP-1$^{R551/554A}$::mScarlet-I. **B.** Violin plot of percent enrichment of SRGP-1(C)::GFP at junctions. **** = $p < 0.0001$ (Unpaired Student's t-test). e = embryos; n = junctions analyzed. **C.** HMP-1::GFP average intensity in wild-type, *srgp-1*(*gk441841*), and HMP-1$^{R551/554A}$::GFP backgrounds. WT: n=21; *srgp-1*(gk441841): n=16; HMP-1(R551/554A): n=27. **D.** Fluorescence recovery after photobleaching (FRAP) for HMP-1::GFP in WT and *srgp-1*(*gk441841*) (n=11 for each genotype). **E.** DIC images of representative *hmp-1*(*fe4*) and *hmp-1*(*fe4*); *srgp-1*(RNAi) embryos from ventral enclosure through elongation.

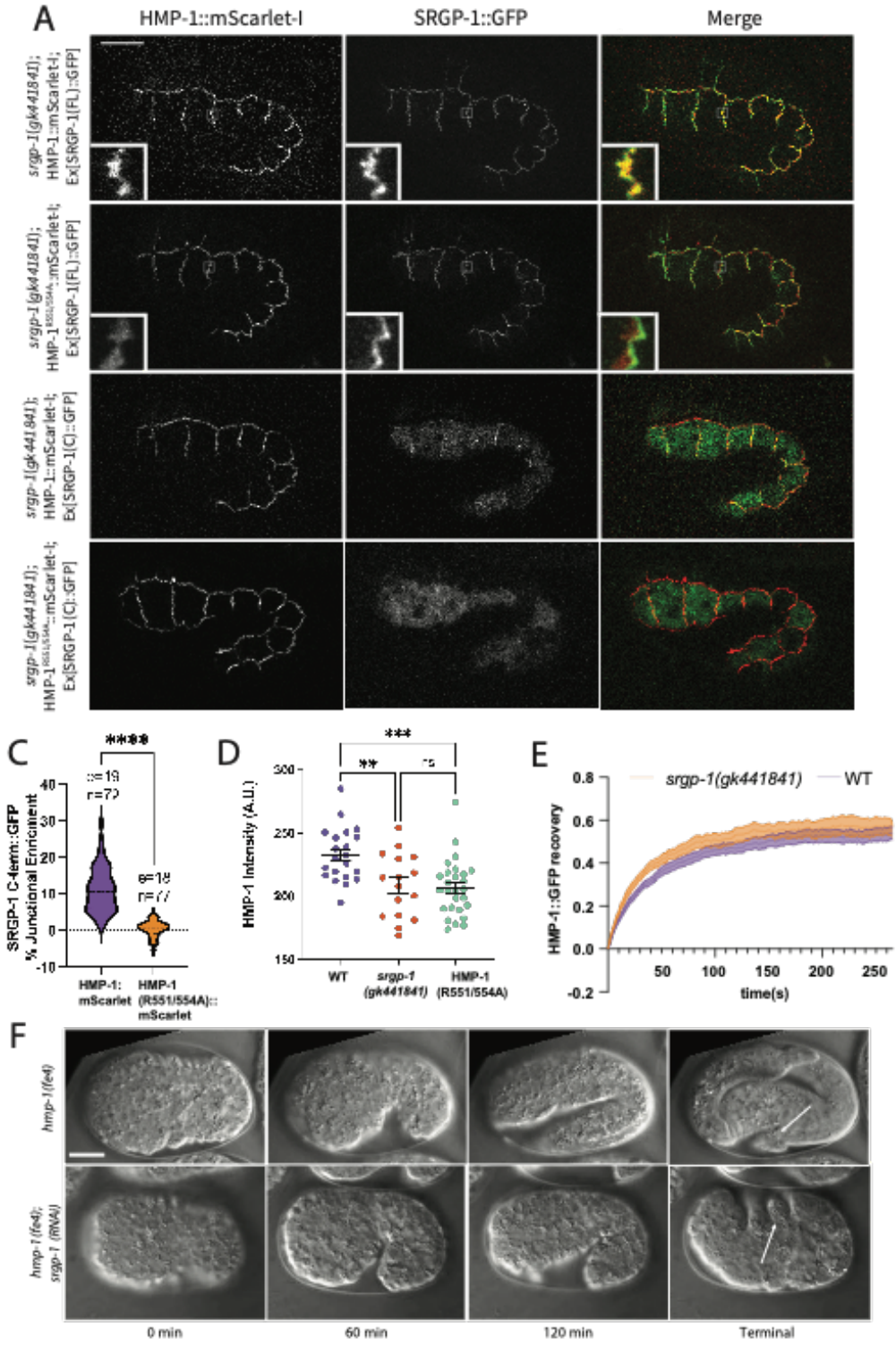
A
HMP-1::mScarlet-I
SRGP-1::GFP
Merge
srgp-1(gk441841); HMP-1::mScarlet-I; Ex[SRGP-1(FL)::GFP]
srgp-1(gk441841); HMP-1(R551/554A)::mScarlet-I; Ex[SRGP-1(FL)::GFP]
srgp-1(gk441841); HMP-1::mScarlet-I; Ex[SRGP-1(C)::GFP]
srgp-1(gk441841); HMP-1(R551/554A)::mScarlet-I; Ex[SRGP-1(C)::GFP]
C
****
n=19
n=72
n=18
n=77
SRGP-1 C-term::GFP % Junctional Enrichment
HMP-1: mScarlet
HMP-1 (R551/554A):: mScarlet
D
***
**
ns
HMP-1 Intensity (A.U.)
WT
srgp-1 (gk441841)
HMP-1 (R551/554A)
E
srgp-1(gk441841)
WT
HMP-1::GFP recovery
time(s)
F
hmp-1(fe4)
hmp-1(fe4); srgp-1 (RNAi)
0 min
60 min
120 min
Terminal

Figure 4. The SRGP-1 C terminus is required for embryonic elongation in an adhesion-sensitized background. A. In *hmp-2(qm39)* homozygotes ventral enclosure and elongation proceed normally in almost all embryos. **B.** Homozygous *hmp-2(qm39); srgp-1(gk441841)* embryos begin to fail at 120 minutes, and embryos form dorsal humps (arrow). **C.** *srgp-1(gk441841); hmp-2(qm39); Ex[srgp-1::gfp]* embryos are mostly rescued. **D.** *srgp-1(gk441841); hmp-2(qm39); Ex[srgp-1(ΔGAP)::gfp]* embryos appear largely wild-type, with some embryos dying during elongation. **E.** *srgp-1(gk441841); hmp-2(qm39); Ex[srgp-1(ΔC)::gfp]* embryos die with dorsal humps during elongation (black arrow, 120 min.). **F.** *srgp-1(gk441841); hmp-2(qm39); Ex[srgp-1(C term)::gfp]* embryos with humps die during elongation (black arrow, 120 min). Scale bar = 10 μm. **G.** Quantification of rescue in *srgp-1(gk441841); hmp-2(qm39)* strains. In all cases, GFP-expressing embryos were compared to their non-expressing siblings. Embryos expressing full-length SRGP-1::GFP or SRGP-1(ΔGAP)::GFP have significantly less embryonic lethality than their non-expressing siblings, while embryos expressing SRGP-1(ΔC)::GFP and SRGP-1(C term)::GFP are not significantly different from siblings. (n values indicated for each genotype; * = $p < 0.05$; n.s. = not significant, Fisher's Exact Test). **H.** Model for SRGP-1 function. SRGP-1 interacts with membrane lipids through its F-BAR domain (dark blue) and binds the M domain of HMP-1/α-catenin through its C terminus. Tension causes conformational changes in, but not full extension of, the M domain of HMP-1/α-catenin that promote SRGP-1 binding, thereby stabilizing the cadherin-catenin complex during morphogenesis.

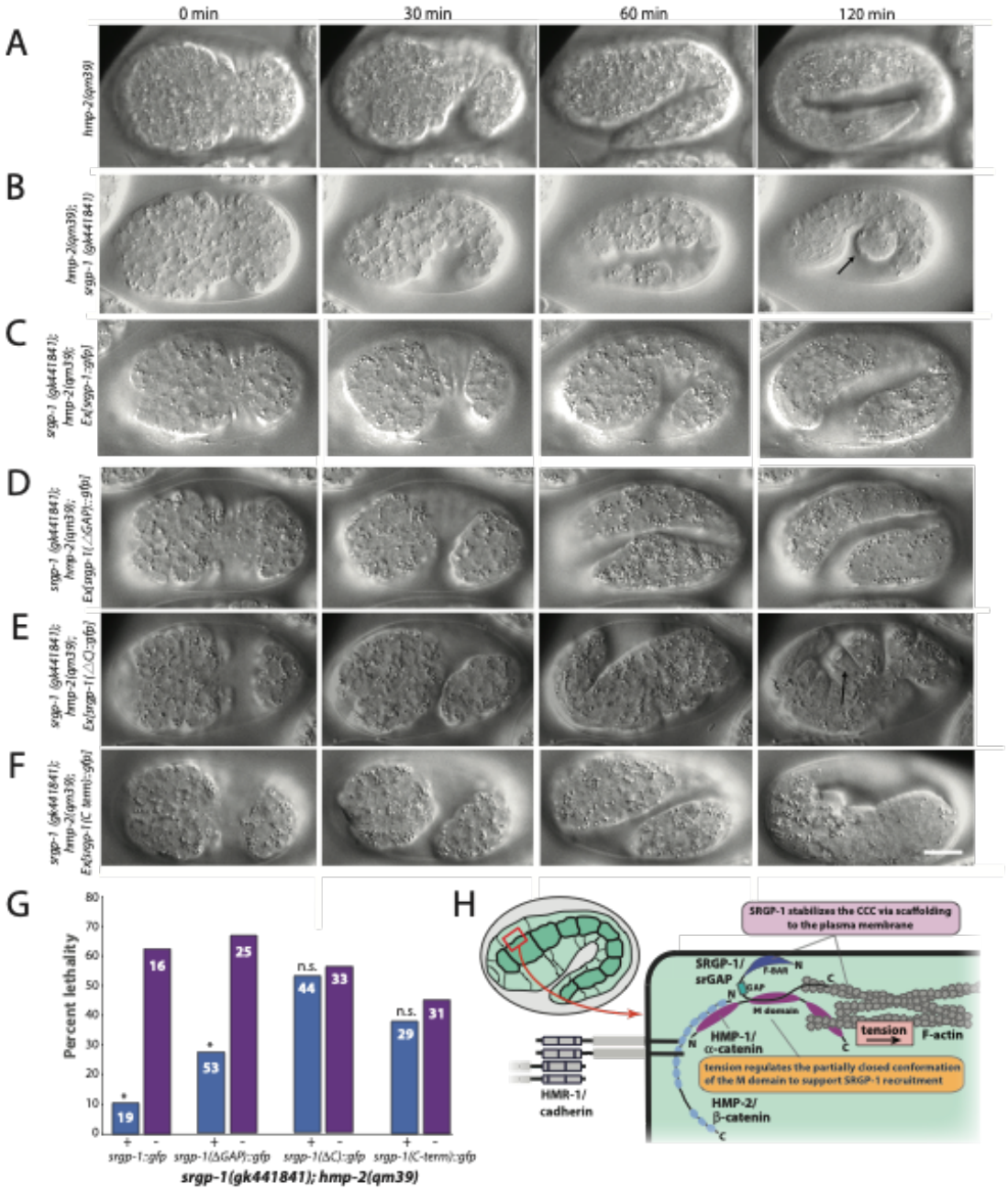
0 min
30 min
60 min
120 min
A
hmp-2(qm39)
B
hmp-2(qm39); srgp-1 (gk441841)
C
srgp-1 (gk441841); hmp-2(qm39); Ex[srgp-1::gfp]
D
srgp-1 (gk441841); hmp-2(qm39); Ex[srgp-1(ΔGAP)::gfp]
E
srgp-1 (gk441841); hmp-2(qm39); Ex[srgp-1(ΔC)::gfp]
F
srgp-1 (gk441841); hmp-2(qm39); Ex[srgp-1(C term)::gfp]
G
Percent lethality
srgp-1::gfp
srgp-1(ΔGAP)::gfp
srgp-1(ΔC)::gfp
srgp-1(C-term)::gfp
srgp-1(gk441841); hmp-2(qm39)
H
SRGP-1 stabilizes the CCC via scaffolding to the plasma membrane
SRGP-1/ srGAP
F-BAR
GAP
M domain
tension
F-actin
HMP-1/ α-catenin
tension regulates the partially closed conformation of the M domain to support SRGP-1 recruitment
HMR-1/ cadherin
HMP-2/ β-catenin

APPENDIX 4:

Contribution of spontaneous mutations to quantitative and molecular variation at the highly repetitive rDNA locus in yeast

This work has been prepared for submission to *Genetics*. The authors are Nathaniel P. Sharp, Denise R. Smith, Gregory Driscoll, Kexin Sun, Catherine M. Vickerman, Sterling C.T. Martin

My contributions to this work include *in silico* modeling of a mutation in RIF1 to explore its potential impact on DNA binding. This work provides a plausible explanation for why this mutant has a phenotype and why two other intramolecular mutations (which were outside the DNA binding domain, and solvent exposed) do not. This is included in Supplemental Figure 5.

Summary

The ribosomal DNA array in *Saccharomyces cerevisiae* consists of many tandem repeats whose copy number is believed to be functionally important but highly labile. Regulatory mechanisms have evolved to maintain copy number by directed mutation, but how spontaneous variation at this locus is generated and selected has not been well characterized. We applied a mutation accumulation approach to quantify the impacts of mutation and selection on this unique genomic feature across hundreds of mutant strains. We find that mutational variance for this trait is relatively high, and that un-selected mutations throughout the genome can disrupt copy number maintenance. In consequence, copy number generally declines, consistent with a model of regulation where copy number is normally increased when low. This pattern holds across ploidy levels and strains in the standard lab environment, but differs under some stressful conditions. We identify several alleles, gene categories and genomic features that likely affect copy number, including aneuploidy for chromosome XII. Copy number change is associated with reduced growth in diploids, consistent with stabilizing selection. Levels of standing variation in copy number are well predicted by a balance between mutation and stabilizing selection, suggesting this trait is not subject to strong diversifying selection in the wild. The rate and spectrum of point mutations within the rDNA locus itself is distinct from the rest of the genome, and predictive of polymorphism locations. Our findings help differentiate the roles of mutation and selection and indicate that spontaneous mutation patterns shape several aspects of ribosomal DNA evolution.

Introduction

To understand patterns of genome evolution we need to examine the forces that introduce and eliminate genetic variation. The mutation process adds variation, the nature of which depends on genomic context. Natural selection reduces variation by favoring some alleles over others. The stochastic influence of genetic drift is strongest for alleles with weak effects in relatively small populations. Disentangling these forces can allow us to quantify their individual contributions to genetic variation, including structural genomic variation (Conrad and Hurles 2007; Flynn *et al.* 2017, 2018). Here we apply this perspective to the highly repetitive ribosomal DNA (rDNA) locus in the model yeast *Saccharomyces cerevisiae*.

Eukaryotic genomes contain many copies of the rDNA locus in one or more tandem arrays, and the genes at this locus encode rRNAs that are key components of ribosomes. There is good evidence that rDNA copy number (CN) is relevant for organismal function and fitness: in addition to its direct connection to protein synthesis, the size of the rDNA array has been implicated in gene expression and silencing (Michel *et al.* 2005; Paredes *et al.* 2011; Gibbons *et al.* 2014), genome integrity (Ide *et al.* 2010; Kobayashi 2011, 2014; Fine *et al.* 2019), stress response (Salim *et al.* 2017; Salim and Gerton 2019), development (Delany *et al.* 1994), and cancer (Wang and Lemos 2017; Lindström *et al.* 2018). While many features of rDNA arrays are conserved across taxa (Salim and Gerton 2019; Symonová 2019), a key experimental model for this research has been *S. cerevisiae*, in which the rDNA array accounts for 4-15% of the nuclear genome.

The rDNA array can change both through point mutations (single-nucleotide substitutions and small insertions and deletions) as well as the number of repeats in the array (CN), and may be particularly susceptible to the latter type of change. DNA damage at a given copy in the array can be repaired by single-strand annealing between adjacent copies or recombinational repair between distant copies, resulting in the loss of one or more copies (Kobayashi 2006, 2011). The high rate of rDNA transcription increases the risk of DNA damage in this region due to replication-transcription conflict; the protein Fob1 unidirectionally blocks the replication fork in each repeat copy, preventing head-on collisions with transcription of 35S-rDNA, but increasing the risk of DNA double-strand breaks (Kobayashi 2003).

Under these circumstances, where the size of the rDNA array is both prone to spontaneous change and relevant for fitness, it is unsurprising that genetic mechanisms appear to have evolved that compensate for spontaneous CN change (Kobayashi 2011; Mansisidor *et al.* 2018; Iida and Kobayashi 2019a; Nelson *et al.* 2019). The transcription of 35S rRNA by RNA polymerase I is activated by a specific upstream activation factor complex, UAF, which normally associates with rDNA. In a cell with low CN, excess UAF instead suppresses the expression of the silencing protein Sir2 (Iida and Kobayashi 2019a), which normally represses the activity of E-pro, a bidirectional non-coding promoter within the rDNA locus. The activation of E-pro transcription in low-CN cells displaces the cohesin complex that binds sister chromatids at each intragenic spacer region (Kobayashi and Ganley 2005). When Fob1-dependent double-strand breaks are repaired, any lack of sister chromatid cohesion increases the opportunity for unequal recombination, thereby amplifying rDNA copy number. This homeostatic system is believed to

promote stability of the rDNA array length by increasing the rate of amplification mutations in the presence of low CN (Iida and Kobayashi 2019b).

In principle, natural selection alone could result in CN stability by simply disfavoring individuals with non-optimal values, assuming their fitness is affected. Given the high mutability of CN, the evolution of "canalizing" mechanisms like the model described above makes sense, as this will limit the production of unfit progeny (de Visser *et al.* 2003). However, the canalizing mechanisms themselves will presumably be subject to mutation. The amount of standing genetic variation due to mutation-selection balance for alleles that affect canalizing mechanisms will depend on the rate that such alleles arise and the strength of selection on CN. Additional standing variation could be present if the optimal CN value is not constant, but varies among environments.

In order to predict how much genetic variation should be present under mutation-selection balance we need to quantify these forces separately. We can obtain an unbiased view of mutation patterns by preventing selection from acting effectively in experimental populations. This is the basis for mutation accumulation (MA) experiments, where a given genotype is propagated in many very small populations, typically for many generations (Halligan and Keightley 2009). As new mutations appear in these populations, their fixation or loss depends on chance, rather than selection, as long as their effects on fitness are not too large. The resulting MA lines can be sequenced to identify mutations at the molecular level, allowing the rate and spectrum of mutations to be determined. The genetic variation among MA lines for fitness or any other trait of interest represents the "mutational variance" for that trait, multiplied by the length of the

experiment in generations. The combination of genome sequences and trait data from MA lines can also provide opportunities to identify genotype-phenotype associations.

We studied the evolution of the rDNA locus in yeast by characterizing CN in yeast MA lines, estimated using sequence data calibrated with digital droplet PCR (ddPCR) data. Our results indicate that mutations typically result in CN decline, but occasionally produce large increases. Environmental variation can give rise to different genome-wide mutational patterns (Liu and Zhang 2019), and we find this applies to CN as well. Using fitness estimates for MA lines we find evidence that CN is subject to stabilizing selection. By comparing these results to datasets on natural variation in CN, we conclude that the mutation-selection balance model is likely sufficient to explain the observed level of standing variance in this trait. We also present results on genotype-phenotype associations that implicate specific alleles and gene categories in CN maintenance, and report rates of point mutation and recombination events within the rDNA repeats themselves.

Results

Quantitative genetics of CN variation

Mean CN declines under mutation accumulation.

Unless otherwise noted, our analyses of copy number (CN) refer to the estimated number of rDNA copies per chromosome XII (Table S2). These values are generally similar for haploids and diploids, meaning that diploids have roughly twice as many copies per cell in total. Below we also discuss copy number for those strains with three copies of chromosome XII. The ancestral control strains, which were not subjected to MA, have CN values of 84.2 on average. All but one of the nine control samples have CN in the range 83–96, similar to the average of

wild isolates (Sharma *et al.* 2021) with the exception being our single case of a diploid *rdh54Δ* control strain, which has a CN of 55. This relatively low value, which is consistent with the ddPCR data for this strain, might reflect an immediate diploid-specific effect of *rdh54Δ* in the absence of MA, but we can't conclude that based on a single strain. Excluding this strain, there is no evidence that ploidy or *RDH54* status affect CN in controls (ploidy: $t = 1.086$, $P = 0.33$; *RDH54*: $t = –0.038$, $P = 0.97$). This suggests that the transformation protocol we used to generate *rdh54Δ* haploids did not have detectable effects on CN (cf. (Kwan *et al.* 2016).

Fig. 3 shows CN for all strains over generations of MA (with ancestral controls at zero generations). Pooling ploidy levels and *RDH54* conditions, the average CN of MA lines was 66.3, significantly lower than the control average (Welch t-test, $t = 4.28$, $P = 0.0016$). We used linear models to examine the effects of MA generations, ploidy, and *RDH54* status on CN. Interaction terms were non-significant and removed from the model. We find a significant effect of MA generations, with mean CN declining due to MA ($t = –2.002$, $P = 0.046$), and a significant effect of *RDH54* status, with *rdh54Δ* strains exhibiting lower CN ($t = –3.893$, $P = 1.31 \times 10^{–4}$). We do not detect a significant difference in CN between haploids and diploids ($t = 0.508$, $P = 0.612$). This model indicates that CN declines by 0.0083 per generation on average due to mutation pressure (95% CI: 0.0001–0.0165), and that the *rdh54Δ* strains have lower CN by 10.3 copies on average (95% CI: 5.1–15.4).

CN variance increases under mutation accumulation.

Under MA we expect the genetic variance for traits of interest to increase over time as different MA lines acquire different mutational changes, i.e., mutational variance, V_M (Lynch and Walsh

1998). The variance in CN among MA lines will reflect both mutational variance and measurement error, V_E. To estimate V_E we used the variance in CN among a set of three diploid *RDH54*$^+$ ancestral control lines sequenced at the same time, which should be genetically identical, and find $V_E = 9.6$ (environmental coefficient of variation 3.35%). We calculated V_M for *RDH54*$^+$ diploids as $(V[\text{CN}] - V_E)/t$, where t is the mean number of generations of MA in this treatment group (Lynch and Walsh 1998, pp. 331). We find $V_M = 0.31$, indicating that the variance in CN increases by 0.31 copies per chromosome per generation due to mutation.

To compare V_M among traits and populations we can calculate the mutational coefficient of variation, CV_M as $\left(\sqrt{V_M}/E[\text{CN}]\right) \times 100$, where E[CN] is the mean copy number among MA lines in this treatment group (Houle *et al.* 1996). We find that $CV_M = 0.75\%$ (approximate 95% confidence interval 0.73–0.78%; Lynch and Walsh 1998, pp. 821). Compared with various other "metric" traits that have been studied (although not in *S. cerevisiae*), this value is moderately high (Houle *et al.* 1996). Indeed, this is about 9.5 times greater than the equivalent measurement for growth rate in this same set of MA lines (0.08%).

Environmental impact on CN change under MA.

To test the generality of these results we applied the same estimation procedure to another yeast MA dataset (Liu and Zhang 2019). These authors identified several ways in which the media environment during MA influenced the rate and spectrum of new mutations, but did not examine CN. The distribution of CN in MA lines grown in each of the seven environments are shown in Fig. 4. There is significant variation among treatment groups (ANOVA, $F_{6,159} = 15.6$, $P = 4.66 \times 10^{-14}$). In the YPD environment, which is the same as the Sharp *et al.* (2018) experiment, average

CN declined significantly from the ancestral value (linear model: $t = –2.09$, $P = 0.048$), at a rate of 0.015 copies per generation, which is similar to the estimated average rate of decline in the diploid *RDH54*$^{+}$ lines of Sharp *et al.* (2018), 0.011 per generation (Welch's t-test: $t = 1.89$, df = 78.8, $P = 0.062$). Several environments show examples of lines that acquired high CN (Fig. 4), and in two environments mean CN increased relative to the ancestor, though not significantly (YNB: $t = 0.67$, $P = 0.51$; NaCl: $t = 0.70$, $P = 0.49$). All groups of lines from this study also show high levels of mutational variance for CN (mean $CV_M = 0.69\%$, range 0.25–1.24%).

Stabilizing selection on CN.

Precise data on the growth rates of MA lines relative to ancestral controls were acquired by Sharp *et al*. (2018), with 4000 measurements in total. For diploid MA lines, growth rate was shown to be strongly correlated with genome size (i.e., the presence of aneuploidy for one or more chromosomes of various sizes). We first examined the relationship between growth rate and CN while excluding MA lines with aneuploidy mutations, and the results are shown in Fig. 5. For each ploidy level we fit quadratic models of relative growth rate on the change in CN ($CN_{MA} – CN_{control}$), where ancestral controls have no CN change and relative fitness of 0 by definition. We found a significant quadratic term for diploids ($t = –3.82$, $P = 3.1 \times 10^{–4}$) but not for haploids ($t = –0.67$, $P = 0.51$). The significant quadratic term for diploids persists when we include aneuploid lines with genome size as a covariate ($t = –4.21$, $P = 5.3 \times 10^{–5}$). These results indicate stabilizing selection for CN in diploids, but no detectable stabilizing selection in haploids. Excluding the ancestors, there is a significant negative correlation between CN and growth rate in haploid MA lines ($t = –2.17$, $P = 0.032$).

We can use the quadratic regression coefficient to quantify the strength of stabilizing selection on CN in diploids, V_S (Lande and Arnold 1983; Stinchcombe *et al.* 2008), where larger values of V_S correspond to a "flatter" fitness surface, and hence weaker stabilizing selection. Standardized by V_E, our estimate of selection is weaker than the range observed for most traits (V_S/V_E = 9328 for CN, versus 100–10 for other traits; Falconer and Mackay 1996, pp. 349-53). We therefore find significant but weak stabilizing selection on CN in diploids.

Rates and effect sizes of CN mutations.

We used data on *RDH54*$^+$ lines to model the underlying rate of mutations that alter CN and the distribution of their effects on the trait, assuming that each line can carry a combination of mutations that decrease or increase CN. Posterior distributions and modes of model parameters are shown in Fig. S1, with separate results for haploids and diploids are shown in Fig. S2-3. The results suggest that mutations that alter CN occur at a rate of 0.0008 per genome per generation (Fig. S1A), of which 3.8% cause CN to increase (Fig. S1B). We can use these values to estimate the realized number of mutations with upward or downward effects (Fig. S1C); these results suggest that most MA lines have several mutations with downward effects, and about 5% of MA lines have a mutation with an upward effect, consistent with the general CN distribution among lines (Fig. 3). The model also estimates the mean and variance of effect sizes, and suggests that downward mutations have effects that are approximately normally-distributed, reducing CN by about 7 copies on average (Fig. S1D-F). In contrast, the model suggests that mutations that increase CN have a low mean and high variance, resulting in a strongly skewed distribution where most mutations have small effects and rare mutations have large effects (Fig. S1G-I). As

an alternative approach, we used the same techniques as above to fit a model where mutations affect the rate of CN change in subsequent generations, rather than causing a one-time change. This approach is somewhat more stochastic because the timing of mutations becomes relevant, but the overall picture is similar, except that both upward and downward mutations show strongly skewed distributions of effects (Fig. S4).

Mutational versus standing variance in CN.

Using sequence data from Peter *et al.* (2018) on a large number of natural *S. cerevisiae* isolates, Sharma *et al.* (2021) estimated CN using a method based on modal coverage. The CN distribution from their dataset is shown in Fig. 6, along with the distribution among *RDH54*$^+$ MA lines from this study (Sharma *et al.* (2021) did not detect an effect of ploidy on CN among natural isolates). Both distributions show a right tail; the ancestral control mean of *RDH54*$^+$ lines from this study is similar to the mean of natural isolates (88.6 vs. 92.1; Welch t-test: $t = 1.51$, $df = 8.5$, $P = 0.17$), with most MA lines showing CN decline, as described above. The coefficients of variation for each clade range from 9% to 43%, bracketing the CV for the MA lines (32%).

As an estimate of standing genetic variance (V_G) in natural isolates, we took the average variance among the 23 clades defined previously (Peter *et al.* 2018), after subtracting V_E, giving $V_G \approx 604$ ($63V_E$, range: $5V_E$ – $165V_E$, larger than the among-clade component of variance). We can compare this observed value to the variance expected under alternative models of trait evolution.

If standing variance is determined solely by the balance between mutation and genetic drift, i.e., the trait is neutrally-evolving, the expected standing variance is approximately $2N_eV_M$, where N_e

is the effective population size and V_M is the mutational variance (Walsh and Lynch 2018, p. 419). The observed standing variance is less than the neutral expectation as long as $N_e > V_G/(2V_M) = 990$, which is orders of magnitude lower than available estimates of N_e in this species and close relatives ($N_e \cong 10^7$; Tsai *et al.* 2008; Liu and Zhang 2021), confirming that selection has acted to limit variance in CN, as expected.

The observed relationship between growth rate and CN suggests that selection on CN is stabilizing, at least in diploids (i.e., intermediate trait values are favored; Fig. 5). Several models have been proposed for the equilibrium genetic variance under mutation-stabilizing selection balance, and we consider the simplest two alternatives (see Falconer and Mackay 1996, pp. 352-3; Walsh and Lynch 2018, pp. 1031-3). The first approximation, originated by Kimura (1965), assumes a continuum of alleles at each locus and is most suitable when mutation is strong relative to stabilizing selection. We find that $V_M/V_E = 3.2 \times 10^{-2}$ for this trait, which is somewhat stronger than the "typical" range reported (10^{-4} to 10^{-2}); our estimate of $V_S/V_E = 9328$ is also much weaker than the range observed for most traits (100–10, lower values indicate stronger selection; Falconer and Mackay 1996, pp. 349-53). In the presence of strong mutational variance and weak stabilizing selection, we expect $V_G = \sqrt{2nV_MV_S}$, where n is the number of mutationally-equivalent loci underlying the trait. Given our estimates, at least 6.7 loci would be needed to explain observed levels of standing variance under this model, which seems highly plausible. The highest observed V_G value would imply 46 equivalent loci contribute to the trait, or 22 if we apply the upper 95% confidence limit for V_S.

Under the alternative "house of cards" approximation (Walsh and Lynch 2018, pp. 1036), we expect standing variance to be approximately $4V_SU$, where U is the rate of mutations affecting the trait, which we estimated above (Fig. S1). Our best estimate of $4V_SU$ is 289, or about 48% of the mean standing variance among clades. Applying our upper 95% confidence limit for V_S, mutation-selection balance can explain as much as 100.4% of the mean V_G. Applying the upper 95% credible value for U, mutation-selection balance can explain more variance than the largest value observed among clades (2218 vs. 1587).

While each of the terms and models used above is associated with uncertainty, our results indicate that standing genetic variance in CN can readily be explained by mutation-stabilizing selection balance. This conclusion is even more likely if we consider that mutational variance for CN may be elevated in alternative environments (Fig. 4), and that selection on CN may be particularly weak in natural haploid strains (Fig. 5).

Molecular patterns of rDNA variation

Specific point mutations implicated in CN change.

Our dataset may include cases where mutations of large effect cause extreme CN values. The most obvious example is a haploid line with a CN estimate of 187, highlighted in Fig. 7A. This line has non-synonymous mutations in eight genes, one of which, *RIF1*, has known associations with DNA repair and rDNA stability (Chapman *et al.* 2013; Shyian *et al.* 2016; Mattarocci *et al.* 2017; Hiraga *et al.* 2018). Rif1 is believed to inhibit replication origin firing, including at the rDNA locus; the inhibition of rDNA replication and the resulting replication fork stalling gives rise to DNA breakage (Shyian *et al.* 2016). Interestingly, two other haploid MA lines also have

missense mutations in *RIF1* (H984D; N1087K), but have typical CN. (This apparent coincidence may be due to the fact that *RIF1* is in a late-replicating region and near the end of the chromosome, conditions found to elevate the mutation rate in haploids (Sharp *et al.* 2018)). To understand the contrasting effects of these mutations we examined their positions in a published protein structure (Mattarocci *et al.* 2017) using Mol* (Sehnal *et al.* 2021). In this model, Rif1 forms a head-to-tail dimer, creating a high-affinity DNA-binding site (Mattarocci *et al.* 2017). As shown in Fig. S5, the lysine residue at position 1212 is predicted to interact with DNA, whereas the other two mutant residues are not close to the DNA-protein interface. Comparative data also suggest that K1212 is more constrained than the other amino acids, as it is present in the related species *S. paradoxus* and *S. eubayanus*, unlike H984 (C in both other species) or N1087 (Y in *S. paradoxus* and D in *S. eubayanus*). These results suggest K1212 has a conserved role in DNA binding, the disruption of which has a large effect on CN.

Most mutations in the diploid MA lines are heterozygous and may therefore have less obvious effects on CN, but several loss-of-heterozygosity events occurred during MA. We find that the diploid line with the lowest CN (33) has a homozygous missense mutation, K37T, in a gene implicated in rDNA stability, *MUS81* (Fig. 7A; Ii *et al.* 2007; Thu *et al.* 2015; Phung *et al.* 2020). Unlike this point mutation, *mus81Δ* results in increased CN (Ii *et al.* 2007). Finally, the diploid line with the highest CN has a heterozygous missense mutation, S89R, in the gene *DPB4* (Fig. 7A). In a large-scale screen, the deletion of this gene was found to decrease rDNA stability (Saka *et al.* 2016). Our finding that MA lines with extreme CN values also have point mutations in genes known to contribute to rDNA maintenance suggests that the function of these genes may sometimes be substantially altered by simple genetic changes.

Gene ontology terms associated with CN change.

To understand broad categories of genes involved in rDNA maintenance we examined the correlation between CN and the number of mutations occurring in genes annotated with 99 "biological process" gene ontology terms. Following multiple-testing correction, one term was statistically significant: GO:0051726 "regulation of cell cycle" ($t = 3.56$, un-corrected $P = 4.56 \times 10^{-4}$, corrected $P = 0.045$). Each additional non-synonymous mutation affecting genes annotated with this term resulted in a 15.7% higher CN on average (Fig. 7B). Cell cycle regulation has known connections with rDNA and the nucleosome (Lindström *et al.* 2018), and it appears that this relationship is detectable in the impacts of random point mutations.

Combining the CN estimates and genomic information from the Liu and Zhang (2019) dataset, we looked for GO terms associated with CN using linear mixed-effect models with a random effect of MA environment, after multiple testing correction. We do not find any significant results when considering only genes with missense and nonsense mutations, but when we include genes with synonymous mutations the term "transcription from RNA polymerase I promoter" (GO:0006360) is significant (likelihood ratio test: $\chi^2 = 14.62$, uncorrected $P = 1.32 \times 10^{-4}$, corrected $P = 0.013$). MA lines with one or more mutated genes in this category have about 24% higher CN than other lines, on average. RNA polymerase I is responsible solely for transcription of pre-rRNA at the rDNA repeats, and so these results suggest that mutations in genes with a role in RNA polymerase I activity, including synonymous mutations, tend to lead to increased CN. This is consistent with the results of Iida and Kobayashi (2019a), who showed that upstream

activating factors for RNA polymerase I also regulate *SIR2*, which in turn represses rDNA expansion.

Strains with trisomy-XII have lower CN.

A number of aneuploidy mutations arose in diploid lines during MA (Sharp *et al.* 2018), including five cases of trisomy for chromosome XII (the location of the rDNA array). Trisomy represents an instant 1.5-fold increase in the total number of rDNA copies per cell, which could down-regulate the activity of homeostatic rDNA amplification mechanisms, allowing CN per chromosome to decline. Consistent with this idea, the five trisomy-XII strains show lower copy numbers (per chromosome) than the other diploid strains and haploids (versus disomic diploids: $t = -4.1$, $P = 0.007$; versus haploids: $t = -3.6$, $P = 0.011$; Fig. 7C). There is no evidence that aneuploidy for other chromosomes is associated with CN ($t = 0.146$, $P = 0.88$). Alternatively, low CN strains could be more susceptible to aneuploidy for chromosome XII. In spite of the difference in copies per chromosome, strains with trisomy-XII still have more rDNA copies per genome overall (146 on average) compared with the other diploid strains (133 on average).

Point mutations within the rDNA locus.

Following variant screening, we identified 87 single-nucleotide mutations (SNMs) at the rDNA locus across 69 MA lines, as well as four small indels in four MA lines (three deletions and one insertion, all less than four bp; Table S3). We expect the number of genuine mutations in a line to be correlated with our power to detect such events, i.e., the product of MA generations, CN, and ploidy, although CN change throughout MA will weaken this correlation. Using the endpoint CN values, the number of rDNA point mutations observed in a given MA line was significantly

correlated with detection power (generalized linear model, $z = 4.5$, $P = 7.1 \times 10^{-6}$), suggesting that this dataset reflects true point mutations and not errors resulting from sequencing or alignment issues.

Accounting for endpoint CN in each line, we estimate a per-nucleotide SNM rate for the rDNA locus of 2.86×10^{-10} in haploids and 2.71×10^{-10} in diploids, with no significant difference between ploidy states (binomial test: $P = 0.82$; overall rate: 2.76×10^{-10}, 95% CI: $2.21–3.40 \times 10^{-10}$). These rates are similar to the genome-wide SNM rate inferred for diploids (2.89×10^{-10}), and lower than that of haploids (4.04×10^{-10}; Sharp *et al.* 2018). There was no evidence that the status of *RDH54* affected the SNM rate in either haploids or diploids (binomial tests, $P = 1$ and 0.15 respectively). A rough estimate of the indel rate from these data is 1.27×10^{-11} (95% CI: $0.35–3.25 \times 10^{-11}$), similar to the genome-wide rate estimates for these lines (haploids: 1.63×10^{-11}, diploids: 2.03×10^{-11}). These results would suggest that the point mutation rate is not greatly elevated at the highly-transcribed rDNA locus, but are likely to be biased by copy turnover, as discussed below.

We used the frequency of each mutant allele along with the rDNA copy number estimate in the corresponding MA line to estimate the number of rDNA copies that contain the mutant allele. If there were no dynamic change in CN we'd expect all mutant alleles to be present in a single copy. CN change could cause mutant alleles to be lost or amplified, but we might predict that such changes will usually not involve a mutant copy, owing to its low initial frequency. As expected, most of the mutations we detected appear to be present in just one or two copies, with rare cases of higher copy number (Fig. 8A). The two cases of very high mutant copy number are

both in diploid lines, occur in *RDN18* and *NTS2*, have mutant frequencies of 0.35 and 0.31, and do not appear to be unusual in terms of overall CN (76 and 102 copies per chromosome respectively). While genetic variation at the rDNA locus itself could affect CN by altering the dynamics of copy loss and amplification, in our experiment most such variants affect only a small fraction of copies, which will likely limit their impact on overall CN.

The regular loss and gain of rDNA copies means that point mutations could occur and then subsequently be lost, leading us to underestimate the mutation rate at this locus. A similar issue occurs genome-wide in diploids, where loss-of-heterozygosity events can cause heterozygous mutant sites to become homozygous for the ancestral allele, slightly biasing mutation rate estimates downwards (Sharp *et al.* 2018). At the rDNA locus we may be able to account for this bias in a rudimentary fashion by using the observed number of multi-copy point mutations, which represent amplification events, as an estimate of the number of mutation events that were lost and not observed. This assumes that amplification and loss occur at equal rates, and that single-copy point mutations are not the result of a combination of amplification and subsequent loss. Estimating the true number of single-nucleotide point mutations across lines as $n_{\text{single-copy}} + 2n_{\text{multi-copy}}$, we estimate a haploid mutation rate at this locus of 3.28×10^{-10}, which is 81% of the genome-wide rate for haploids (Sharp *et al.* 2018) and not significantly different (proportion test: $\chi^2 = 1.16$, $P = 0.28$). In contrast, this bias correction results in a diploid mutation rate estimate of 4.07×10^{-10}, which is 41% higher than the genome-wide rate for diploids (Sharp *et al.* 2018), and significantly different (proportion test: $\chi^2 = 10.28$, $P = 0.001$). We therefore see some evidence for an elevated mutation rate at this locus, but this result involves an *ad hoc* bias correction procedure and appears to be restricted to diploids.

We examined the spectrum of SNMs at the rDNA locus, pooling data from all MA lines, and compared this with the genome-wide pattern previously identified in these lines (Sharp *et al.* 2018). The frequencies shown in Fig. 8B account for G/C content, which is greater in the rDNA region than the rest of the genome (45% versus 38%). Comparing rDNA with the rest of the genome, the SNM spectrum differs at both A:T sites ($\chi^2 = 28.8$, $df = 2$, $P = 5.5 \times 10^{-7}$) and C:G sites ($\chi^2 = 15.8$, $df = 2$, $P = 3.7 \times 10^{-4}$), and A to C transversions are especially common. Accounting for nucleotide composition, the rate of mutation from A/T to C/G at the rDNA locus is 1.7-times that of the opposite rate, in contrast to the corresponding genome-wide ratio of 0.35, which could reflect strong GC-biased gene conversion in this region of the genome (Hillis *et al.* 1991; Escobar *et al.* 2011).

The mutations we identified are distributed across the rDNA locus, but appear more frequently in NTS regions (non-transcribed spacers, also called intergenic spacers, IGS) than expected if mutations occur uniformly across the locus (Fig. 8C, Fisher's exact test: odds ratio 1.93, $P = 0.0047$). This bias is unlikely to be due to differences in selection, given that the mutations affect only a few copies of the rDNA locus and selection under MA is largely ineffective. James *et al.* (2009) studied polymorphism at the rDNA locus within and among 34 strains of *S. cerevisiae* from various origins. They found that a large majority of polymorphisms occurred in the NTS regions, and attributed this pattern to functional constraint in the core regions of the locus. Examining 100-bp windows along the locus, we find that the number of single-nucleotide mutations we observed in a window is a significant predictor of polymorphism (Fig. 8D; quasi-Poisson regression, $t = 3.13$, $P = 2.4 \times 10^{-3}$). This suggests that the high rate of evolution in

spacer regions relative to core regions may be driven, at least in part, by mutation bias. In particular, the spacer region NTS1 contains a replication fork barrier, which is believed to be a hotspot for double-strand breaks and recombination (Kobayashi *et al.* 2001); high rates of DNA damage and repair in this region may help drive rapid evolution, rather solely a lack of purifying selection.

Rate and effects of loss-of-heterozygosity (LOH) events.

Sharp *et al.* (2018) detected 21 homozygous point mutations in diploid MA lines distal to the rDNA locus on chromosome XII. Our simulations indicate that the underlying rate of recombination events at the rDNA locus leading to distal LOH along the chromosome is approximately 0.0023 per diploid genome per generation, or one event in every 434 cell divisions (posterior distribution in Fig. S6; 95% credible interval: 0.0013–0.0096). In other words, over 400 events likely occurred that homogenized chromosome XII distal to the rDNA region over the course of the MA experiment, but we detected only those 21 instances that led to homozygosity for pre-existing point mutations.

The high LOH rate we observe, relative to the point mutation rate, implies that the lines where LOH was detected are likely not exceptional with respect to their recombination rates. Lines where LOH was detected do not differ in CN (linear model with *RDH54* status as a covariate, $t = 0.52$, $P = 0.61$), but they do show higher numbers of SNMs and indels within the rDNA region itself (generalized linear models accounting for detection power; SNMs: $z = 2.94$, $P = 0.003$; indels: $z = 2.2$, $P = 0.029$). 35.0% of point mutations within the rDNA locus occurred in lines where LOH was detected, whereas 19.3% would be expected by chance, indicating an

association between LOH and point mutation in this region. There was no evidence that these point mutations differed in frequency (Wilcox test, $W = 530$, $P = 0.49$) or spectrum ($\chi^2 = 3.23$, $df = 4$, $P = 0.52$) depending on LOH status. Our data provide a quantitative estimate of the spontaneous rate of LOH in this region, and indicate that LOH occurs much more frequently than point mutations, rapidly eliminating heterozygosity in this region in the absence of effective selectio

DISCUSSION

The rDNA repeat locus displays unique evolutionary dynamics; while we can gain insight by treating CN as a quantitative trait, in reality it is a "genomic trait" with high heritability and high intrinsic mutability. Models of evolution at this locus suggest that it is canalized against biased mutational change through mechanisms of directed mutation. We might therefore expect CN changes to persist only when mutations affect these canalizing mechanisms. The evolution of canalization for a quantitative trait implies that selection favors intermediate trait values, but the role of selection in CN maintenance is unclear. Our MA approach allows us to separate the effects of mutation and selection to quantify the evolutionary forces acting on this unique genomic region.

Under mutation accumulation, we repeatedly observed declines in mean CN; this pattern was evident in both haploids and diploids derived from the SEY6211 strain (Fig. 3; Sharp *et al.* 2018), and in diploids of the BY4743 strain propagated in both the standard media environment and several other environments (Fig. 4; Liu and Zhang 2019). The observed rates translate into a net loss of one copy every 67–120 generations, on average. A study of rDNA in mutation

accumulation lines of *Daphnia pulex* found that CN was relatively stable under normal conditions but declined under exposure to heavy metals (Harvey *et al.* 2020). The fact that genome-wide mutations are more likely to result in decreases rather than increases in CN is consistent with a model of CN maintenance where DNA repair errors tend to cause the loss of one or more copies, which is normally counteracted by homeostatic amplification mechanisms (Kobayashi 2006, 2011; Iida and Kobayashi 2019a); mutations appearing throughout the genome can compromise these amplification mechanisms, generally resulting in CN decline. Mutations might also cause CN increases by altering how amplification mechanisms respond to current copy number, but this outcome seems to be less common.

We also observed increases in CN variance among lines under mutation accumulation. Standardizing by the trait mean allows us to compare our estimates to other "metric" traits that have been studied, such as bristle numbers in *Drosophila melanogaster*; based on a number of experiments, the average CV_M is 0.38% and 0.47% for abdominal and sternoplural bristle numbers, respectively (Houle *et al.* 1996), lower than the level we estimate for CN (0.75%). This implies that CN has moderate or high susceptibility to mutation, either because many loci affect the trait, mutations at these loci have large effects, or both. Our model of mutation rates and effects (Fig. S1) suggests that large-effect variants are not uncommon; we also estimate that a mutation that alters CN in some way occurs every 1250 cell divisions, which would represent >13% of the overall mutation rate in these lines. Our alternative model, which assumes instead that mutations alter the rate of subsequent CN change—and can therefore contribute to high CN variance if they arise early in MA (Fig. S4)—is more conservative, implying that 5% of all mutations alter CN. Our analyses of GO terms detectably associated with CN in two datasets

implicate 5.8% of genes in total. These values seem high, but are consistent with the findings of Saka *et al.* (2016), who concluded that >10% of yeast genes contribute to CN maintenance based on the effects of gene deletions. These various approaches all support the idea that CN variation will arise rapidly due to spontaneous mutation alone, i.e., CN is a large "mutational target".

High variation in CN will not necessarily result in high variation for fitness, and several observations suggest that yeast growth rates are relatively insensitive to CN variation. First, the overall variance in growth caused by mutations in the Sharp *et al.* (2018) lines is considerably less than the corresponding variance in CN (CV_M of 0.08% versus 0.75%). Second, the association between growth rates and CN indicates weak apparent stabilizing selection in diploids, and little or no selection in haploids (Fig. 5). Finally, the observed level of standing variation in CN within clades can plausibly be explained by a balance between strong mutation and weak stabilizing selection, i.e., diversifying selection does not seem to be playing a major role, but neutral evolution can also be excluded. This kind of comparison between mutational and standing variation for a trait is a useful approach to understanding the forces that maintain genetic variation, since mutation-selection balance will always contribute variation to traits under selection, and other contributors are harder to quantify (Charlesworth and Hughes 1999; Charlesworth 2015; Farhadifar *et al.* 2016; Huang *et al.* 2016; Sharp and Agrawal 2018). While it is possible to imagine selection favoring higher or lower CN in alterative environments and leading to additional diversity, it appears that much of the standing variation for this trait can be explained more simply by mutation-selection balance. In addition, there is evidence that environmental differences can add to mutational variation in CN (Fig. 4; Harvey *et al.* 2020), making mutation even more likely as an explanation for standing variation.

Our analysis doesn't account for the effects of other mutations on growth, with the exception of aneuploidy, and if CN change were correlated with the rate of point mutations we could detect a spurious relationship between fitness and CN. We don't find evidence for such a correlation (diploids: $r = 0.035$, $P = 0.71$; haploids: $r = 0.020$, $P = 0.84$), and so other mutations will likely cause us to underestimate the strength of the CN-fitness association. The CN variation we can examine is un-selected but not completely random, since there appears to be a mutational bias towards CN reduction; ideally we would want to know how CN affects fitness in the absence of other genetic differences. Studies that have examined the growth of strains with a broad range of CN find little evidence for growth rate differences (Kobayashi *et al.* 1998; French *et al.* 2003), though the strains studied are generally haploid, which our results suggest might be less sensitive to CN variation than diploids.

Our study was not designed specifically to screen for genes that contribute to rDNA maintenance. Nevertheless, we note that the MA lines with extreme CN values tend to carry mutations in genes already known to be involved in rDNA maintenance (Fig. 7A), including mutations in *RIF1* with apparently contrasting effects depending on their exact location in the protein (Fig. S5). The fact that each MA line carries multiple point mutations (9 on average) makes it harder to attribute phenotypes to specific mutations, and we have not conducted direct manipulations to verify the effects of specific alleles. However, we also see statistical associations between CN and certain gene ontology categories (Fig. 7B), as well as trisomy for chromosome XII (Fig. 7C), reflecting some of the underlying molecular causes of CN variation.

In addition to variation in copy number, point mutations can occur within the rDNA repeats themselves. We detected 91 point mutations, whose spectrum differs considerably from the genome-wide pattern (Fig. 8B). The loss of rDNA copies and their restoration using remaining copies should ultimately lead to sequence homogenization across copies (Ganley and Kobayashi 2007, 2011; Haig 2021), and this process is reflected by the frequency distribution of point mutations (Fig. 8A), which are mostly rare but occasionally spread to many copies. The same process will lead to the loss of point mutations in this region, causing us to underestimate its mutation rate. Applying a basic correction for this bias, we see some evidence that the mutation rate in diploids is higher at the rDNA locus than it is in the rest of the genome, consistent with the idea that high levels of transcription can increase the rate of point mutation (Kim and Jinks-Robertson 2012; Chen and Zhang 2014; Salim and Gerton 2019). However, aspects of the rDNA locus beyond transcription could also contribute to elevated mutation rates, including frequent DNA breakage and repair. We find a positive association between the point mutation rate at the rDNA locus and recombination in the form of loss of heterozygosity (LOH) events affecting chromosome XII. LOH in this region is observed frequently (Heil *et al.* 2017; Fisher *et al.* 2018; James *et al.* 2019; Pankajam *et al.* 2020), and our results suggest these events may be linked to the generation of new variants at the rDNA locus itself. We also find that point mutations and polymorphisms within the rDNA locus occur at correlated locations, particularly the non-transcribed spacer regions that are hotspots for DNA breaks (Fig. 8C-D), indicating that mutational bias also contributes to the excess of variation observed in these regions.

Our main goal was to add a quantitative perspective to our understanding of rDNA evolution, distinguishing the impacts mutation and selection on an important genomic trait. We made use of

existing models of quantitative trait evolution, but theoretical work incorporating the unique dynamics of this region would be valuable for designing and interpreting future experiments.

MATERIALS AND METHODS

Mutation accumulation and sequencing.

The methods used for mutation accumulation (MA) in haploid and diploid yeast lines have been reported previously (Sharp *et al.* 2018). Briefly, we began with a single cell of strain SEY6211 (*MAT*a *ho leu2-3, 112 ura3-52 his3-Δ200 trp1-Δ901 ade2- 101 suc2-Δ9*), induced a mating-type switch, and generated replicate haploid lines of each mating type, as well as a diploid obtained by crossing the mating types. In parallel, we deleted the gene *RDH54* via transformation in each mating type of this genetic background, and mated them. In summary, the MA lines consist of haploid and diploid lines with or without the *RDH54* deletion, with 220 lines in total. We cryopreserved these strains as ancestral controls and plated to single colonies to begin the bottlenecking procedure. This strain does not appear to possess the "weak" allele at rDNA replication origins that has previously been found in some strains (Kwan *et al.* 2013).

We conducted MA in each line by transferring a single random colony to a new plate daily, streaking to obtain new single colonies, and conducting cell counts from random colonies to monitor rates of cell division. Following 100 bottlenecks, we cryopreserved all lines and extracted DNA from ~10^9 cells using a phenol/chloroform method. We used 0.4 ng of DNA per strain to construct libraries using the Illumina Nextera XT kit and protocol. Libraries were pooled such that diploid samples had twice the concentration of haploid samples (to give equivalent coverage per chromosome) and sequenced in an Illumina NextSeq lane with paired-

end 150-bp reads (average coverage per line before screening: haploid 24.5×, diploid 47.6×). MA line sequence data are available from the National Center for Biotechnology Information Sequence Read Archive (accession no. SRP139886). We conducted additional blocks of sequencing for ancestral control strains, and re-sequenced one MA line that showed unusual coverage patterns. We aligned reads to the S288c reference genome using Burrows-Wheeler aligner *mem* (Li and Durbin 2009).

Digital droplet PCR (ddPCR).

To quantify copy number of the rDNA region using ddPCR we used the gene *RDN25*, which encodes the 25S ribosomal subunit (Fig. 1), as well as a single-copy reference gene on the same chromosome arm, *RAD5*, for comparison. Using a standard on the same chromosome ensures that the results are not influenced by aneuploidy. We used the primer design program *Primer3web* (Köressaar and Remm 2007; Untergasser *et al.* 2012; Köressaar *et al.* 2018) to generate primers and probes for the target and reference genes. Primers and probes were further screened for primer-dimer interactions using the program *PrimerDimer* from *PrimerSuite* (Lu *et al.* 2017). Primer and probe sequences are listed in Table S1. Primers were purchased from Integrated DNA Technologies (Coralville, IA) and TaqMan MGB probes from Thermo Fisher Scientific (Waltham, MA).

Using DNA samples from MA and control lines, we performed a restriction digest using the enzyme DraI (New England BioLabs, Ipswich, MA), which has cut sites flanking our probe locations for *RDN25* (Fig. 1), and *RAD5* (not shown), according to the manufacturer's directions; 0.5 µg of DNA was cut using 10 U of DraI in a 50 µl reaction at 37°C for 30 minutes, then

incubated at 65°C to stop digestion. This resulted in 0.02 µg/µL of digested DNA. We made serial dilutions in 10 mM Tris, 0.1 mM EDTA using the digested DNA down to 1:2000. Test runs of ddPCR determined that the proper working dilution of the digested DNA was 1:50 for *RAD5* and 1:1250 for *RDN25*.

For the ddPCR assay, we made 21 µL of reaction mix for each sample according to the manufacturer's directions (Bio-Rad Laboratories, Hercules, CA). Each reaction consisted of 2× ddPCR Supermix for Probes, 0.2 µM of each RDN25 primer or 0.4 µM of each RAD5 primer, 0.58 µM of the RDN25 probe or 0.115 µM of the RAD5 probe, 1 µL of the proper DNA dilution, and sterile Type I water. We generated droplets from 20 µL of reaction mix and 70 µL of Droplet Generation Oil using the QX200 Droplet Generator (Bio-Rad Laboratories). We ran polymerase chain reactions in a Bio-Rad C1000 Touch Thermal Cycler, and used gradient reactions to determine that the optimal annealing temperature was 53°C which was used thereafter (95°C for 10 min, 40 cycles of 94°C for 30 sec and 53°C for 1 min, 98°C for 10 min). Finally, we analyzed amplified DNA in droplets with a QX200 Droplet Reader (Bio-Rad Laboratories). In total we collected 180 pairs of measurements from 56 MA and control lines. The average number of droplets was 12724 for *RDN25* and 12813 for *RAD5*.

We used Quantasoft® software (version 1.5.38.118) to determine the absolute quantification of each target, expressed as copies/µL. We allowed thresholds to be determined automatically by Quantasoft unless the number of droplets analyzed was <10,000, in which case we examined the data and manually set an appropriate threshold. We estimated the copy number of *RDN25* per

chromosome by dividing the dilution-adjusted copies/μL of *RDN25* by the dilution-adjusted copies/μL of *RAD5*.

Calibration of NGS-based copy number estimates.

Depth of sequencing coverage has been used previously to characterize the copy number of multi-copy genetic elements (Alkan *et al.* 2009; Sudmant *et al.* 2010; Gibbons *et al.* 2014, 2015; Glusman *et al.* 2015; Lofgren *et al.* 2019), but could be affected by several types of sequencing bias (Buckler *et al.* 1997; Benjamini and Speed 2012; Morton *et al.* 2019; Sharma *et al.* 2021). A more precise method is available in ddPCR (Hindson *et al.* 2011), but this is resource intensive for hundreds of strains. We therefore used ddPCR estimates from a subset of strains to calibrate a coverage-based estimation procedure.

We examined the replicate estimates of rDNA copy number from ddPCR (2.8 replicates per strain, on average), and found that the time since dilution was a significant predictor of copy number (linear mixed model with main effect of log-dilution age and random effect of strain on slope and intercept, likelihood ratio test, $\chi^2 = 15.922$, $df = 1$, $P = 6.6 \times 10^{-5}$), with higher copy number inferred from more-recent dilutions. We therefore used the predicted value from this model with a dilution age of zero for each strain as our ddPCR estimates of copy number.

Our next goal was to use the 56 strains with both NGS and ddPCR data to determine which genomic regions show relative coverage levels (and therefore putative rDNA copy numbers) that best correspond with our ddPCR estimates. To do this we used an optimization approach to identify those genomic regions to use for coverage analysis which led to the strongest correlation

with our ddPCR estimates. We first calculated the "background" coverage level for chromosome XII in each strain as the average coverage in the regions 100,000 bp to 400,000 bp and 600,000 bp to 1,000,000 bp. These regions represent 65% of the reference chromosome length and were selected to exclude the rDNA repeat region and the chromosome ends. Five of the diploid MA lines are aneuploid (trisomic) for chromosome XII, and multiple other lines have aneuploidy for other chromosomes; using coverage from chromosome XII rather than the genome-wide average ensures that aneuploidy will not have confounding effects on our copy number estimates.

In principle, the rDNA copy number for a given strain could be indicated by the average coverage in the entire rDNA region (ChrXII:451418–468929) relative to the background coverage, but given the degree of coverage variation across this region (Fig. 1) we opted to instead allow an optimization algorithm to determine the regions which best predicted the ddPCR values. As the rDNA region is represented by 1.92 copies in the reference genome (Johnston *et al.* 1997; Cherry *et al.* 2012), we considered two segments of equal length: the first from position 451418 + *a* to 451418 + *a* + *b*, and the second from 460554 + *a* to 460554 + *a* + *b*, where 460554 is the starting point of the second reference repeat, *a* represents a gap on the left side of each segment (minimum 0), and *b* represents the length of each segment. For given values of *a* and *b* the NGS-based copy number estimate for a strain was calculated as the average coverage for the selected region divided by the background coverage, and multiplied by two (to account for the presence of two copies in the reference sequence). We then applied a linear model of ddPCR-based copy number on NGS-based copy number with sequencing block as a covariate, using all 56 strains, and obtained the r^2 value. We searched for optimal values of *a* and *b*, i.e., those that result in a higher r^2 value, using the Nelder-Mead algorithm implemented in the

bbmle:*mle2* function in *R* (Bolker 2021; R Core Team 2021). The optimal values of $a = 0$ and $b = 4790$ resulted in a highly-significant model fit ($F = 44.94$, $df = 4, 51$, $P < 10^{-15}$) with an r^2 value of 0.78, and the selected regions overlap the ddPCR probe locations (Fig. 1, Fig. 2). We used this model to estimate NGS-based copy number for all 229 MA and ancestral control strains.

Environmental impact on CN change under MA.

To gain additional insight into the contributions of mutation to CN evolution in yeast we examined data from another set of 167 diploid MA lines, in which MA occurred in one of seven different media environments for about 1000 generations (Liu and Zhang 2019). Following MA, each strain was grown in a common, benign media environment prior to DNA extraction and sequencing (H. Liu, pers. comm.), which should remove any direct effect of the various environmental conditions on CN. We obtained raw data from this experiment from Sequence Read Archive (NCBI BioProject: PRJNA510430), including reads from an ancestral control strain, performed the same alignment steps as with the Sharp *et al*. (2018) dataset, and used coverage at the same regions of the rDNA locus to infer CN (Fig. 2). Note that we did not apply ddPCR to these strains, and so absolute CN values for this dataset will only be accurate if the calibration based on one set of MA lines is applicable to a distinct set of lines.

Inferring rates and effects of CN-altering mutations.

Data on trait values of MA lines can be used to infer the most likely underlying rates and effects of mutations in a model framework (Keightley 1994; García-Dorado and Marín 1998; Keightley and Bataillon 2000; Hall *et al.* 2007). Our general observations are useful in determining the

elements needed for such a model: while it is apparent that many mutations likely cause decreased copy number, there are clear examples of lines with increased copy number; additionally, mutations that increase versus decrease copy number may differ in the distributions of their effects, i.e., the mean and variance. Given this number of parameters, it would be computationally challenging to analyze an explicit maximum likelihood model. Instead, we used an approximate Bayesian computation (ABC) approach, in which parameters are drawn from a prior distribution and used to simulate data, and parameters are retained that produce summary statistics similar to the observed data. For this analysis we considered only *RDH54*$^{+}$ lines from Sharp *et al.* (2018). Results were very similar for haploids and diploids so we present results for these lines pooled (n = 116; Fig. S1), with separate results for haploids and diploids shown in Fig. S2-3.

The simulation model draws some number of mutations per line from a Poisson distribution with mean Utc, where U is the rate of mutation per genome per generation to alleles that affect rDNA copy number, t is the number of generations of MA, and c is the number of chromosomes that can mutate (1 for haploids and 2 for diploids). Each mutation has probability p_{up} of increasing copy number and otherwise decreases copy number. For mutations leading to reduced (increased) copy number, effects were simulated from a gamma distribution with mean μ_{down} (μ_{up}) and variance σ^2_{down} (σ^2_{up}), with downward effects converted to negative values. We chose the gamma function to simulate mutational effect distributions because it can take on a number of different shapes and is bounded by zero. The combination of these parameters determined the genetic value simulated for each line. We used uniform prior distributions for all parameters with a minimum of zero and a maximum of 0.01 for U, 1.0 for p_{up}, and 100 otherwise. Finally,

realized values were simulated by adding a random normal deviate with a mean of zero and an error variance of 9.245, which is derived from the variance among three measures of copy number from ancestral wild-type diploids, obtained from the same sequencing run.

To efficiently explore the parameter space we used the function *ABC_mcmc* from the *R* package *EasyABC* (Jabot *et al.* 2015), applying the method *Marjoram* (Marjoram *et al.* 2003; Wegmann *et al.* 2010) that uses a Markov Chain Monte Carlo approach to generate observations from the posterior distribution. The distance between simulated and observed values was described by the difference in means, the difference in variances, and the sum of absolute differences in cumulative density. We first performed a calibration step of 10^5 simulations to automatically determine MCMC settings, and then sampled 10^5 points from approximately 1.1 x 10^6 simulations to obtain posterior distributions. We determined posterior modes using the *density* function for kernel density estimation.

Gene ontology analysis.

We examined the relationship between CN and the number of mutations occurring in genes associated with particular biological processes. We downloaded gene ontology (GO) "biological process" annotations from Saccharomyces Genome Database (Cherry *et al.* 2012), which includes 99 unique terms. For each term, we determined the number of genes annotated with that term that were affected by non-synonymous mutations in each MA line. We then fit a linear model of CN on the number of genes affected, with *RDH54* status, ploidy, and trisomy-XII as covariates. For each GO term we stored the *P*-value associated with the number of genes

affected. Finally, we applied a multiple-testing correction to the 99 *P*-values using the Benjamini-Hochberg procedure (Benjamini and Hochberg 1995).

Calling point mutations within the rDNA locus.

A prior study of these MA lines (Sharp *et al.* 2018) did not attempt to identify point mutations in the rDNA repeat region. Using their alignment data we obtained reads that aligned to the relevant region of the reference genome. Next, we used *bwa mem* (Li and Durbin 2009) to re-align those reads to a custom reference sequence composed of just the first rDNA repeat from the reference genome. We then used *samtools mpileup* (Li *et al.* 2009; Li 2011) followed by *varscan2* (version 2.3.9; (Koboldt *et al.* 2012) to call single-nucleotide variants and indels, with a minimum base quality score of 30, and retained variants associated with a P-value of 0.01 or less. Finally, we considered only variants called in a single MA line, which should eliminate false positives while retaining the vast majority of true mutations (Sharp *et al.* 2018).

Loss of heterozygosity rate.

During MA, mitotic recombination can result in loss of heterozygosity (LOH), which is detectable when a pre-existing point mutation becomes homozygous. In this dataset such events are particularly common on chromosome XII distal to the rDNA repeat region, in which 21 out of 28 point mutations are homozygous (all in different lines, see Fig. S7 in Sharp *et al.* 2018). Assuming that all LOH distal to the rDNA region originates as recombination events at the rDNA locus, rather than smaller gene conversion events (see (Lindstrom *et al.* 2011), we can use the number of homozygous point mutations in this region to estimate the rate of LOH-inducing events at the rDNA locus.

We can detect LOH events only when they occur after at least one point mutation in this region in the same MA line; of these events, only half will be detected if point mutations are present only on one homologous chromosome, because LOH can cause the mutant allele to be lost; if point mutations are present on both homologs LOH will always be detectable. We created stochastic simulations assuming that point mutations occur at the diploid rate reported by Sharp *et al.* (2018) over the course of MA, along with some rate of LOH events that cause homozygosity for one of the two homologous chromosomes, selected at random. We again used the *ABC_mcmc* function to identify underlying rates of LOH that could give rise to the observed number of homozygous variants in this region. We retained 500 of approximately 5000 simulations following calibration with 100 simulations.

References

Alkan C., J. M. Kidd, T. Marques-Bonet, G. Aksay, F. Antonacci, *et al.*, 2009 Personalized Copy-Number and Segmental Duplication Maps using Next-Generation Sequencing. Nat Genet 41: 1061–1067. https://doi.org/10.1038/ng.437

Benjamini Y., and Y. Hochberg, 1995 Controlling the False Discovery Rate: A Practical and Powerful Approach to Multiple Testing. J Royal Statistical Soc Ser B Methodol 57: 289–300. https://doi.org/10.1111/j.2517-6161.1995.tb02031.x

Benjamini Y., and T. P. Speed, 2012 Summarizing and correcting the GC content bias in high-throughput sequencing. Nucleic Acids Res 40: e72–e72. https://doi.org/10.1093/nar/gks001

Bolker B., 2021 bbmle: Tools for general maximum likelihood estimation. R package version 1.0.24. https://CRAN.R-project.org/package=bbmle

Buckler E. S., A. Ippolito, and T. P. Holtsford, 1997 The evolution of ribosomal DNA: divergent paralogues and phylogenetic implications. Genetics 145: 821–32. https://doi.org/10.1093/genetics/145.3.821

Chapman J. R., P. Barral, J.-B. Vannier, V. Borel, M. Steger, *et al.*, 2013 RIF1 Is Essential for 53BP1-Dependent Nonhomologous End Joining and Suppression of DNA Double-Strand Break Resection. Mol Cell 49: 858–871. https://doi.org/10.1016/j.molcel.2013.01.002

Charlesworth B., and K. A. Hughes, 1999 The maintenance of genetic variation in life-history traits, in *Evolutionary genetics: From molecules to morphology*, edited by Singh R., Krimbas C. Cambridge University Press, Cambridge UK.

Charlesworth B., 2015 Causes of natural variation in fitness: Evidence from studies of Drosophila populations. Proc National Acad Sci 112: 1662–1669. https://doi.org/10.1073/pnas.1423275112

Chen X., and J. Zhang, 2014 Yeast mutation accumulation experiment supports elevated mutation rates at highly transcribed sites. Proc National Acad Sci 111: E4062–E4062. https://doi.org/10.1073/pnas.1412284111

Cherry J. M., E. L. Hong, C. Amundsen, R. Balakrishnan, G. Binkley, *et al.*, 2012 Saccharomyces Genome Database: the genomics resource of budding yeast. Nucleic Acids Res 40: D700–D705. https://doi.org/10.1093/nar/gkr1029

Conrad D. F., and M. E. Hurles, 2007 The population genetics of structural variation. Nat Genet 39: S30–S36. https://doi.org/10.1038/ng2042

Delany M. E., D. E. Muscarella, and S. E. Bloom, 1994 Effects of rRNA Gene Copy Number and Nucleolar Variation on Early Development: Inhibition of Gastrulation in rDNA-Deficient Chick Embryo. J Hered 85: 211–217. https://doi.org/10.1093/oxfordjournals.jhered.a111437

de Visser J. A. G. M., J. Hermisson, G. P. Wagner, L. A. Meyers, H. Bagheri-Chaichian, *et al.*, 2003 Perspective: Evolution and detection of genetic robustness. Evolution 57: 1959–1972. https://doi.org/10.1111/j.0014-3820.2003.tb00377.x

Escobar J. S., S. Glémin, and N. Galtier, 2011 GC-Biased Gene Conversion Impacts Ribosomal DNA Evolution in Vertebrates, Angiosperms, and Other Eukaryotes. Mol Biol Evol 28: 2561–2575. https://doi.org/10.1093/molbev/msr079

Falconer D. S., and T. F. C. Mackay, 1996 *Introduction to Quantitative Genetics*. Longman Group Ltd., Essex UK.

Farhadifar R., J. M. Ponciano, E. C. Andersen, D. J. Needleman, and C. F. Baer, 2016 Mutation Is a Sufficient and Robust Predictor of Genetic Variation for Mitotic Spindle Traits in Caenorhabditis elegans. Genetics 203: 1859–1870. https://doi.org/10.1534/genetics.115.185736

Fine R. D., N. Maqani, M. Li, E. Franck, and J. S. Smith, 2019 Depletion of Limiting rDNA Structural Complexes Triggers Chromosomal Instability and Replicative Aging of Saccharomyces cerevisiae. Genetics 212: genetics.302047.2019. https://doi.org/10.1534/genetics.119.302047

Fisher K. J., S. W. Buskirk, R. C. Vignogna, D. A. Marad, and G. I. Lang, 2018 Adaptive genome duplication affects patterns of molecular evolution in Saccharomyces cerevisiae. Plos Genet 14: e1007396. https://doi.org/10.1371/journal.pgen.1007396

Flynn J. M., I. Caldas, M. E. Cristescu, and A. G. Clark, 2017 Selection Constrains High Rates of Tandem Repetitive DNA Mutation in Daphnia pulex. Genetics 207: 697–710. https://doi.org/10.1534/genetics.117.300146

Flynn J. M., S. E. Lower, D. A. Barbash, and A. G. Clark, 2018 Rates and Patterns of Mutation in Tandem Repetitive DNA in Six Independent Lineages of Chlamydomonas reinhardtii. Genome Biol Evol 10: 1673–1686. https://doi.org/10.1093/gbe/evy123

French S. L., Y. N. Osheim, F. Cioci, M. Nomura, and A. L. Beyer, 2003 In Exponentially Growing Saccharomyces cerevisiae Cells, rRNA Synthesis Is Determined by the Summed RNA Polymerase I Loading Rate Rather than by the Number of Active Genes. Mol Cell Biol 23: 1558–1568. https://doi.org/10.1128/mcb.23.5.1558-1568.2003

Ganley A. R. D., and T. Kobayashi, 2007 Highly efficient concerted evolution in the ribosomal DNA repeats: Total rDNA repeat variation revealed by whole-genome shotgun sequence data. Genome Res 17: 184–191. https://doi.org/10.1101/gr.5457707

Ganley A. R. D., and T. Kobayashi, 2011 Monitoring the Rate and Dynamics of Concerted Evolution in the Ribosomal DNA Repeats of Saccharomyces cerevisiae Using Experimental Evolution. Mol Biol Evol 28: 2883–2891. https://doi.org/10.1093/molbev/msr117

García-Dorado A., and J. M. Marín, 1998 Minimum distance estimation of mutational parameters for quantitative traits. Biometrics 54: 1097–114.

Gibbons J. G., A. T. Branco, S. Yu, and B. Lemos, 2014 Ribosomal DNA copy number is coupled with gene expression variation and mitochondrial abundance in humans. Nat Commun 5: 4850. https://doi.org/10.1038/ncomms5850

Gibbons J. G., A. T. Branco, S. A. Godinho, S. Yu, and B. Lemos, 2015 Concerted copy number variation balances ribosomal DNA dosage in human and mouse genomes. Proc National Acad Sci 112: 2485–2490. https://doi.org/10.1073/pnas.1416878112

Glusman G., A. Severson, V. Dhankani, M. Robinson, T. Farrah, *et al.*, 2015 Identification of copy number variants in whole-genome data using Reference Coverage Profiles. Frontiers Genetics 6: 45. https://doi.org/10.3389/fgene.2015.00045

Haig D., 2021 Concerted evolution of ribosomal DNA: Somatic peace amid germinal strife. Bioessays 2100179. https://doi.org/10.1002/bies.202100179

Hall D. W., R. Mahmoudizad, A. W. Hurd, and S. B. Joseph, 2007 Spontaneous mutations in diploid Saccharomyces cerevisiae: another thousand cell generations. Genet Res 90: 229–241. https://doi.org/10.1017/s0016672308009324

Halligan D. L., and P. D. Keightley, 2009 Spontaneous Mutation Accumulation Studies in Evolutionary Genetics. Annu Rev Ecol Evol Syst 40: 151–172. https://doi.org/10.1146/annurev.ecolsys.39.110707.173437

Harvey E. F., M. E. Cristescu, J. Dale, H. Hunter, C. Randall, *et al.*, 2020 Metal exposure causes rDNA copy number to fluctuate in mutation accumulation lines of Daphnia pulex. Aquat Toxicol 226: 105556. https://doi.org/10.1016/j.aquatox.2020.105556

Heil C. S. S., C. G. DeSevo, D. A. Pai, C. M. Tucker, M. L. Hoang, *et al.*, 2017 Loss of Heterozygosity Drives Adaptation in Hybrid Yeast. Mol Biol Evol 34: 1596–1612. https://doi.org/10.1093/molbev/msx098

Hillis D. M., C. Moritz, C. A. Porter, and R. J. Baker, 1991 Evidence for Biased Gene Conversion in Concerted Evolution of Ribosomal DNA. Science 251: 308–310. https://doi.org/10.1126/science.1987647

Hindson B. J., K. D. Ness, D. A. Masquelier, P. Belgrader, N. J. Heredia, *et al.*, 2011 High-Throughput Droplet Digital PCR System for Absolute Quantitation of DNA Copy Number. Anal Chem 83: 8604–8610. https://doi.org/10.1021/ac202028g

Hiraga S., C. Monerawela, Y. Katou, S. Shaw, K. R. Clark, *et al.*, 2018 Budding yeast Rif1 binds to replication origins and protects DNA at blocked replication forks. Embo Rep 19: e46222. https://doi.org/10.15252/embr.201846222

Houle D., B. Morikawa, and M. Lynch, 1996 Comparing mutational variabilities. Genetics 143: 1467–83.

Huang W., R. F. Lyman, R. A. Lyman, M. A. Carbone, S. T. Harbison, *et al.*, 2016 Spontaneous mutations and the origin and maintenance of quantitative genetic variation. Elife 5: e14625. https://doi.org/10.7554/elife.14625

Ide S., T. Miyazaki, H. Maki, and T. Kobayashi, 2010 Abundance of Ribosomal RNA Gene Copies Maintains Genome Integrity. Science 327: 693–696. https://doi.org/10.1126/science.1179044

Ii M., T. Ii, and S. J. Brill, 2007 Mus81 functions in the quality control of replication forks at the rDNA and is involved in the maintenance of rDNA repeat number in Saccharomyces cerevisiae. Mutat Res Fundam Mol Mech Mutagen 625: 1–19. https://doi.org/10.1016/j.mrfmmm.2007.04.007

Iida T., and T. Kobayashi, 2019a RNA Polymerase I Activators Count and Adjust Ribosomal RNA Gene Copy Number. Mol Cell 73: 645-654.e13. https://doi.org/10.1016/j.molcel.2018.11.029

Iida T., and T. Kobayashi, 2019b How do cells count multi-copy genes?: "Musical Chair" model for preserving the number of rDNA copies. Curr Genet 65: 883–885. https://doi.org/10.1007/s00294-019-00956-0

Jabot F., T. Faure, N. Dumouli, and C. Albert, 2015 EasyABC: Efficient Approximate Bayesian Computation Sampling Schemes. R package version 1.5. https://CRAN.R-project.org/package=EasyABC

James S. A., M. J. T. O'Kelly, D. M. Carter, R. P. Davey, A. van Oudenaarden, *et al.*, 2009 Repetitive sequence variation and dynamics in the ribosomal DNA array of Saccharomyces cerevisiae as revealed by whole-genome resequencing. Genome Res 19: 626–635. https://doi.org/10.1101/gr.084517.108

James T. Y., L. A. Michelotti, A. D. Glasco, R. A. Clemons, R. A. Powers, *et al.*, 2019 Adaptation by Loss of Heterozygosity in Saccharomyces cerevisiae Clones Under Divergent Selection. Genetics 213: 665–683. https://doi.org/10.1534/genetics.119.302411

Johnston M., L. Hillier, L. Riles, K. Albermann, B. André, *et al.*, 1997 The nucleotide sequence of Saccharomyces cerevisiae chromosome XII. Nature 387: 87–90. https://doi.org/10.1038/387s087

Keightley P. D., 1994 The distribution of mutation effects on viability in Drosophila melanogaster. Genetics 138: 1315–1322. https://doi.org/10.1093/genetics/138.4.1315

Keightley P. D., and T. M. Bataillon, 2000 Multigeneration maximum-likelihood analysis applied to mutation-accumulation experiments in Caenorhabditis elegans. Genetics 154: 1193–201. https://doi.org/10.1093/genetics/154.3.1193

Kim N., and S. Jinks-Robertson, 2012 Transcription as a source of genome instability. Nat Rev Genet 13: 204–214. https://doi.org/10.1038/nrg3152

Kimura M., 1965 A stochastic model concerning the maintenance of genetic variability in quantitative characters. Proc National Acad Sci 54: 731–736. https://doi.org/10.1073/pnas.54.3.731

Kobayashi T., D. J. Heck, M. Nomura, and T. Horiuchi, 1998 Expansion and contraction of ribosomal DNA repeats in Saccharomyces cerevisiae: requirement of replication fork blocking (Fob1) protein and the role of RNA polymerase I. Gene Dev 12: 3821–3830. https://doi.org/10.1101/gad.12.24.3821

Kobayashi T., M. Nomura, and T. Horiuchi, 2001 Identification of DNA cis Elements Essential for Expansion of Ribosomal DNA Repeats inSaccharomyces cerevisiae. Mol Cell Biol 21: 136–147. https://doi.org/10.1128/mcb.21.1.136-147.2001

Kobayashi T., 2003 The Replication Fork Barrier Site Forms a Unique Structure with Fob1p and Inhibits the Replication Fork. Mol Cell Biol 23: 9178–9188. https://doi.org/10.1128/mcb.23.24.9178-9188.2003

Kobayashi T., and A. R. D. Ganley, 2005 Recombination Regulation by Transcription-Induced Cohesin Dissociation in rDNA Repeats. Science 309: 1581–1584. https://doi.org/10.1126/science.1116102

Kobayashi T., 2006 Strategies to maintain the stability of the ribosomal RNA gene repeats. Genes Genet Syst 81: 155–161. https://doi.org/10.1266/ggs.81.155

Kobayashi T., 2011 Regulation of ribosomal RNA gene copy number and its role in modulating genome integrity and evolutionary adaptability in yeast. Cell Mol Life Sci 68: 1395–1403. https://doi.org/10.1007/s00018-010-0613-2

Kobayashi T., 2014 Ribosomal RNA gene repeats, their stability and cellular senescence. Proc Jpn Acad Ser B Phys Biological Sci 90: 119–129. https://doi.org/10.2183/pjab.90.119

Koboldt D. C., Q. Zhang, D. E. Larson, D. Shen, M. D. McLellan, *et al.*, 2012 VarScan 2: Somatic mutation and copy number alteration discovery in cancer by exome sequencing. Genome Res 22: 568–576. https://doi.org/10.1101/gr.129684.111

Köressaar T., and M. Remm, 2007 Enhancements and modifications of primer design program Primer3. Bioinform Oxf Engl 23: 1289–91. https://doi.org/10.1093/bioinformatics/btm091

Köressaar T., M. Lepamets, L. Kaplinski, K. Raime, R. Andreson, *et al.*, 2018 Primer3_masker: integrating masking of template sequence with primer design software. Bioinformatics 34: 1937–1938. https://doi.org/10.1093/bioinformatics/bty036

Kwan E. X., E. J. Foss, S. Tsuchiyama, G. M. Alvino, L. Kruglyak, *et al.*, 2013 A Natural Polymorphism in rDNA Replication Origins Links Origin Activation with Calorie Restriction and Lifespan. Plos Genet 9: e1003329. https://doi.org/10.1371/journal.pgen.1003329

Kwan E. X., X. S. Wang, H. M. Amemiya, B. J. Brewer, and M. K. Raghuraman, 2016 rDNA Copy Number Variants Are Frequent Passenger Mutations in Saccharomyces cerevisiae Deletion Collections and de Novo Transformants. G3 Genes Genomes Genetics 6: 2829–2838. https://doi.org/10.1534/g3.116.030296

Lande R., and S. J. Arnold, 1983 The measurement of selection on correlated characters. Evolution 37: 1210–1226. https://doi.org/10.1111/j.1558-5646.1983.tb00236.x

Li H., and R. Durbin, 2009 Fast and accurate short read alignment with Burrows–Wheeler transform. Bioinformatics 25: 1754–1760. https://doi.org/10.1093/bioinformatics/btp324

Li H., B. Handsaker, A. Wysoker, T. Fennell, J. Ruan, *et al.*, 2009 The Sequence Alignment/Map format and SAMtools. Bioinformatics 25: 2078–2079. https://doi.org/10.1093/bioinformatics/btp352

Li H., 2011 A statistical framework for SNP calling, mutation discovery, association mapping and population genetical parameter estimation from sequencing data. Bioinformatics 27: 2987–2993. https://doi.org/10.1093/bioinformatics/btr509

Lindstrom D. L., C. K. Leverich, K. A. Henderson, and D. E. Gottschling, 2011 Replicative Age Induces Mitotic Recombination in the Ribosomal RNA Gene Cluster of Saccharomyces cerevisiae. Plos Genet 7: e1002015. https://doi.org/10.1371/journal.pgen.1002015

Lindström M. S., D. Jurada, S. Bursac, I. Orsolic, J. Bartek, *et al.*, 2018 Nucleolus as an emerging hub in maintenance of genome stability and cancer pathogenesis. Oncogene 37: 2351–2366. https://doi.org/10.1038/s41388-017-0121-z

Liu H., and J. Zhang, 2019 Yeast Spontaneous Mutation Rate and Spectrum Vary with Environment. Curr Biol 29: 1584-1591.e3. https://doi.org/10.1016/j.cub.2019.03.054

Liu H., and J. Zhang, 2021 The rate and molecular spectrum of mutation are selectively maintained in yeast. Nat Commun 12: 4044. https://doi.org/10.1038/s41467-021-24364-6

Lofgren L. A., J. K. Uehling, S. Branco, T. D. Bruns, F. Martin, *et al.*, 2019 Genome-based estimates of fungal rDNA copy number variation across phylogenetic scales and ecological lifestyles. Mol Ecol 28: 721–730. https://doi.org/10.1111/mec.14995

Lu J., A. Johnston, P. Berichon, K. Ru, D. Korbie, *et al.*, 2017 PrimerSuite: A High-Throughput Web-Based Primer Design Program for Multiplex Bisulfite PCR. Sci Rep-uk 7: 41328. https://doi.org/10.1038/srep41328

Lynch M., and B. Walsh, 1998 *Genetics and analysis of quantitative traits*. Sinauer, Sunderland MA.

Mansisidor A., T. Molinar, P. Srivastava, D. D. Dartis, A. P. Delgado, *et al.*, 2018 Genomic Copy-Number Loss Is Rescued by Self-Limiting Production of DNA Circles. Mol Cell 72: 583-593.e4. https://doi.org/10.1016/j.molcel.2018.08.036

Marjoram P., J. Molitor, V. Plagnol, and S. Tavaré, 2003 Markov chain Monte Carlo without likelihoods. Proc National Acad Sci 100: 15324–15328. https://doi.org/10.1073/pnas.0306899100

Mattarocci S., J. K. Reinert, R. D. Bunker, G. A. Fontana, T. Shi, *et al.*, 2017 Rif1 maintains telomeres and mediates DNA repair by encasing DNA ends. Nat Struct Mol Biol 24: 588–595. https://doi.org/10.1038/nsmb.3420

Michel A. H., B. Kornmann, K. Dubrana, and D. Shore, 2005 Spontaneous rDNA copy number variation modulates Sir2 levels and epigenetic gene silencing. Gene Dev 19: 1199–1210. https://doi.org/10.1101/gad.340205

Morton E. A., A. N. Hall, E. Kwan, C. Mok, K. Queitsch, *et al.*, 2019 Challenges and Approaches to Genotyping Repetitive DNA. G3 Genes Genomes Genetics 10: 417–430. https://doi.org/10.1534/g3.119.400771

Nelson J. O., G. J. Watase, N. Warsinger-Pepe, and Y. M. Yamashita, 2019 Mechanisms of rDNA Copy Number Maintenance. Trends Genet 35: 734–742. https://doi.org/10.1016/j.tig.2019.07.006

Pankajam A. V., S. Dash, A. Saifudeen, A. Dutta, and K. T. Nishant, 2020 Loss of Heterozygosity and Base Mutation Rates Vary Among Saccharomyces cerevisiae Hybrid Strains. G3 Genes Genomes Genetics 10: 3309–3319. https://doi.org/10.1534/g3.120.401551

Paredes S., A. T. Branco, D. L. Hartl, K. A. Maggert, and B. Lemos, 2011 Ribosomal DNA Deletions Modulate Genome-Wide Gene Expression: "rDNA–Sensitive" Genes and Natural Variation. Plos Genet 7: e1001376. https://doi.org/10.1371/journal.pgen.1001376

Peter J., M. D. Chiara, A. Friedrich, J.-X. Yue, D. Pflieger, *et al.*, 2018 Genome evolution across 1,011 Saccharomyces cerevisiae isolates. Nature 556: 339–344. https://doi.org/10.1038/s41586-018-0030-5

Phung H. T. T., D. H. Tran, and T. X. Nguyen, 2020 The cruciform DNA-binding protein Crp1 stimulates the endonuclease activity of Mus81–Mms4 in Saccharomyces cerevisiae. Febs Lett 594: 4320–4337. https://doi.org/10.1002/1873-3468.13931

R Core Team, 2021 *R: A language and environment for statistical computing*. R Foundation for Statistical Computing, Vienna, Austria.

Saka K., A. Takahashi, M. Sasaki, and T. Kobayashi, 2016 More than 10% of yeast genes are related to genome stability and influence cellular senescence via rDNA maintenance. Nucleic Acids Res 44: 4211–4221. https://doi.org/10.1093/nar/gkw110

Salim D., W. D. Bradford, A. Freeland, G. Cady, J. Wang, *et al.*, 2017 DNA replication stress restricts ribosomal DNA copy number. Plos Genet 13: e1007006. https://doi.org/10.1371/journal.pgen.1007006

Salim D., and J. L. Gerton, 2019 Ribosomal DNA instability and genome adaptability. Chromosome Res 27: 73–87. https://doi.org/10.1007/s10577-018-9599-7

Sehnal D., S. Bittrich, M. Deshpande, R. Svobodová, K. Berka, *et al.*, 2021 Mol* Viewer: modern web app for 3D visualization and analysis of large biomolecular structures. Nucleic Acids Res 49: W431–W437. https://doi.org/10.1093/nar/gkab314

Sharma D., S. H.-L. Denmat, N. J. Matzke, K. Hannan, R. D. Hannan, *et al.*, 2021 A new method for determining ribosomal DNA copy number shows differences between Saccharomyces cerevisiae populations. Biorxiv 2021.01.21.427686. https://doi.org/10.1101/2021.01.21.427686

Sharp N. P., and A. F. Agrawal, 2018 An experimental test of the mutation-selection balance model for the maintenance of genetic variance in fitness components. Proc Royal Soc B 285: 20181864. https://doi.org/10.1098/rspb.2018.1864

Sharp N. P., L. Sandell, C. G. James, and S. P. Otto, 2018 The genome-wide rate and spectrum of spontaneous mutations differ between haploid and diploid yeast. Proc National Acad Sci 115: 201801040. https://doi.org/10.1073/pnas.1801040115

Shyian M., S. Mattarocci, B. Albert, L. Hafner, A. Lezaja, *et al.*, 2016 Budding Yeast Rif1 Controls Genome Integrity by Inhibiting rDNA Replication. Plos Genet 12: e1006414. https://doi.org/10.1371/journal.pgen.1006414

Stinchcombe J. R., A. F. Agrawal, P. A. Hohenlohe, S. J. Arnold, and M. W. Blows, 2008 Estimating Nonlinear Selection Gradients Using Quadratic Regression Coefficients: Double Or Nothing. Evolution 62: 2435–2440. https://doi.org/10.1111/j.1558-5646.2008.00449.x

Sudmant P. H., J. O. Kitzman, F. Antonacci, C. Alkan, M. Malig, *et al.*, 2010 Diversity of Human Copy Number Variation and Multicopy Genes. Science 330: 641–646. https://doi.org/10.1126/science.1197005

Symonová R., 2019 Integrative rDNAomics—Importance of the Oldest Repetitive Fraction of the Eukaryote Genome. Genes 10: 345. https://doi.org/10.3390/genes10050345

Thu H. P. T., T. A. Nguyen, P. R. Munashingha, B. Kwon, Q. D. Van, *et al.*, 2015 A physiological significance of the functional interaction between Mus81 and Rad27 in homologous recombination repair. Nucleic Acids Res 43: 1684–1699. https://doi.org/10.1093/nar/gkv025

Tsai I. J., D. Bensasson, A. Burt, and V. Koufopanou, 2008 Population genomics of the wild yeast Saccharomyces paradoxus: Quantifying the life cycle. Proc National Acad Sci 105: 4957–4962. https://doi.org/10.1073/pnas.0707314105

Untergasser A., I. Cutcutache, T. Koressaar, J. Ye, B. C. Faircloth, *et al.*, 2012 Primer3—new capabilities and interfaces. Nucleic Acids Res 40: e115–e115. https://doi.org/10.1093/nar/gks596

Walsh B., and M. Lynch, 2018 *Evolution and Selection of Quantitative Traits*. Oxford University Press, Oxford UK.

Wang M., and B. Lemos, 2017 Ribosomal DNA copy number amplification and loss in human cancers is linked to tumor genetic context, nucleolus activity, and proliferation. Plos Genet 13: e1006994. https://doi.org/10.1371/journal.pgen.1006994

Wegmann D., C. Leuenberger, S. Neuenschwander, and L. Excoffier, 2010 ABCtoolbox: a versatile toolkit for approximate Bayesian computations. Bmc Bioinformatics 11: 116. https://doi.org/10.1186/1471-2105-11-116

Figure 1: The genomic region of interest. The two rDNA repeats in the reference genome are shown, with grey boxes indicating genes drawn to scale; not all genes are labeled. The upper panel shows the median relative coverage pattern across MA lines relative to the genomic baseline, illustrating variation in relative coverage across the region. The regions used for ddPCR analyses are shown in red, and are flanked by DraI restriction sites (green triangles). The regions of the genome where relative coverage best reflects the ddPCR-based CN estimates are shown in blue.

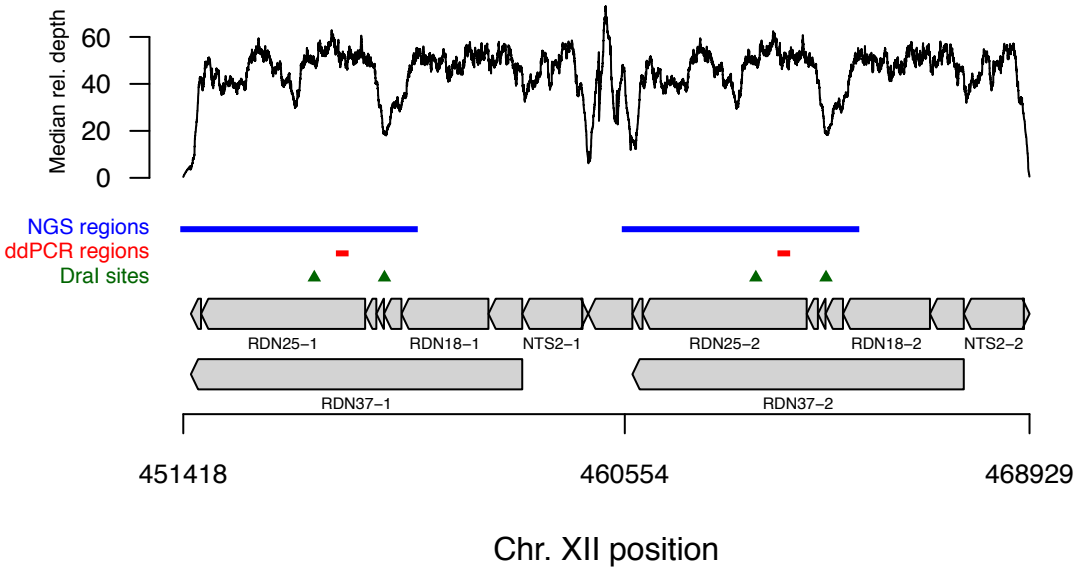
Median rel. depth
60
40
20
0
NGS regions
ddPCR regions
DraI sites
RDN25−1
RDN18−1
NTS2−1
RDN25−2
RDN18−2
NTS2−2
RDN37−1
RDN37−2
451418
460554
468929
Chr. XII position

Figure 2: Comparison of CN estimates from ddPCR versus sequencing coverage. The CN inferred based on ddPCR is strongly correlated with CN inferred from sequencing coverage of selected regions from the corresponding strains (blue regions in Fig. 1, $r^2 = 0.78$), considering both haploid and diploid strains.

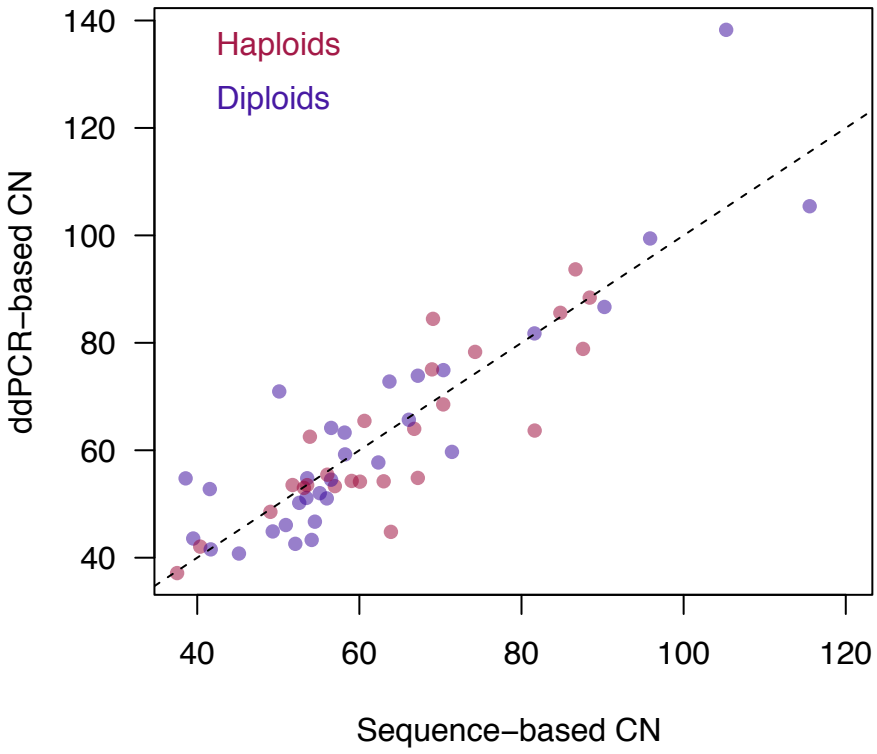
Haploids
Diploids
ddPCR−based CN
Sequence−based CN
140
120
100
80
60
40
40
60
80
100
120

Figure 3: Change in CN under mutation accumulation in haploids and diploids. The number of generations of MA is based on cell counts performed throughout the experiment (Sharp *et al.* 2018). Some lines were lost during the experiment and re-initiated from previously-frozen timepoints, and so some lines experienced fewer generations of MA.

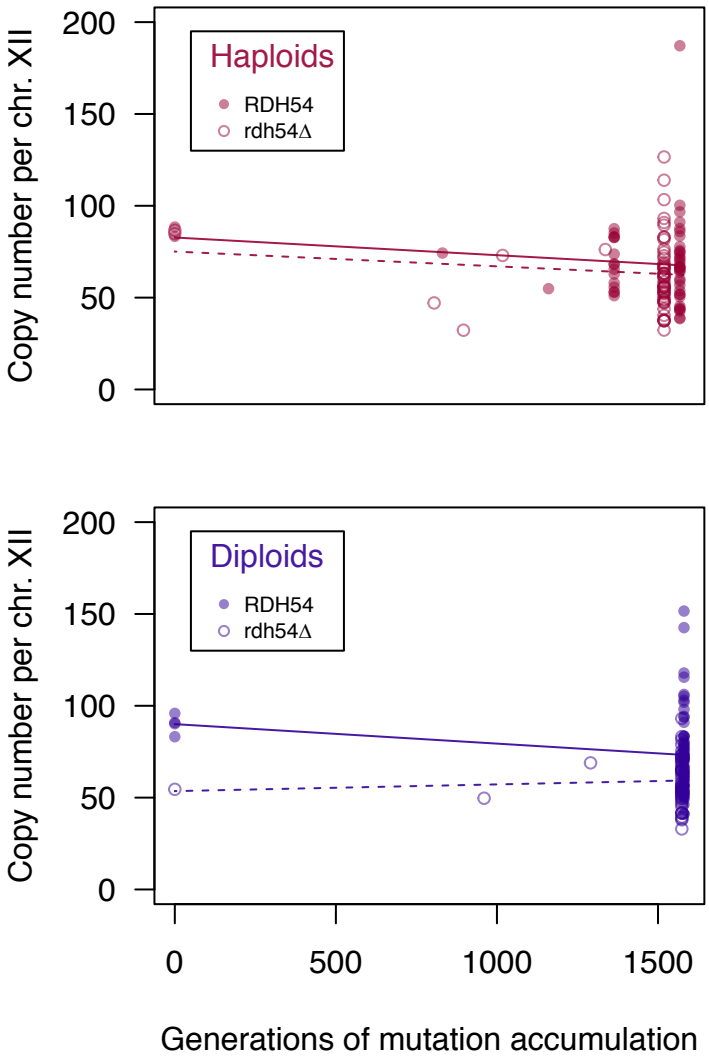
Haploids
RDH54
rdh54Δ
Diploids
RDH54
rdh54Δ
Copy number per chr. XII
Copy number per chr. XII
200
150
100
50
0
0
500
1000
1500
Generations of mutation accumulation

Figure 4. CN following mutation accumulation in alternative environments. CN estimates for the MA lines of Liu and Zhang (2019) maintained in seven different media environments, shown as violin plots. White dots represent medians. The ancestral CN value is indicated with a horizontal dashed line.

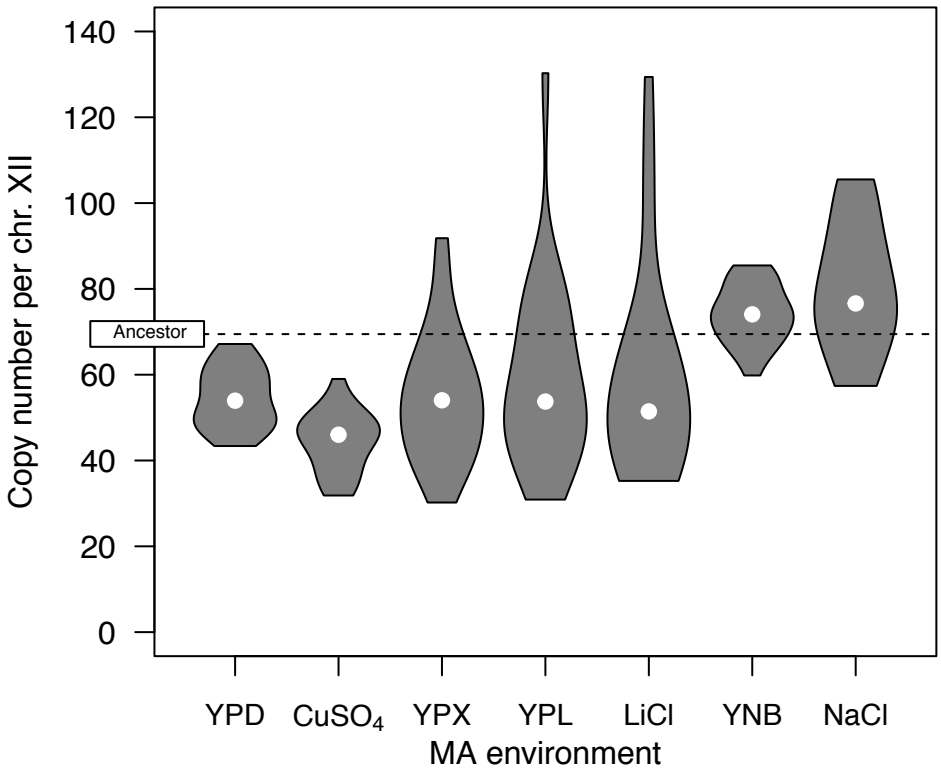
140
120
100
80
60
40
20
0
Copy number per chr. XII
Ancestor
YPD
CuSO4
YPX
YPL
LiCl
YNB
NaCl
MA environment

Figure 5. Relationship between CN and fitness in haploids and diploids. Quadratic regression fits are shown; shaded regions represent 95% confidence bands. The ancestral condition is indicated by a black dot at the origin.

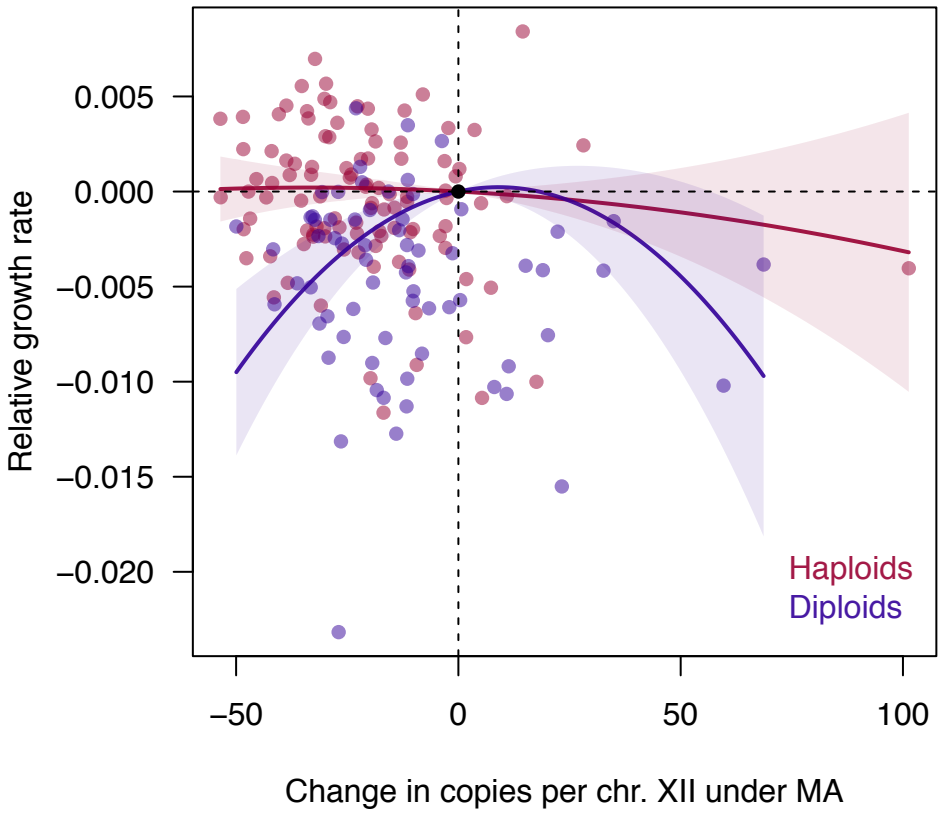
0.005
0.000
−0.005
−0.010
−0.015
−0.020
Relative growth rate
−50
0
50
100
Change in copies per chr. XII under MA
Haploids
Diploids

Figure 6. CN distributions in wild strains and MA lines. Density plots of CN for 788 natural isolates (Sharma *et al*. 2021, green), and *RDH54*+ MA lines (Sharp *et al*. 2018 lines, purple). Triangles indicate the mean for natural isolates and the ancestral value for MA lines. The distribution shown for MA lines is weighted to match the relative frequency of haploids and diploids among the wild isolates.

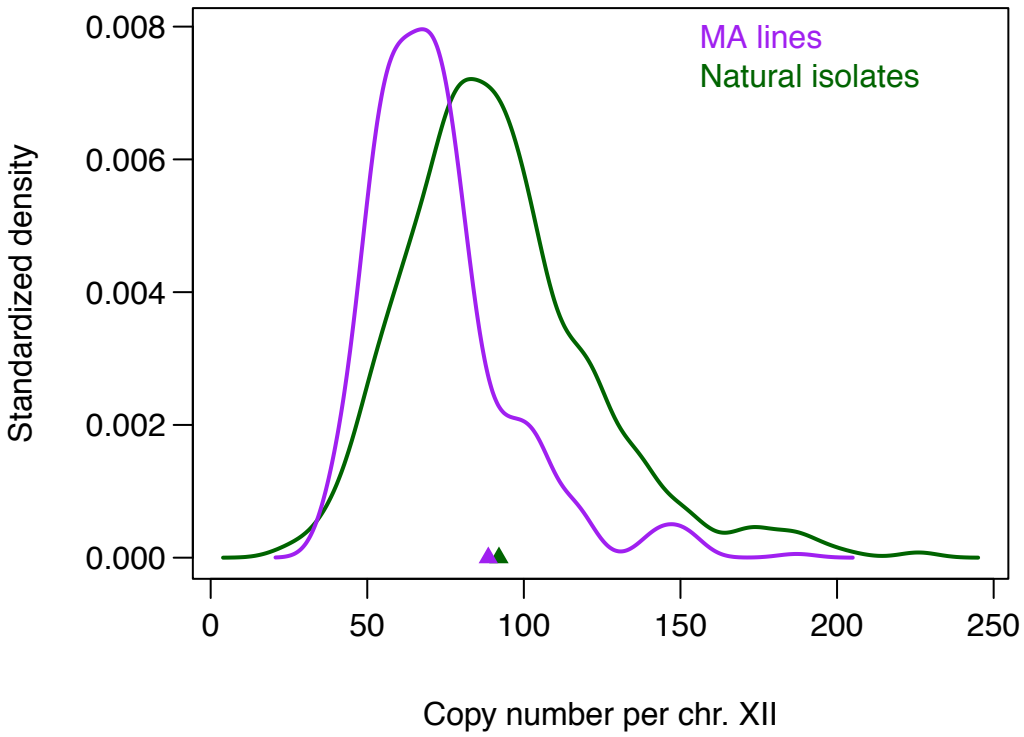
MA lines
Natural isolates
Standardized density
0.008
0.006
0.004
0.002
0.000
0
50
100
150
200
250
Copy number per chr. XII

Figure 7. Effects of specific genetic variants on CN. In each panel CN values are plotted with random horizontal jitter. (A) A high-CN haploid strain has a mutation in *RIF1* that plausibly affects CN maintenance, whereas other mutations in this gene among the lines do not appear to affect CN (open circles; see also Fig. S5). The diploid lines with highest and lowest CN values have heterozygous or homozygous mutations in genes implicated in CN maintenance (open circles). (B) A screen of GO terms identified nonsynonymous mutations in 'regulation of cell cycle' genes as a significant predictor of CN after multiple test correction. Lines indicate linear model fits for haploids and diploids. (C) MA lines that gained a copy of chromosome XII have lower CN than both haploids and non-aneuploid diploids; different letters indicate groups that differ significantly.

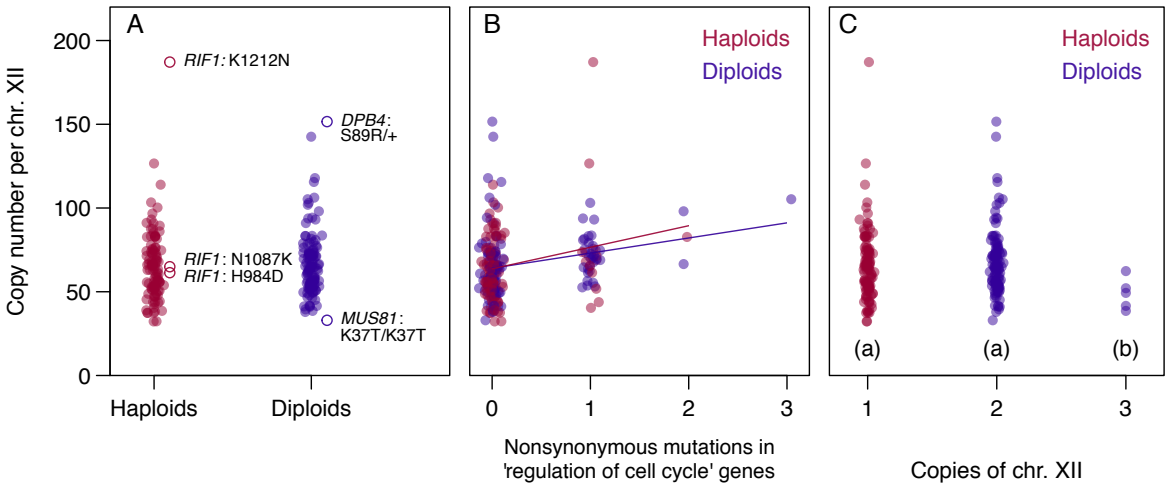
A
B
C
Copy number per chr. XII
200
150
100
50
0
RIF1: K1212N
DPB4: S89R/+
RIF1: N1087K
RIF1: H984D
MUS81: K37T/K37T
Haploids
Diploids
Haploids
Diploids
Haploids
Diploids
(a)
(a)
(b)
0
1
2
3
1
2
3
Nonsynonymous mutations in 'regulation of cell cycle' genes
Copies of chr. XII

Figure 8. Mutations within the rDNA locus. Variants detected in haploid and diploid lines are pooled for these analyses. Note that some mutations likely occurred in this region that were later lost and not detected. (A) Estimated number of copies containing each variant, based on variant frequencies and CN estimates. Most variants within the rDNA locus affect only one or a few copies, with rare cases found in many copies. (B) The substitution spectrum at the rDNA locus differs from the genome-wide spectrum in the corresponding MA lines (based on 1899 single-nucleotide substitutions; complementary changes are included). (C) Spatial distribution of variants across the locus (one copy, with some genes indicated below). Variants occur more often in the NTS regions. (D) The number of polymorphisms in 100-bp windows across the locus (based on James *et al.* 2009) is positively correlated with the number of mutations observed in the window.

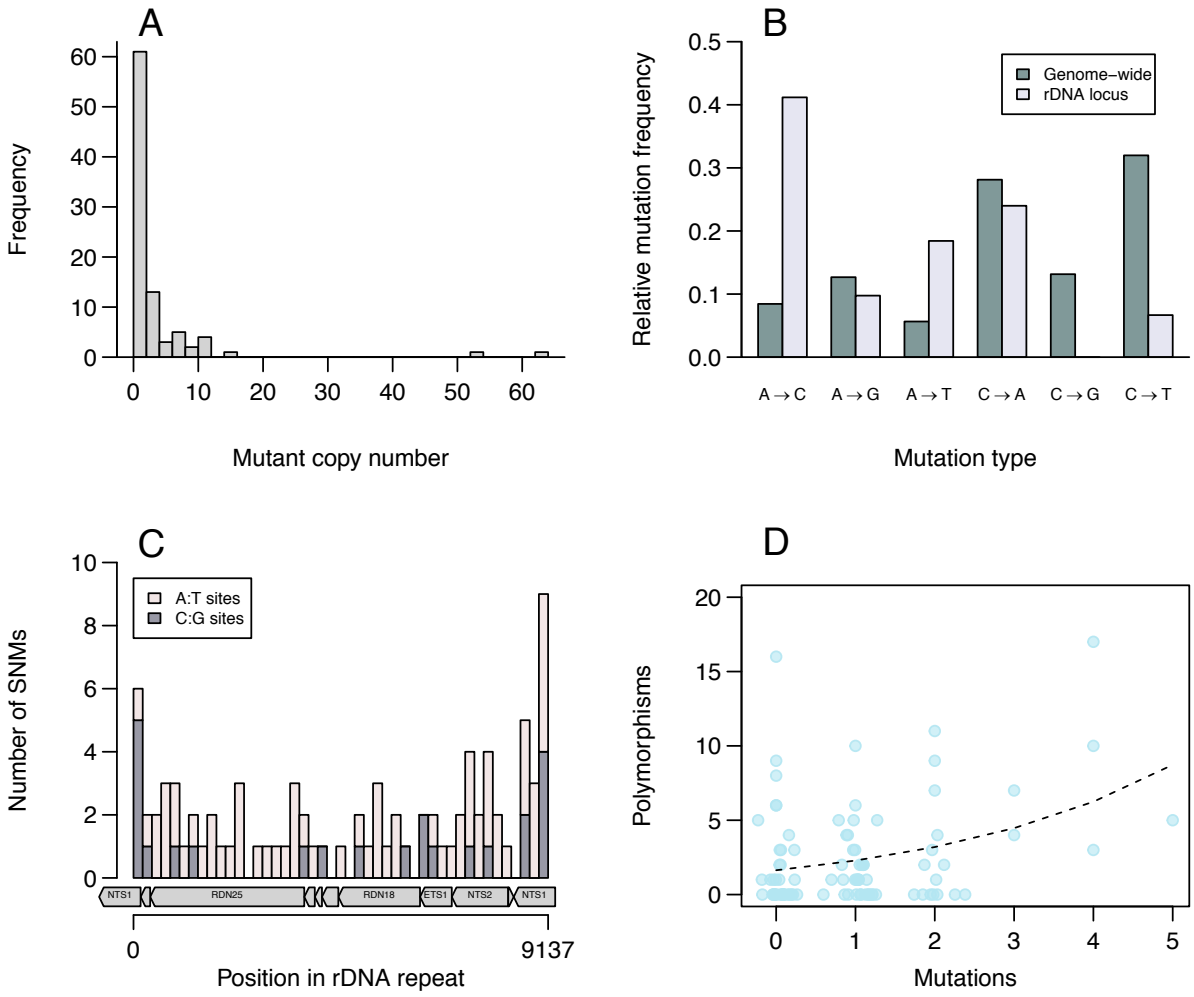
A
Frequency
Mutant copy number
B
Relative mutation frequency
Genome−wide
rDNA locus
A→C
A→G
A→T
C→A
C→G
C→T
Mutation type
C
Number of SNMs
A:T sites
C:G sites
NTS1
RDN25
RDN18
ETS1
NTS2
NTS1
0
9137
Position in rDNA repeat
D
Polymorphisms
Mutations

Figure S1. Results of ABC model of mutation rates and effects. In plots of posterior density the modal value is indicated with a dashed line. (A). Posterior density for the rate of mutations affecting CN per genome per generation. (B). Posterior density for the probability that a mutation increases rather than decreases CN. (C). The number of mutations expected in each MA line that decrease or increase CN given the results shown in panels A and B. (D). Posterior density for the mean effect of mutations that cause CN reduction. (E). Posterior density for the variance in effects of mutations that cause CN reduction. (F). Inferred distribution of effects for mutations that cause CN reduction given the results shown in panels D and E. (G). Posterior density for the mean effect of mutations that cause CN increase. (H). Posterior density for the variance in effects of mutations that cause CN increase. (I). Inferred distribution of effects for mutations that cause CN increase given the results shown in panels G and H.

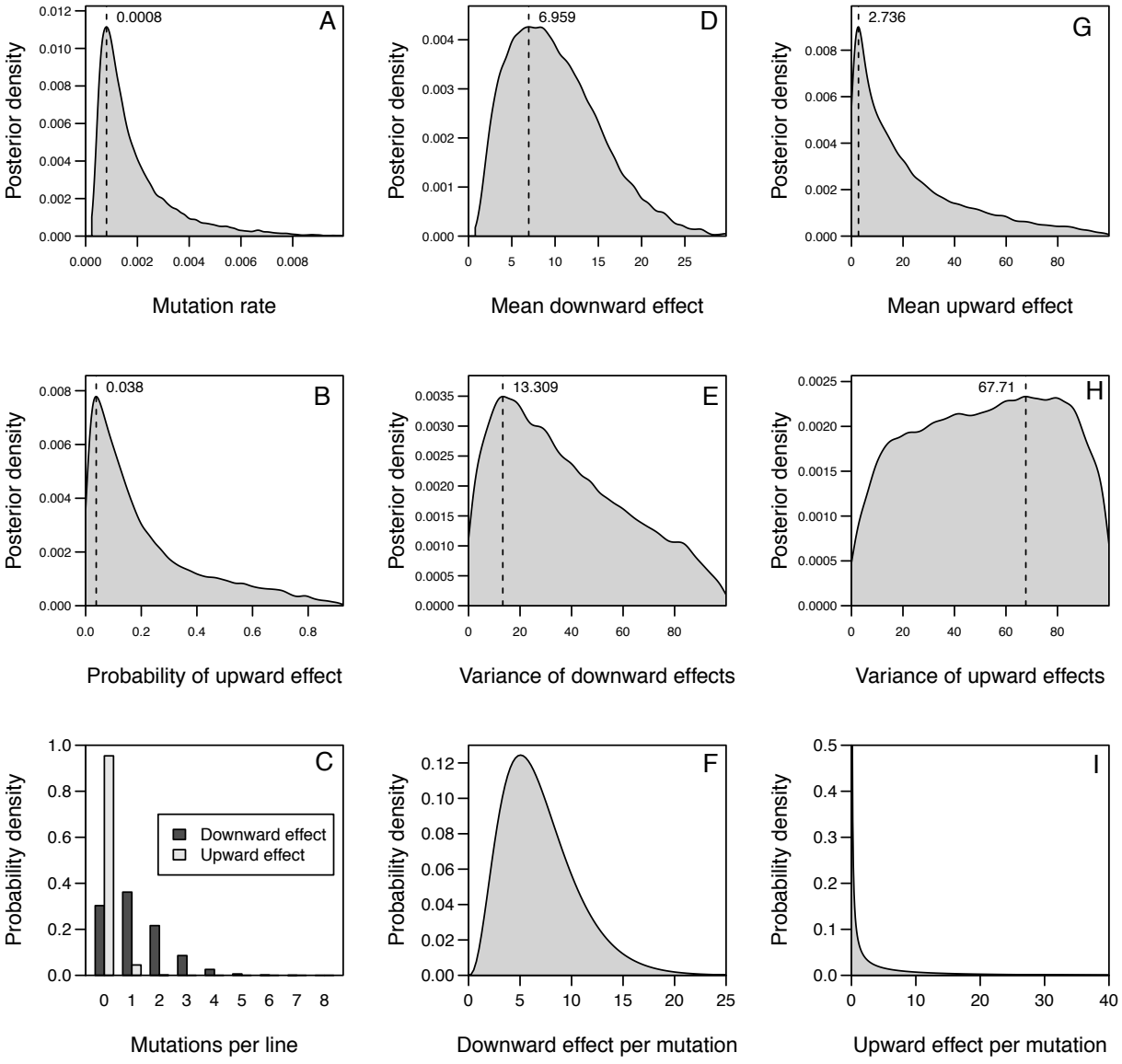
A
0.0008
Posterior density
Mutation rate
D
6.959
Posterior density
Mean downward effect
G
2.736
Posterior density
Mean upward effect
B
0.038
Posterior density
Probability of upward effect
E
13.309
Posterior density
Variance of downward effects
H
67.71
Posterior density
Variance of upward effects
C
Downward effect
Upward effect
Probability density
Mutations per line
F
Probability density
Downward effect per mutation
I
Probability density
Upward effect per mutation

Figure S2. Results of ABC model of mutation rates and effects, for diploids only. See Fig. S1 legend for description of each panel.

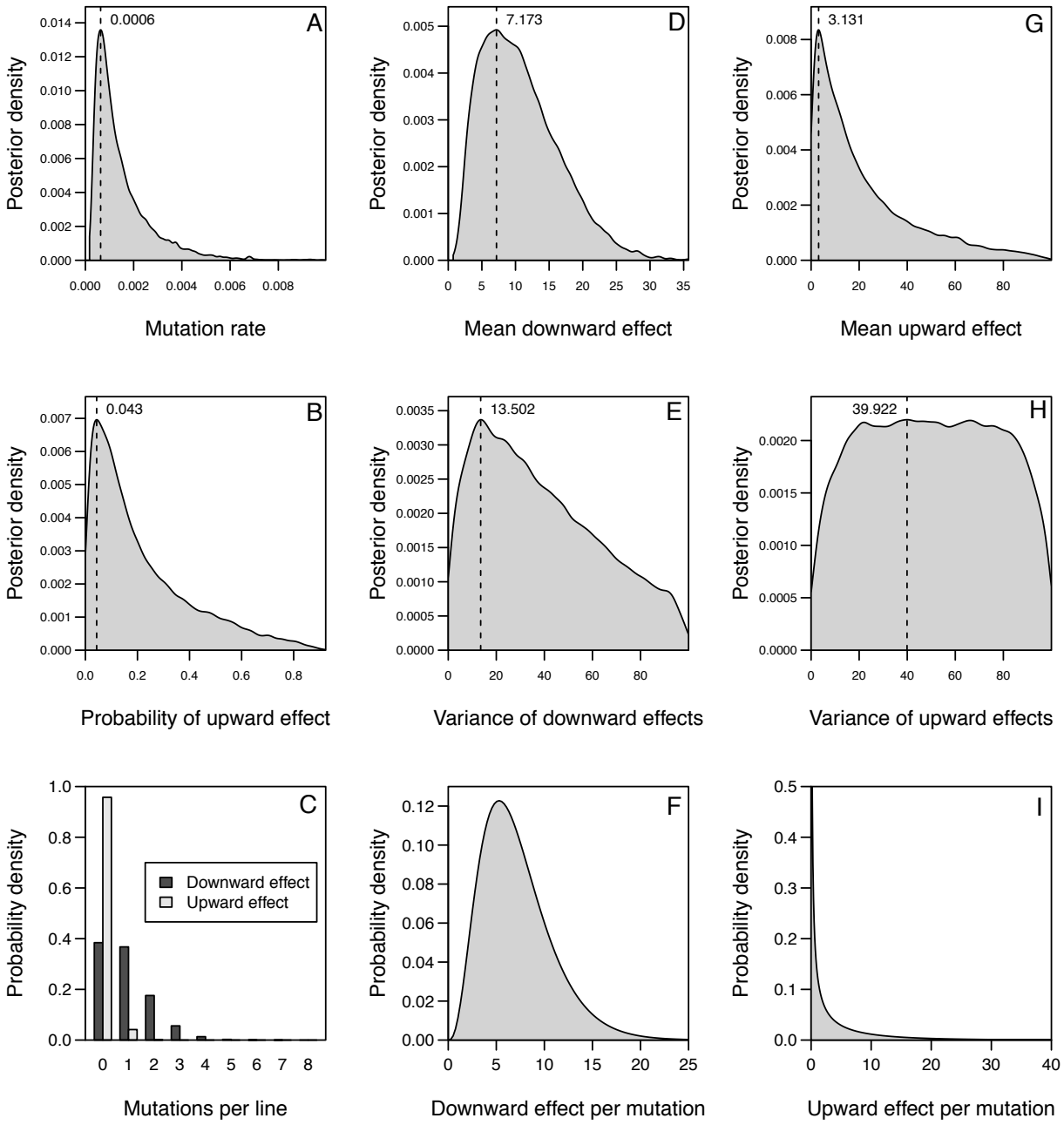
A
0.0006
Posterior density
Mutation rate
D
7.173
Posterior density
Mean downward effect
G
3.131
Posterior density
Mean upward effect
B
0.043
Posterior density
Probability of upward effect
E
13.502
Posterior density
Variance of downward effects
H
39.922
Posterior density
Variance of upward effects
C
Downward effect
Upward effect
Probability density
Mutations per line
F
Probability density
Downward effect per mutation
I
Probability density
Upward effect per mutation

Figure S3. Results of ABC model of mutation rates and effects, for haploids only. See Fig. S1 legend for description of each panel.

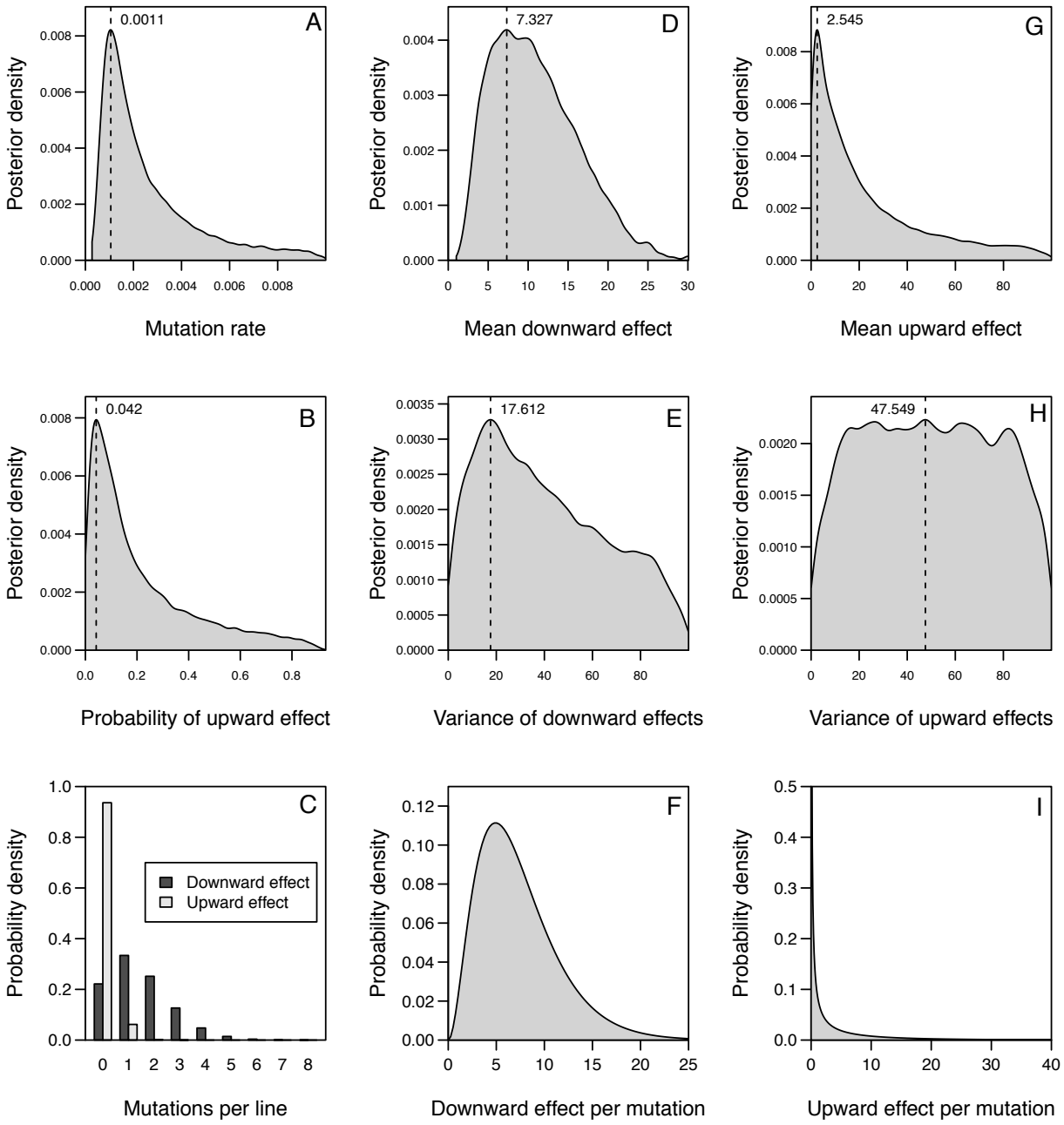
A
0.0011
Posterior density
Mutation rate
D
7.327
Posterior density
Mean downward effect
G
2.545
Posterior density
Mean upward effect
B
0.042
Posterior density
Probability of upward effect
E
17.612
Posterior density
Variance of downward effects
H
47.549
Posterior density
Variance of upward effects
C
Downward effect
Upward effect
Probability density
Mutations per line
F
Probability density
Downward effect per mutation
I
Probability density
Upward effect per mutation

Figure S4. Results of ABC model of mutation rates and effects, when mutations affect the rate of CN change. See Fig. S1 legend for description of each panel.

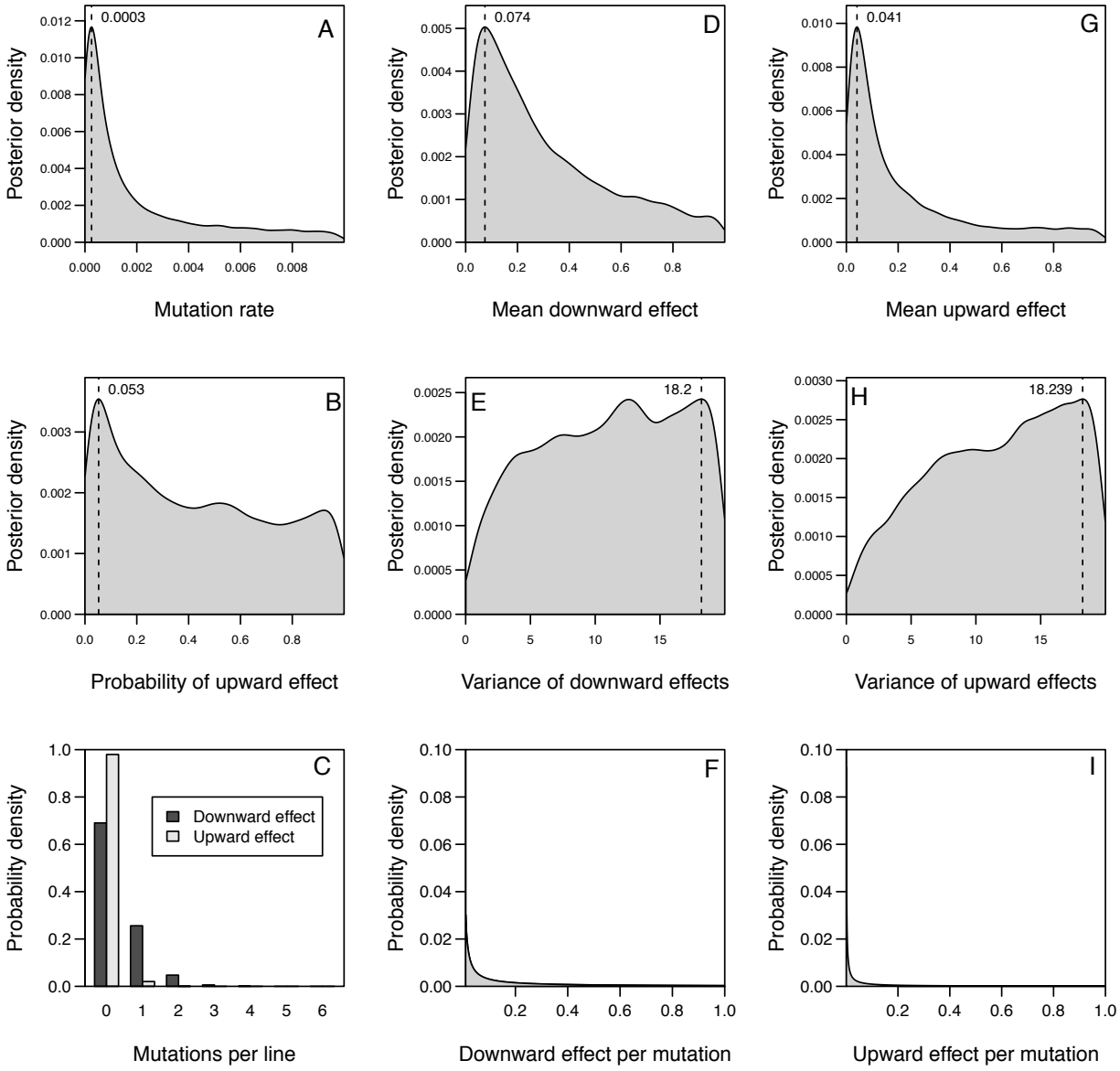
A
0.0003
Posterior density
Mutation rate
D
0.074
Posterior density
Mean downward effect
G
0.041
Posterior density
Mean upward effect
B
0.053
Posterior density
Probability of upward effect
E
18.2
Posterior density
Variance of downward effects
H
18.239
Posterior density
Variance of upward effects
C
Downward effect
Upward effect
Probability density
Mutations per line
F
Probability density
Downward effect per mutation
I
Probability density
Upward effect per mutation

Figure S5. Mutations in RIF1 in relation to protein structure. The Rif1 homodimer (PDB 5NW5) is shown in orange and green; DNA is shown in pink and purple. Mutation K1212N is predicted to affect the interaction with DNA, unlike N1087K or H984D.

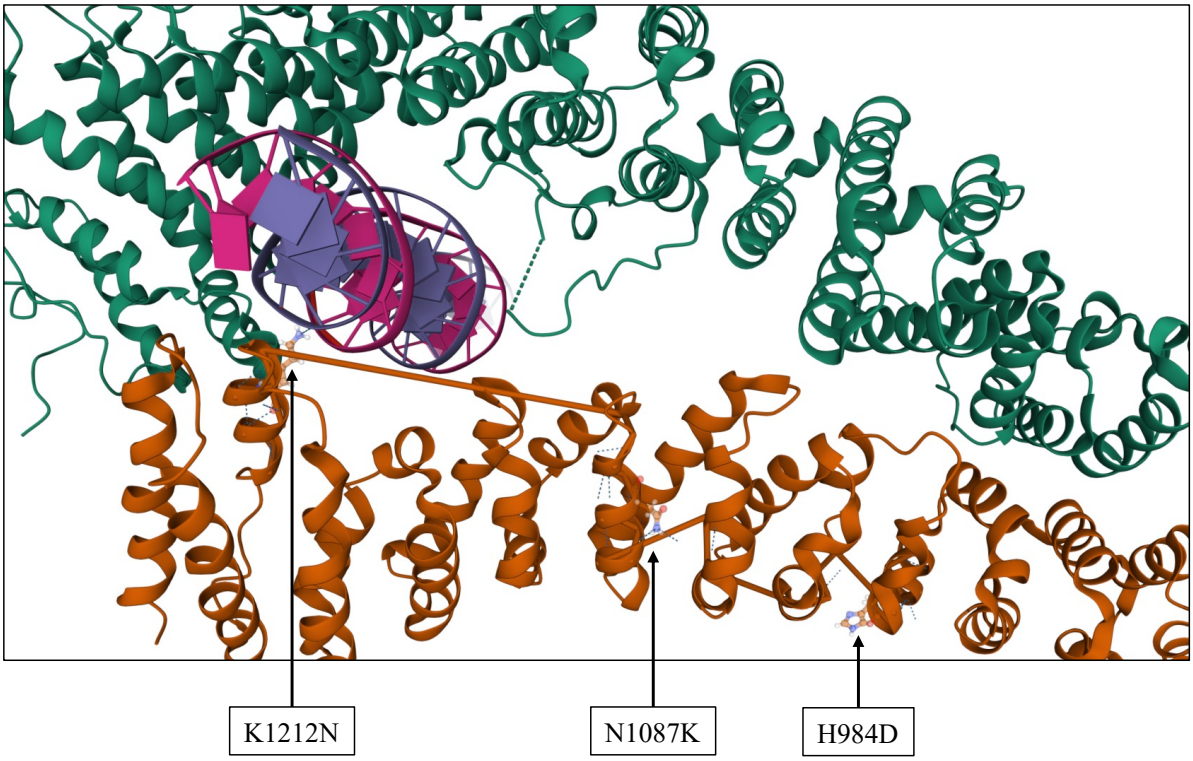
K1212N
N1087K
H984D

Figure S6. Results of ABC model of LOH rates. The posterior density for the rate of LOH is shown, along with the posterior mode (dashed line).

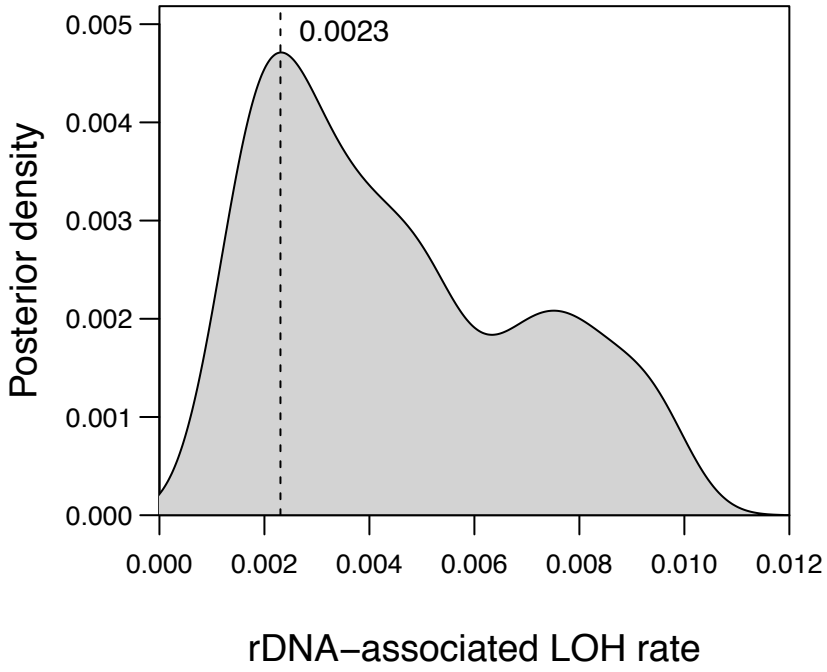
0.0023
Posterior density
0.005
0.004
0.003
0.002
0.001
0.000
0.000
0.002
0.004
0.006
0.008
0.010
0.012
rDNA−associated LOH rate

Table S1. Sequences of primers and probes used for ddPCR.

Gene	Type	Sequence
RAD5	Forward primer	5’-GCTAGCAAAACCTATATTAAAAAC
RAD5	Reverse primer	5’-GTGAGGACAAGATAAAACTAAAG
RAD5	Probe	5’-VIC/ATCAGATGAAATGGGGTTGGGTA/MGB/NFQ
RDN25	Forward primer	5’-TGAAATTGTTGAAAGGGAAG
RDN25	Reverse primer	5’-GGCAAGCTACATTCCTA
RDN25	Probe	5’-6FAM/CTCCTTGTGGGTAGGGGAATC/MGB/NFQ